JOHANNES GUTENBERG
UNIVERSITÄT MAINZ

FIELD OF SCIENCE: NATURAL SCIENCES

SCIENTIFIC DISCIPLINE: PHYSICAL SCIENCES

DOCTORAL THESIS

Observation of top-quark pair production in heavy-ion collisions in the ATLAS experiment at the LHC

Author: Patrycja Potępa

First supervisor: prof. dr hab. inż. Iwona Grabowska-Bołd
Second supervisor: Prof. Dr. Matthias Schott

Completed in: Faculty of Physics and Applied Computer Science,
AGH University of Krakow,

Faculty of Physics, Mathematics and Computer Science,
Johannes Gutenberg University Mainz

Kraków, 2025

Abstract

Hard probes are expected to provide crucial input for nuclear parton distribution functions (nPDF), as well as to bring valuable insights into the quark-gluon plasma (QGP). In this thesis, measurements of heavy-ion collisions using top quarks in the ATLAS experiment at the Large Hadron Collider are presented. Analysed data from proton–lead (p+Pb) and lead–lead (Pb+Pb) collisions were collected with the ATLAS detector during Run 2 (2015–2018) at a nucleon–nucleon centre-of-mass energy of $\sqrt{s_{\mathrm{NN}}} = 8.16$ TeV and $\sqrt{s_{\mathrm{NN}}} = 5.02$ TeV, respectively.

Electrons play an important role in the top-quark pair ($t\bar{t}$) decay modes, specifically in the ℓ+jets and dilepton channels, which involve electrons in the final state. Electron performance is evaluated in p+Pb and Pb+Pb collisions, using electrons from the $Z \to e^+e^-$ resonance decay. Electron scale-factor corrections are derived in p+Pb collisions and applied in the measurement of $t\bar{t}$ production. Moreover, electron identification is optimised for Pb+Pb collisions and currently serves as the baseline approach in Run 3 (2022–2026).

The $t\bar{t}$ process is studied in the ℓ+jets and dilepton channels in p+Pb collisions. The inclusive $t\bar{t}$ cross-section is measured with the total relative uncertainty of 9%, leading to the most precise $t\bar{t}$ cross-section measurement in heavy-ion collisions achieved so far. The signal significance exceeds five standard deviations separately in the ℓ+jets and dilepton modes, resulting in the first observation of $t\bar{t}$ production in the dilepton channel in p+Pb collisions. The nuclear modification factor for the $t\bar{t}$ process is also extracted for the first time. The results are in agreement with theoretical predictions for various state-of-the-art nPDF sets.

The production of $t\bar{t}$ pairs is also analysed in the dilepton decay mode in Pb+Pb collisions. The inclusive $t\bar{t}$ cross-section is extracted with the total relative uncertainty of 31%, providing the most precise $t\bar{t}$ cross-section measurement in Pb+Pb collisions to date. The observed signal significance amounts to 5.0 standard deviations, establishing the first observation of the $t\bar{t}$ process in Pb+Pb collisions. The obtained result is consistent with the measurement by the CMS Collaboration and theoretical predictions based on the latest nPDF sets.

The conducted studies open a new path for further research on heavy-ion collisions at ultra-relativistic energies. The precise measurement of $t\bar{t}$ production in p+Pb collisions provides valuable input for constraining nPDFs in the high Bjorken-x region. The observation of the $t\bar{t}$ process in Pb+Pb collisions marks the start of the heavy-ion program with top quarks, and in particular, opens a possibility of exploring the time structure of the QGP in the future.

Streszczenie

Twarde sondy są kluczowym źródłem informacji dla nuklearnych funkcji dystrybucji partonów (nPDF), a także dostarczają cenny wgląd w plazmę kwarkowo-gluonową (QGP). W niniejszej pracy przedstawiono pomiary zderzeń ciężkich jonów z wykorzystaniem kwarków szczytowych w eksperymencie ATLAS na Wielkim Zderzaczu Hadronów. Analizowane dane ze zderzeń proton–ołów (p+Pb) i ołów–ołów (Pb+Pb) zostały zebrane za pomocą detektora ATLAS podczas drugiej kampanii zbierania danych (2015–2018) przy energii środka masy na parę nukleonów wynoszącej odpowiednio $\sqrt{s_{\mathrm{NN}}} = 8.16$ TeV i $\sqrt{s_{\mathrm{NN}}} = 5.02$ TeV.

Elektrony odgrywają ważną rolę w rozpadach pary kwarków szczytowych ($t\bar{t}$), zwłaszcza w kanałach ℓ+dżety i dwuleptonowych, które obejmują elektrony w stanie końcowym. Wydajność elektronów jest wyznaczona zarówno w zderzeniach p+Pb, jak i Pb+Pb, z wykorzystaniem elektronów pochodzących z rozpadu rezonansowego $Z \rightarrow e^{+}e^{-}$. Współczynniki skalujące dla elektronów zostały wyznaczone w zderzeniach p+Pb i następnie zastosowane w pomiarze produkcji $t\bar{t}$. Ponadto, identyfikacja elektronów została zoptymalizowana dla zderzeń Pb+Pb i stanowi obecnie podstawowe podejście w trzeciej kampanii zbierania danych (2022–2026).

Proces $t\bar{t}$ został zbadany w kanałach ℓ+dżety i dwuleptonowych w zderzeniach p+Pb. Całkowity przekrój czynny $t\bar{t}$ jest zmierzony z całkowitą względną niepewnością wynoszącą 9%, co prowadzi do najdokładniejszego dotychczas pomiaru przekroju czynnego $t\bar{t}$ w zderzeniach ciężkich jonów. Istotność sygnału przekracza pięć odchyleń standardowych osobno w kanałach ℓ+dżety i dwuleptonowych, co skutkuje pierwszą obserwacją produkcji $t\bar{t}$ w kanale dwuleptonowym w zderzeniach p+Pb. Współczynnik modyfikacji jądrowej dla procesu $t\bar{t}$ został również wyznaczony po raz pierwszy. Wyniki są zgodne z przewidywaniami teoretycznymi dla różnych wiodących zestawów nPDF.

Produkcja par $t\bar{t}$ jest również analizowana w dwuleptonowym kanale rozpadu w zderzeniach Pb+Pb. Całkowity przekrój czynny $t\bar{t}$ został wyznaczony z całkowitą względną niepewnością wynoszącą 31%, co stanowi najdokładniejszy jak dotąd pomiar przekroju czynnego $t\bar{t}$ w zderzeniach Pb+Pb. Zaobserwowana istotność sygnału wynosi 5.0 odchyleń standardowych, ustanawiając pierwszą obserwację procesu $t\bar{t}$ w zderzeniach Pb+Pb. Otrzymany wynik jest zgodny z pomiarem współpracy CMS i przewidywaniami teoretycznymi opartymi na najnowszych zestawach nPDF.

Przeprowadzone badania otwierają nową ścieżkę dla dalszych badań nad zderzeniami ciężkich jonów przy ultrarelatywistycznych energiach. Dokładny pomiar produkcji $t\bar{t}$ w zderzeniach p+Pb dostarcza cennych informacji do wyznaczenia nPDF w wysokim zakresie Bjorken-x. Obserwacja procesu $t\bar{t}$ w zderzeniach Pb+Pb wyznacza początek programu ciężkich jonów z udziałem kwarków szczytowych, a w szczególności otwiera możliwość badania struktury czasowej QGP w przyszłości.

Zusammenfassung

Das Studium tiefinelastischer Streuung in Schwerionkollisionen ist nicht nur auf die Partondichteverteilung von Atomkernen (nPDF) sensitiv, sondern erlaubt auch das Studium des entstehenden Quark-Gluon Plasmas (QGP). In dieser Arbeit werden Top-Quarks aus Schwerionenkollisionen analysiert. Die zur Analyse verwendeten Daten wurden während der zweiten Datennahmeperiode am LHC (2015–2018) in Proton–Blei (p–Pb) und Blei–Blei (Pb–Pb) Kollisionen mithilfe des ATLAS Detektors aufgenommen. Die Nukleon-Nukleon Schwerpunktsenergie betrug $\sqrt{s_{\mathrm{NN}}} = 8.16$ TeV bzw. $\sqrt{s_{\mathrm{NN}}} = 5.02$ TeV.

Elektronen spielen eine wichtige Rolle in den Zerfallskanälen von Top-Quark-Paaren ($t\bar{t}$), insbesondere in den ℓ+Jets und Dilepton Endzuständen. Die Rekonstruktionseffizienz der Elektronen in p–Pb und Pb–Pb Kollisionen wird mit Elektronen aus dem Zerfall $Z \rightarrow e^{+}e^{-}$ bestimmt. Die aus p–Pb Kollisionen bestimmten Skalierungs-Faktoren werden als Korrekturen in der $t\bar{t}$ Messung angewendet. Darüberhinaus ist die Identifikation von Elektronen in Pb–Pb Kollisionen optimiert worden. Der verbesserte Identifikations-Algorithmus dient derzeit als Grundlage für LHC-Run 3 (2022–2026) Analysen.

Der $t\bar{t}$-Prozess wird in den ℓ+Jets und Dileptonischen Zerfallskanälen in p–Pb Kollisionen untersucht. Der inklusive $t\bar{t}$ Wirkungsquerschnitt wird mit einer relativen Unsicherheit von 9% gemessen und ist damit die präziseste $t\bar{t}$ Wirkungsquerschnittsmessung in Kollisionen von Schwerionen. Jeder der beiden Zerfallskanäle wurde mit einer Signifikanz von über fünf Standardabweichungen gemessen. Damit ist dies die erste Beobachtung von $t\bar{t}$ Produktion im Dileptonischen Zerfallskanal in p–Pb Kollisionen überhaupt. Der Kernmodifikationsfaktor für den $t\bar{t}$ Prozess wird ebenfalls zum ersten Mal bestimmt. Die Ergebnisse stimmen mit den theoretischen Vorhersagen verschiedener aktueller nPDF-Sätzen überein.

Des Weiteren wird die $t\bar{t}$ Paarproduktion in Pb–Pb Kollisionen im Dileptonischen Zerfallskanal untersucht. Der inklusive Wirkungsquerschnitt wird mit einer relative Unsicherheit von 31% gemessen und stellt damit die präziseste $t\bar{t}$ Messung in Pb–Pb Kollisionen dar. Die Signifikanz des $t\bar{t}$ Signals beträgt 5.0 Standardabweichungen ist somit die erste Beobachtung des $t\bar{t}$ Prozesses in Pb–Pb Kollisionen überhaupt. Dieses Ergebnis ist mit Resultaten der CMS Kollaboration sowie den anhand der neuesten nPDF Sätzen berechneten theoretischen Vorhersagen kompatibel.

Die durchgeführten Studien eröffnen einen neuen Weg für weitere Forschung zu Schwerionenkollisionen bei ultrarelativistischen Energien. Die präzise Messung der $t\bar{t}$-Produktion in p–Pb-Kollisionen liefert wertvolle Beiträge zur genaueren Bestimmung von nPDFs im hohen Bjorken-x-Bereich. Die Beobachtung des $t\bar{t}$-Prozesses in Pb–Pb Kollisionen stellt den Beginn der Top Quark Messungen in Schwerionenkollisionen dar, mit denen es in Zukunft möglich sein wird die Zeitstruktur des QGP zu untersuchen.

Acknowledgements

This work was partly supported by the National Science Centre of Poland under grants 2016/23/B/ST2/01409, 2020/37/B/ST2/01043, and 2024/53/N/ST2/00869, by program „Excellence initiative – research university" project no 9722 for the AGH University of Krakow, and by PL-Grid Infrastructure.

Author's contribution

The Author of this thesis has been involved in work in the ATLAS experiment since her Bachelor's studies in 2018. At the beginning of the PhD programme in 2021, the Author started a yearly qualification task. The project focused on deriving electron scale-factor corrections in p+Pb collisions (Section 3.2) and optimisation of electron identification in Pb+Pb collisions in Run 3 data taking (Section 3.3). The results of this task have been integrated by the Author into the software of the ATLAS experiment and can be used by future measurements using electrons in the final states of p+Pb and Pb+Pb collisions. They were also a key input for the measurement of top-quark pair production in p+Pb collisions. The Author's contribution to this analysis also involved detailed jet performance studies (Section 4.5.2) and derivation of the nuclear modification factor (Section 4.10.2). The Author was the main analyser in the observation of top-quark pair production in Pb+Pb collisions. The Author's contributions included developments of the analysis framework to support heavy-ion collisions, definition of the MC simulation strategy (Section 5.3), optimisation of the event selection (Section 5.4), estimation of the fake-lepton background (Section 5.6), studies of systematic uncertainties (Section 5.7), establishing the fit strategy (Section 5.8), and derivation of the $t\bar{t}$ production cross section (Section 5.9.1). Moreover, the Author was appointed an analysis contact for this measurement in the ATLAS Collaboration. In the case of both measurements, the Author contributed to the preparation of the internal documentation of the analyses, the approval of results in the ATLAS Collaboration, and coordination of the editing process of the publications.

The Author's work was published in the following scientific articles authored by the ATLAS Collaboration:

- ATLAS Collaboration, *Observation of $t\bar{t}$ production in the lepton+jets and dilepton channels in p+Pb collisions at $\sqrt{s_{\mathrm{NN}}} = 8.16$ TeV with the ATLAS detector*, JHEP 11 (2024) 101,
- ATLAS Collaboration, *Observation of top-quark pair production in lead-lead collisions at $\sqrt{s_{\mathrm{NN}}} = 5.02$ TeV with the ATLAS detector*, Phys. Rev. Lett. 134 (2025) 142301.

The Author's contribution is also reflected in the following conference proceedings:

- P. Potępa, *Searching for electrons in heavy-ion collisions in the ATLAS experiment at the LHC*, Institute of Nuclear Physics PAS (2022) 57,
- P. Potępa, *Measurement of high-p_{T} electron performance in proton-lead collisions in the ATLAS experiment*, PoS LHCP2022 (2023) 314,
- P. Potępa, *Hunting for jets in proton-lead collisions in the ATLAS experiment at the LHC*, Institute of Nuclear Physics PAS (2023) 6,

- P. Potępa, *Comparison of two approaches to jet reconstruction in proton-lead collisions in ATLAS*, PoS LHCP2023 (2024) 259,
- P. Potępa, *Probing initial state effects in nuclear collisions via jet and top-quark measurements with the ATLAS detector*, EPJ Web Conf. 296 (2024) 10012.

The results of this work were presented by the Author on behalf of the ATLAS Collaboration at the following conferences:

- P. Potępa, **poster:** *Performance of high-p_{T} electrons in proton-lead collisions in the ATLAS experiment*, XXIXth International Conference on Ultra-relativistic Nucleus-Nucleus Collisions, 4–10 Apr 2022, Kraków, Poland,
- P. Potępa, **talk:** *$t\bar{t}$ production in HI collisions*, ATLAS Top Workshop, 4–6 May 2022, Valencia, Spain,
- P. Potępa, **poster:** *Measurement of high-p_{T} electron performance in proton–lead collisions in the ATLAS experiment*, 10th Edition of the Large Hadron Collider Physics Conference, 16–20 May 2022, Taipei, Taiwan,
- P. Potępa, **talk:** *Electron ID optimisation in HI collisions for Run 3*, ATLAS Egamma Workshop, 14–17 Mar 2023, Geneva, Switzerland,
- P. Potępa, **poster:** *Measurement of jet performance in proton–lead collisions in the ATLAS experiment*, 11th International Conference on Hard and Electromagnetic Probes of High-Energy Nuclear Collisions, 26–31 Mar 2023, Aschaffenburg, Germany,
- P. Potępa, **poster:** *Comparison of two approaches to jet reconstruction in proton–lead collisions in ATLAS*, 11th Edition of the Large Hadron Collider Physics Conference, 22–26 May 2023, Belgrade, Serbia,
- P. Potępa, **talk:** *Probing initial state effects in nuclear collisions via jet and top quark measurements with the ATLAS detector*, XXXth International Conference on Ultra-relativistic Nucleus–Nucleus Collisions, 3–9 Sep 2023, Houston, USA,
- P. Potępa, **talk:** *Top-quark pair production in heavy-ion collisions in the ATLAS experiment*, Seminarium HEP Białasówka, 5 Jan 2024, Kraków, Poland,
- P. Potępa, **talk:** *Evidence of top-quark pair production in lead–lead collisions*, ATLAS Top Workshop, 28 Apr – 3 May 2024, Benasque, Spain,
- P. Potępa, **talk:** *Top quark pair production in Heavy Ion Collisions with the ATLAS experiment*, 12th International Conference on Hard and Electromagnetic Probes of High-Energy Nuclear Collisions, 22–27 Sep 2024, Nagasaki, Japan,
- P. Potępa, **poster:** *Observation of top-quark pair production in heavy-ion collisions in the ATLAS experiment*, 12th International Conference on Hard and Electromagnetic Probes of High-Energy Nuclear Collisions, 22–27 Sep 2024, Nagasaki, Japan,

- P. Potępa, **talk:** *$t\bar{t}$ production in heavy-ion collisions with the ATLAS and CMS detectors*, LHC TOP WG meeting, 11–13 Nov 2024, Geneva, Switzerland,
- P. Potępa, **talk:** *Top-quark pair production in Pb+Pb collisions in the ATLAS experiment*, XXXI International Conference on Ultra-relativistic Nucleus–Nucleus Collisions, 6–12 Apr 2025, Frankfurt, Germany,
- P. Potępa, **talk:** *QGP-like signatures in UPCs – Experimental overview*, The Thirteenth Annual Large Hadron Collider Physics conference, 5–9 May 2025, Taipei, Taiwan,
- P. Potępa, **poster:** *Top-quark pair production in heavy-ion collisions in the ATLAS experiment*, The Thirteenth Annual Large Hadron Collider Physics conference, 5–9 May 2025, Taipei, Taiwan.

The Author has also contributed to the following grants:

- Scholarship in OPUS-12 NCN 2016/23/B/ST2/01409 (2017–2021): *The study of processes with high transverse momentum in heavy ion collisions in the ATLAS experiment at the LHC*,
- Scholarship in OPUS-19 NCN 2020/37/B/ST2/01043 (2021–2025): *Research on ultra-relativistic heavy ion collisions and the search for new physics with hard probes at the LHC*,
- Principal investigator in PRELUDIUM-23 NCN 2024/53/N/ST2/00869 (2024–2027): *Top-quark pairs as novel probes of ultra-relativistic heavy-ion collisions in the ATLAS experiment at the LHC*.

Contents

Chapter 1

Theoretical overview

1.1 Standard Model

The Standard Model (SM) of particle physics encapsulates our current understanding of elementary particles and the fundamental forces that govern the universe. In this theory, two groups of particles are distinguished: fermions and bosons. Fermions are characterised by half-integer spin and obey Fermi–Dirac statistics [1, 2], leading to the Pauli exclusion principle, while bosons are defined by integer spin and follow Bose–Einstein statistics [3, 4]. The fermionic sector is further divided into quarks, carrying a colour charge, and leptons, which are devoid of this type of charge. According to the SM, matter is composed of fermions and forces are mediated by bosons.

The term "Standard Model" was introduced in 1975 by Abraham Pais and Sam Treiman [5], reflecting the growing acceptance of a unified theory that described all known elementary particles up to that time. However, the foundations of the SM were laid much earlier, in 1928, by Paul Dirac [6], who introduced the Dirac equation, predicting the existence of antimatter. In 1954, Chen-Ning Yang and Robert Mills [7] adapted the concept of gauge theory to the strong interaction. One of the first quantum field theories, Quantum Electrodynamics (QED), was formulated independently by Shin'ichirō Tomonaga [8], Julian Schwinger [9], and Richard Feynman [10] during the late 1940s. A unified description for the weak and electromagnetic interactions, referred to as the electroweak interaction, was proposed in 1961 by Sheldon Glashow [11]. A mechanism of spontaneous symmetry breaking that imparts mass to particles was developed in 1964, by three independent groups of physicists: François Englert and Robert Brout [12], Peter Higgs [13], and Gerald Guralnik, Carl Hagen, and Tom Kibble [14]. In 1967, Steven Weinberg [15] and Abdus Salam [16] incorporated this mechanism into the electroweak interaction, demonstrating how it could impart mass to particles. In 1973, the concept of colour charge as the source of the strong interaction was developed by Harald Fritzsch, Murray Gell-Mann, and Heinrich Leutwyler [17], marking the beginning of Quantum Chromodynamics (QCD). Later that year, David Gross and Frank Wilczek [18], and independently David Politzer [19], postulated the concept of asymptotic freedom for strongly interacting particles.

A complete depiction of the SM is presented in Figure 1.1. The fermionic group consists of six quarks and six leptons, organised into three particle generations. The first generation comprises the common constituents of matter, including the up and down quarks, which are the primary components of protons and neutrons, and the electron, which together form all possible atoms. Particles from the second generation, which are unstable and rapidly decay into first-generation components, are naturally observed in cosmic rays. The third-generation particles, which are significantly heavier than their lower-generation counterparts, are typically produced in high-energy environments, such as particle collisions at the Large Hadron Collider (LHC).

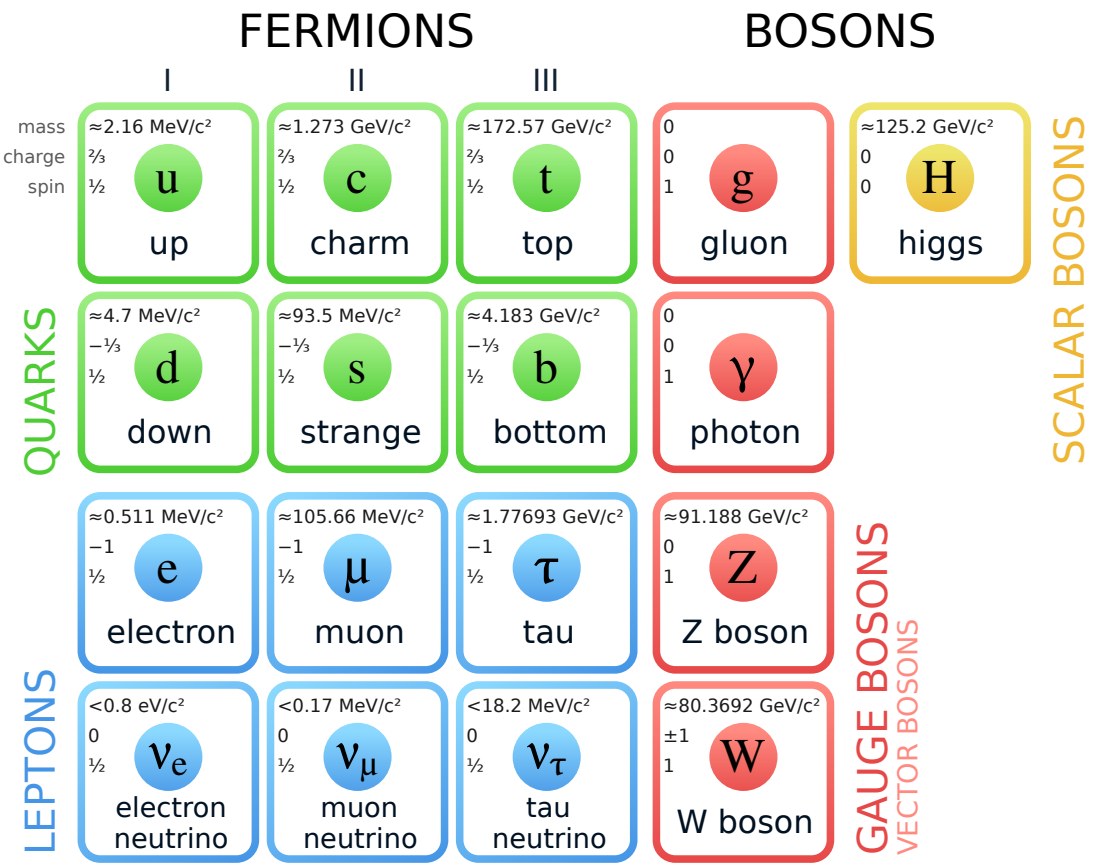

Figure 1.1: Scheme of the Standard Model [20].

The bosonic sector of the SM comprises four gauge bosons, which transmit the fundamental forces, and one scalar boson, the Higgs, which imparts mass to particles. Table 1.1 summarises all four interactions with the corresponding mediators. The graviton, a hypothetical spin-2 boson responsible for the gravitational force, has not yet been incorporated into the SM theory. The electromagnetic and weak forces exhibit comparable strength and unify into a single electroweak interaction [21] at an energy of approximately 246 GeV, corresponding to the vacuum expectation value of the Higgs field.[1] According to the Grand Unified Theory [22], strong, electromagnetic, and weak interactions are predicted to unify into one electronuclear force at extremely high energies on the order of 10^{16} GeV. Unification of all four fundamental interactions, including gravity, is referred to as the theory of everything [23].

[1] Natural units with the convention $\hbar = c = 1$ are used throughout this thesis.

Table 1.1: Summary of four fundamental interactions.

Interaction	**Mediator**	**Relative strength**	**Range [m]**
Strong	gluon	1	10^{-15}
Electromagnetic	photon	10^{-2}	∞
Weak	W, Z bosons	10^{-5}	10^{-18}
Gravitational	graviton (hypothetical)	10^{-38}	∞

1.2 Parton distribution functions

1.2.1 Proton parton distribution functions

A proton is characterised by a complex structure, which depends on the probing energy scale Q, defined as the four-momentum transfer between particles. No substructure is observed at low energies of $Q \ll 1$ GeV, and the proton behaves as a point-like particle. At higher energies, proton properties, such as its charge and quantum numbers, are determined by three valence quarks: two up and one down, referred to as the parton model [24]. At high-energy scales, contributions from gluons and sea quarks, arising from the strong interaction, become relevant. In that regime, the proton structure is described using parton distribution functions (PDFs), which represent probability distributions of the longitudinal momentum fraction, x, carried by a given parton, referred to as Bjorken-x.

At sufficiently high energies, the strong coupling constant α_s becomes small enough to allow the use of perturbative techniques, referred to as perturbative QCD [25]. However, the partonic structure of the proton cannot be determined using perturbative QCD, due to the relatively low energy scales. The evolution of PDFs with Q, starting at an initial energy scale of Q_0, is well known and determined using the Dokshitser–Gribov–Lipatov–Altarelli–Parisi (DGLAP) equations [26–28]. However, the Bjorken-x dependence cannot be obtained analytically. Therefore, the standard procedure to obtain PDFs involves using global fits to experimental data. There are many PDF parametrisations, including CT18 [29], NNPDF3.1 [30], and MSHT20 [31], among others. Figure 1.2 shows the kinematic coverage of the CT18 dataset presented in the (x, Q) space, with a total of 3681 individual data points contributing to the fit. Three main groups of experimental data can be distinguished: fixed-target deep-inelastic scattering and Drell–Yan processes (blue area), HERA I+II deep-inelastic scattering data (red area), and hadron collider data (green area).

Proton PDFs for individual quarks and the gluon, obtained in the CT18 analysis, are presented in Figure 1.3 at two exemplary energy scales. At the lower scale of $Q = 2$ GeV, the momentum of the proton is primarily carried by the three valence quarks, resulting in peaks for the up and down quarks around $x = 0.2$. The contribution to the proton's momentum from gluons and sea quarks becomes notably enhanced at the larger energy scale of $Q = 100$ GeV.

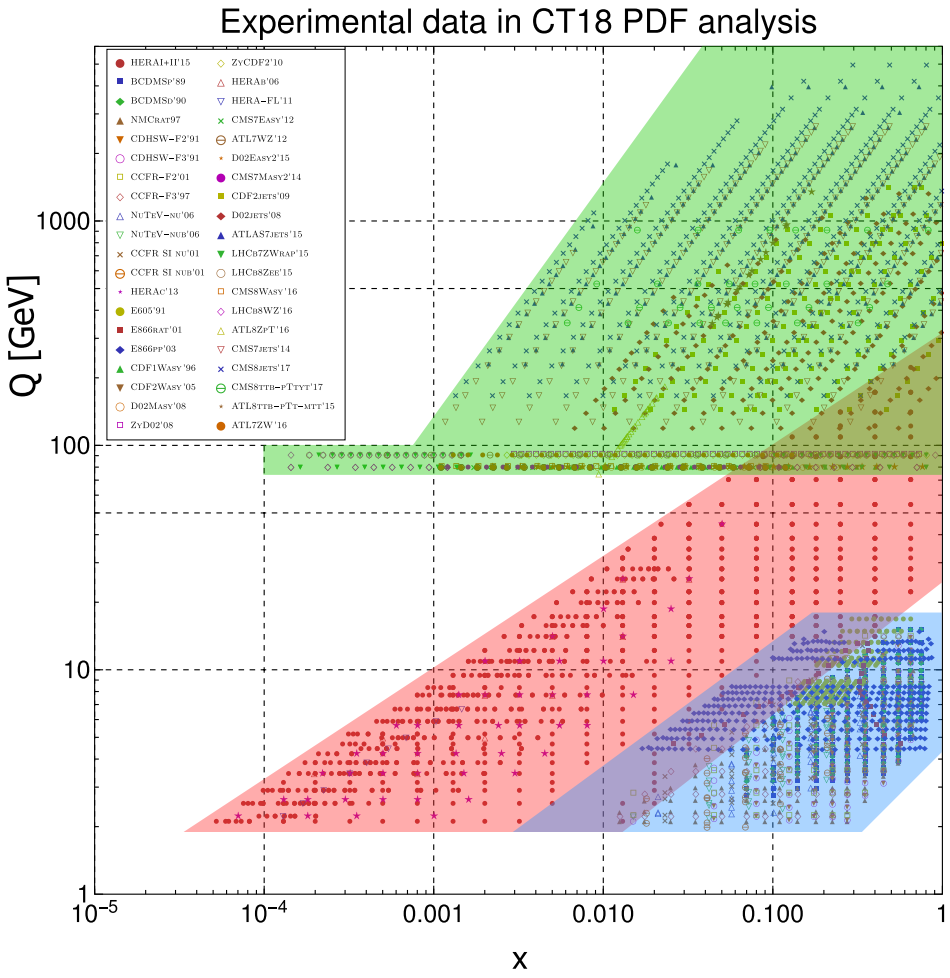

Figure 1.2: The kinematic coverage of the CT18 dataset, represented in the partonic (x, Q) space [29]. Fixed-target deep-inelastic scattering and Drell–Yan processes are represented by the blue area, results from HERA I+II are indicated by the red area, while hadron collider data are enclosed within the green area.

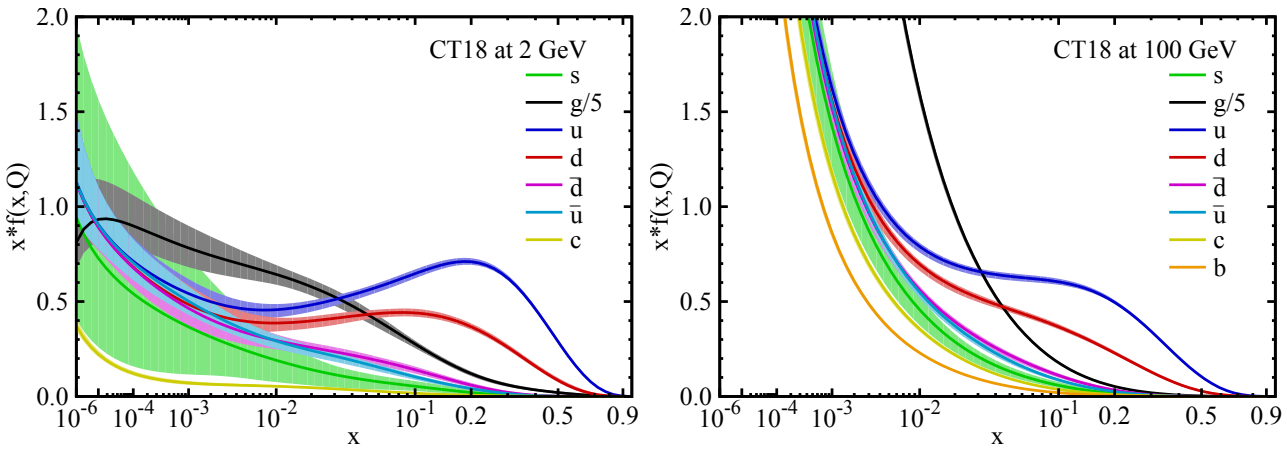

(a) (b)

Figure 1.3: The CT18 PDFs at two different energy scales: (a) $Q = 2$ GeV and (b) $Q = 100$ GeV, for the (anti)quarks (u, $\bar{u}$, d, $\bar{d}$, $s = \bar{s}$) and the gluon [29]. The gluon PDF has been scaled down as $g(x, Q)/5$.

1.2.2 Nuclear parton distribution functions

Momentum distributions of quarks and gluons in nucleons confined within nuclei have been proven to differ from those in a free proton. This phenomenon was first observed in 1983 by the European Muon Collaboration [34]. In order to successfully describe experimental data, nuclear modifications have to be considered in the form of nuclear PDFs (nPDFs). Similarly to the free proton case, the Q evolution is given by the DGLAP equations and the x dependence is obtained using global data fits. Therefore, experimental results from heavy-ion collisions play a crucial role in constraining nPDFs.

Figure 1.4 displays a selection of the ever-growing global dataset, which can be used in nPDF analyses. Large kinematic ranges are covered by LHC results, including prompt D^0 meson production in proton-lead (p+Pb) collisions by LHCb [35], dijet production in p+Pb collisions by CMS [36], and ATLAS measurements of dijets in p+Pb [37] and ultra-peripheral lead–lead (Pb+Pb) [38] collisions. Additionally, the kinematic range of a recent measurement of $t\bar{t}$ production in p+Pb collisions by ATLAS [39], with a leading contribution by the author of this thesis, is presented. It could provide input to nPDFs at a constant energy scale of $Q^2 \sim m_t^2 \sim 3 \cdot 10^4$ GeV^2, where m_t stands for the top-quark mass, and a broad Bjorken-x range of $3 \cdot 10^{-3} - 0.5$. Future

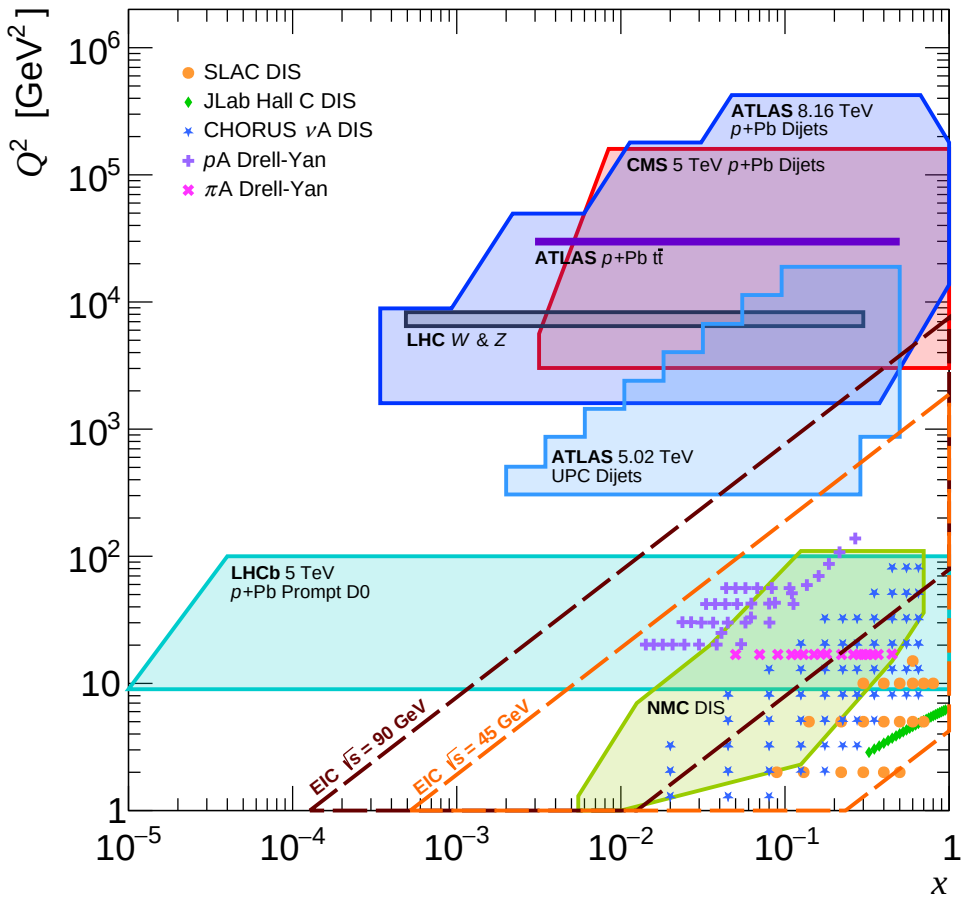

Figure 1.4: Selection of global dataset constraining nPDFs, represented in the partonic (x, Q^2) space [32, 33]. Predictions for the future EIC data taking are included.

predictions are also shown, including Electron-Ion Collider (EIC) data taking at two centre-of-mass energies of $\sqrt{s} = 45$ and 90 GeV.

Ratios of nuclear over free proton and neutron densities for the quarks (R_i^{Pb}) and the gluon (R_g^{Pb}) are presented in Figure 1.5. Results for the up and down quarks, obtained using the EPPS21 nPDF set, appear to be consistent between the two quark flavours. The nuclear modifications to the gluon PDF are shown for four state-of-the-art nPDF sets: EPPS21 [40], nNNPDF3.0 [41], nCTEQ15WZSIH [42], and TUJU21 NLO [43]. Values below (above) unity indicate a suppression (enhancement) of a given process in nuclear collisions compared to a geometric expectation from the free nucleon case. In general, four distinct Bjorken-x regions can be distinguished [44]. At low values of $x \lesssim 0.01$, a suppression from shadowing is observed, arising primarily from the coherent interaction of the probe with multiple nucleons. An enhancement is visible at around $x \approx 0.1$, which is believed to compensate for degradation caused by shadowing. In the range of $0.2 \lesssim x \lesssim 0.7$, the EMC effect, named after the European Muon Collaboration, manifests as a suppression, which is assumed to occur due to short-range nucleon–nucleon correlations, although a comprehensive theoretical explanation remains elusive. Finally, at large values of $x \gtrsim 0.7$, the ratio is dominated by the intrinsic motion of nucleons within an atomic nucleus, referred to as Fermi motion [45], resulting in a huge enhancement.

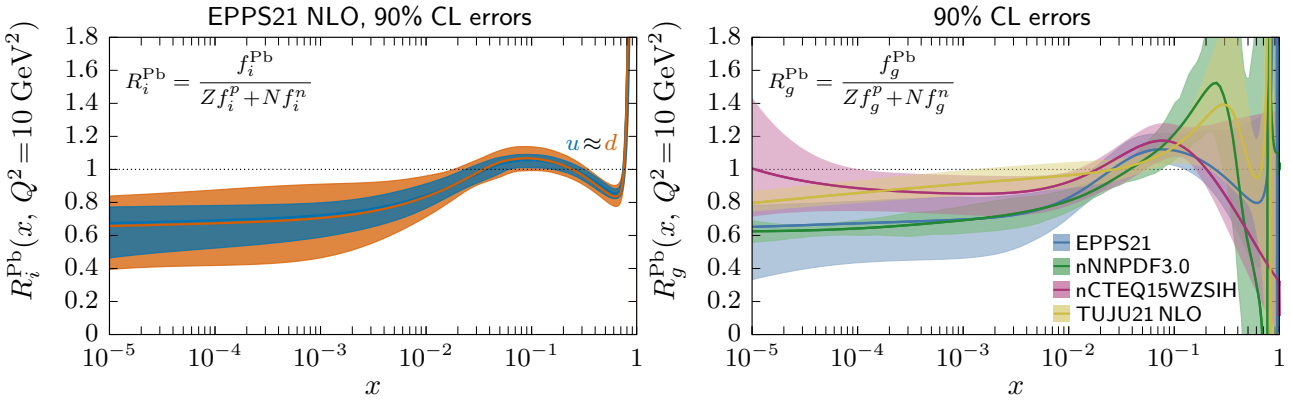

(a) (b)

Figure 1.5: Nuclear modifications to (a) the up and down quark, and (b) the gluon PDFs for bound nucleons in lead [46]. Results for four different nPDF sets for gluons are shown.

The $t\bar{t}$ process in p+Pb and Pb+Pb collisions is predicted to probe nPDFs at high Bjorken-x values, as shown in Figure 1.6. Since $t\bar{t}$ production is dominated by gluon fusion, the process is primarily sensitive to the gluon nPDF. Top quarks provide access to the antishadowing region, where an enhancement of $t\bar{t}$ production is expected compared to the free-nucleon case. The predicted effect on the nuclear modification to the gluon PDF, based on the EPS09 PDF set, is estimated using pseudo data at LHC energies for the full heavy-ion programme. Due to low foreseen statistics, only a moderate impact on the gluon nPDF is found, with the predicted error bands being approximately 10% narrower than the original EPS09 ones. By combining p+Pb and Pb+Pb measurements and assuming independent data samples from the ATLAS and CMS collaborations, the total improvement on the gluon nPDF could reach 30% [47].

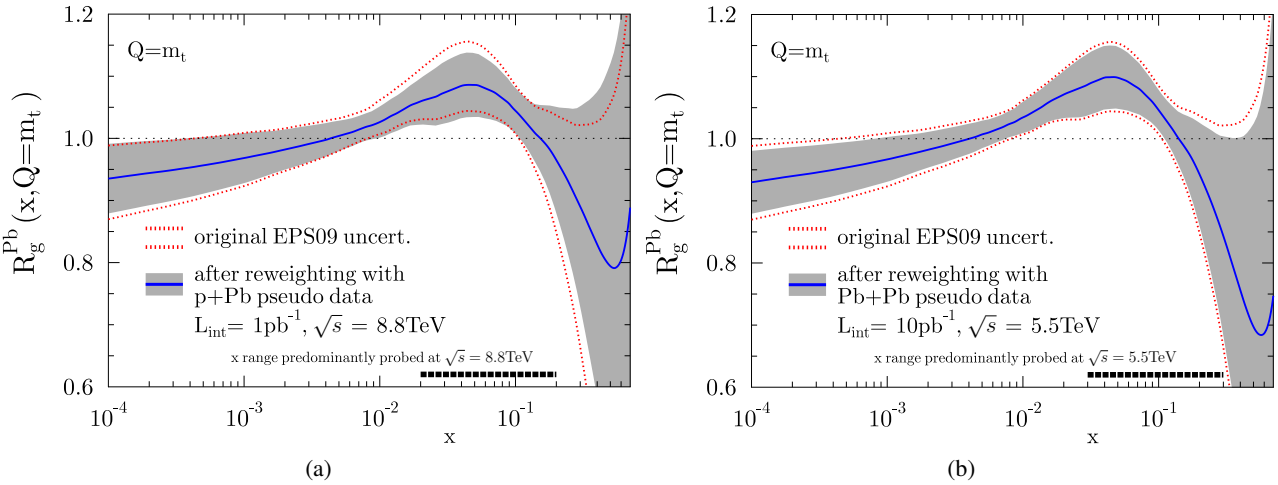

Figure 1.6: Predicted impact of the $t\bar{t}$ process on the nuclear modification to the gluon PDF, using pseudo data in the (a) p+Pb and (b) Pb+Pb systems [47]. The red dotted lines indicate the uncertainty band of the original EPS09 PDF set. Bjorken-x ranges for the $t\bar{t}$ process are denoted by the black dotted lines.

1.3 Quark-gluon plasma

The strength of the strong interaction is quantified using the strong coupling constant, α_s [49], which varies with the energy scale, as shown in Figure 1.7. The value of α_s can be extracted from various experimental results,

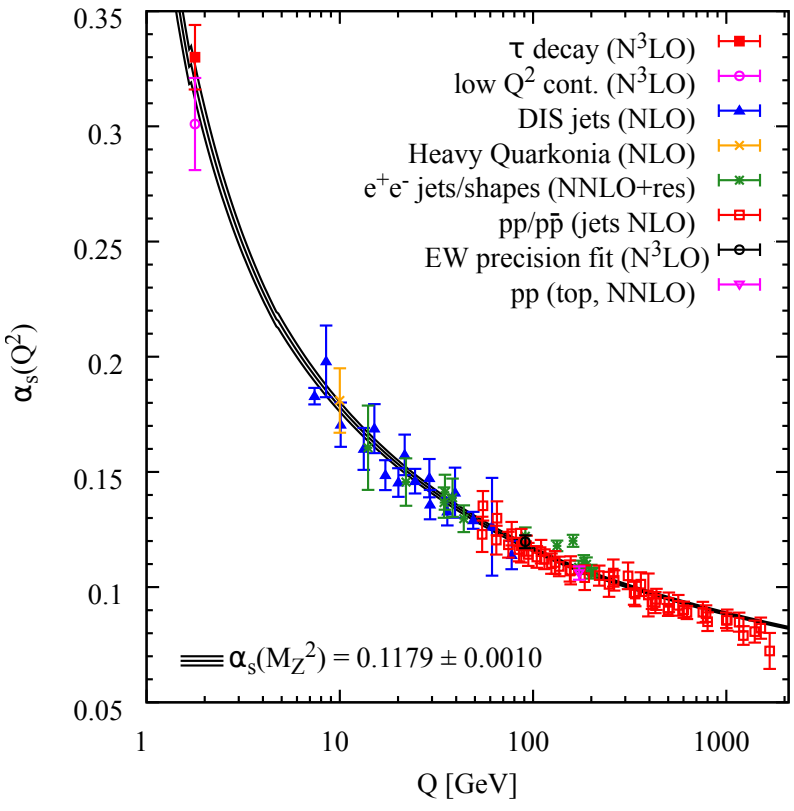

Figure 1.7: Strong coupling constant, α_s, as a function of the energy scale, Q [48].

including tau, jet, and quarkonia measurements, using perturbation theory with specified levels of precision: next-to-leading order (NLO), next-to-next-to-leading order (NNLO), NNLO matched to a resummed calculation (NNLO+res.), and next-to-next-to-next-to-leading order (N^{3}LO). Due to the large value of α_s at low Q, partons exist only in bound, colour-neutral states, which is known as colour confinement [50]. Three colour charges – red, green, and blue – allow for two types of bound states: quark–antiquark pairs, called mesons, and three-quark configurations, named baryons. Both types are collectively referred to as hadrons, and the process in which they are formed is known as hadronisation. The value of α_s decreases as a function of Q, resulting in a weaker interaction at high energies. At sufficiently large energies, α_s asymptotically approaches zero, which is referred to as the asymptotic freedom of QCD. Under such conditions, quarks are no longer confined within hadrons and can move freely.

It is assumed that strongly interacting matter exhibits different phases, similar to the solid, liquid, and gas phases of water. The different phases of strongly interacting matter and the transitions between them are summarised in the form of the QCD phase diagram [52], shown in Figure 1.8. It is typically presented as a function of temperature and baryon chemical potential μ_{B}, which is defined as the energy cost of adding a baryon to the system while keeping the entropy and volume constant. At low temperatures and μ_{B}, baryons form a dilute gas of hadrons, which includes the normal nuclear matter. Under low temperatures and significantly high μ_{B}, corresponding to high baryon densities, quark pairs are predicted to emerge, resulting in colour superconductivity. Such conditions are believed to exist in the cores of neutron stars [53]. Finally, at extremely high temperatures, partons undergo deconfinement, leading to the quark-gluon plasma (QGP) phase. It is believed that the early universe was filled with this exotic state of matter, composed of free quarks and gluons. The QCD theory pre-

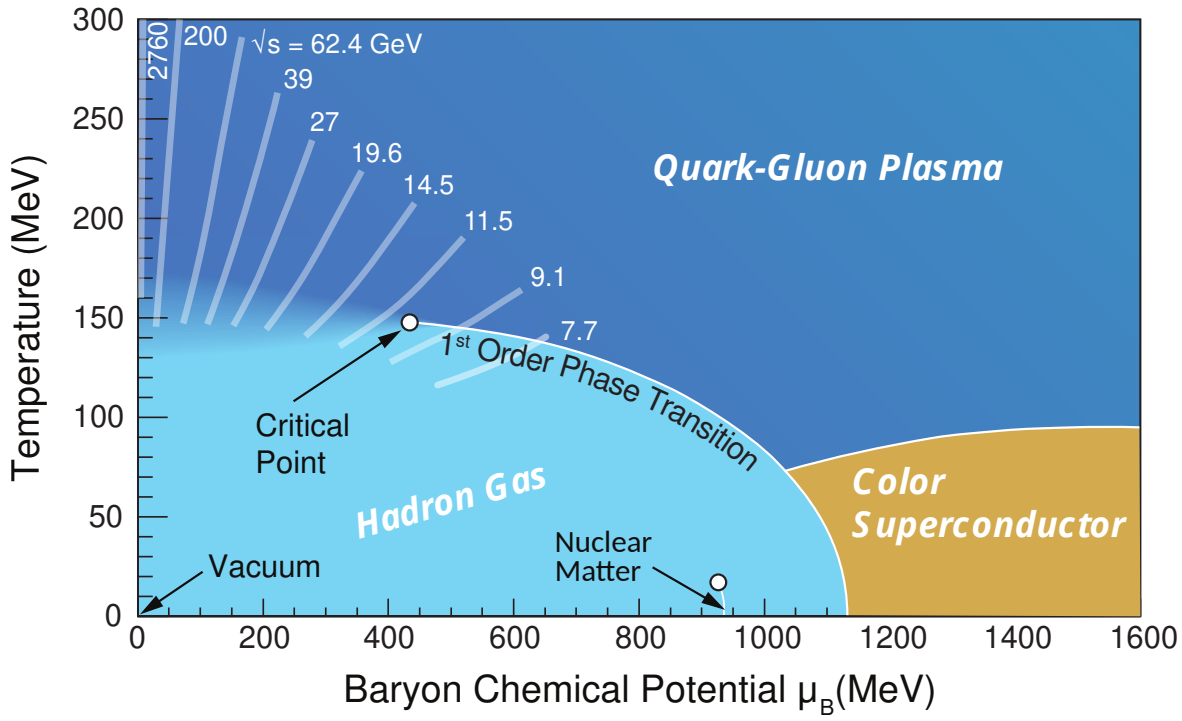

Figure 1.8: QCD phase diagram in the thermodynamic parameter space [51]. White lines indicate the corresponding centre-of-mass collision energy ranges for different accelerator facilities.

dicts a first-order phase transition between the hadron gas and the QGP at large μ_{B} and a smooth crossover at $\mu_{\mathrm{B}} = 0$ around a critical temperature of $T_{\mathrm{C}} \approx 155$ MeV.

Signatures of the QGP can be created under laboratory conditions in ultra-relativistic heavy-ion collisions at the LHC and the Relativistic Heavy Ion Collider (RHIC) at Brookhaven National Laboratory (BNL) [54]. Figure 1.9 presents the stages of QGP evolution that are expected to occur in heavy-ion collisions at hadron colliders. Due to the extremely short life-time of the QGP, on the order of 10 fm ($\approx 10^{-23}$ s), direct measurements are impossible. Therefore, particles produced in the collisions, passing through the QGP, are used to probe the properties of strongly interacting matter.

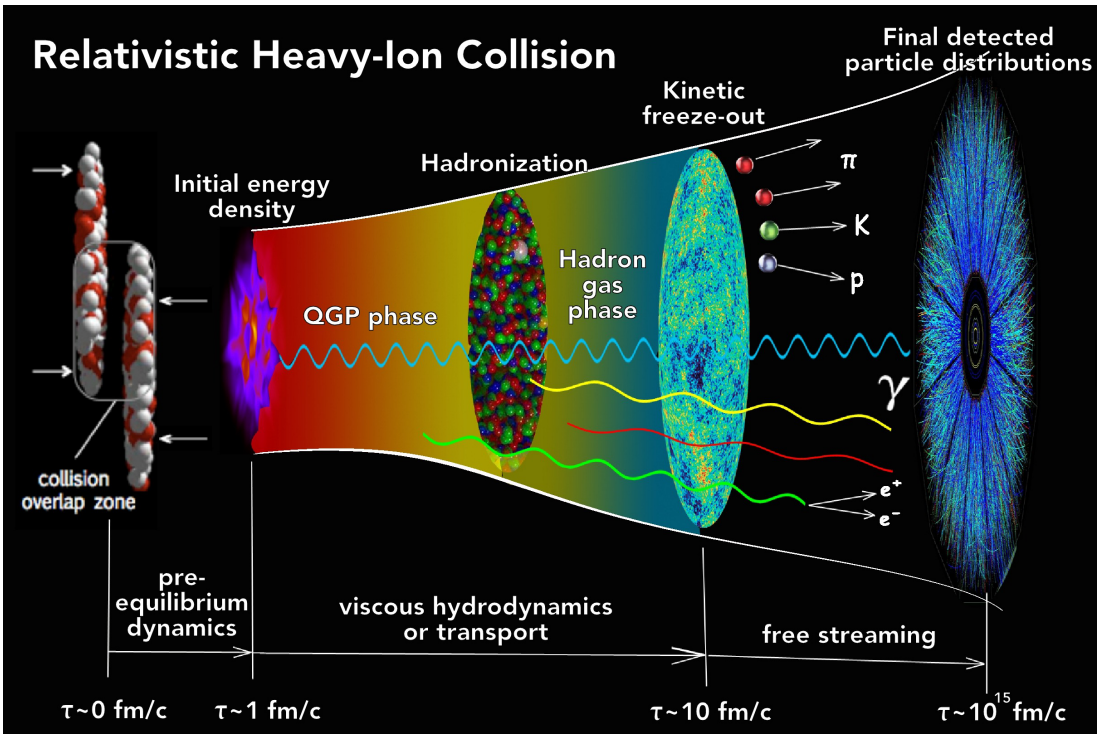

Figure 1.9: The stages of QGP evolution in heavy-ion collisions [55].

In particular, collimated sprays of particles from quark and gluon hadronisation, referred to as jets, undergo observable energy loss through interactions with the QGP – a phenomenon known as jet quenching [56]. Figure 1.10 shows modifications to jet yields, quantified using the nuclear modification factor, R_{AA}, as a function of jet transverse momentum (p_{T}) in Pb+Pb collisions at $\sqrt{s_{\mathrm{NN}}} = 5.02$ GeV for four centrality classes [57], with 0% and 100% representing the most central and most peripheral collisions, respectively. The determination of centrality intervals in the ATLAS experiment is described in detail in Section 2.4. A clear suppression of jet production is observed in Pb+Pb collisions relative to proton–proton (pp) collisions, with R_{AA} reaching as low as 0.45 at jet $p_{\mathrm{T}} \approx 100$ GeV. The suppression is more pronounced in central collisions, where the QGP is more likely to form.

With the first observations of the W boson [58, 59], the Z boson [60, 61], the bottom quark [62, 63] and the tau [64, 65] by the ATLAS and CMS experiments, only two elementary particles remain to be directly

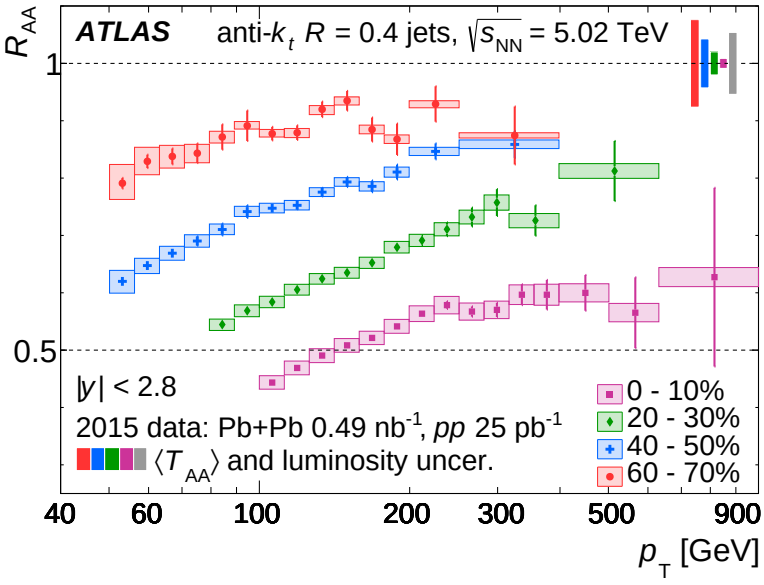

Figure 1.10: The nuclear modification factor, R_{AA}, as a function of jet p_{T} for inclusive jets in Pb+Pb collisions for four centrality intervals [57].

observed in Pb+Pb collisions: the Higgs boson and the top quark. While the detection of the Higgs boson production in Pb+Pb collisions at the LHC is currently unfeasible due to its low cross section, the observation of top-quark production is within reach. Top quarks produced in heavy-ion collisions are predicted to provide new experimental insights into the QGP. In particular, the time structure of the QGP could be studied via hadronically decaying W bosons from top-quark decays [66].

1.4 Top-quark production

With its mass of 172.57 GeV [48], the top quark is the heaviest elementary particle in the SM. Due to its large mass, the top quark is characterised by a short lifetime on the order of 0.15 fm ($\approx 5 \cdot 10^{-25}$ s), which is shorter than the average time for top-quark hadronisation of around 0.3 fm ($\approx 10^{-24}$ s). This provides a unique opportunity to study pseudo-bare quarks. Also, because of the short lifetime, all characteristics of the top quark are transferred to its decay products. Therefore, properties such as spin correlations are not affected by hadronisation smearing and can be studied directly using the decay products.

At LHC energies, top quarks are primarily produced in $t\bar{t}$ pairs, which dominate over single-top-quark production [67]. $t\bar{t}$ pairs are predominantly created via the strong interaction, with contributions from electroweak processes below the percent level, smaller than the uncertainties of current theoretical predictions [68]. Two main classes of $t\bar{t}$ production at leading order (LO) include gluon-fusion processes and quark–antiquark annihilation, as shown in Figure 1.11. In pp collisions, gluon fusion dominates production, as anti-quarks originate solely from the quark sea, reducing the contribution from quark–antiquark annihilation. The ratio between the two production classes also depends on the collision centre-of-mass energy. As the gluon density rises with increasing collision energy, the relative contribution of gluon-fusion processes becomes larger.

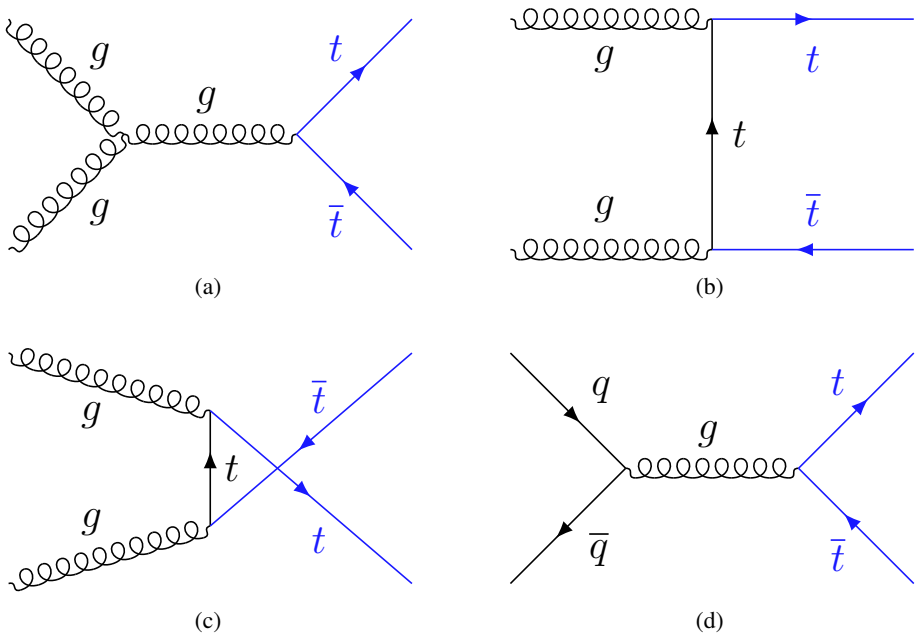

Figure 1.11: Feynman diagrams for top-quark pair production processes: (a) gg fusion s-channel, (b) gg fusion t-channel, (c) gg fusion u-channel, and (d) $q\bar{q}$ annihilation.

The top quark decays immediately via the weak interaction into a W boson and a lighter quark ($t \to W^+q,\ q = b, s, d$). Due to the large top-quark mass, its decay involves a bottom quark in more than 99% of cases, with other flavours, governed by the Cabibbo–Kobayashi–Maskawa matrix elements [69], being significantly suppressed. The subsequent W-boson decay proceeds either hadronically ($W \to q\bar{q}'$) or leptonically ($W \to \ell\nu_\ell,\ \ell = e, \mu, \tau$) in 67.4% and 32.6% of cases, respectively [48]. Based on the W-boson decay modes, three main channels of $t\bar{t}$ decay are distinguished: all-hadronic, semi-leptonic (ℓ+jets), and fully-leptonic (dilepton), as presented in Figure 1.12.

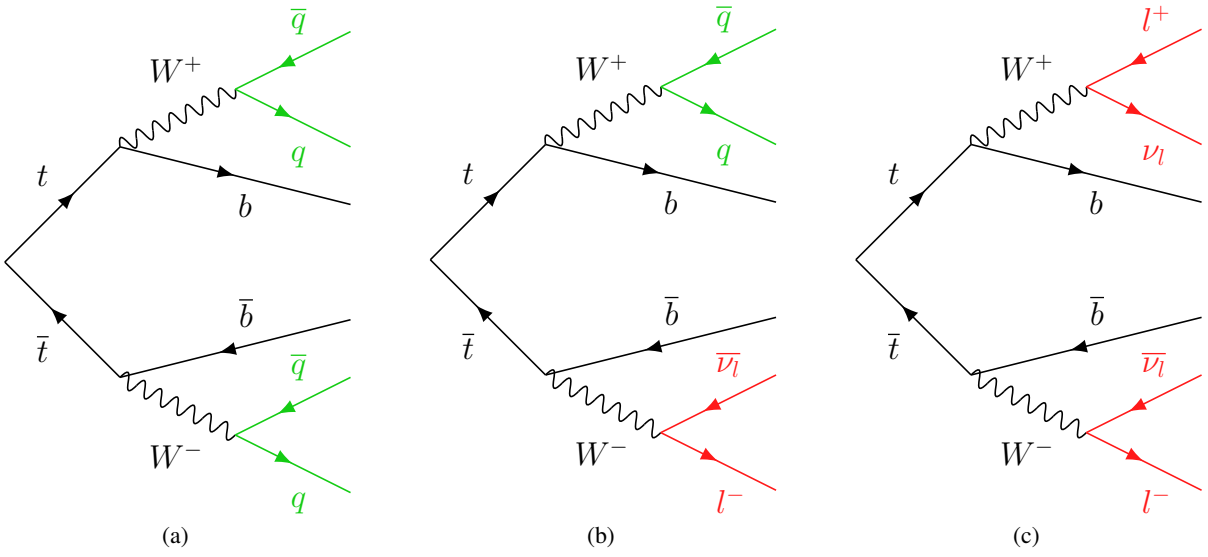

Figure 1.12: Feynman diagrams for top-quark pair decay channels: (a) all-hadronic, (b) ℓ+jets, and (c) dilepton.

All possible final states of $t\bar{t}$ decays with corresponding branching ratios are summarised in Figure 1.13. The all-hadronic channel benefits from the highest branching ratio of approximately 46%. However, it also suffers from large background contributions, including a multijet background component that is difficult to model. The ℓ+jets final state provides a similar branching ratio with a significantly higher signal-to-background ratio, compared to the all-hadronic channel. Despite the lowest branching ratio, the dilepton channel is characterised by the purest final state. Due to the short lifetime of the τ lepton, it cannot be measured directly in the experiment. Therefore, only final states involving e and μ flavours are typically considered, including those with leptonically decaying τ leptons.

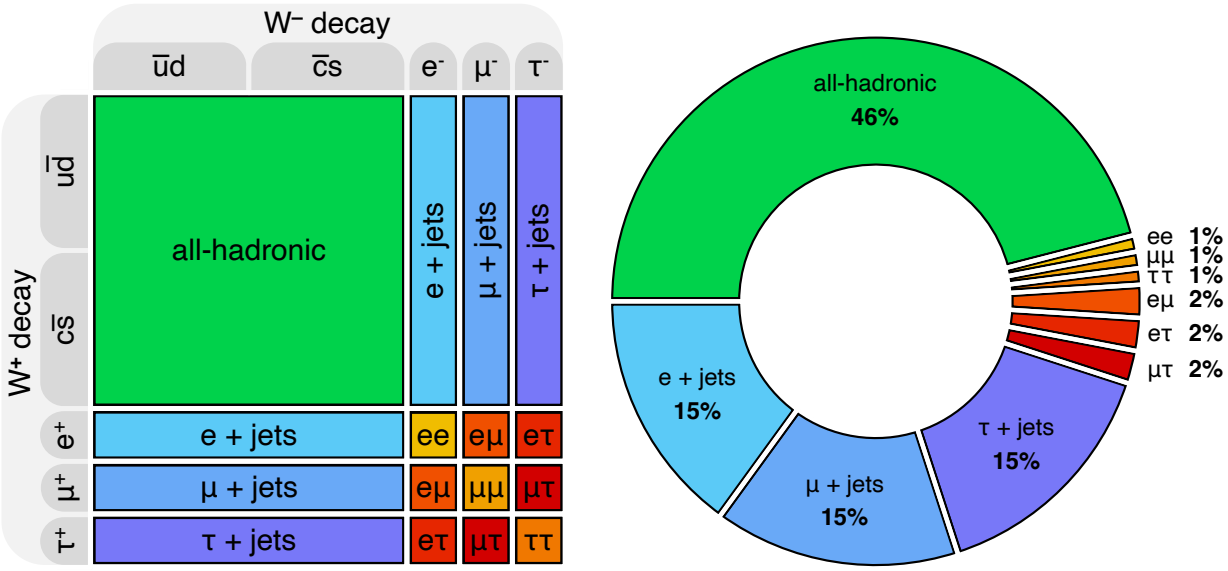

(a) (b)

Figure 1.13: (a) Decay modes of the $t\bar{t}$ process. (b) Branching ratios for the $t\bar{t}$ final states [48].

The $t\bar{t}$ production cross section also increases with the collision centre-of-mass energy, as a lower proton momentum fraction is required to reach the $t\bar{t}$ production threshold. Figure 1.14 shows the collision energy dependence of the $t\bar{t}$ cross section, measured at multiple centre-of-mass energies in pp collisions in the ATLAS experiment [70]. Experimental results are in excellent agreement with the theoretical prediction based on the PDF4LHC21 PDF set [71].

In the context of heavy-ion collisions, measurements in pp collisions at lower energy serve as a crucial reference. In particular, the measurements at centre-of-mass energies of $\sqrt{s} = 8$ and 5.02 TeV can be compared with p+Pb and Pb+Pb collisions, respectively, collected at centre-of-mass energies of $\sqrt{s_{\mathrm{NN}}} = 8.16$ and 5.02 TeV per nucleon pair at the LHC. Figure 1.15 presents a combined result of the $t\bar{t}$ cross section at $\sqrt{s} = 7$ and 8 TeV by ATLAS and CMS, measured using the $e\mu$ channel of the $t\bar{t}$ decay. Figure 1.16 displays measurements of the $t\bar{t}$ cross section at $\sqrt{s} = 5.02$ TeV, including results in the dilepton and ℓ+jets channels by both ATLAS and CMS.

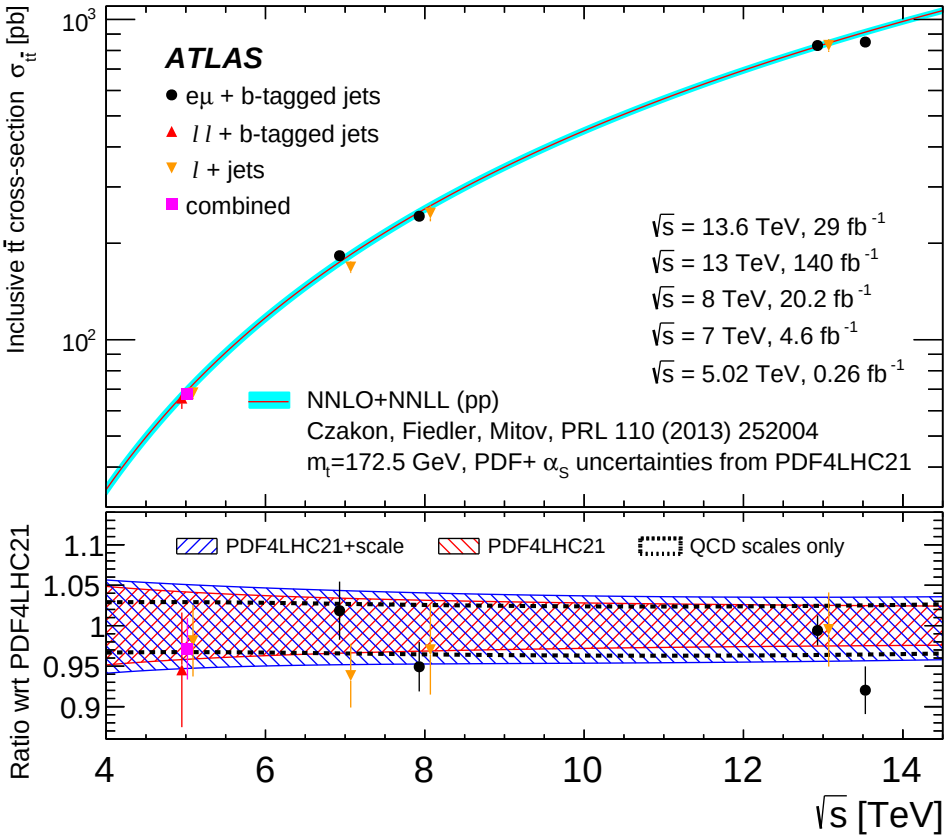

Figure 1.14: Comparison of the measured $t\bar{t}$ cross sections in pp collisions at various centre-of-mass energies and the theoretical prediction using the PDF4LHC21 PDF set [70].

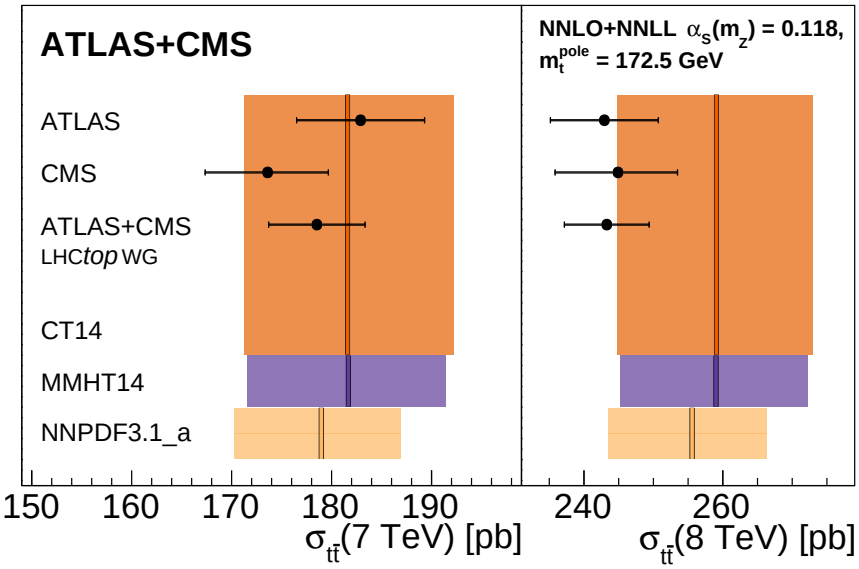

Figure 1.15: Measured $t\bar{t}$ production cross sections in pp collisions at $\sqrt{s} = 7$ and 8 TeV [72], compared with the theoretical predictions using different PDF sets.

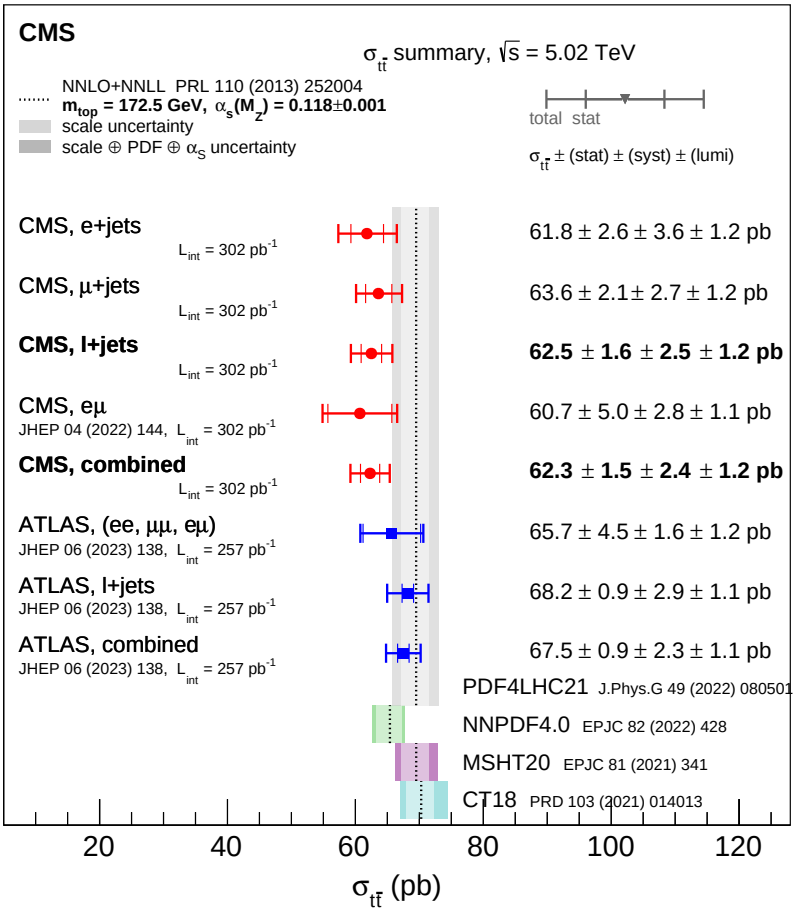

Figure 1.16: Measured $t\bar{t}$ production cross sections in pp collisions at $\sqrt{s} = 5.02$ TeV [73], compared with the theoretical predictions using different PDF sets.

The measurement of the $t\bar{t}$ process is significantly more challenging in heavy-ion collisions due to their complexity and limited data statistics collected to this date. The intricate environment of heavy-ion collisions leads to high detector occupancy and substantial backgrounds. The first observation of $t\bar{t}$ production in p+Pb collisions has been reported by CMS [74], using the ℓ+jets channel. The result, shown in Figure 1.17a, is consistent with the theoretical prediction using the CT14 free-nucleon PDF [75] for protons and the EPPS16 nPDF [76] for lead ions, and the measurements in pp collisions at $\sqrt{s} = 8$ TeV in the $e\mu$ [77] and ℓ+jets [78] channels, scaled by the lead mass number ($A_{\mathrm{Pb}} = 208$) and extrapolated to $\sqrt{s_{\mathrm{NN}}} = 8.16$ TeV. In Pb+Pb collisions, jets are additionally affected by the quenching effect, which impacts the reconstruction of $t\bar{t}$ pairs. Therefore, jet energy scale has to be adjusted for the energy loss using dedicated corrections. Considering this, a $t\bar{t}$ measurement in the dilepton channel, featuring only two jets in the final state, is the most viable decay mode. The first evidence of $t\bar{t}$ production in the dilepton final state in Pb+Pb collisions, with an observed significance of 4.8 standard deviations, has been reported by CMS [79]. The measurement, presented in Figure 1.17b, is in agreement with the CT14+EPPS16 theoretical prediction, and the cross section in pp collisions [80] scaled by A_{Pb}^2. These results are first milestones in the research of $t\bar{t}$ production in the p+Pb and Pb+Pb systems and have paved the way for further studies of this process in heavy-ion collisions at the LHC.

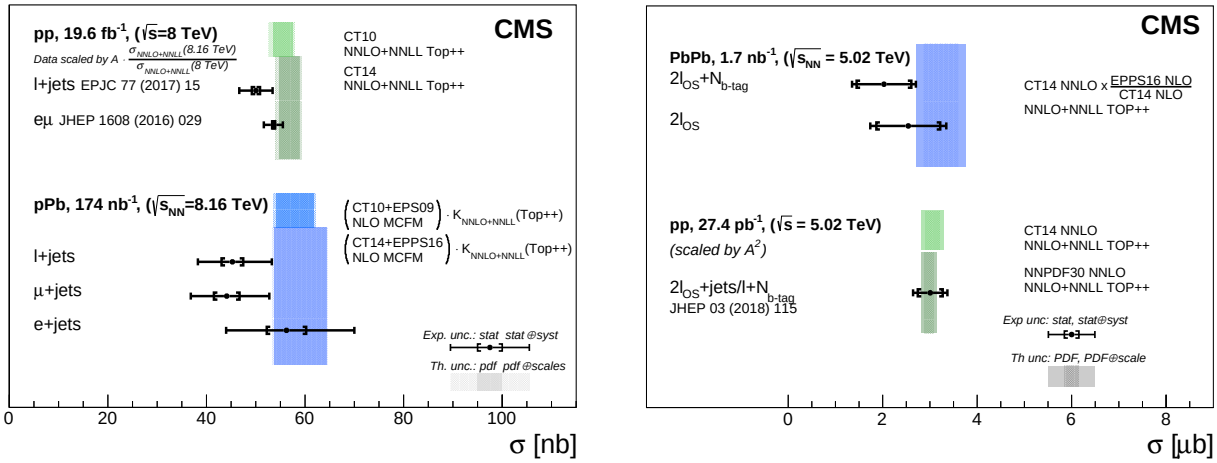

(a) (b)

Figure 1.17: Measured $t\bar{t}$ production cross sections in (a) p+Pb collisions at $\sqrt{s_{\mathrm{NN}}} = 8.16$ TeV [74], and (b) Pb+Pb collisions at $\sqrt{s_{\mathrm{NN}}} = 5.02$ TeV [79], compared with the theoretical predictions and scaled results in pp collisions.

The aim of this thesis is the observation of $t\bar{t}$ production in p+Pb and Pb+Pb collisions with the ATLAS detector. Due to the complexity of measuring $t\bar{t}$ production in heavy-ion collisions, mainly ATLAS and CMS experiments are capable of studying this process. In particular, the lower acceptance of the ALICE detector, combined with lower particle p_{T} spectra and limited heavy-ion data statistics, makes the $t\bar{t}$ analysis in the ALICE experiment challenging. The $t\bar{t}$ cross section in heavy-ion collisions can be measured with higher precision compared to the previous CMS measurements [74, 79], thanks to lower p_{T} thresholds imposed on leptons and jets in the ATLAS experiment. In p+Pb collisions, the dilepton channel of $t\bar{t}$ decays can be studied for the first time. Additionally, the nuclear modification factor, $R_{p\mathrm{A}}$, can be extracted for the $t\bar{t}$ process. In Pb+Pb collisions, the full Pb+Pb data collected in 2015 and 2018 with the ATLAS detector can be used, allowing for the first observation of $t\bar{t}$ production with a significance above five standard deviations.

Chapter 2

ATLAS experiment

2.1 Large Hadron Collider

The LHC [81], the largest and highest-energy particle accelerator to date, is located on the French-Swiss border near Geneva. It occupies a 27 km-long circular tunnel, previously used by the Large Electron-Positron (LEP) collider, 45–170 m underground. In 1997, the European Organization for Nuclear Research (CERN) officially approved the project, with construction lasting from 1998 to 2008. Over 10,000 scientists from more than 100 countries collaborated on the project. The first collisions took place in 2010, reaching an energy of 3.5 TeV per beam, nearly four times higher than the previous record set by the Tevatron located at the Fermi National Accelerator Laboratory (Fermilab) [82].

The first operational period at high energy, referred to as Run 1, took place in 2010–2013. At the time, the LHC was accelerating protons up to an energy of 4 TeV, resulting in pp collisions at a centre-of-mass energy of up to $\sqrt{s} = 8$ TeV. Since 2010, the collider has been adjusted to provide heavy-ion collisions, resulting in Pb+Pb and p+Pb data-taking periods at centre-of-mass energies of $\sqrt{s_{\mathrm{NN}}} = 2.76$ and 5.02 TeV per nucleon pair, respectively. The second operational run (Run 2) lasted from 2015 to 2018, following a two-year maintenance break. The collision energy was increased, resulting in centre-of-mass energies per nucleon pair of $\sqrt{s} = 13$ TeV and $\sqrt{s_{\mathrm{NN}}} = 5.02$ TeV for pp and Pb+Pb systems, respectively. Two p+Pb data-taking periods took place at centre-of-mass energies of $\sqrt{s_{\mathrm{NN}}} = 5.02$ and 8.16 TeV per nucleon pair. Additionally, a short run of xenon–xenon (Xe+Xe) data was recorded in 2017 at a centre-of-mass energy of $\sqrt{s_{\mathrm{NN}}} = 5.44$ TeV per nucleon pair. The current data-taking period, Run 3, started in 2022 and is planned to last until the middle of 2026. Data from pp collisions have been collected at a record energy of $\sqrt{s} = 13.6$ TeV, while Pb+Pb data have been recorded at a slightly higher energy of $\sqrt{s_{\mathrm{NN}}} = 5.36$ TeV per nucleon pair. The periods of 2013–2014 and 2019–2021 are referred to as Long Shutdown 1 and 2, respectively, and were dedicated to detector upgrades and maintenance.

The particle acceleration process at the LHC is divided into multiple stages, as shown in Figure 2.1. The proton injection chain starts by stripping hydrogen atoms of their electrons in a duoplasmatron. The obtained protons are accelerated in the linear accelerator LINAC 4, which boosts them to an energy of 160 MeV. Protons are

then directed through circular accelerators: Proton Synchrotron Booster (PSB), Proton Synchrotron (PS), and Super Proton Synchrotron (SPS), achieving energies of 1.4 GeV, 25 GeV, and 450 GeV at each stage. Finally, particles are split into two counter-circulating beams and injected into the LHC, where they reach their target energy.

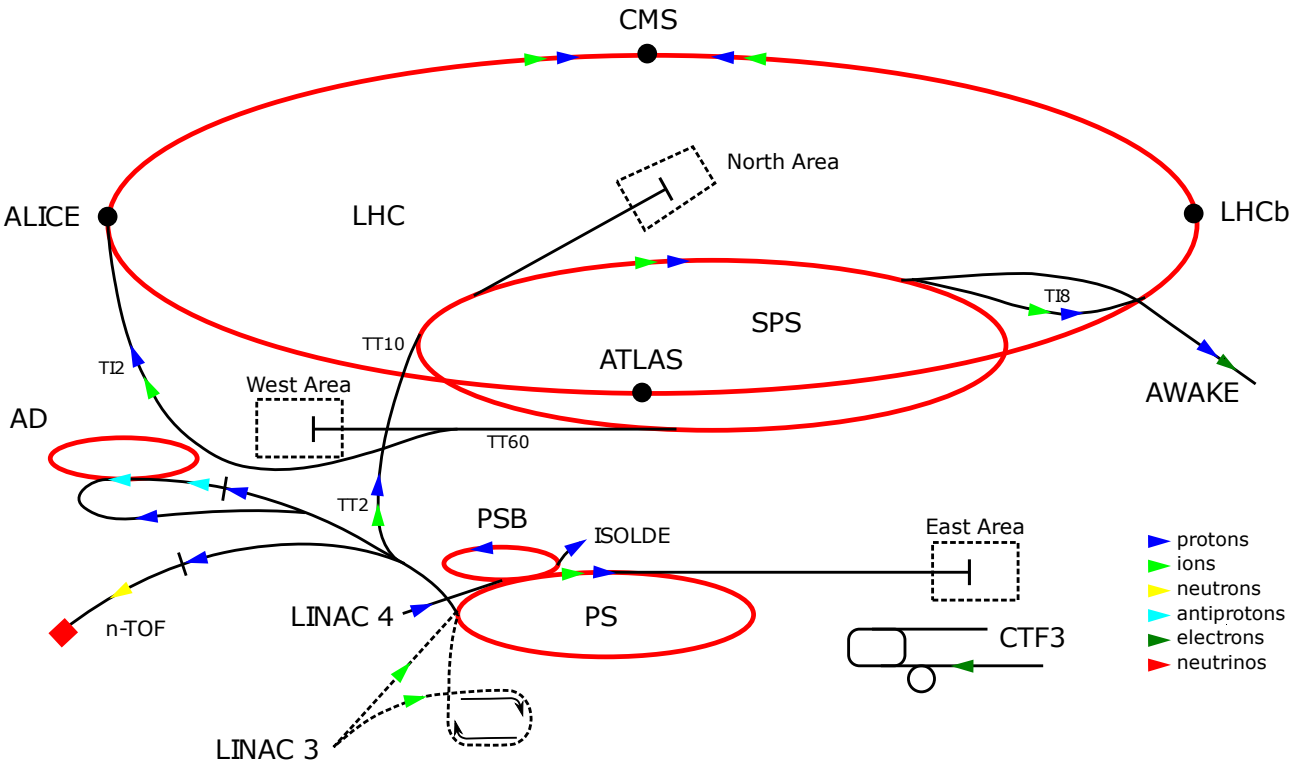

Figure 2.1: Scheme of the CERN accelerator complex [83].

Lead (Pb) ions require a dedicated acceleration chain, which starts by injecting Pb^{27+} nuclei from the electron cyclotron resonance (ECR) source into the linear accelerator LINAC 3. They are boosted to an energy of 4.2 MeV/nucleon and stripped to Pb^{54+} ions using a 0.3 µm-thick carbon foil. Particles are then accelerated in the Low Energy Ion Ring (LEIR) and the PS to energies of 72 MeV/nucleon and 6 GeV/nucleon, respectively. They are fully stripped into Pb^{82+} ions using an aluminium foil before reaching the SPS. After being boosted to an energy of 177 GeV/nucleon, Pb ions are transferred to the LHC to reach the nominal energy.

Beams of particles are split into bunches, nominally containing about 10^{11} protons or 10^{8} lead ions. Approximately 2,000 proton or 1,000 lead bunches are injected into the LHC, with bunch crossings occurring every 25 ns (50 ns) in pp (heavy-ion) collisions during Run 2, providing a collision rate of up to 40 MHz. The average number of simultaneous interactions per bunch crossing, $\langle\mu\rangle$, referred to as pileup, is about 30 (50) in Run 2 (Run 3) in the pp system. Heavy-ion collisions are collected under low-pileup conditions, with $\langle\mu\rangle \ll 1$. Particles are collided at one of the four interaction points (IP) around the LHC.

Nine independent experiments have been established at the LHC to date, located near the IPs. Four main detectors are situated at each IP: ATLAS (A Toroidal LHC Apparatus) [84], CMS (Compact Muon Solenoid) [85], ALICE (A Large Ion Collider Experiment) [86], and LHCb (Large Hadron Collider Beauty) [87]. The first

two, ATLAS and CMS, are multi-purpose detectors designed to study a wide range of rare processes, primarily oriented toward precision measurements of Higgs physics. ALICE specialises in heavy-ion collisions to investigate properties of the QGP, with precision measurements and particle identification down to very low energies. LHCb focuses on b-hadron physics, including charge-parity (CP) violation, with detector geometry covering the forward region where the probability of B meson production is maximal. Five smaller experiments are also accommodated at the LHC, sharing IPs with the main experiments. TOTEM (TOTal Elastic and diffractive cross-section Measurement) [88] is dedicated to measurements of the total elastic scattering and diffractive cross sections. LHCf (Large Hadron Collider forward) [89] is intended to measure the number and energy of neutral pions produced in the forward region of LHC collisions. MoEDAL (Monopole and Exotics Detector at the LHC) [90] aims to search for magnetic monopoles. FASER (ForwArd Search ExpeRiment) [91] is designed to search for new light and weakly coupled particles. SND (Scattering and Neutrino Detector) [92], the newest experiment at the LHC, focuses on studying neutrinos produced at the LHC and searching for feebly interacting particles.

2.2 ATLAS detector

ATLAS [84] is the largest general-purpose particle detector at the LHC, intended for precise measurements of particle physics studies at high energies. It is designed with a cylindrical geometry around the IP, providing solid angle coverage of almost 4π. The construction is barrel-shaped, 44 m long, 25 m high, and has a mass of approximately 7000 tons. It is split into a cylindrical part, referred to as the barrel, and two terminal pieces, named endcaps. The schematic of the ATLAS detector is shown in Figure 2.2.

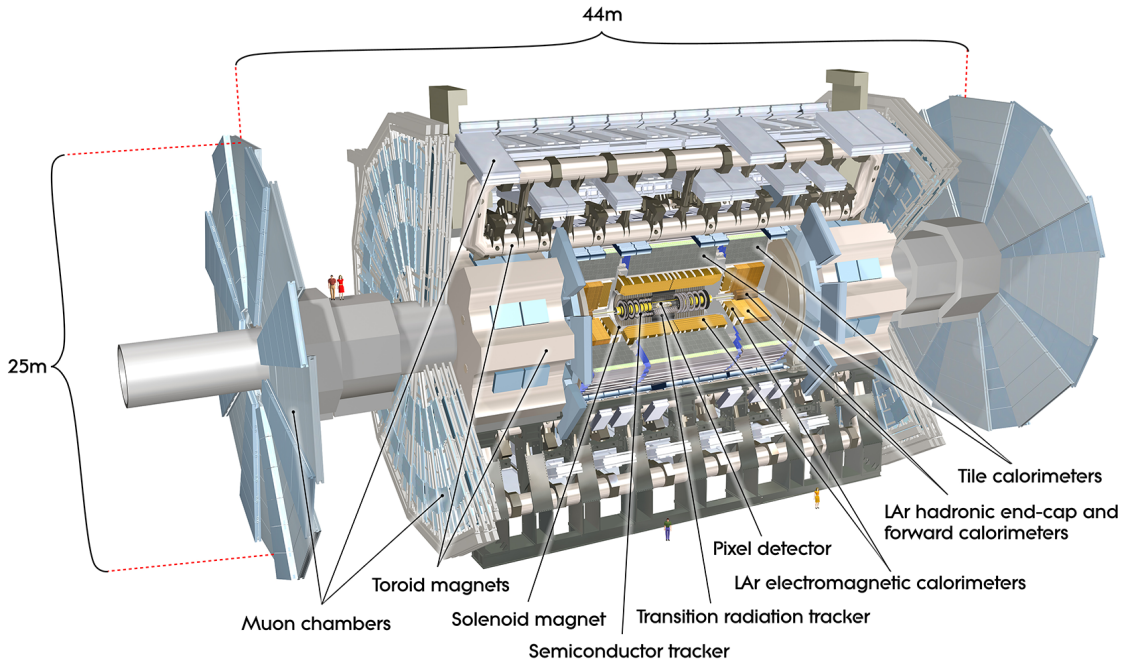

Figure 2.2: Overview of the ATLAS detector [93].

The physics programme of the ATLAS experiment is comprehensive and diverse, covering precision measurements of the SM as well as searches for new physics beyond it. The detector is designed to operate efficiently under the demanding conditions of unprecedented high energies, necessitating the use of fast and radiation-hard detection modules and electronics. To precisely determine the physical quantities of collision products, the construction comprises several detector layers, designed to collect various types of information about traversing particles.

2.2.1 Global coordinate system

The ATLAS global coordinate system is presented in Figure 2.3. The origin of the system, corresponding to the geometric centre of the detector, is located at the nominal IP. The right-handed Cartesian coordinate system is defined with the x-axis pointing towards the centre of the LHC ring, the y-axis oriented upwards, and the z-axis parallel to the beam in the anticlockwise direction. Along the z-axis, the detector is divided into two parts with positive and negative z values, referred to as side A and side C, respectively.

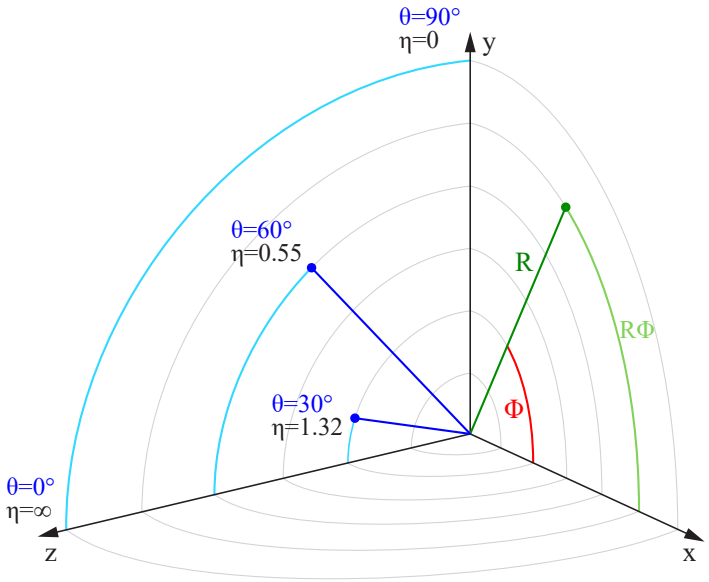

Figure 2.3: Visualisation of the ATLAS global coordinate system [94].

The detector's geometry justifies the use of spherical coordinates. The azimuthal angle ϕ is determined in the x-y plane from the x-axis towards the y-axis. The polar angle θ is defined from the positive side of the z-axis. The radial coordinate R is measured from the origin of the system. The radial distance between two objects, ΔR, is defined by the following expression:

$$\Delta R = \sqrt{(\Delta\eta)^2 + (\Delta\phi)^2}. \tag{2.1}$$

The x–y plane is used to define transverse quantities, such as transverse momentum, p_{T}, and transverse energy, E_{T}, which are expressed by the following formulas:

$$p_{\mathrm{T}} = \sqrt{p_x^2 + p_y^2}, \tag{2.2}$$

$$E_{\mathrm{T}} = \sqrt{p_{\mathrm{T}}^2 + m^2}. \tag{2.3}$$

Instead of the θ angle, the rapidity y is mainly used, which is defined as follows:

$$y = \frac{1}{2} \ln \left(\frac{1 + \beta \cos\theta}{1 - \beta \cos\theta} \right), \tag{2.4}$$

where $\beta = v/c$ is the ratio of particle velocity to the speed of light. In the limit where a particle is massless or its velocity is close to the speed of light, rapidity converges to pseudorapidity, defined as

$$\eta = -\ln \left(\tan \frac{\theta}{2} \right). \tag{2.5}$$

The use of rapidity and pseudorapidity is motivated by the fact that Δy and $\Delta\eta$ distances are Lorentz invariant under the boost along the z-axis.

2.2.2 Inner detector

The inner detector [95], located closest to the IP, is designed for precise measurement of charged-particle trajectories. It allows for determining the momentum and charge of traversing particles from the track curvature. The measured tracks are used to reconstruct primary and secondary collision vertices. The vertexing capabilities enable the separation of events of interest from pileup collisions and identification of particles with short lifetimes, such as b-hadrons, which result in displaced decay vertices. Figure 2.4 shows the transverse and longitudinal impact parameters, d_0 and z_0, defined as the distances of closest approach between a particle track and the primary vertex in the transverse and longitudinal directions, respectively. The sign of d_0 depends on the angle between the d_0 vector and the track direction, and is defined as positive (negative) for an angle of $\pi/2$ ($-\pi/2$). The measured uncertainties in the impact parameters are denoted as $\sigma(d_0)$ and $\sigma(z_0)$.

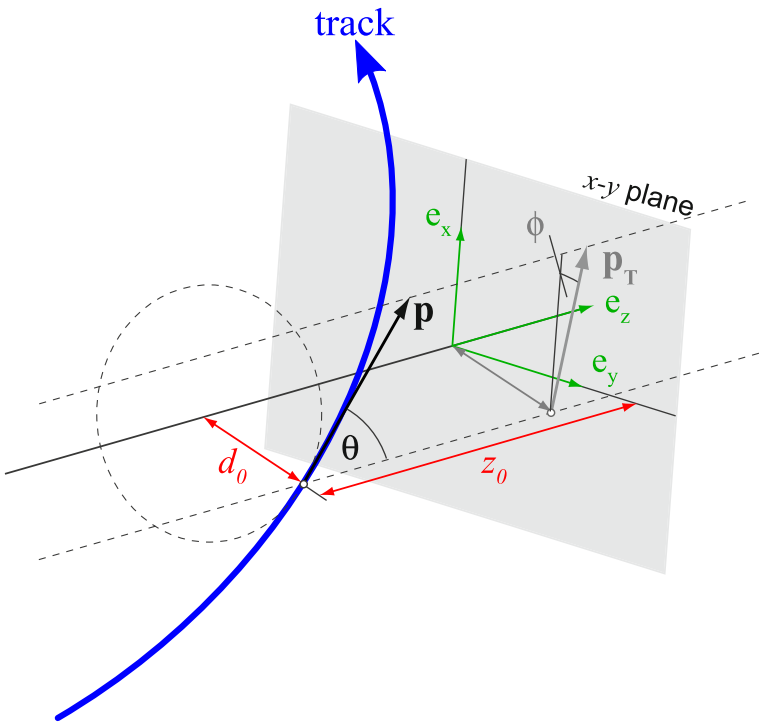

Figure 2.4: Scheme of the track parameters, including d_0 and z_0 [96].

The inner detector is 2.1 m in diameter and 6.2 m long, providing pseudorapidity coverage of $|\eta| < 2.5$. It is immersed in a 2 T axial magnetic field generated by the central solenoid magnet, causing the trajectories of charged particles to bend. As charged particles pass through the inner detector, they produce electrical signals at specific points, referred to as hits, which are used for track reconstruction. Figure 2.5 presents an overview of the inner detector.

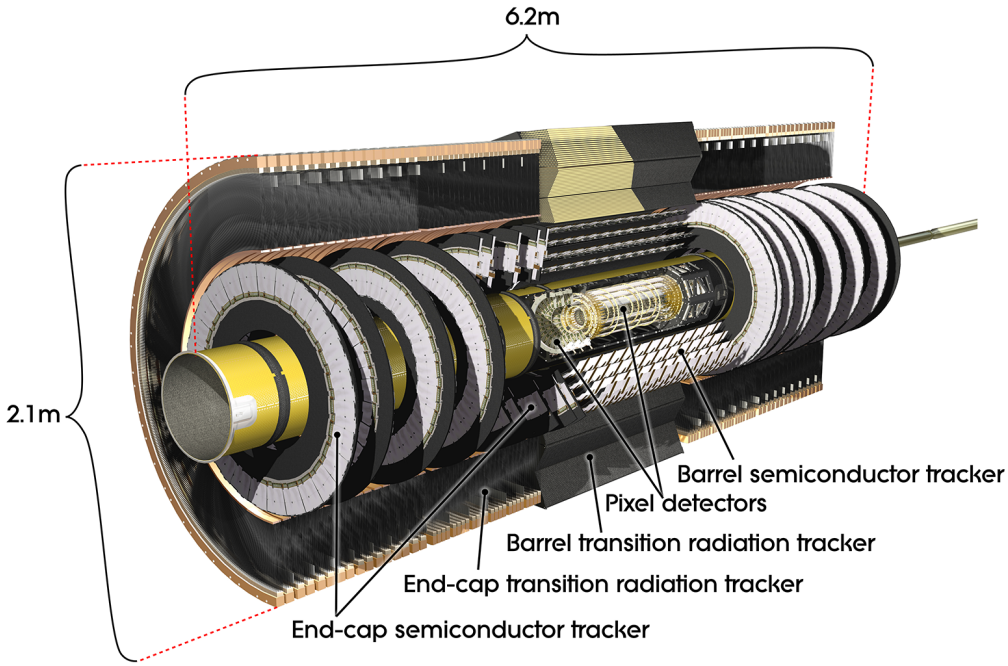

Figure 2.5: Overview of the ATLAS inner detector [97].

The pixel detector [98], the innermost system of the inner detector, consists of four layers of highly granular silicon sensors. The insertable B-Layer (IBL) [99], situated closest to the beam, was added in 2014 during Long Shutdown 1. Located 33.5 mm away from the IP, it is specifically designed to improve secondary vertexing, crucial for b-hadron identification. The remaining three layers are installed at distances of 50.5 mm, 88.5 mm, and 122.5 mm from the beam axis. Three pixel disks are positioned on each side of the detector in the endcap region, located at $|z|$ distances of 495 mm, 580 mm, and 650 mm. Silicon detectors provide exceptional spatial resolution, with a minimal pixel size of 50×250 µm and 50×400 µm in the IBL and external layers, respectively. Over 80 million read-out channels in total measure three-dimensional particle positions for track reconstruction. On average, they provide four hits per track, with the first hit most likely registered in the IBL.

The semiconductor tracker (SCT) [100], situated outside the silicon pixel detector, consists of 15,912 silicon microstrips grouped into 4,088 modules. They are formed into four layers around the IP in the barrel region, installed at distances of 299 mm, 371 mm, 443 mm, and 514 mm from the beam, and into nine disks on each detector side, located at the $|z|$ distance between 850 mm and 2720 mm. Pairs of strips are rotated by a 40 mrad angle, providing three-dimensional position measurements. The SCT provides over 6 million read-out channels, allowing for spatial resolution of 17 µm in the ϕ direction and 580 µm in the z (R) direction in the barrel (endcap) region. A charged particle leaves on average eight hits in the SCT.

The transition radiation tracker (TRT) [101], the outermost part of the inner detector, is a gaseous detector system. It consists of more than 350,000 drift tubes, referred to as straws, which are 144 cm in length and 4 mm in diameter, with a 30 µm gold-plated tungsten wire at the centre. All straws are filled with a xenon-based gas mixture of 70% Xe, 27% CO_2, and 3% O_2. Groups of straws are interlayered with polypropylene fibres or foils in the barrel and endcap regions, respectively, inducing transition radiation emitted by traversing charged particles. The emission of transition radiation is significantly more probable for electrons compared to hadrons, which is used for electron identification. The TRT provides two-dimensional spatial resolution of approximately 130 µm in the R–ϕ plane. On average, 36 hits per track are registered by over 350,000 read-out channels.

2.2.3 Calorimeters

The calorimeter system [102] is engineered to absorb most particles, including electrons, photons, and hadrons, except muons and neutrinos. Its main purpose is to accurately measure particle energy and position. It also allows determination of missing E_{T} and plays a key role in the identification of electrons and photons. The system is designed to fully contain most particle cascades produced by incoming primary particles, referred to as showers. Two fundamental types of particle showers are recognized: electromagnetic (EM) showers, generated by particles interacting via the EM force, mainly photons and electrons; and hadronic showers, caused by hadrons. The system is divided into two components: the EM calorimeter and the hadronic calorimeter, designed to register the corresponding showers. Both calorimeter types consist of alternating layers of absorber, generating particle showers, and active material, measuring particle energy. A transition region between the barrel and endcaps ($1.37 < |\eta| < 1.52$), colloquially called the crack in the detector, is devoid of sampling material, resulting in reduced particle detection efficiency. An overview of the calorimeter system is displayed in Figure 2.6.

The EM calorimeter subsystem uses liquid argon (LAr) technology [104], which employs argon in the liquid state as the active material and lead coated in stainless steel as the absorber. The electric charge from argon ionisation is collected by copper-kapton electrodes. Layers of the sampling material and the absorber are formed in an accordion shape, providing full coverage in the azimuthal angle. Three longitudinal layers are installed in the barrel region ($|\eta| < 1.475$) with fine granularity in the η-ϕ space. The endcap region is divided into inner ($1.375 < |\eta| < 2.5$) and outer ($2.5 < |\eta| < 3.2$) parts with three and two layers, respectively. The total thickness of the EM calorimeter, represented using the radiation length X_0, exceeds $22X_0$ in the barrel and $24X_0$ in the endcaps, fully absorbing most particle showers.

The tile hadronic calorimeter [105], built around the EM calorimeter, utilises organic scintillator as the sampling material, while iron is used as the absorber. The barrel region is divided into a central barrel part ($|\eta| < 1.0$) and two extended barrel parts ($0.8 < |\eta| < 1.7$), each with three calorimeter layers. In the endcap region, hadronic calorimetry is provided by the hadronic endcap calorimeter (HEC), covering forward pseudorapidities ($1.5 < |\eta| < 3.2$). The HEC system utilises LAr technology with copper plates used as the absorber. In each endcap, it is segmented into four calorimeter layers.

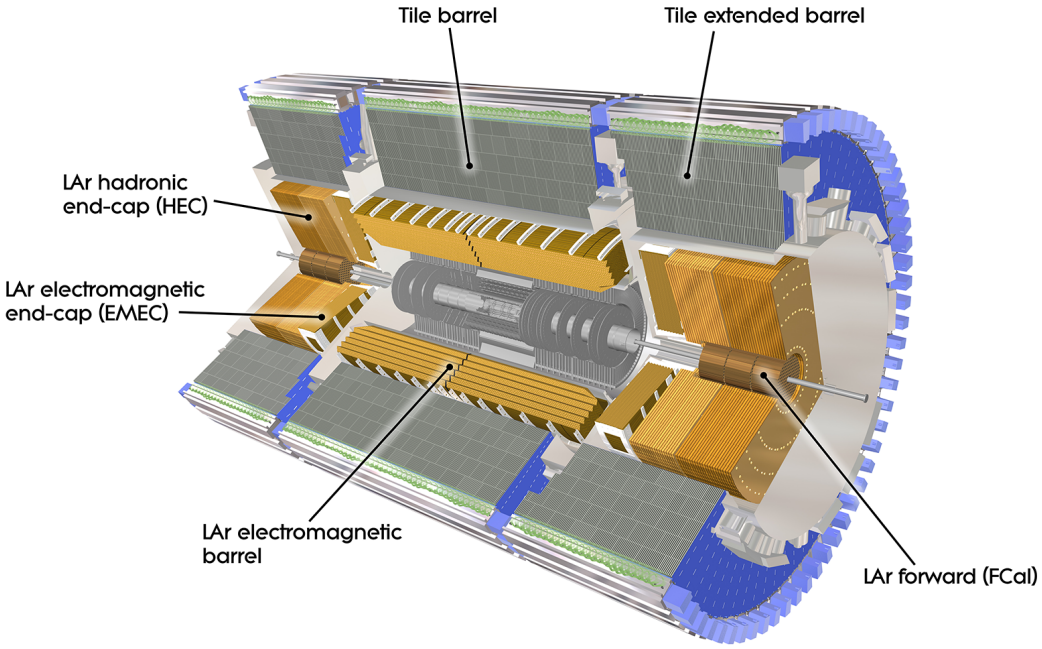

Figure 2.6: Overview of the ATLAS calorimeter system [103].

The forward calorimeter (FCal) [106], located at a distance of approximately 4.7 m from the IP, provides coverage in the most forward region ($3.1 < |\eta| < 4.9$). It consists of two parts, installed in each endcap, with one EM and two hadronic layers. Both layer types use LAr as the active material, while the absorber is made of copper and tungsten in the EM and hadronic layers, respectively.

2.2.4 Muon spectrometer

The muon spectrometer (MS) [107], as the outermost subdetector system, determines the dimensions of the ATLAS detector. It is installed around the calorimeter, covering a radial distance from 4.25 m to 11 m from the IP. It is designed to register the trajectories of muons, which escape previous detector layers due to their high mass and weak interaction with matter. Three superconducting air-core toroid magnets provide the magnetic field to curve muon tracks, allowing for precise momentum measurement. Each magnet is composed of eight coils, with the barrel magnet of 0.5 T covering the central region ($|\eta| < 1.4$) and two endcap magnets of 1 T covering the forward region ($1.6 < |\eta| < 2.7$). The transition region of $1.4 < |\eta| < 1.6$ is covered by a combination of barrel and endcap fields. A small gap in MS acceptance is located in the $|\eta| < 0.1$ region, allowing access to the calorimeters, the inner detector, and the solenoid magnet. The MS combines four types of muon chambers, grouped into three layers around the barrel and three layers in the endcaps perpendicular to the beam. Figure 2.7 shows an overview of the MS system.

Monitored drift tubes (MDT) [109] provide precision tracking for muons in the $|\eta| < 2.7$ range. They comprise aluminium tubes with a diameter of 3 cm, filled with a gas mixture of 93% Ar and 7% CO_2. Ions produced by traversing muons are collected by tungsten-rhenium wires, installed at the centre of the tubes. Measuring the drift time improves the position resolution of muons. Cathode strip chambers (CSC) [107] supplement tracking

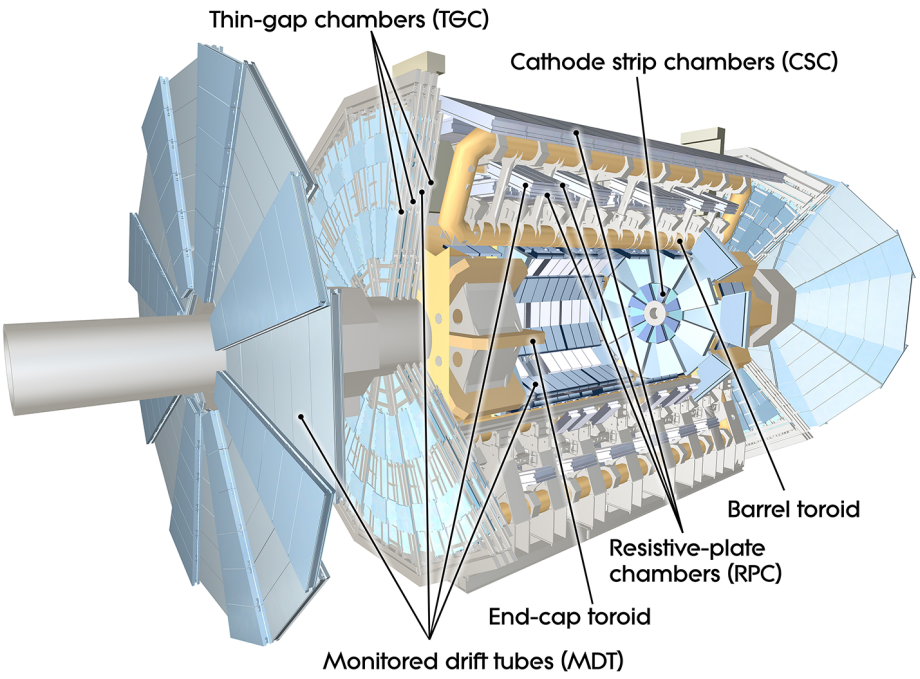

Figure 2.7: Overview of the ATLAS muon spectrometer system [108].

in the forward region of $2.0 < |\eta| < 2.7$, where higher muon rates are expected. They are based on multiwire proportional chambers, filled with a gas mixture of 80% Ar and 20% CO_2. Eight large and eight small trapezoid plates provide full azimuthal coverage.

Resistive plate chambers (RPC) [110], with good time resolution of ∼1 ns, provide dedicated triggering for muons in the barrel region ($|\eta| < 1.05$). Each chamber consists of two phenolic-melaminic electrode plates separated by a 2 mm gap, filled with a gas mixture of 94.7% $C_2H_2F_4$, 5% C_4H_{10}, and 0.3% SF_6. RPC modules are arranged in three concentric layers, covering the full azimuthal angle. Thin gap chambers (TGC) [107] are responsible for muon triggering in the endcap region ($1.05 < |\eta| < 2.4$). They utilise multiwire proportional chambers, filled with a gas mixture of 55% CO_2 and 45% n-C_5H_{12}. Additionally, TGC modules provide position measurements in the azimuthal angle.

2.3 Luminosity

Luminosity, one of the most important parameters of an accelerator, determines the number of collisions delivered to the detector. The instantaneous luminosity $\mathcal{L}$ is independent of the process and can be expressed entirely by beam parameters using the formula [111]

$$\mathcal{L} = \frac{f_{\mathrm{r}} n_{\mathrm{b}} N_1 N_2}{4\pi\sigma_x\sigma_y} F, \tag{2.6}$$

where f_{r} denotes the revolution frequency, n_{b} is the number of bunches per beam, N_1 (N_2) represents the number of particles in the first (second) bunch, while σ_x (σ_y) is the transverse beam size in the x (y) direction, assuming the particles in the beam are Gaussian distributed. A typical unit of instantaneous luminosity used in high-energy physics is $1\ \mathrm{b}^{-1}\mathrm{s}^{-1} = 10^{24}\ \mathrm{cm}^{-2}\mathrm{s}^{-1}$.

In the case of collisions at the crossing angle θ_c, the luminosity is reduced by the geometrical reduction factor F, which amounts to

$$F = \left(1 + \left(\frac{\theta_c \sigma_z}{2\sigma_x}\right)^2\right)^{-\frac{1}{2}}, \tag{2.7}$$

where σ_z is the longitudinal beam size in the z direction. The integrated luminosity L is calculated by integrating the instantaneous luminosity over a period of time, namely

$$L = \int \mathcal{L}\, dt. \tag{2.8}$$

The expected number of events of a process with cross section σ is given by

$$N = \sigma L. \tag{2.9}$$

The total integrated luminosity recorded by ATLAS in pp collisions at $\sqrt{s} = 13$ TeV in Run 2 amounts to 147 fb^{-1}, as presented in Figure 2.8. During special data-taking campaigns, pp collisions at $\sqrt{s} = 5.02$ TeV were collected in 2015 and 2017, corresponding to integrated luminosities of 25 and 257 pb^{-1}, respectively. These data provide a reference system for heavy-ion collisions at the same centre-of-mass energy.

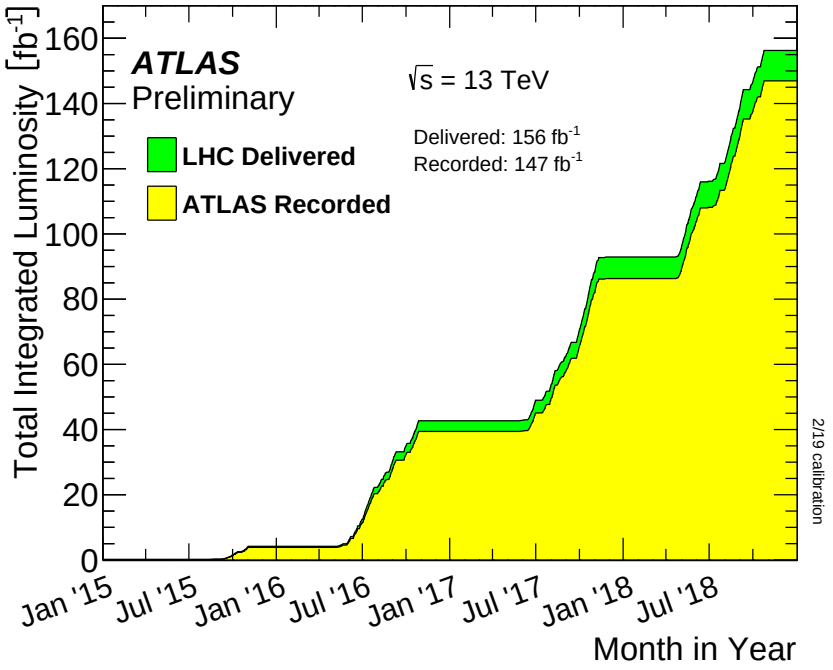

Figure 2.8: Total integrated luminosity delivered to ATLAS (green) and recorded by ATLAS (yellow) during stable beams for pp collisions at $\sqrt{s} = 13$ TeV in Run 2 (2015–2018) [112].

Heavy-ion collisions are typically collected for one month per year. ATLAS recorded 2.3 nb^{-1} of Pb+Pb data at $\sqrt{s_{\mathrm{NN}}} = 5.02$ TeV during Run 2 and 180 nb^{-1} of p+Pb data at $\sqrt{s_{\mathrm{NN}}} = 8.16$ TeV in 2016. Figure 2.9 shows the total integrated luminosity versus time for Pb+Pb collisions delivered in 2015 and 2018. Of the data collected during Run 2, 1.9 nb^{-1} of Pb+Pb collisions and 165 nb^{-1} of p+Pb collisions are validated to be of good quality for physics measurements.

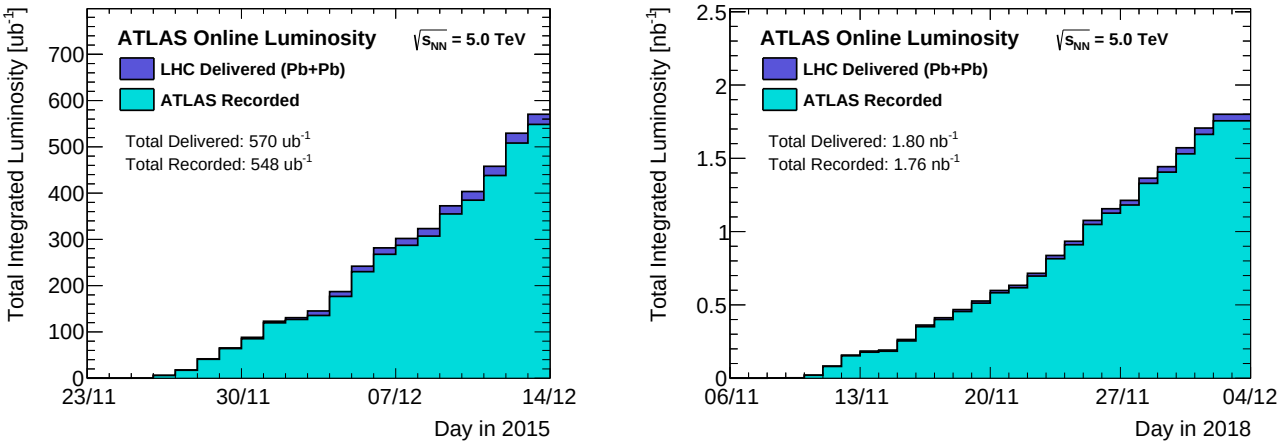

(a) (b)

Figure 2.9: Total integrated luminosity delivered to ATLAS (blue) and recorded by ATLAS (cyan) in Pb+Pb collisions at $\sqrt{s} = 5.02$ TeV in (a) 2015 and (b) 2018 during Run 2 [112].

The average number of simultaneous interactions per bunch crossing, referred to as pileup [113], can be expressed by the formula [114]

$$\mu = \frac{\sigma_{\text{inel}}\mathcal{L}}{f_{\text{r}} n_{\text{b}}}, \tag{2.10}$$

where σ_{inel} is the total inelastic cross section. Multiple interactions within a single bunch crossing are called in-time pileup, while interactions from preceding or subsequent bunch crossings are referred to as out-of-time pileup. Figure 2.10 presents in-time pileup values in pp and Pb+Pb collisions during Run 2. The average number of interactions per bunch crossing in pp data is about $\langle\mu\rangle = 30$. Meanwhile, heavy-ion collisions are collected under low-pileup conditions. Pb+Pb data in 2015 and 2018 were collected at $\langle\mu\rangle = 1.76 \cdot 10^{-3}$ and $\langle\mu\rangle = 2.58 \cdot 10^{-3}$, respectively, while p+Pb data in 2016 were recorded at $\langle\mu\rangle = 0.18$.

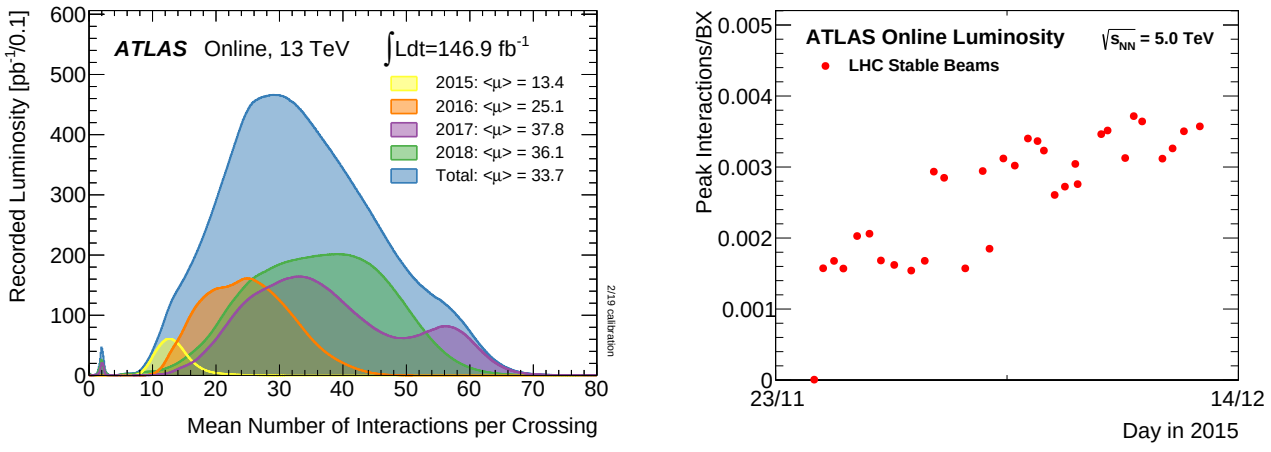

(a) (b)

Figure 2.10: (a) Mean number of interactions per bunch crossing during stable beams for pp collisions in Run 2 (2015–2018). (b) The maximum number of interactions per bunch crossing in Pb+Pb collisions in 2015 during Run 2 [112].

2.4 Heavy-ion collisions

During the heavy-ion data-taking period at the LHC, both nucleus–nucleus and proton–nucleus collisions are recorded. Due to multiple nucleon–nucleon interactions, the energy released in a collision is substantially higher than in pp collisions. Depending on the collision geometry, only a certain fraction of the nucleons participate in interactions. Nucleons that undergo interactions are referred to as participants, while the remaining ones are called spectators, as illustrated in Figure 2.11. The transverse distance between the centres of the two colliding nuclei is described by the impact parameter b. Central collisions are characterised by b close to 0, while peripheral collisions have b close to $2R_{\mathrm{A}}$, where R_{A} is the radius of the nucleus. For $b > 2R_{\mathrm{A}}$, the approaching nuclei interact mainly electromagnetically – a scenario referred to as ultra-peripheral collisions.

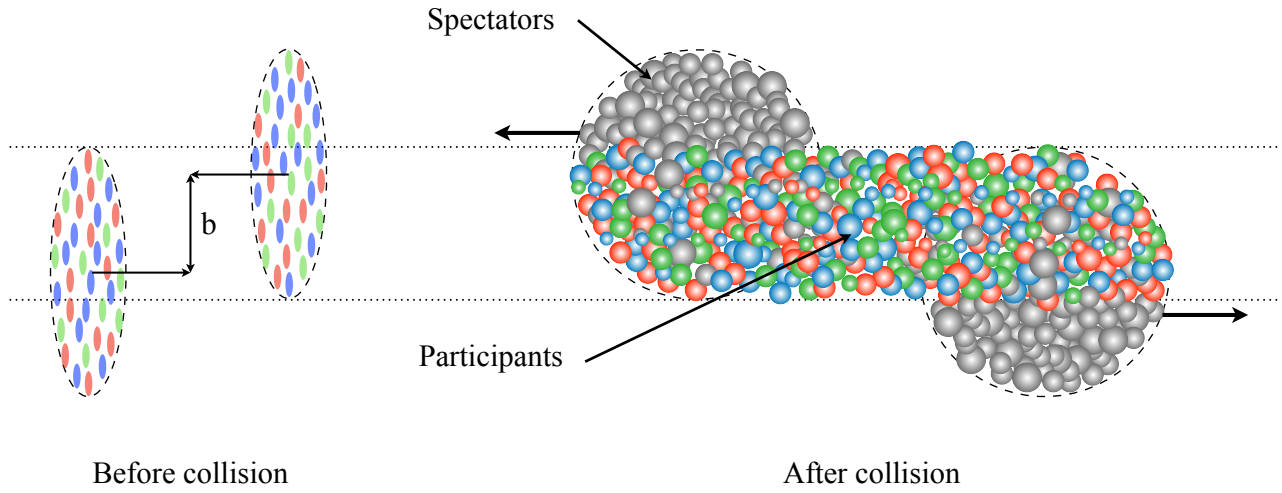

Figure 2.11: A schematic view of a heavy-ion collision with the impact parameter b [115].

The collision geometry can be approximated using the Glauber model [116], as shown in Figure 2.12. In this method, a nucleus–nucleus collision is described as the sum of multiple independent nucleon–nucleon interactions. Two parameters are used in calculations: the nuclear density, ρ, and the inelastic nucleon–nucleon cross section, $\sigma_{\mathrm{inel}}^{\mathrm{NN}}$. The nuclear density as a function of the distance from the nucleus centre can be described by a Fermi distribution,

$$\rho(r) = \rho_0 \frac{1 + w\left(\frac{r}{R}\right)^2}{1 + \exp\left(\frac{r-R}{a}\right)}, \tag{2.11}$$

where ρ_0 denotes the nucleon density in the centre of the nucleus, R corresponds to the nuclear radius, a refers to the skin depth, and w characterises deviations from a spherical shape. Typical parameters for the lead nucleus are $\rho_0 = 0.156$, $R = 6.62$ fm, $a = 0.546$ fm, and $w = 0$ fm [117, 118]. The probability of a nucleon being located at the transverse position $\vec{s}$ within nucleus A can be written as

$$\hat{T}_{\mathrm{A}}(\vec{s}) = \int \rho_{\mathrm{A}}(\vec{s}, z)\, dz, \tag{2.12}$$

where ρ_{A} is the nuclear density of nucleus A per unit volume and z is the longitudinal coordinate. The nuclear overlap function is defined as the integrated probability of finding nucleons in both nuclei A and B separated

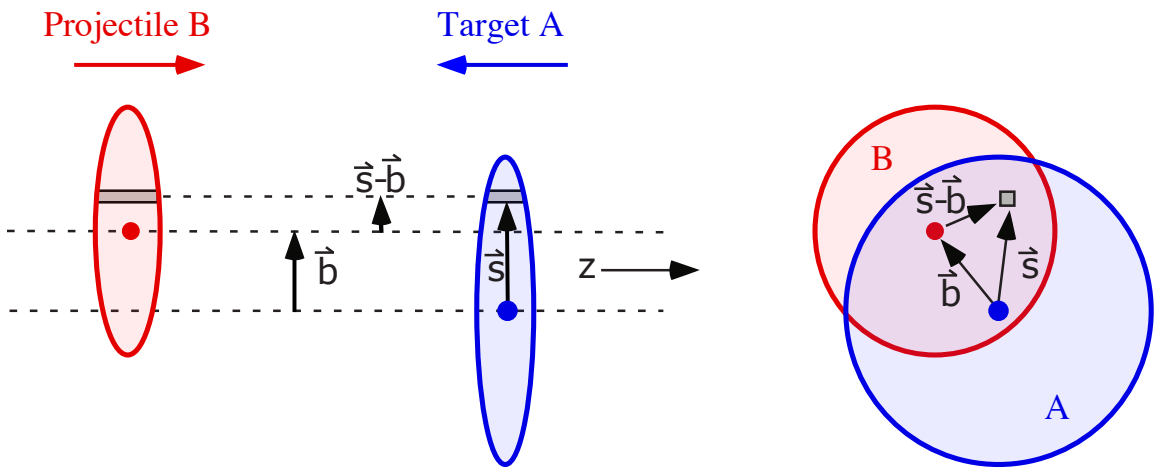

Figure 2.12: Schematic representation of the Glauber model geometry [116].

by the impact parameter $\vec{b}$, namely

$$\hat{T}_{\mathrm{AB}}(\vec{b}) = \int \hat{T}_{\mathrm{A}}(\vec{s})\, \hat{T}_{\mathrm{B}}(\vec{s}-\vec{b})\, d^2s. \tag{2.13}$$

It could be noted that $\hat{T}_{\mathrm{AB}}(\vec{b})$ has the unit of inverse area, similar to the luminosity, and therefore can be interpreted as the effective overlap area for a nucleon–nucleon interaction. The probability of n such interactions between nuclei A and B with N_{A} and N_{B} nucleons, respectively, can be described using a binomial distribution,

$$P(n,\vec{b}) = \binom{N_{\mathrm{A}}N_{\mathrm{B}}}{n} \left(\hat{T}_{\mathrm{AB}}(\vec{b})\, \sigma_{\mathrm{inel}}^{\mathrm{NN}}\right)^n \left(1 - \hat{T}_{\mathrm{AB}}(\vec{b})\, \sigma_{\mathrm{inel}}^{\mathrm{NN}}\right)^{N_{\mathrm{A}}N_{\mathrm{B}}-n}. \tag{2.14}$$

The total number of nucleon–nucleon collisions, N_{coll}, is then given by the mean of the above binomial distribution, namely

$$N_{\mathrm{coll}}(\vec{b}) = \sum_{n=1}^{N_{\mathrm{A}}N_{\mathrm{B}}} nP(n,\vec{b}) = N_{\mathrm{A}}N_{\mathrm{B}}\, \hat{T}_{AB}(\vec{b})\sigma_{\mathrm{inel}}^{\mathrm{NN}}. \tag{2.15}$$

The number of participants N_{part}, also referred to as wounded nucleons, can be expressed as

$$\begin{aligned} N_{\mathrm{part}}(\vec{b}) = N_{\mathrm{A}} \int \hat{T}_A(\vec{s}) \left(1 - \left(1 - \hat{T}_B(\vec{s}-\vec{b})\, \sigma_{\mathrm{inel}}^{\mathrm{NN}}\right)^{N_{\mathrm{B}}}\right) d^2s + \\ N_{\mathrm{B}} \int \hat{T}_B(\vec{s}-\vec{b}) \left(1 - \left(1 - \hat{T}_A(\vec{s})\, \sigma_{\mathrm{inel}}^{\mathrm{NN}}\right)^{N_{\mathrm{A}}}\right) d^2s. \end{aligned} \tag{2.16}$$

The geometric parameters b, N_{coll}, and N_{part} are not directly accessible experimentally. Since the size of the interaction region affects many final-state observables, it is crucial to account for the collision geometry in measurements. Therefore, experimental quantities that depend on the overlap region between two nuclei are considered, such as the energy in the forward region or the number of charged-particle tracks. These quantities are used to define classes of collision centrality, with 0% and 100% representing the most central and peripheral collisions, respectively. In this context, the 0–10% class corresponds to the 10% most central collisions. Each

centrality class is associated with average geometric parameters, $\langle b \rangle$, $\langle N_{\mathrm{coll}} \rangle$, and $\langle N_{\mathrm{part}} \rangle$, which are estimated using the Glauber model. In the ATLAS experiment, the collision centrality is measured using the total transverse energy deposited in the FCal, denoted as FCal $\sum E_{\mathrm{T}}$. Figure 2.13 presents the distribution of FCal $\sum E_{\mathrm{T}}$ in Pb+Pb collisions, with multiple centrality classes highlighted.

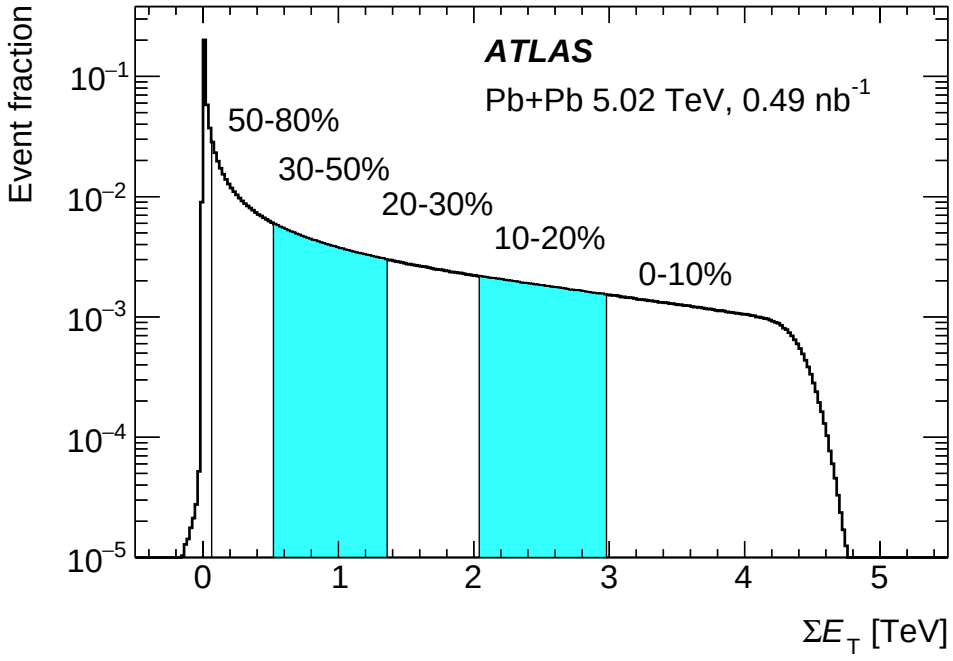

Figure 2.13: Distribution of FCal $\sum E_{\mathrm{T}}$ in minimum-bias Pb+Pb collisions at $\sqrt{s_{\mathrm{NN}}} = 5.02$ TeV. Alternating shaded and unshaded regions denote centrality ranges [119].

Chapter 3

Electron performance in heavy-ion collisions

3.1 Motivation

Electrons constitute a crucial component of final states in collisions at the LHC, as they are produced in various signal and background processes. In particular, they are an essential part of the $t\bar{t}$ decay modes, specifically the ℓ+jets and dilepton channels involving electrons in the final state. Owing to their efficient detection in the LHC experiments, electrons play a key role in precise measurements of $t\bar{t}$ production.

The standard approach to electron reconstruction and identification in the ATLAS experiment is described in detail in Sections 3.2.3 and 3.2.4, respectively. Electron reconstruction and identification are particularly challenging in the complex environment of heavy-ion collisions. Specialised electron performance studies are required to account for the detector and trigger inefficiencies in data, as well as potential mismodelling in the simulation. Additionally, a dedicated electron calibration needs to be considered for the low-pileup environment of heavy-ion collisions at the LHC.

This work was carried out by the Author of this thesis as part of the qualification task and has been integrated into the software of the ATLAS experiment. The results can be used in future measurements involving electrons in the final states of p+Pb and Pb+Pb collisions.

3.2 Electron performance in *p*+Pb collisions

Electron kinematic distributions are subject to the efficiency of the selection applied in experimental measurements. Four distinct efficiencies are considered, related to electron reconstruction, identification, isolation, and trigger. Eventual mismodelling in the simulation may lead to discrepancies in efficiencies between data and generated samples. They are addressed by applying dedicated corrections to simulated events, referred to as scale factors. Scale factors are extracted using a Tag-and-Probe method [120], a well-established technique for electron efficiency measurement in the ATLAS experiment. The obtained corrections play a crucial role in the recent measurement of $t\bar{t}$ production in the ℓ+jets and dilepton channels in p+Pb collisions [39].

3.2.1 Data and simulation samples

The data used in this study were collected by ATLAS during the p+Pb data-taking period in 2016, corresponding to a total integrated luminosity of 165 nb^{-1}. The proton and lead beams were configured with energies of 6.5 TeV and 2.56 TeV per nucleon, respectively, resulting in a nucleon–nucleon centre-of-mass energy of $\sqrt{s_{\mathrm{NN}}} = 8.16$ TeV. The data taking was split into p+Pb and Pb+p beam-direction configurations, with 57 and 108 nb^{-1} of data, respectively. The collisions were recorded under low-pileup conditions with $\langle\mu\rangle = 0.18$.

Event yields in data are compared to corresponding Monte Carlo (MC) samples of events, simulated and reconstructed under the same conditions as those present during the data taking. MC samples are processed using the full ATLAS detector simulation [121] based on the GEANT4 framework [122]. The signal $Z \to e^+e^-$ process is simulated at NLO precision in QCD using POWHEG BOX V2 [123] MC generator for the matrix element (ME) calculation. It is interfaced with PYTHIA8 [124] for the parton-shower (PS) and hadronisation modelling, using the CTEQ6L1 [125] PDF set and the AZNLO [126] set of tuned parameters. Four MC samples are generated, covering combinations of two isospin configurations, proton–proton and proton–neutron, and two beam-direction configurations, p+Pb and Pb+p. Nucleon–nucleon collisions are embedded into real p+Pb data for accurate underlying-event modelling. All samples are normalised using the theoretical $Z \to e^+e^-$ cross section at $\sqrt{s_{\mathrm{NN}}} = 8.16$ TeV, calculated at NLO precision in QCD.

3.2.2 Tag-and-Probe method

The Tag-and-Probe method makes use of the characteristic signatures of electron pairs originating from well-known resonance decays, such as $Z \to e^+e^-$ or $J/\psi \to e^+e^-$. One electron candidate from the pair, referred to as tag, has to meet strict selection requirements for tagging the event, while another electron, called probe, is used as an unbiased object for the efficiency measurement. In pp collisions, a wide kinematic region is covered by the method, employing $J/\psi \to e^+e^-$ and $Z \to e^+e^-$ processes for electrons with E_{T} in the ranges of 4.5–20 GeV and 15–200 GeV, respectively. The presented study focuses on high-E_{T} electrons in p+Pb collisions, and therefore only $Z \to e^+e^-$ decays are used to extract electron efficiencies.

The total efficiency to detect an electron ($\varepsilon_{\mathrm{total}}$) is divided into four components, corresponding to electron reconstruction ($\varepsilon_{\mathrm{reco}}$), identification ($\varepsilon_{\mathrm{id}}$), isolation ($\varepsilon_{\mathrm{iso}}$) and trigger ($\varepsilon_{\mathrm{trig}}$), namely

$$\begin{aligned}\varepsilon_{\mathrm{total}} &= \varepsilon_{\mathrm{reco}} \times \varepsilon_{\mathrm{id}} \times \varepsilon_{\mathrm{iso}} \times \varepsilon_{\mathrm{trig}} \\ &= \frac{N_{\mathrm{reco}}}{N_{\mathrm{clus}}} \times \frac{N_{\mathrm{id}}}{N_{\mathrm{reco}}} \times \frac{N_{\mathrm{iso}}}{N_{\mathrm{id}}} \times \frac{N_{\mathrm{trig}}}{N_{\mathrm{iso}}},\end{aligned} \tag{3.1}$$

where N_{clus}, N_{reco}, N_{id}, N_{iso}, and N_{trig} denote the numbers of EM clusters, reconstructed, identified, isolated, and triggered electrons, respectively.

Events with at least two electron candidates are selected for the measurement. The tag electron must have $E_{\mathrm{T}} > 25$ GeV and $|\eta| < 2.47$, satisfy Tight identification criteria [127], and lie outside of the calorimeter transition region of $1.37 < |\eta| < 1.52$. The probe electron needs to have $E_{\mathrm{T}} > 15$ GeV and $|\eta| < 2.47$, and meet certain criteria for a given efficiency measurement. Events with the invariant mass of the electron pair, m_{ee}, within the Z-boson mass window of $m_{ee} \in (75, 105)$ GeV are used in the efficiency calculation. Figure 3.1 shows the

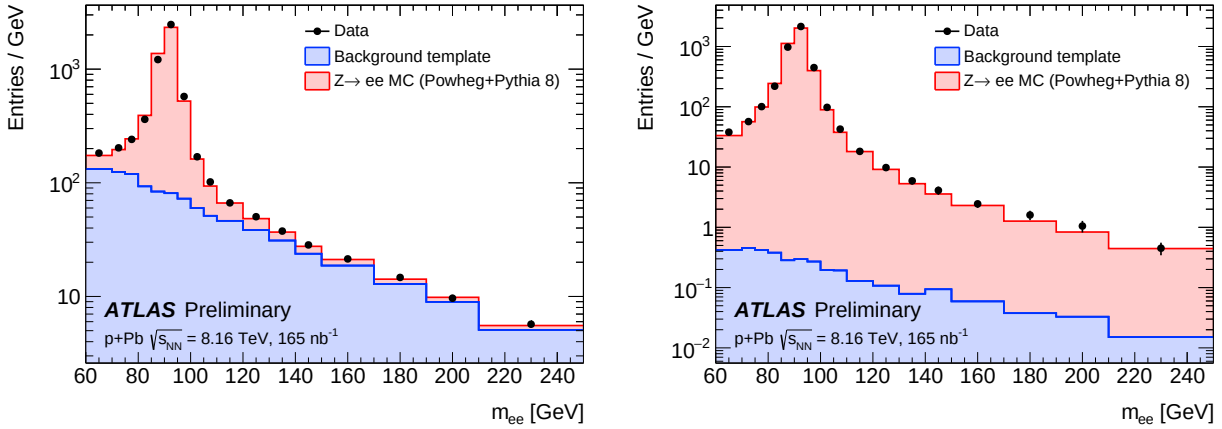

Figure 3.1: Invariant-mass distributions of (a) reconstructed and (b) identified electron tag-probe pairs in p+Pb collisions [128].

distributions of invariant mass of electron pairs satisfying the reconstruction and identification criteria, with the Z-boson mass peak clearly visible at around 91 GeV.

Selected data include mostly prompt electrons, referred to as signal, which are produced directly in collisions or originate from particle decays. However, a contamination from background objects, such as electrons from photon conversions, electrons from semileptonic heavy-flavour decays, or hadrons misidentified as electrons, is also present. The background contribution is estimated using data-driven techniques and subtracted from distributions in data using templates. The background template is obtained using probes failing identification and isolation criteria. After subtracting the signal, which is provided by MC simulation, the template is normalised to an invariant-mass sideband region of $m_{ee} \in (120, 250)$ GeV.

To estimate systematic uncertainties on the electron efficiency, several measurement variations are considered. The background subtraction is changed using a different background template. For electrons with $E_{\mathrm{T}} < 30$ GeV, the template is normalised to a different invariant-mass range of $m_{ee} \in (60, 70)$ GeV. For remaining electrons with $E_{\mathrm{T}} > 30$ GeV, the nominal normalisation region is used, and instead selection criteria are varied. The Z-boson mass window is modified using three different m_{ee} regions: 80–100 GeV, 75–105 GeV, and 70–110 GeV. The tag electron requirements are varied by using three sets of selection criteria: Tight identification with isolation, only Tight identification, and Medium identification with isolation. The central value of the efficiency is obtained by averaging results across all variations. The systematic uncertainty is determined as the root mean square of the individual results, aiming to represent a 68% confidence interval. The statistical uncertainty is calculated as the arithmetic mean of the statistical uncertainties of all the variations.

The scale factors are defined as the ratio between the efficiencies obtained in data and MC simulation. Since the electron performance depends on the kinematic properties of the electron, the measurement is performed in two-dimensional bins in the E_{T}-η space. The bin size in η follows the detector geometry and is optimised for available data statistics. In physics analyses, the obtained multiplicative correction is applied to simulated events, which compensates for efficiency mismodelling in MC simulation.

3.2.3 Electron reconstruction

Electron reconstruction is divided into three main steps: cluster reconstruction, track reconstruction and cluster-track matching. Groups of energy deposits in the EM calorimeter, referred to as EM clusters, are formed using the sliding-window algorithm [129], which searches for seed clusters with the total E_{T} above 2.5 GeV within a window of 3×5 calorimeter cells in the η–ϕ space.[1] Duplicate seeds are removed, and clusters of the size of 3×7 (5×5) are formed in the barrel (endcap) region. Cluster reconstruction in the ATLAS detector is estimated to be highly effective, exceeding 99% efficiency for electrons with $E_{\mathrm{T}} > 15$ GeV [129]. Electron-track candidates are built from track seeds consisting of three hits in the silicon detectors with $p_{\mathrm{T}} > 1$ GeV. Tracks with at least one hit in the pixel detector and at least seven total hits in the silicon detectors are considered as good-quality tracks, while remaining ones are labelled as bad-quality tracks. Finally, track candidates are matched to EM clusters based on the position in the η–ϕ space. If multiple tracks are matched to a single cluster, the best-matched one is chosen as the primary track and used in further calculations.

Events with at least one tag electron and one EM cluster are selected for the reconstruction efficiency estimation. The number of reconstructed electrons, N_{reco} (Equation 3.1), includes only EM clusters with a good-quality track, while the number of EM clusters, N_{clus}, consists of EM clusters with a good-quality, bad-quality or no associated track. Background subtraction is performed separately for each category of EM clusters. The background estimation for EM clusters with a good-quality or bad-quality track follows the procedure described in Section 3.2.2, with an additional requirement on track quality being satisfied or not satisfied, respectively. For EM clusters with no associated track, which are interpreted as photons, the background contribution is extracted as a third-order polynomial fitted to the sidebands of the m_{ee} distribution of electron–photon pairs. Figure 3.2 shows invariant-mass distributions of tag-and-probe pairs in both the denominator and numerator of the reconstruction efficiency.

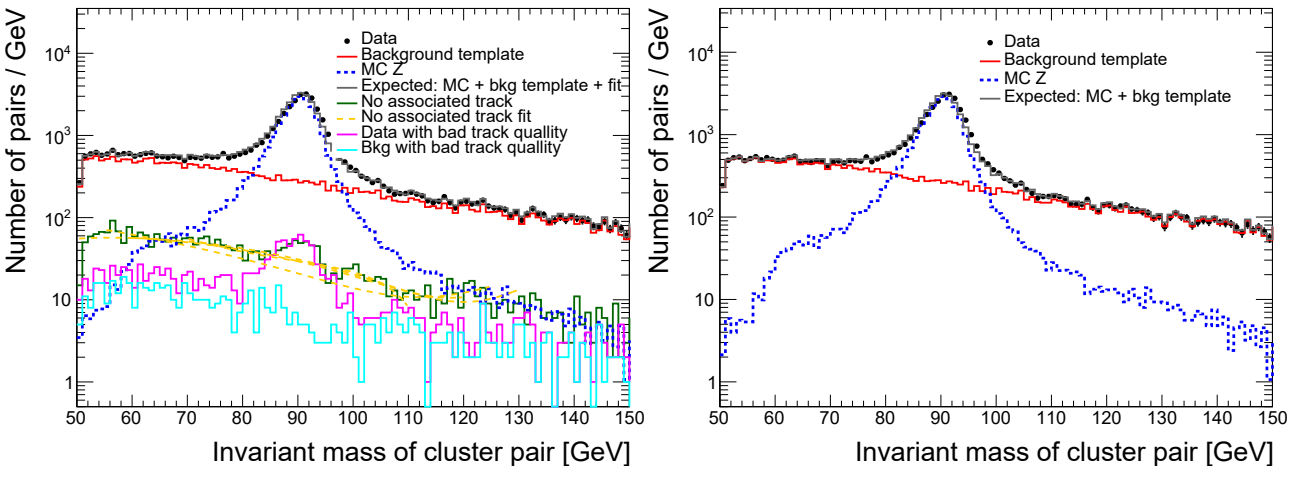

Figure 3.2: Invariant-mass distributions of tag-and-probe pairs in the (a) denominator and (b) numerator of the reconstruction efficiency.

[1] This approach was used during Run 2.

Systematic uncertainties on reconstruction efficiency are evaluated using measurement variations described in Section 3.2.2. Additionally, the m_{ee} sidebands used in the polynomial fit for the photon background are varied between four ranges: $m_{ee} \in (70, 80) \cup (100, 110)$, $m_{ee} \in (60, 80) \cup (100, 120)$, $m_{ee} \in (50, 80) \cup (100, 130)$, and $m_{ee} \in (55, 70) \cup (110, 125)$.

Electron reconstruction efficiency in data is presented in Figure 3.3 as a function of electron E_{T} and η. The efficiency rises with electron E_{T} from 93% at $E_{\mathrm{T}} = 15$ GeV and reaches a plateau of 97.5% at around $E_{\mathrm{T}} = 50$ GeV. The efficiency is higher for electrons in the central η region and drops down to 93% at electron $|\eta| > 1.37$. No significant differences are observed between data and MC simulation, with scale factors mostly consistent with unity. The total uncertainties are dominated by the statistical component of the limited data sample. Figure 3.4 displays scale factors for electron reconstruction as a function of electron E_{T} and η. The scale factor correction is close to unity for the majority of E_{T}-η bins. The largest deviations from unity of 0.96 and 1.04 are found for electron η in the calorimeter crack region. Limited statistics in this η range also lead to increased total uncertainties.

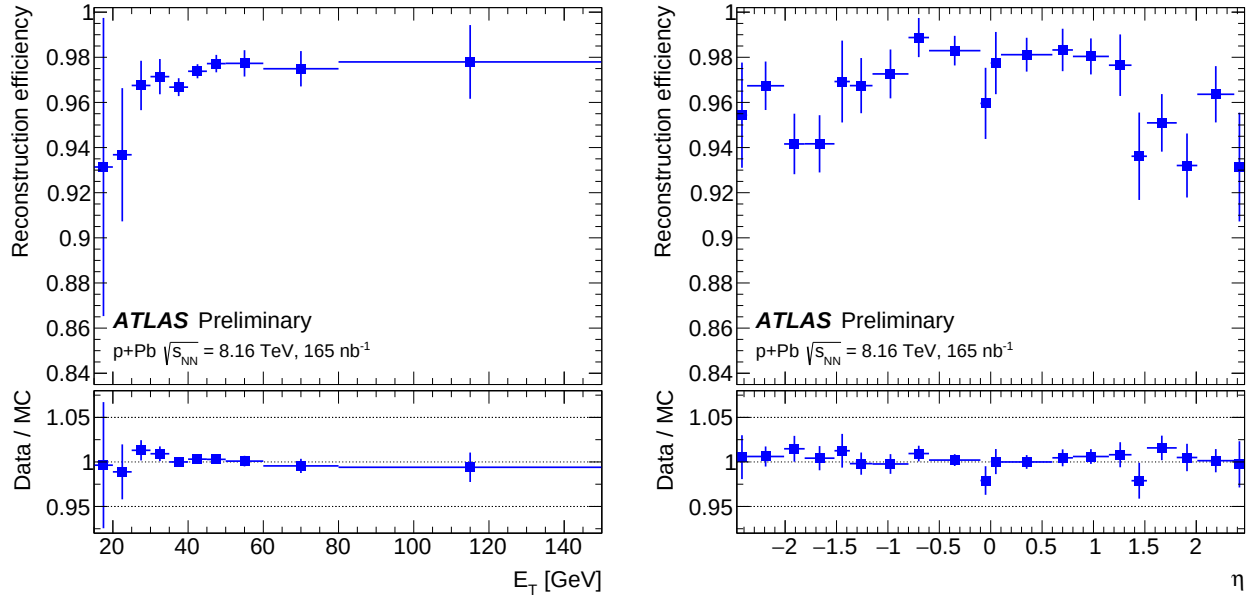

(a) (b)

Figure 3.3: The electron reconstruction efficiency in $Z \to e^+e^-$ events as a function of electron (a) E_{T} and (b) η evaluated in 2016 p+Pb data. The bottom panels show the data-to-simulation ratio. Error bars represent the total uncertainties composed of statistical and systematic components added in quadrature [128].

3.2.4 Electron identification

The purpose of identification algorithms is to enhance the purity of the selected electrons. Various electron discriminating variables, summarised in Table 3.1, are used as input to these algorithms. They are divided into three main categories: shower shapes, which are quantities from the calorimeter; track conditions, which are properties from the inner detector; and track-cluster matching, which combines tracking and calorimeter information. One of the main identification methods in Run 2 data, the cut-based algorithm, applies a set of fixed

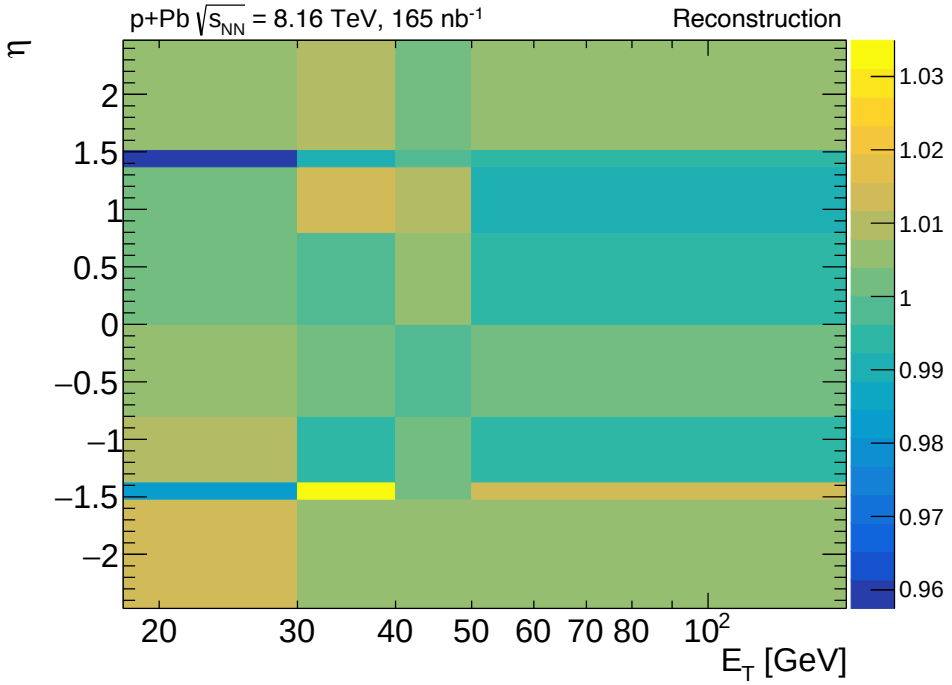

Figure 3.4: Scale factors for electron reconstruction efficiency as a function of electron E_{T} and η. Total uncertainties are composed of statistical and systematic components added in quadrature.

requirements on each electron quantity. A more advanced method, referred to as the likelihood algorithm, combines probability density functions of the discriminating variables for signal and background electrons. This strategy is used as the baseline identification algorithm in Run 2. The algorithm is based on the likelihood function of the signal (background) L_{S} (L_{B}), defined as the product of n individual probability density functions, namely

$$L_{\mathrm{S(B)}}(\vec{x}) = \prod_{i=1}^{n} P_{\mathrm{S(B)},i}(x_i). \tag{3.2}$$

The vector $\vec{x}$ represents a list of electron discriminating variables, while $P_{\mathrm{S(B)},i}(x_i)$ denotes the probability density function for quantity i at value x_i for signal (background) electrons. A discriminant d_{L} is constructed from L_{S} and L_{B}, given by the formula

$$d_{\mathrm{L}} = \frac{L_{\mathrm{S}}}{L_{\mathrm{S}} + L_{\mathrm{B}}}. \tag{3.3}$$

A distribution of d_{L} has a sharp peak at either zero or unity for signal and background electrons, respectively. To avoid the necessity of extremely fine binning, d_{L} is transformed using an inverse sigmoid function, yielding a log-transformed discriminant d'_{L} of the form

$$d'_{\mathrm{L}} = -\tau \ln(d_{\mathrm{L}}^{-1} - 1), \tag{3.4}$$

where the parameter τ is fixed to 15 [130]. Figure 3.5 presents d'_{L} distributions for signal and background electrons. Sets of requirements on the value of the d'_{L} discriminant, depending on electron E_{T} and η, are used to define identification working points. Electron candidates with the value of d'_{L} above a given threshold are considered signal, while the remaining ones are classified as background. Four levels of identification criteria are typically optimised, labelled as VeryLoose, Loose, Medium, and Tight. An additional operating point, referred to as LooseAndBLayer, uses Loose identification criteria with an extra requirement on the number of

Table 3.1: Definition and description of electron discriminating variables used in the electron likelihood identification [127].

Type	Name	Definition
Shower shapes	f_1	Ratio of the energy in the first EM calorimeter layer over the total energy in the EM calorimeter
	f_3	Ratio of the energy in the third EM calorimeter layer over the total energy in the EM calorimeter
	R_η	Ratio of the energy of 3×7 cells over the energy of 7×7 cells centred at the cluster position
	R_ϕ	Ratio of the energy of 3×3 cells over the energy of 3×7 cells centred at the cluster position
	R_{had}	Ratio of total E_{T} in the hadronic calorimeter over E_{T} of the EM cluster
	$w_{\eta 2}$	Lateral shower width
	E_{ratio}	Ratio of the energy difference between the maximum and secondary maximum deposits in the first EM calorimeter layer over the sum of these energies
Track conditions	$\Delta p/p$	Ratio of the momentum loss by the track between the perigee and the last hit over the momentum at perigee
	d_0	Transverse impact parameter relative to the beam line
	$\lvert d_0/\sigma(d0)\rvert$	Ratio of transverse impact parameter over its uncertainty
	eProbabilityHT	Likelihood probability based on transition radiation in the TRT
Track-cluster matching	$\Delta\eta_1$	$\Delta\eta$ between the position of the EM cluster in the first EM calorimeter layer and the extrapolated track
	$\Delta\phi_{\mathrm{res}}$	$\Delta\phi$ between the position of the EM cluster in the second EM calorimeter layer and the momentum-rescaled track

hits in the B-Layer of the inner detector. The subsequent selections are subsets of one another, with VeryLoose and Tight selections accepting the most and the least electron candidates, respectively. Looser working points are characterised by higher efficiency, allowing more background, while tighter selections provide improved background rejection and higher signal purity at the cost of lower efficiency.

Figure 3.6 displays electron identification efficiency as a function of E_{T} and η for four working points. The efficiency increases with E_{T} from 82% (68%) at $E_{\mathrm{T}} = 15$ GeV and reaches a plateau at around $E_{\mathrm{T}} = 60$ GeV with 92% (87%) for the Medium (Tight) criteria. For electrons with $E_{\mathrm{T}} \approx 30$ GeV, the efficiency in MC simulation is 1–4% higher than in the data, resulting in data-to-MC ratios below unity. The scale factors are consistent

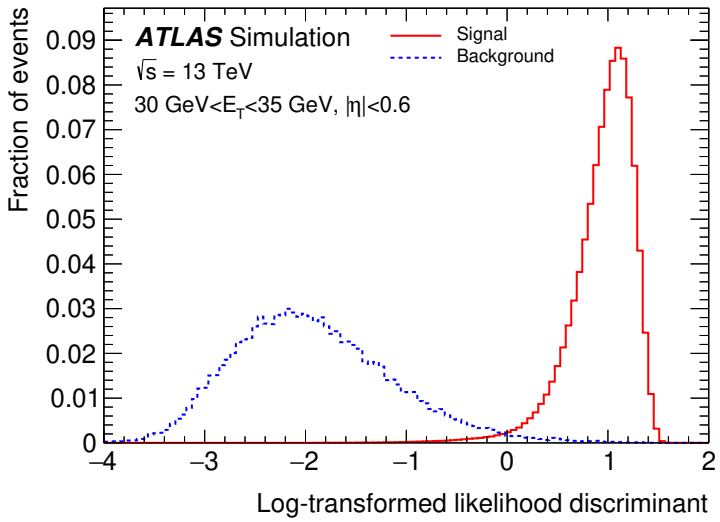

Figure 3.5: Distributions of log-transformed discriminants d'_{L} for reconstructed electron candidates. The red and blue histograms represent signal $Z \to e^+e^-$ and background simulation samples, respectively [130].

with unity for central electron pseudorapidities of $|\eta| < 0.5$ and significantly below unity for $|\eta| > 1$. The total uncertainties are dominated by the statistical component for electrons with $E_{\mathrm{T}} > 30$ GeV, while statistical and systematic uncertainties are comparable for $E_{\mathrm{T}} < 30$ GeV. Scale factors for the Medium operating point in bins of electron E_{T} and η are shown in Figure 3.7. The scale factors are close to unity for most electron E_{T}-η

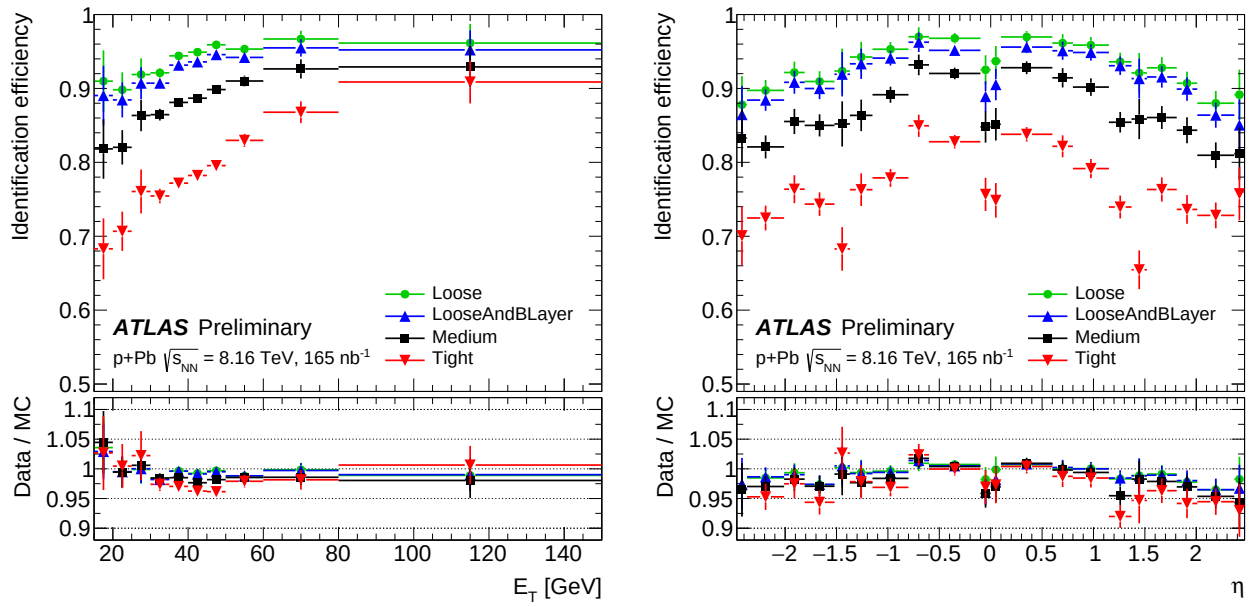

(a) (b)

Figure 3.6: The electron identification efficiency in $Z \to e^+e^-$ events as a function of electron (a) E_{T} and (b) η evaluated in 2016 p+Pb data for the Loose, LooseAndBLayer, Medium, and Tight working points. The bottom panels show the data-to-simulation ratios. Error bars represent the total uncertainties composed of statistical and systematic components added in quadrature [128].

values. Scale-factor correction for the Medium selection ranges from 0.83 to 1.11. Results for the remaining identification working points, Loose, LooseAndBLayer, and Tight, are provided in Appendix A.1.1.

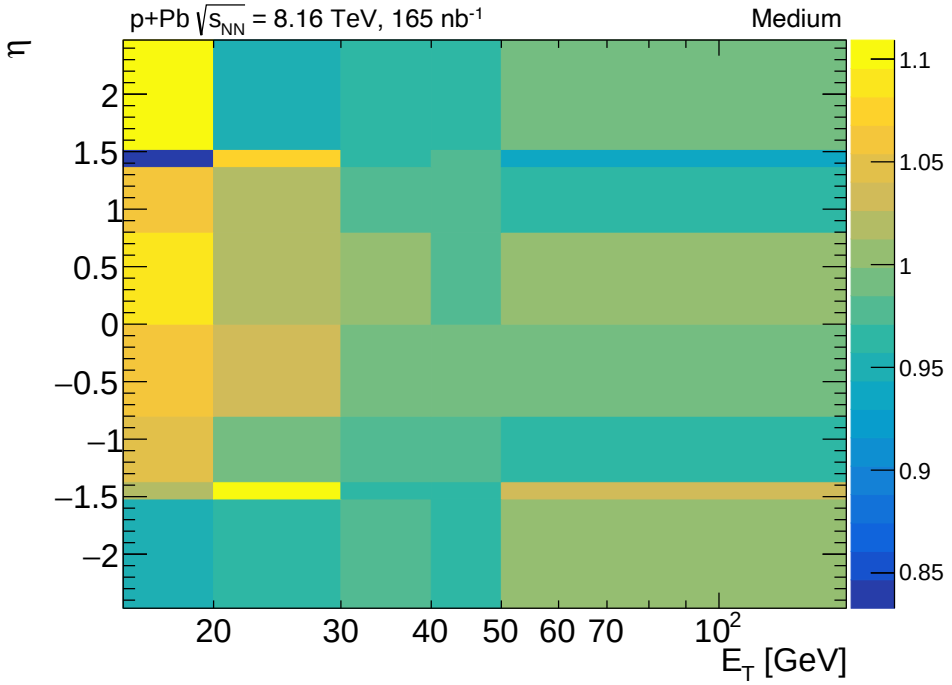

Figure 3.7: Scale factors for electron identification efficiency as a function of electron E_{T} and η for the Medium working point. Total uncertainties are composed of statistical and systematic components added in quadrature.

3.2.5 Electron isolation

Applying isolation requirements on electron candidates allows further distinguishing signal from background. A signature of prompt electrons is typically represented by minimal activity around the candidate object in both the calorimeter and the inner detector. Background electrons, originating from heavy-quark decays or photon conversion, predominantly result in non-isolated objects. To quantify the amount of activity surrounding the candidate object, isolation variables are constructed. Two main categories of variables are considered, utilising information from the EM calorimeter and the inner detector, referred to as calorimeter-based and track-based isolation, respectively.

The calorimeter-based isolation variable, $E_{\mathrm{T,cone}}^{\mathrm{isol}}$, is defined as the total E_{T} in the EM calorimeter around the candidate object. The raw isolation energy, $E_{\mathrm{T,raw}}^{\mathrm{isol}}$, is computed as the sum of E_{T} of EM clusters whose barycentres lie within a cone of a given radius, typically $\Delta R = 0.2$. The core energy of the electron, $E_{\mathrm{T,cone}}$, estimated as a rectangular cluster of size $\eta \times \phi = 0.125 \times 0.175$ centred at the candidate object, is subtracted as illustrated in Figure 3.8. The candidate electron may deposit energy outside of the fixed rectangular area, and therefore a dedicated leakage correction, evaluated using single-electron MC simulation, is applied. The leaking energy, $E_{\mathrm{T,leakage}}$, is fitted using a Crystal Ball function and parameterised as a function of E_{T}. Additional energy due to the pileup and underlying-event contribution, $E_{\mathrm{T,pileup}}$, is removed using the pileup subtraction [131]. The fully corrected calorimeter-based isolation variable is obtained after subtracting all the

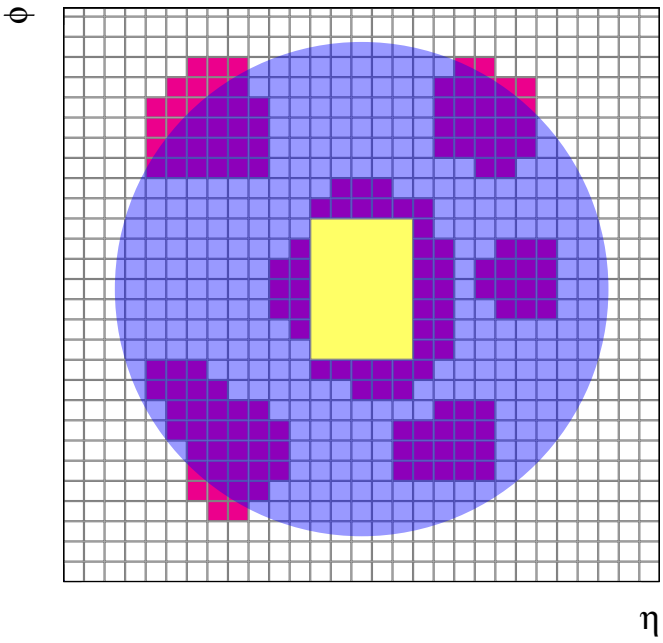

Figure 3.8: Scheme of the calorimeter isolation calculation. The grid represents the second-layer calorimeter cells in the η-ϕ space. EM clusters and the core energy deposit are marked in red and yellow, respectively. The purple circle denotes the isolation cone around the candidate electron [130].

components, namely

$$E_{\mathrm{T,cone}}^{\mathrm{isol}} = E_{\mathrm{T,raw}}^{\mathrm{isol}} - E_{\mathrm{T,core}} - E_{\mathrm{T,leakage}} - E_{\mathrm{T,pileup}}. \tag{3.5}$$

The track-based isolation, $p_{\mathrm{T,var}}^{\mathrm{isol}}$, quantifies the total energy in the inner detector in the vicinity of the electron candidate. It is defined as the sum of p_{T} of the tracks within a cone of specified radius, constructed around the electron and originating from the primary vertex. Only tracks with $p_{\mathrm{T}} > 1$ GeV, reconstructed within the fiducial region of the inner detector, $|\eta| < 2.5$, and satisfying good-quality requirements, are considered. An additional requirement of $|z_0 \sin\phi| < 3$ mm, imposed on tracks, minimises the impact of pileup. The track of the candidate object is excluded, along with additional electron associated-tracks, originating primarily from bremsstrahlung. All extrapolated tracks within a $\Delta\eta \times \Delta\phi = 0.05 \times 0.1$ window around the electron cluster are treated as part of the candidate and removed. The high inner-detector granularity allows for a varying cone size, ΔR, which progressively decreases as a function of electron p_{T}, given by the formula

$$\Delta R = \min\left(\frac{10\ \mathrm{GeV}}{p_{\mathrm{T}}}, R_{\mathrm{max}}\right), \tag{3.6}$$

where R_{max} denotes the maximum cone size and is typically set to 0.2. The value of 10 GeV is optimised using $t\bar{t}$ MC simulation to maximise background rejection.

Electron isolation working points are defined by imposing requirements on calorimeter-based and track-based isolation variables. Table 3.2 lists the isolation operating points optimised specifically for electrons. They are divided into two main categories based on the type of selection criteria: fixed-requirement and efficiency-targeted. Selections in the former class, including FCLoose, FCTight, and FCHighPtCaloOnly, apply fixed thresholds

Table 3.2: Definition of the isolation selections used in the analysis. Tables show fixed-requirement (top) and efficiency-targeted (bottom) working points.

Working point	**Cut value**	
	calorimeter isolation	**track isolation**
FCLoose	$E_{\mathrm{T,cone}}^{\mathrm{isol}}/p_{\mathrm{T}} < 0.20$	$p_{\mathrm{T,var}}^{\mathrm{isol}}/p_{\mathrm{T}} < 0.15$
FCTight	$E_{\mathrm{T,cone}}^{\mathrm{isol}}/p_{\mathrm{T}} < 0.06$	$p_{\mathrm{T,var}}^{\mathrm{isol}}/p_{\mathrm{T}} < 0.06$
FCHighPtCaloOnly	$E_{\mathrm{T,cone}}^{\mathrm{isol}} < \max(0.015 \times p_{\mathrm{T}}, 3.5\ \mathrm{GeV})$	-

Working point	**Isolation efficiency**		
	calorimeter isolation	**track isolation**	**total efficiency**
Gradient	$0.1143\% \times p_{\mathrm{T}} + 92.14\%$	$0.1143\% \times p_{\mathrm{T}} + 92.14\%$	90(99)% at 25(60) GeV

on one or both isolation types relative to the track p_{T}. Working points in the latter class, such as Gradient, impose varying requirements to achieve a target isolation efficiency. In analyses with low-E_{T} electrons, fixed-requirement operating points are typically used to ensure high background rejection. In studies with high-E_{T} electrons, efficiency-targeted working points are preferred, which provide high selection efficiency.

Electron isolation efficiency is presented in Figure 3.9 as a function of electron E_{T} and η for four working points. The efficiency is estimated as the fraction of isolated electrons with respect to electrons satisfying the

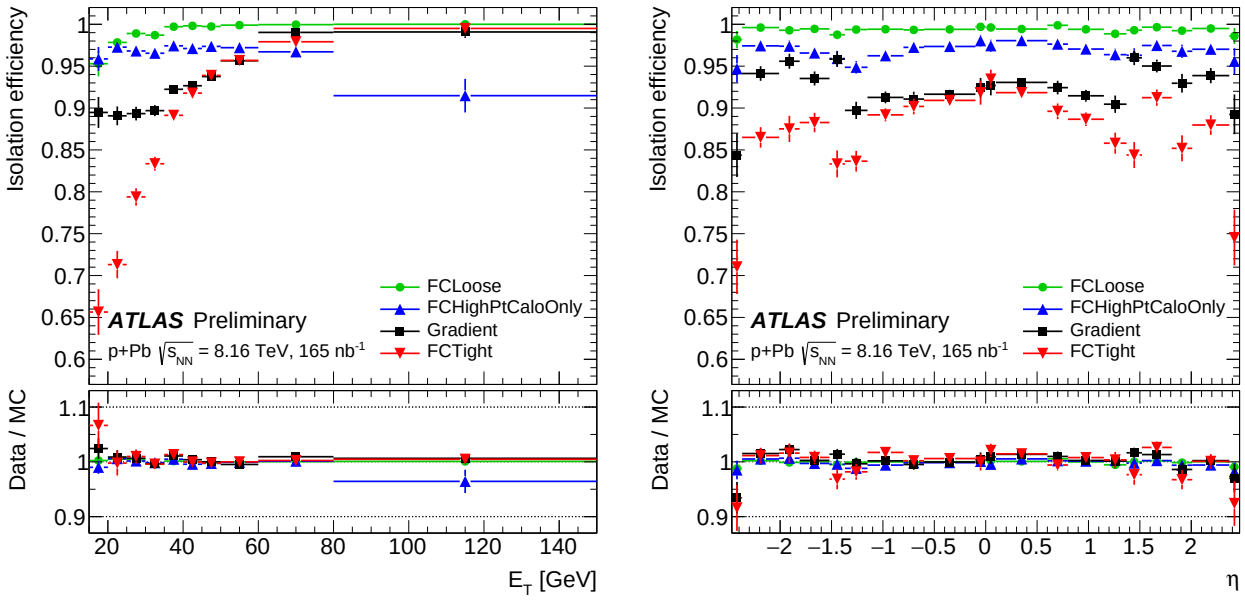

(a) (b)

Figure 3.9: The electron isolation efficiency in $Z \to e^+e^-$ events as a function of electron (a) E_{T} and (b) η evaluated in 2016 p+Pb data for the FCLoose, HighPtCaloOnly, Gradient, and FCTight working points. The bottom panels show the data-to-simulation ratios. Error bars represent the total uncertainties composed of statistical and systematic components added in quadrature [128].

Medium identification criteria. The efficiencies range between 65–96% at $E_{\mathrm{T}} = 15$ GeV for various working points and reach a plateau of 99% at $E_{\mathrm{T}} = 80$ GeV, except for the FCHighPtCaloOnly selection. Scale factors do not show significant deviations from unity. The total uncertainties are dominated by the statistical component of the limited data sample. Figure 3.10 shows scale factors for electron isolation efficiency in bins of electron E_{T} and η for the Gradient operating point. Central values are close to unity with maximum variations from 0.98 to 1.10. Results for the remaining isolation working points, FCLoose, FCHighPtCaloOnly, and FCTight, are documented in Appendix A.1.2.

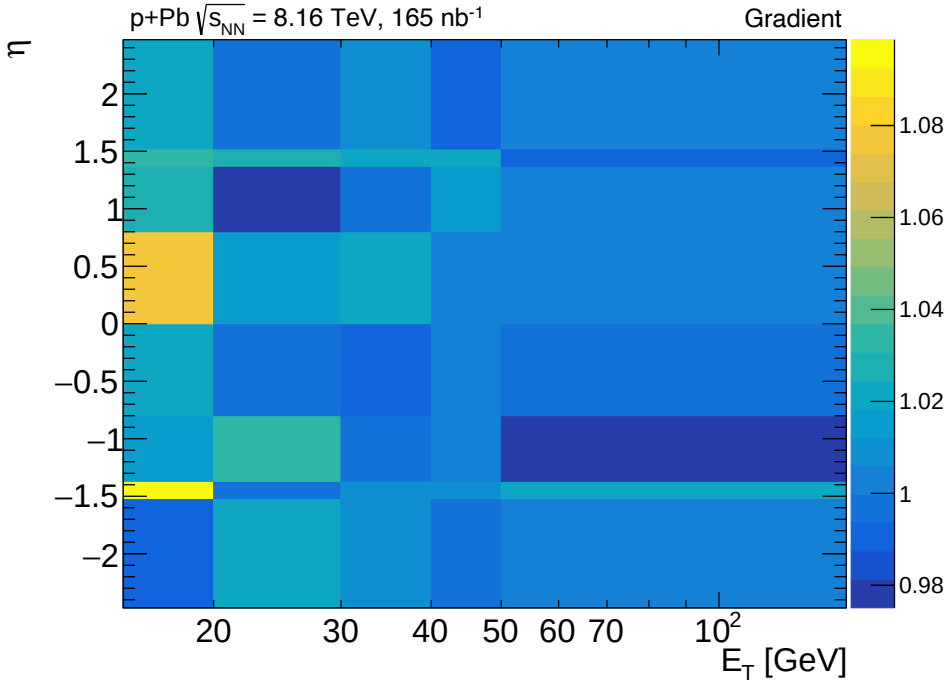

Figure 3.10: Scale factors for electron isolation efficiency as a function of electron E_{T} and η for the Gradient working point. Total uncertainties are composed of statistical and systematic components added in quadrature.

3.2.6 Electron trigger

A two-level trigger system [132] is employed to select events of interest in real time during the data taking. The first-level (L1) trigger, implemented in custom hardware, reduces the event rate from 40 MHz to below 100 kHz. It uses coarse-granularity signals from the calorimeter and the MS to define regions-of-interest with potential physics objects. Events accepted by L1 are further processed by the high-level trigger (HLT), based on software algorithms, which reduces the rate down to about 1 kHz. It uses tracking information from the inner detector, fine-granularity calorimeter signals, and precision measurements from the MS to make the final decision on recording events to disc.

The Tag-and-Probe method is widely used to evaluate HLT trigger performance, including electron triggers. In this study, the efficiency of the e15_lhloose trigger [133], used in 2016 p+Pb data taking, is measured. It is a single-electron trigger with a minimum p_{T} threshold of 15 GeV and requiring Loose likelihood identification criteria. The efficiency is estimated as the fraction of triggered electrons satisfying the Medium identification and Gradient isolation criteria with respect to all electrons passing the same identification and isolation criteria.

Figure 3.11 displays electron trigger efficiency as a function of electron E_{T} and η. The efficiency increases with electron E_{T} from 82% at $E_{\mathrm{T}} = 15$ GeV and reaches a plateau of 98% at $E_{\mathrm{T}} = 40$ GeV. Scale factors deviate from unity up to 5% at low electron E_{T} and forward η values. The total uncertainties are dominated by the statistical component of the limited data sample. Scale factors for electron trigger efficiency are shown in Figure 3.12 as a function of electron E_{T} and η. Scale-factor values are close to unity with the largest deviations of 0.63 and 1.21 for low-E_{T} electrons in the calorimeter crack region.

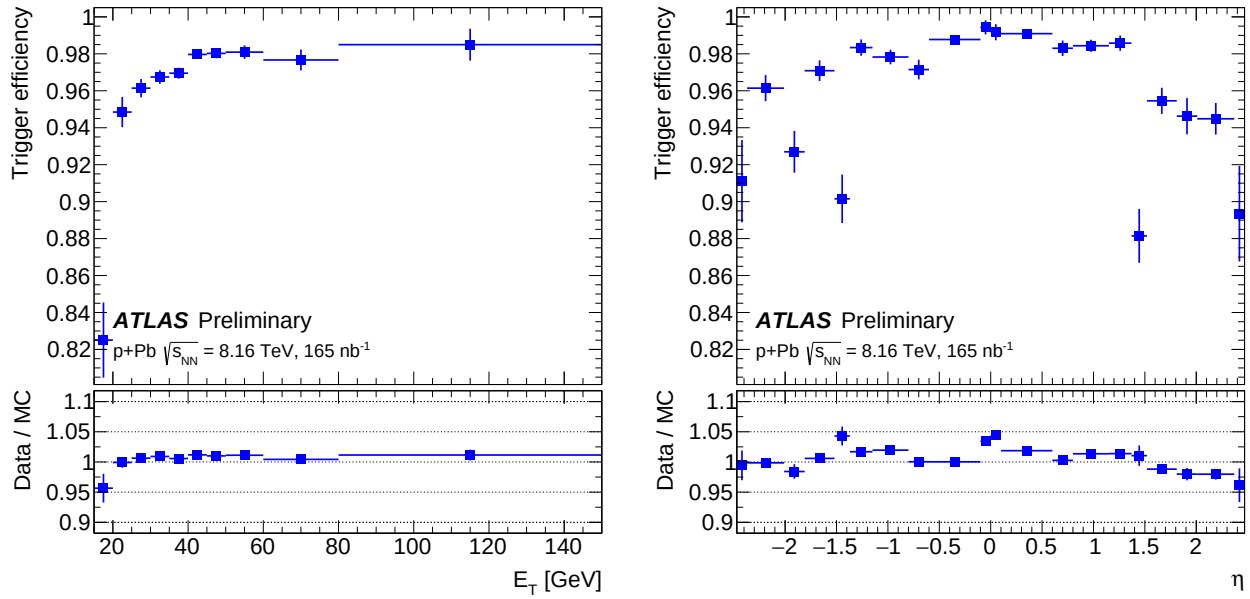

(a) (b)

Figure 3.11: The electron trigger efficiency in $Z \to e^+e^-$ events as a function of electron (a) E_{T} and (b) η evaluated in 2016 p+Pb data for the e15_lhloose trigger. The bottom panels show the data-to-simulation ratio. Error bars represent the total uncertainties composed of statistical and systematic components added in quadrature [128].

3.3 Electron performance in Pb+Pb collisions

Electron identification is especially challenging in the high-detector-occupancy environment of Pb+Pb collisions. The likelihood method is also used as the default algorithm for electron identification in heavy-ion collisions. The standard electron identification working points, derived for pp collisions, may be affected by the higher detector occupancy. The number of electrons produced in heavy-ion collisions increases significantly with the overlap of the colliding nuclei. Therefore, to achieve optimal performance in Pb+Pb conditions, centrality dependence has to be considered. Four electron identification working points, HITight, HIMedium, HILoose, and HIVeryLoose, are optimised for Pb+Pb collisions at the centre-of-mass energy of $\sqrt{s_{\mathrm{NN}}} = 5.02$ TeV per nucleon pair. The obtained operating points are used as the baseline for electron identification in Pb+Pb collisions in Run 3.

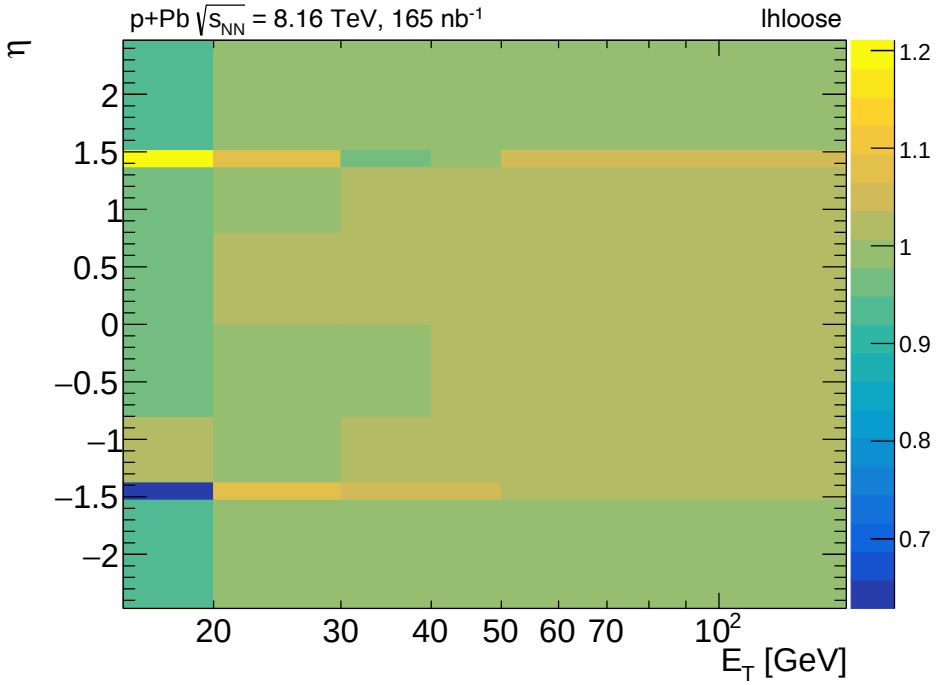

Figure 3.12: Scale factors for electron trigger efficiency as a function of electron E_{T} and η for the e15_lhloose trigger. Total uncertainties are composed of statistical and systematic components added in quadrature.

3.3.1 Simulation samples

The optimisation of electron likelihood identification is performed using MC simulation with signal and background electrons. The signal sample contains prompt electrons originating from $Z \to e^+e^-$ decays, simulated at NLO precision in QCD using POWHEG BOX V2 interfaced with PYTHIA8 with the CTEQ6L1 PDF set and the AZNLO set of tuned parameters. The background sample (JF17) is enriched in non-prompt electrons, coming from semileptonic decays of heavy-flavour hadrons and photon conversions, and light hadrons misidentified as electrons. It is generated at NLO precision in QCD using POWHEG BOX V2 interfaced with PYTHIA8 with the NNPDF2.3LO [134] PDF set and the A14 [135] set of tuned parameters. A p_{T} threshold of 17 GeV is applied to jets at the generator level in MC simulation events. In both samples, simulated pp collisions at $\sqrt{s_{\mathrm{NN}}} = 5.02$ TeV are embedded into HIJING [136] minimum-bias Pb+Pb events for underlying-event modelling. The total number of MC events per sample is 5 million. Due to technical limitations, MC samples are generated with a fixed vertex position. It affects mostly the z coordinate of the vertex (z_0), which follows an approximately Gaussian distribution with a width of around 50 mm in data, while distributions of x and y coordinates of the vertex are characterised by much smaller widths of about 20 μm. To evaluate the impact of the fixed z_0 vertex position, two test samples are simulated with 10 thousand events, with the nominal value of $z_0 = 0$ mm and a value in the tail of the real Gaussian distribution of $z_0 = 64$ mm.

Events with at least one tag–probe electron pair are selected for the study, following the Tag-and-Probe method described in Section 3.2.2. The tag electron needs to have $E_{\mathrm{T}} > 25$ GeV and $|\eta| < 2.47$, and meet Tight identification criteria dedicated for pp collisions at $\sqrt{s} = 13$ TeV. The probe electron must have $E_{\mathrm{T}} > 15$ GeV and $|\eta| < 2.47$, and be reconstructed as a good-quality electron. No requirement is imposed on the invariant

mass of the electron pair. Signal electrons must originate from prompt electrons at the generator level and be isolated from jets with $p_{\mathrm{T}} > 20$ GeV within $\Delta R < 0.4$. The electron discriminating variables, defined in Table 3.1, are used to optimise likelihood identification in Pb+Pb collisions. However, the eProbabilityHT variable is excluded from electron identification due to a different gas mixture in the TRT, consisting mostly of argon, during the Pb+Pb data-taking period. In the standard likelihood method, it is assumed that the TRT is filled primarily with xenon, which shows a higher level of gas ionisation by electrons, providing input for electron identification.

3.3.2 Vertex position

The impact of the fixed z_0 vertex position is assessed by comparing distributions of electron discriminating variables for two fixed z_0 vertex positions, $z_0 = 0$ mm and $z_0 = 64$ mm. Figure 3.13 shows distributions of two example shower shapes, R_η and R_ϕ, for the two fixed z_0 vertex positions, with statistical errors denoted by error bars. All the remaining discriminating variables are provided in Appendix A.2.1. No significant deviations are observed between the z_0 vertex positions, with differences covered by statistical uncertainties in the majority of distribution bins.

In the next step, a log-transformed discriminant d'_{L} is calculated for two fixed z_0 vertex positions, as shown in Figure 3.14, using standard probability density functions derived for pp collisions at $\sqrt{s} = 13$ TeV. The distributions are consistent within statistical uncertainties, with differences between the two fixed z_0 vertex positions below 10% in the peak close to unity.

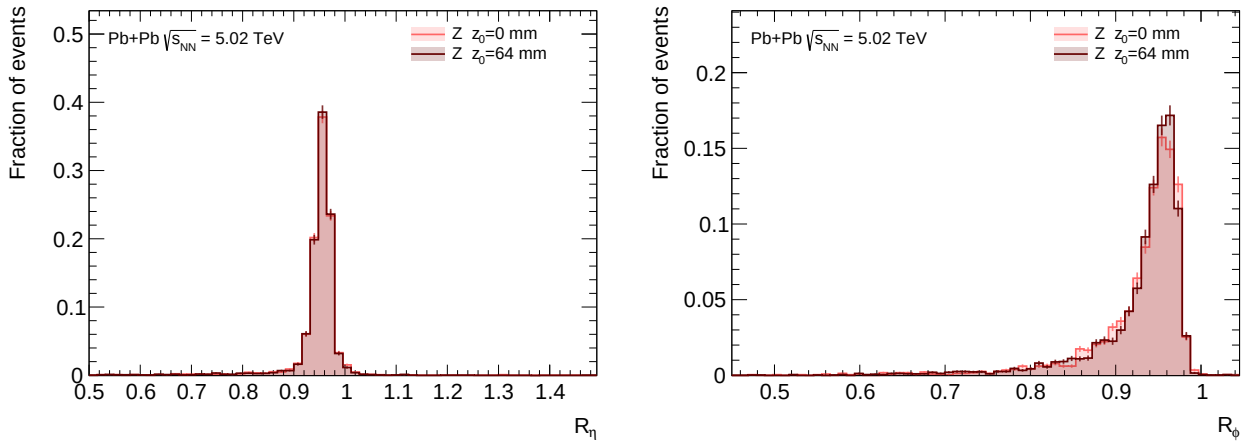

(a) (b)

Figure 3.13: Distributions of (a) R_η and (b) R_ϕ electron discriminating variables for two fixed z_0 vertex positions. Error bars denote statistical uncertainties.

3.3.3 Collision centrality

Electron discriminating variables depend on collision centrality, which impacts the likelihood identification. Both signal and background MC simulation samples are characterised by a minimum-bias centrality distri-

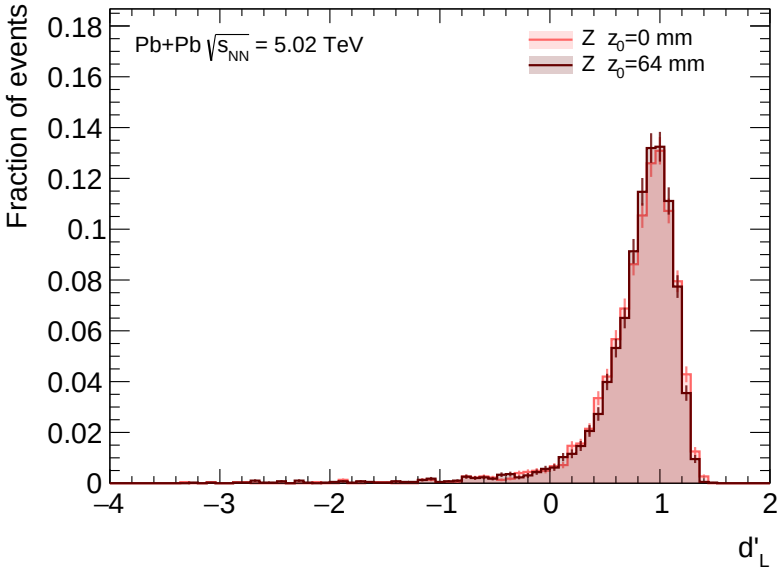

Figure 3.14: Distributions of log-transformed discriminants d'_{L} for two fixed z_0 vertex positions. Error bars denote statistical uncertainties.

bution, as presented in Figure 3.15. Due to the same overlay sample used in the simulation of signal and background, centrality distributions are subject to the same fluctuations.

Distributions of individual discriminating variables vary with centrality for both signal and background electrons. Figure 3.16 shows differences in distributions of an example variable, R_η, in central and peripheral collisions for signal and background electrons, and the centrality dependence of R_η for signal electrons. In this comparison, events with FCal $\Sigma E_{\mathrm{T}} > 1$ TeV are considered central collisions, while the remaining events are treated as peripheral collisions. The R_η variable forms narrower peaks in peripheral collisions, while the

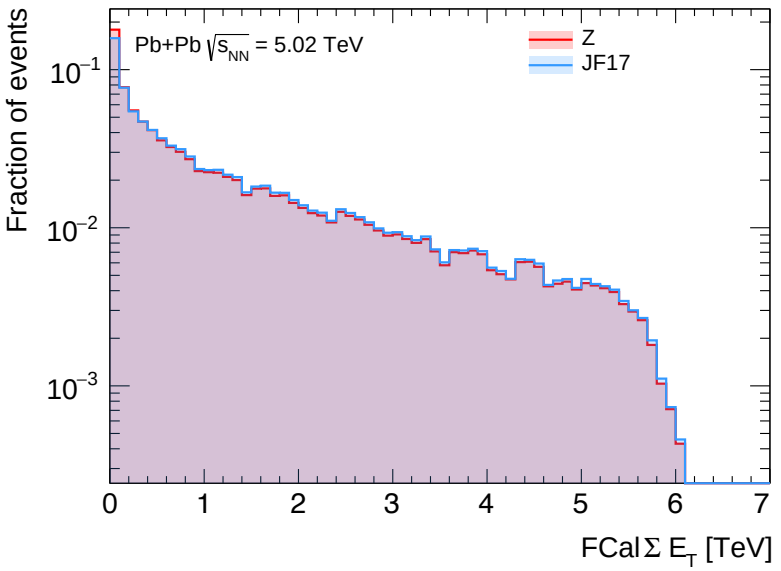

Figure 3.15: Distribution of FCal ΣE_{T} for signal and background samples.

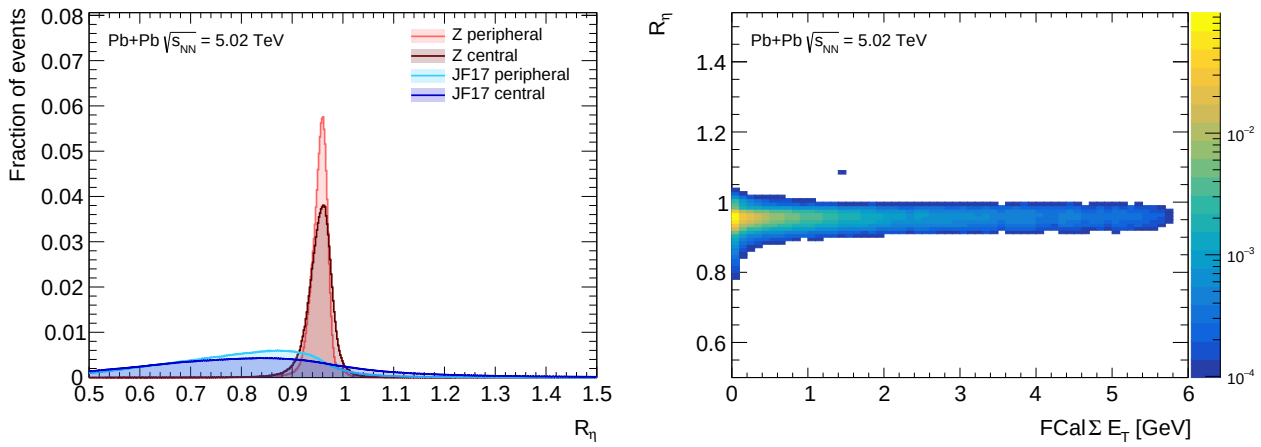

(a) (b)

Figure 3.16: Distribution of the R_η electron discriminating variable (a) for signal and background electrons in central and peripheral Pb+Pb collisions, and (b) for signal electrons as a function of centrality.

distributions become noticeably wider in central collisions. Therefore, better discrimination between signal and background electrons is achieved in peripheral collisions. In contrast, differentiation in central collisions proves more challenging due to high detector occupancy. Results for all the electron discriminating variables are documented in Appendix A.2.2.

Figure 3.17 displays a log-transformed discriminant d'_{L} obtained separately in central and peripheral collisions for signal and background simulation. d'_{L} distributions in peripheral collisions exhibit better separation, resulting in higher electron identification efficiency. In central collisions, higher overlap between signal and background distributions is observed, leading to decreased identification capabilities.

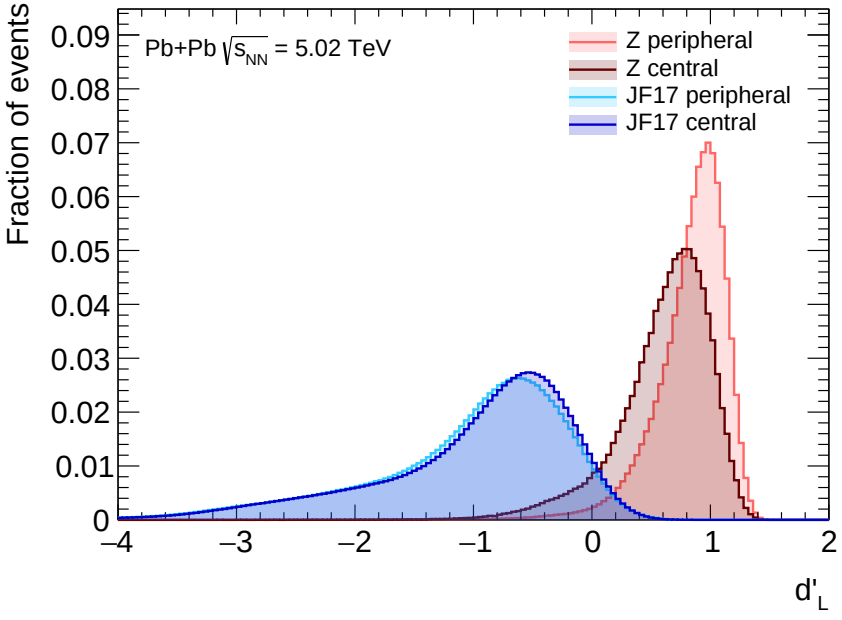

Figure 3.17: Distributions of log-transformed discriminants d'_{L} for central and peripheral collisions.

3.3.4 Probability density functions

A key component of the likelihood identification involves probability density functions for signal and background electrons, which appear in Equation 3.2. As discriminating variables depend significantly on electron kinematics, probability density functions are derived in two-dimensional E_{T}-$|\eta|$ regions. Seven E_{T} intervals are defined with the following boundaries: 4, 7, 10, 15, 20, 30, 40, >40 GeV, and nine $|\eta|$ ranges are used with the following edges: 0.00, 0.60, 0.80, 1.15, 1.37, 1.52, 1.81, 2.01, 2.37, 2.47. Although low E_{T} values down to 4 GeV are considered, it is recommended to use the resulting probability density functions for electrons with $E_{\mathrm{T}} > 15$ GeV, as the studies are based solely on the $Z \to e^{+}e^{-}$ process. To avoid any potential fluctuations, distributions of electron discriminating variables are smoothened using an adaptive kernel density estimator [137]. Figure 3.18 shows probability distribution functions for two variables, R_{η} and R_{ϕ}, in an example kinematic region with $20 < E_{\mathrm{T}} < 30$ GeV and $0 < |\eta| < 0.6$. Probability distribution functions for all the electron discriminating variables are given in Appendix A.2.3.

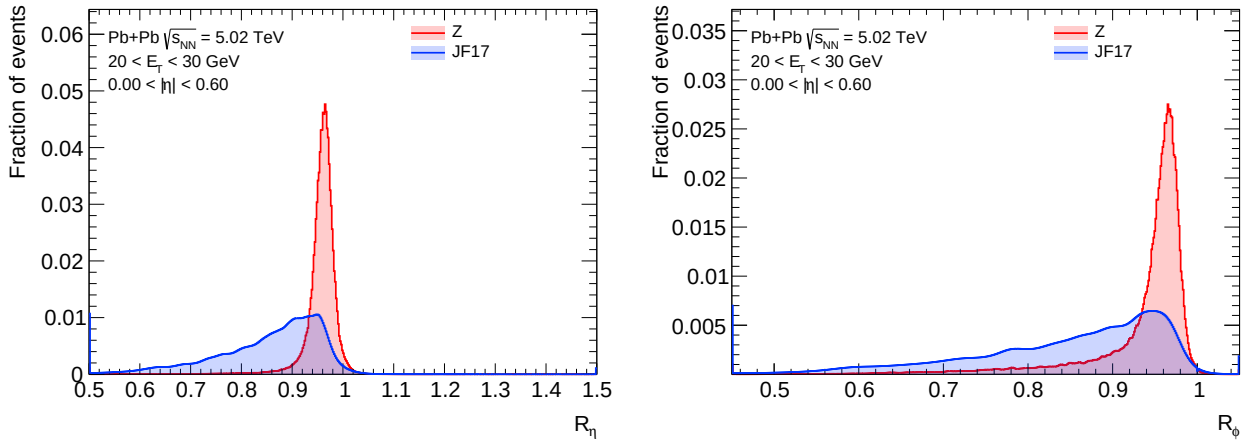

(a) (b)

Figure 3.18: Probability distribution functions of the (a) R_{η} and (b) R_{ϕ} electron discriminating variables for signal and background electrons.

3.3.5 Optimisation of working points

In order to optimise electron identification working points, a set of centrality-dependent cuts on the likelihood discriminant are extracted for four selections: HIVeryLoose, HILoose, HIMedium, and HITight. Distributions of the likelihood discriminant cuts in bins of FCal ΣE_{T}, obtained for each E_{T}–$|\eta|$ region, are smoothened using a quadratic function fit. At the optimisation step, cuts on the likelihood discriminant change stepwise in each centrality interval. The average efficiency of derived operating points amounts to 99%, 97%, 94%, and 87% for the HIVeryLoose, HILoose, HIMedium, and HITight selections, respectively. The signal electron efficiency as a function of centrality for four optimised selections is shown in Figure 3.19. The undulating shape of the efficiency for tighter working points stems from the fact that the quadratic function fit is only an approximation of cuts on the likelihood discriminant.

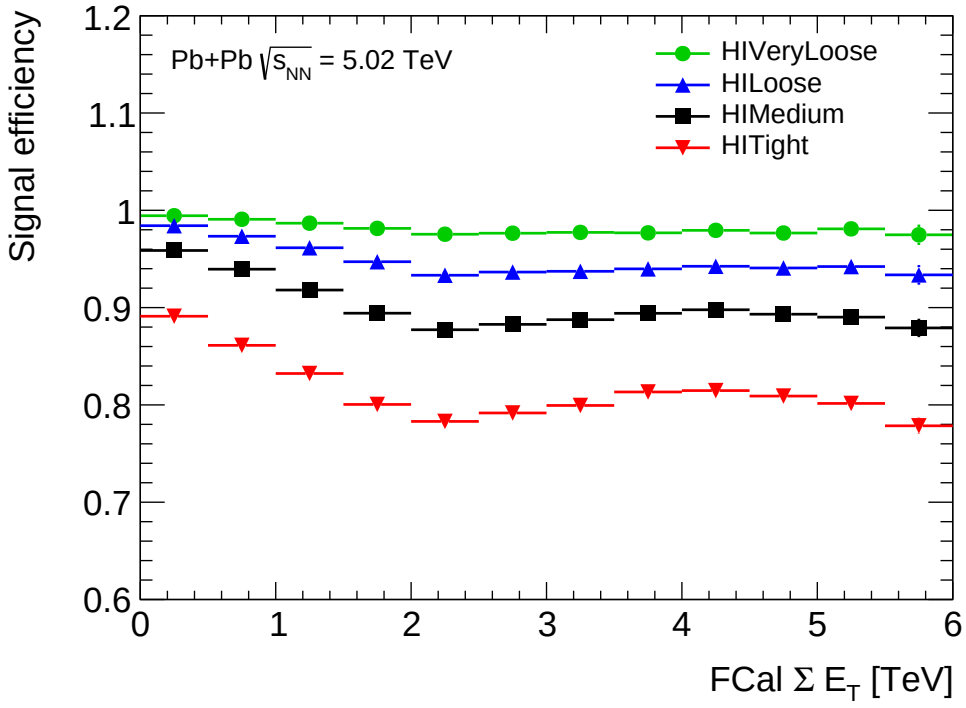

Figure 3.19: The signal efficiency as a function of FCal ΣE_{T} for four identification working points estimated at the optimisation step.

Figure 3.20 presents the signal electron efficiency as a function of electron E_{T} and $|\eta|$. The efficiency profile is designed to increase with electron E_{T} and slightly decrease with electron $|\eta|$ to provide better background rejection at low electron E_{T} and high electron $|\eta|$.

Figure 3.21 displays the signal and background electron efficiencies as a function of electron E_{T} and $|\eta|$ for the HIMedium working point. The lowest signal and the highest background electron efficiencies are observed

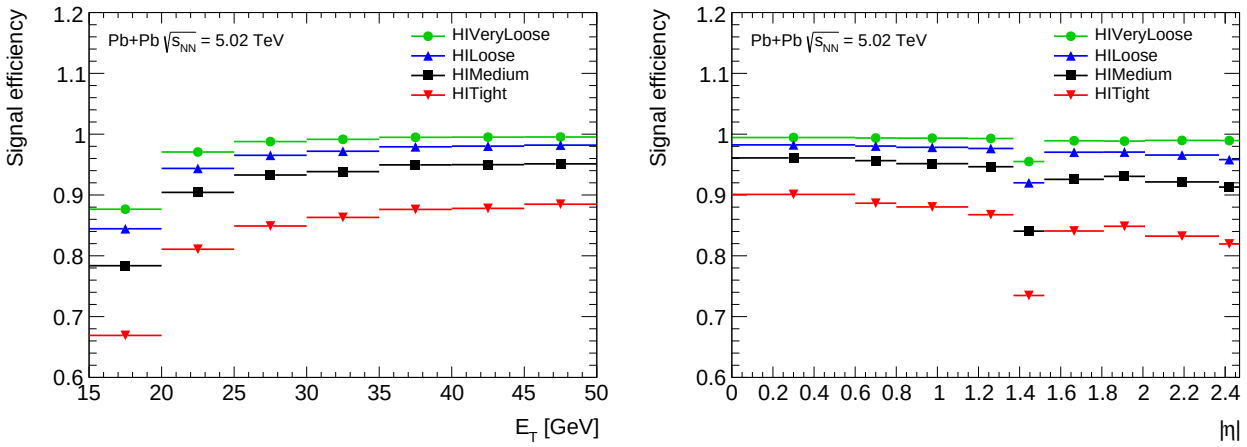

(a) (b)

Figure 3.20: The signal efficiency as a function of electron (a) E_{T} and (b) $|\eta|$ for four identification working points estimated at the optimisation step.

at low electron E_{T} and in the calorimeter transition region. The background level for the HIMedium working point does not exceed 5%. The signal and background electron efficiencies for the remaining working points, HIVeryLoose, HILoose, and HITight, documented in Appendix A.2.4, follow a similar trend.

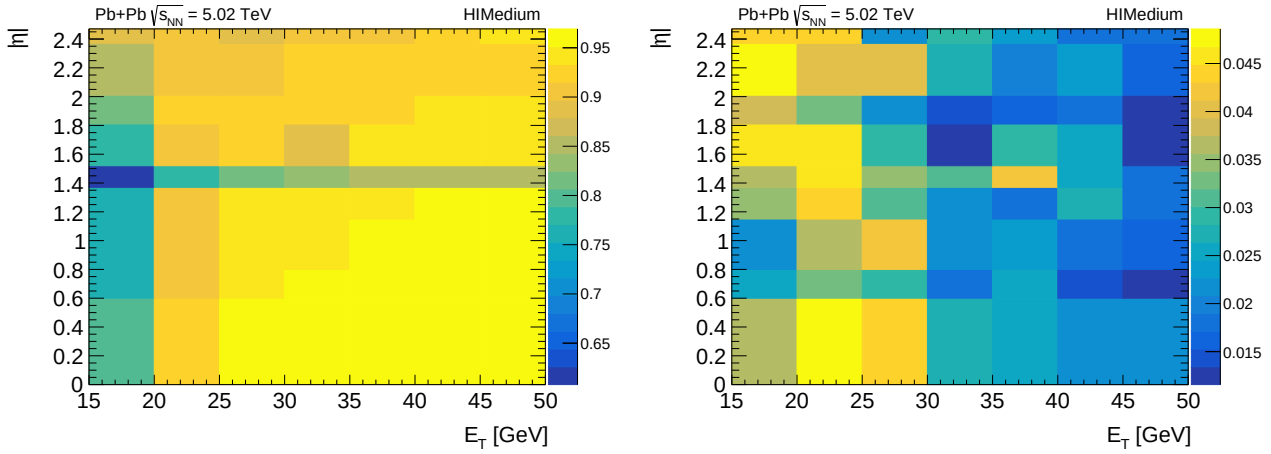

(a) (b)

Figure 3.21: The (a) signal and (b) background efficiencies as a function of electron E_{T} and $|\eta|$ for the HIMedium working point estimated at the optimisation step.

3.3.6 Validation of working points

The obtained working points are validated using the Tag-and-Probe method described in Section 3.2.2. To assess systematic uncertainties on the signal electron efficiency, three mass windows around the Z-boson peak are used: 80–100 GeV, 75–105 GeV, and 70–110 GeV, and two tag electron selections: HITight and HIMedium. Figure 3.22 shows invariant mass distributions of tag–probe electron pairs in signal $Z \to e^+e^-$ MC simulation

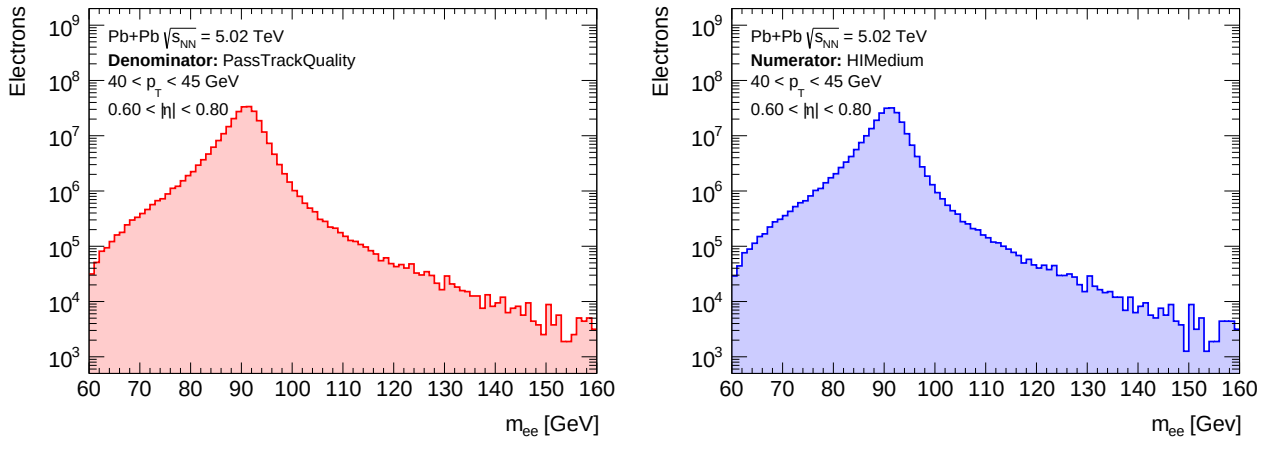

(a) (b)

Figure 3.22: Invariant-mass distributions of electron pairs in signal $Z \to e^+e^-$ MC simulation in the (a) denominator and (b) numerator of the identification efficiency for the HIMedium working point in an exemplary electron E_{T} and $|\eta|$ bin.

in an example electron kinematic region with $40 < E_{\mathrm{T}} < 45$ GeV and $0.6 < |\eta| < 0.8$. Probe electrons in the denominator of the identification efficiency have to be reconstructed as good-quality electrons, while probe electrons in the numerator must satisfy the HIMedium selection. Invariant mass distributions in different electron kinematic slices are given in Appendix A.2.5.

At the validation step, the cuts on the likelihood discriminant no longer change stepwise in each centrality range but are interpolated using central values of each FCal ΣE_{T} bin, which leads to slight differences in measured efficiency. Also, additional requirements are imposed on the number of hits in the inner detector in each identification selection, summarised in Table 3.3.

Table 3.3: Requirements on the number of hits in the inner detector imposed on the identification selections.

Wroking point	**HIVeryLoose**	**HILoose**	**HIMedium**	**HITight**
Hits in the B-Layer	0	0	1	1
Hits in the pixel detector	1	2	2	2
Hits in the silicon detectors	8	8	8	8

The measured identification efficiency and the relative difference between optimised and measured efficiencies as a function of electron E_{T} and $|\eta|$ for the HIMedium working point are presented in Figure 3.23. The relative difference is calculated as the difference between measured and optimised efficiencies divided by the optimised efficiency. The total uncertainties are dominated by systematic ones for electrons with $E_{\mathrm{T}} < 35$ GeV and $|\eta| < 1.37$, while statistical uncertainties dominate for electrons with $E_{\mathrm{T}} > 35$ GeV and $|\eta| > 1.37$. An acceptable agreement is found between the measured and optimised efficiencies. The largest increase in the measured efficiency of up to 19% is observed at low electron E_{T}, while the largest drop of 32% is found in the most forward region of the detector. Similar results, provided in Appendix A.2.6, are obtained for the remaining working points, HIVeryLoose, HILoose, and HITight.

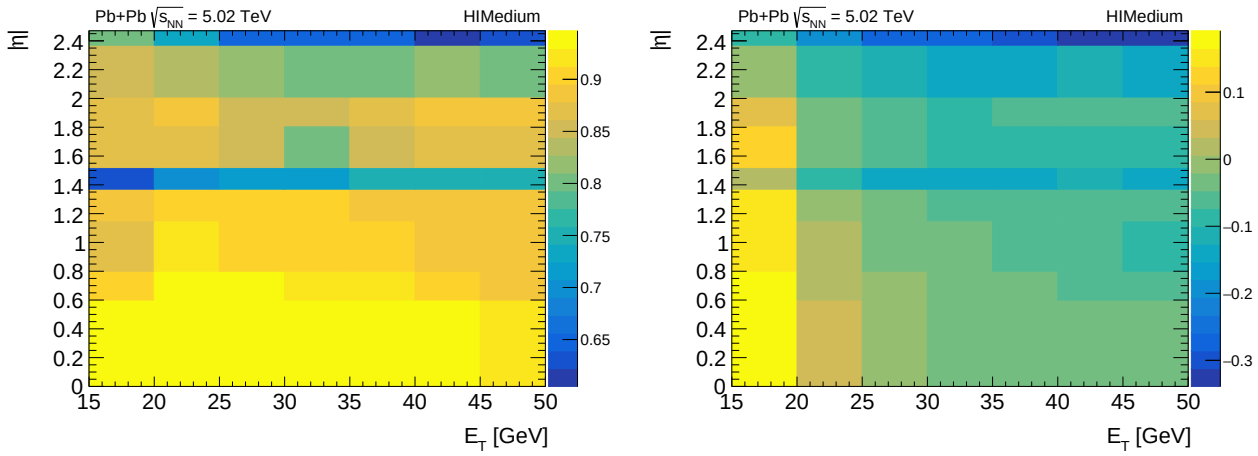

(a) (b)

Figure 3.23: The (a) measured identification efficiency and (b) relative difference between target and measured efficiencies as a function of electron E_{T} and $|\eta|$ for the HIMedium working point.

3.3.7 Comparison of working points

The obtained working points are compared with old electron identification selections used previously for Pb+Pb collisions. Two operating points were defined for early Run-2 analyses, referred to as old HILoose and HIMedium, optimised with the fixed target efficiency of 90% and 80%, respectively [138]. Figure 3.24 presents the measured identification efficiency for the two old working points. The efficiency is mostly constant as a function of electron E_{T}, while an increase in efficiency is observed with electron $|\eta|$. The identification efficiency of the new and old operating points are compared in Figure 3.25. Based on the average efficiency, the old HIMedium (HILoose) selection corresponds to the new HITight (HIMedium) working point. The relative difference is calculated as the difference between efficiencies of the new and old selections divided by the efficiency of the old selection. Compared to the efficiency of the old operating points, the efficiency of the

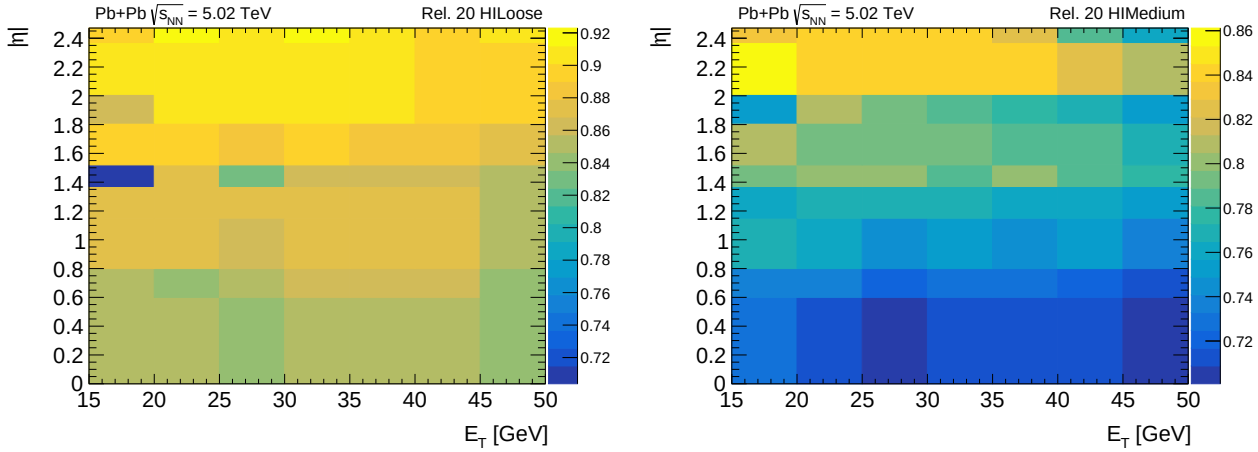

(a) (b)

Figure 3.24: The measured identification efficiency as a function of electron E_{T} and $|\eta|$ for the old (a) HIMedium and (b) HILoose working points.

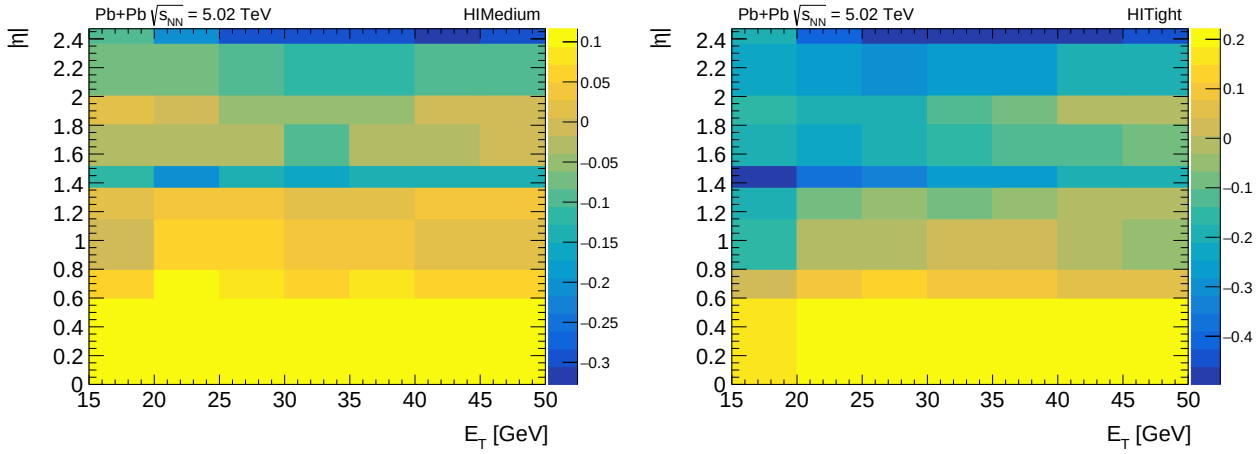

(a) (b)

Figure 3.25: The relative difference between efficiencies for the new and old working points as a function of electron E_{T} and $|\eta|$ for the (a) HIMedium and (b) HITight working points.

new selections is higher, up to 12% (20%) at electron $|\eta| < 1.37$ for the HIMedium (HITight) working point, while the efficiency in the transition region of the detector and in the most forward $|\eta|$ values is lower, down to 33% (50%), to provide higher background reduction. Overall, the new selections show improved performance compared to the old working points and provide two additional working points, HILoose and HIVeryLoose, dedicated for analyses with low background contributions involving electrons in the final state.

3.3.8 Performance in Run 3

The optimised electron identification working points are validated in Pb+Pb collisions at $\sqrt{s_{\mathrm{NN}}} = 5.36$ TeV. The data were collected in 2014 during Run 3, and correspond to the total integrated luminosity of 1.6 nb^{-1}. Figure 3.26 presents invariant-mass distributions of reconstructed and identified electron tag-probe pairs in Pb+Pb data. Both tag and probe electrons are required to have $p_{\mathrm{T}} > 15$ GeV and $|\eta| < 2.5$. The tag electron has to satisfy the HITight identification criteria, while the probe electron must either be only reconstructed or also identified using one of the four electron identification working points. Approximately 132,000, 109,000, 54,000, 31,000, and 23,000 electron pairs pass the reconstruction, HIVeryLoose, HILoose, HIMedium, and HITight selections, respectively. A distinct peak at 91 GeV is observed in all categories, corresponding to the Z-boson mass. Tighter working points provide better background suppression, especially at low invariant-mass values. This result demonstrates good prospects for measurements with high-p_{T} electrons in Pb+Pb data in Run 3.

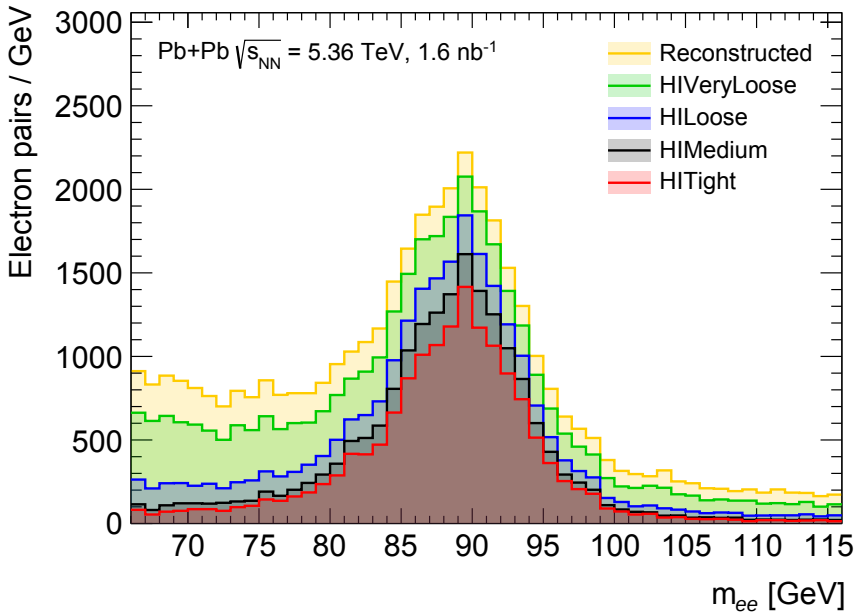

Figure 3.26: Invariant-mass distributions of reconstructed and identified electron tag-probe pairs in Pb+Pb data at $\sqrt{s_{\mathrm{NN}}} = 5.36$ TeV, recorded in 2024 during Run 3.

Chapter 4

Top-quark pair production in p+Pb collisions

4.1 Motivation

In p+Pb collisions, top quarks are expected to provide novel probes of nPDFs at high Bjorken-x values of $3 \cdot 10^{-3} - 0.5$. Since gluon fusion dominates top-quark pair production, the $t\bar{t}$ process is sensitive to the gluon nPDF, which is difficult to access using other available probes. With the large luminosities of p+Pb data collected during Run 2 at $\sqrt{s_{\mathrm{NN}}} = 8.16$ TeV, top-quark yields are predicted to become measurable in decay channels involving electrons and muons in the final state. In this work, the inclusive $t\bar{t}$ cross section is extracted in the combined ℓ+jets and dilepton channel with the highest precision to date, including the first observation of this process in the dilepton decay mode in p+Pb collisions at the LHC. Additionally, differences in $t\bar{t}$ production between p+Pb and pp systems are quantified using the nuclear modification factor, $R_{p\mathrm{A}}$, for the first time. The results of the measurement are published in Ref. [39], with a leading contribution by the Author of this thesis to the preparation of the manuscript and its approval in the ATLAS Collaboration.

4.2 Data

The data used in the measurement were recorded with the ATLAS detector during the p+Pb data-taking period in 2016, which corresponds to a total integrated luminosity of 165 nb^{-1}. Data collection was conducted in two configurations: p+Pb and Pb+p beam directions, yielding total integrated luminosities of 57 nb^{-1} and 108 nb^{-1}, respectively. The proton and lead beams were set up with energies of 6.5 TeV and 2.56 TeV per nucleon, respectively, yielding a nucleon–nucleon centre-of-mass energy of $\sqrt{s_{\mathrm{NN}}} = 8.16$ TeV. The asymmetry between the proton and lead beam energies results in a rapidity boost by ± 0.465 units in the p-going direction relative to the laboratory frame. The data were collected under low-pileup conditions with an average pileup of $\langle\mu\rangle = 0.18$.

Figure 4.1 presents an event display of a p+Pb collision that resulted in $t\bar{t}$ candidate production in the $e\mu$ decay mode. The event contains the reconstructed electron track (blue line) with its associated energy deposit in the electromagnetic calorimeter (green boxes), the reconstructed muon track (red line) with its associated muon chambers (blue boxes), one b-tagged jet (yellow cone), and two non-b-tagged jets (green cones). Tracks in the

inner detector are marked with orange lines, while energy deposits in cells of the hadronic calorimeter are represented by the yellow rectangles.

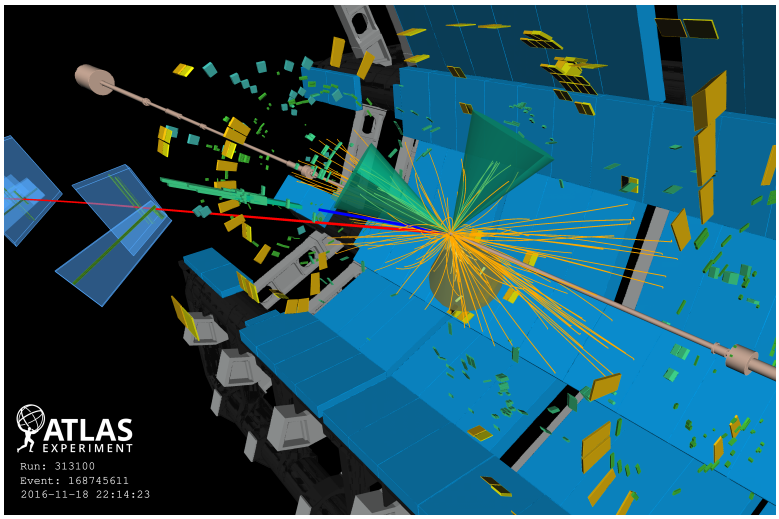

Figure 4.1: Event display of a p+Pb collision at $\sqrt{s_{\mathrm{NN}}} = 8.16$ TeV collected in 2016, containing a $t\bar{t}$ candidate.

4.3 Simulation

MC simulation is used to estimate signal and background contributions and provide predictions for comparison with the data. MC simulation samples are generated using the full ATLAS detector simulation [121], implemented with the GEANT4 framework [122]. Each process consists of four samples, including combinations of two isospin configurations, proton–proton and proton–neutron, and two beam-direction configurations, p+Pb and Pb+p. Generated nucleon–nucleon collisions are embedded into real p+Pb data events to accurately model the underlying event. All processes are normalised to their theoretical cross sections at $\sqrt{s_{\mathrm{NN}}} = 8.16$ TeV, obtained at NNLO precision in QCD. Decays of b- and c-flavoured hadrons are treated using the EVTGEN [139] program in samples produced using POWHEG BOX V2 [123] and MADGRAPH5_AMC@NLO [140] MC generators. Table 4.1 summarises all MC simulation samples used in the analysis, including their parameters: ME generator, PS model, ME PDF set, the set of tuned parameters, and the number of simulated events. Details for individual processes are described in the following sections.

4.3.1 $t\bar{t}$ simulation

Nominal $t\bar{t}$ simulation is generated at NLO precision in QCD using POWHEG BOX V2 MC generator for the ME, interfaced with PYTHIA8 [124] for the PS modelling with the NNPDF3.0NNLO [141] PDF set and the A14 [135] set of tuned parameters. The resummation damping parameter, h_{damp}, which controls the p_{T} of the first additional gluon emission beyond the leading-order Feynman diagram in the PS, is set to $1.5m_t$, where $m_t = 172.5$ GeV is the top-quark mass. The signal $t\bar{t}$ samples are normalised to the NNLO + next-to-next-to-leading logarithmic (NNLL) cross-section prediction from the TOP++ V2 [142] program.

Three alternative $t\bar{t}$ samples are used to estimate systematic uncertainties related to the signal modelling in simulation. Uncertainties in the amount of parton-shower radiation are assessed by increasing the h_{damp} parameter

Table 4.1: List of simulated samples for the $t\bar{t}$ analysis in p+Pb collisions.

Process	ME generator	PS model	ME PDF	Tune	Events
$t\bar{t}$ nominal	POWHEG v2	PYTHIA8	NNPDF3.0NNLO	A14	10M
$t\bar{t}$ $h_{\mathrm{damp}} = 3m_t$	POWHEG v2	PYTHIA8	NNPDF3.0NNLO	A14	10M
$t\bar{t}$ alternative ME	MADGRAPH5	PYTHIA8	NNPDF3.0NNLO	A14	10M
$t\bar{t}$ alternative PS	POWHEG v2	HERWIG7	NNPDF3.0NNLO	H7.2-DEFAULT	10M
Single top tW	POWHEG v2	PYTHIA8	NNPDF3.0NNLO	A14	600k
Single top t-chan	POWHEG v2	PYTHIA8	NNPDF3.0NNLO	A14	600k
Diboson VV	SHERPA v2.2.11		NNPDF3.0NNLO	–	200k
W+b	SHERPA v2.2.11		NNPDF3.0NNLO	–	6M
W+c	SHERPA v2.2.11		NNPDF3.0NNLO	–	6M
W+light	SHERPA v2.2.11		NNPDF3.0NNLO	–	6M
Z+b	SHERPA v2.2.11		NNPDF3.0NNLO	–	3M
Z+c	SHERPA v2.2.11		NNPDF3.0NNLO	–	3M
Z+light	SHERPA v2.2.11		NNPDF3.0NNLO	–	3M

to $3m_t$. Another sample, produced using MADGRAPH5_AMC@NLO with PYTHIA8, is used to evaluate the uncertainty in the ME and PS matching. Uncertainties in PS modelling are obtained using a sample produced with POWHEG BOX v2 and HERWIG v7.2 [143] employing the H7.2-DEFAULT [144] set of tuned parameters.

4.3.2 Single-top simulation

Single-top production consists of three main processes: tW, t-channel, and s-channel. The largest contribution comes from tW production, followed by the t-channel, while the s-channel cross section is negligible and excluded in simulation. tW and t-channel samples are produced using POWHEG BOX v2 interfaced with PYTHIA8 with the NNPDF3.0NNLO PDF set and the A14 set of tuned parameters. The interference between the $t\bar{t}$ and tW final states is treated using the diagram removal scheme [145] in a way recommended by ATLAS.

4.3.3 Diboson simulation

The diboson background includes WW and ZZ production in association with jets, filtered for decays into two leptons and two neutrinos. Samples are generated using SHERPA v2.2.11 [146] for ME and PS modelling, employing the NNPDF3.0NNLO PDF set. MEs are derived at NLO accuracy in QCD for up to one parton and at LO accuracy for up to three partons [147].

4.3.4 Vector-boson simulation

Vector-boson background consists of W- and Z-boson production in association with jets, further filtered for b- (W/Z+b), c- (W/Z+c), and light (W/Z+light) quarks. Simulation is produced with the SHERPA v2.2.11 MC generator, in combination with the NNPDF3.0NNLO PDF set. The samples use MEs at NLO precision in QCD for up to one additional jet and at LO precision for up to three additional jets.

4.4 Event selection

Events are selected using single-electron or single-muon triggers with a minimum p_{T} threshold of 15 GeV [133, 148]. At least one reconstructed vertex is required, which is built from at least two good-quality charged-particle tracks with $p_{\mathrm{T}} > 0.1$ GeV [149]. Six signal regions are defined in total, including four regions in the ℓ+jets channel and two regions in the dilepton channel. The requirements imposed on leptons and jets are described in detail in Sections 4.5.1 and 4.5.2, respectively.

The ℓ+jets decay mode consists of events with exactly one lepton (electron or muon). Events are further required to have at least four jets, including at least one b-tagged jet, as described in Section 4.5.2. The ℓ+jets channel is divided into four signal regions with one electron or muon and exactly one or at least two b-tagged jets, labelled as $1\ell 1b$ ejets, $1\ell 2b$incl ejets, $1\ell 1b$ mujets and $1\ell 2b$incl mujets.

The dilepton channel is formed using events with exactly two oppositely charged leptons. Events with same-flavour lepton pairs with the invariant mass, $m_{\ell\ell}$, within a Z-boson mass window of $80 < m_{\ell\ell} < 100$ GeV are rejected to minimise the contribution from Z+jets production. $m_{\ell\ell}$ is required to be above 15 (45) GeV in the opposite-flavour (same-flavour) channel to match the phase space of the Z+jets simulation, while having minimal impact on the measurement. Events are additionally required to have at least two jets, including at least one b-tagged jet, as described in Section 4.5.2. Signal regions in the dilepton channel with exactly one or at least two b-tagged jets are labelled as $2\ell 1b$ and $2\ell 2b$incl, respectively.

4.5 Object selection

4.5.1 Leptons

Electron candidates are reconstructed from a cluster of energy deposits in the EM calorimeter matched to a track in the inner detector. They have to be associated with the primary vertex, and meet requirements on the impact parameters of $|d_0|/\sigma(d_0) < 5$ and $|\Delta z_0 \sin\theta| < 0.5$ mm. Electrons must have $p_{\mathrm{T}} > 18$ GeV and $|\eta| < 2.47$ and lie outside of the calorimeter transition region, $1.37 < |\eta| < 1.52$. Candidates have to satisfy the Medium identification working point and be isolated using Gradient isolation criteria [127]. Electron efficiency in MC simulation is corrected using dedicated p+Pb scale factors, related to electron reconstruction, identification, isolation, and trigger.

Muon candidates are required to have a reconstructed track in the MS combined with a track in the inner detector. They have to originate from the primary vertex, and satisfy requirements on the impact parameters of $|d_0|/\sigma(d_0) < 3$ and $|\Delta z_0 \sin\theta| < 0.5$ mm. Candidates must have $p_{\mathrm{T}} > 18$ GeV and $|\eta| < 2.5$, meet Medium identification criteria, and be isolated using the FCTight_FixedRad isolation working point [150]. Muon efficiency in MC simulation is corrected using dedicated p+Pb scale factors, obtained for muon reconstruction, isolation, track-to-vertex association, and trigger.

Figure 4.2 presents lepton p_{T} distributions for the selected leptons in the ℓ+jets and dilepton channels. The fake-lepton background is estimated from data, following the method outlined in Section 4.6. Predictions are

obtained after the fit described in Section 4.8. Good agreement is observed between the data and the sum of predictions in all six signal regions.

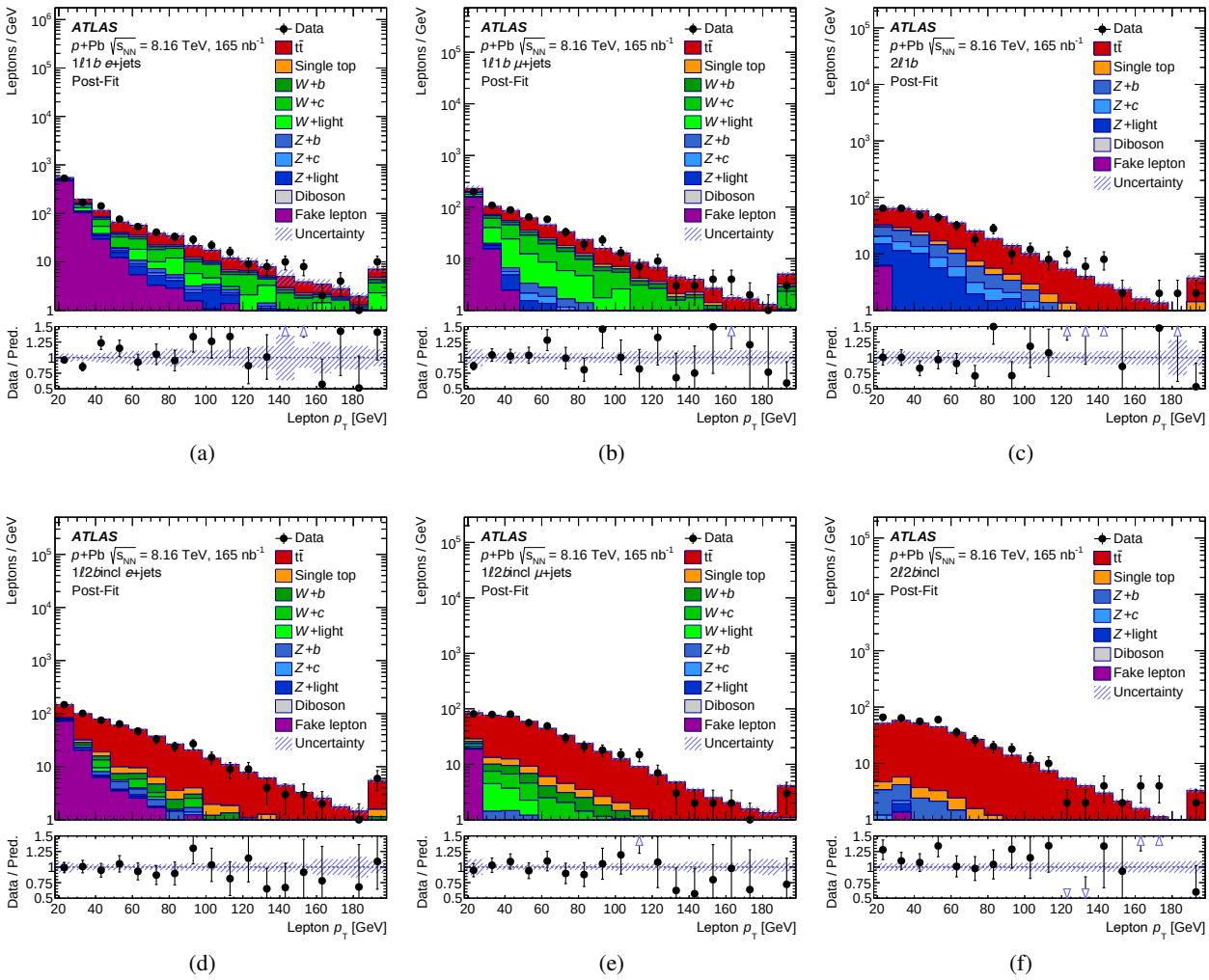

Figure 4.2: Post-fit lepton p_{T} distributions in the six signal regions (e+jets: (a) $1\ell 1b$ and (d) $1\ell 2b\mathrm{incl}$, μ+jets: (b) $1\ell 1b$ and (e) $1\ell 2b\mathrm{incl}$, dilepton: (c) $2\ell 1b$ and (f) $2\ell 2b\mathrm{incl}$). Post-fit uncertainties are represented by the hatched area. The full markers in the bottom panels show a ratio of data and a sum of predictions. Open triangles indicate bins with entries that are outside the ratio range. The last bin includes overflow events [39].

4.5.2 Jets

Jets are reconstructed using the anti-k_t method [151] with a radius of $R = 0.4$, implemented via the FastJet [152] package. Massless calorimeter towers with a size of $\Delta\eta \times \Delta\phi = 0.1 \times \pi/32$ are used as inputs to the algorithm. The background energy originating from the underlying event is subtracted from every tower. A low-pileup jet calibration dedicated for p+Pb collisions at $\sqrt{s_{\mathrm{NN}}} = 8.16$ TeV is applied, using simulations of the calorimeter response and in-situ measurements of the absolute energy scale. In-situ studies are carried out in pp collisions and cross-calibrated to the p+Pb system. Jets are required to have $p_{\mathrm{T}} > 20$ GeV and $|\eta| < 2.5$.

Objects built in this approach, referred to as heavy-ion (HI) jets [153], do not provide b-tagging information. PF jets likely to originate from b-hadrons are considered b-tagged jets, as described in Section 4.5.3.

In order to access b-tagging information, a second type of jets is also used in the analysis. They are reconstructed from particle-flow (PF) objects [154], which combine measurements of topological clusters in the calorimeter and charged-particle tracks in the inner detector, using the anti-k_t algorithm with a radius of $R = 0.4$. Topological clusters with low E_{T} are replaced with track p_{T} matched to those clusters. A high-pileup jet calibration, derived in pp collisions at $\sqrt{s} = 13$ TeV, is used.

The b-tagging information is inherited from PF to HI jets by geometrically matching two jet types in each event, based on the smallest ΔR distance. If a $\Delta R \leq 0.3$ criterion is satisfied for a given jet pair, the HI jet is considered to be b-tagged. Due to differences in calibration of PF and HI jets, approximately 18% of HI jets in data and 15% in MC simulation lack a PF jet counterpart. In this case, the HI jet is treated as non-b-tagged.

Additionally, jet performance is studied in $Z \to \ell\ell$ ($\ell = e, \mu$) events, using two approaches: the truth method and the Z-jet balance [154]. The former technique compares reconstructed jets with generated ones in MC samples. Generated jets, provided by simulation, consist of stable final-state particles originating from the primary vertex, excluding muons and neutrinos. Reconstructed and generated jets are matched based on detector geometry by imposing a condition on the distance between them, $\Delta R < 0.4$. The jet p_{T} response, defined as $p_{\mathrm{T}}^{\mathrm{reco}}/p_{\mathrm{T}}^{\mathrm{truth}}$, is analysed in various jet $p_{\mathrm{T}}^{\mathrm{truth}}$ bins, where $p_{\mathrm{T}}^{\mathrm{reco}}$ and $p_{\mathrm{T}}^{\mathrm{truth}}$ denote transverse momenta of the reconstructed and corresponding generated jet, respectively. The mean jet response $\langle p_{\mathrm{T}}^{\mathrm{reco}}/p_{\mathrm{T}}^{\mathrm{truth}} \rangle$ is derived as the mean of a Gaussian function fitted to the jet p_{T} response distribution. The jet p_{T} resolution, which represents the amount of fluctuation in the jet energy reconstruction, is obtained as the ratio of the standard deviation over the mean of the same Gaussian fit.

Figure 4.3 displays the mean jet response and p_{T} resolution estimated in MC simulation for the two types of jets: PF and HI. The mean jet response is observed to be above unity, which comes from a quark-dominated

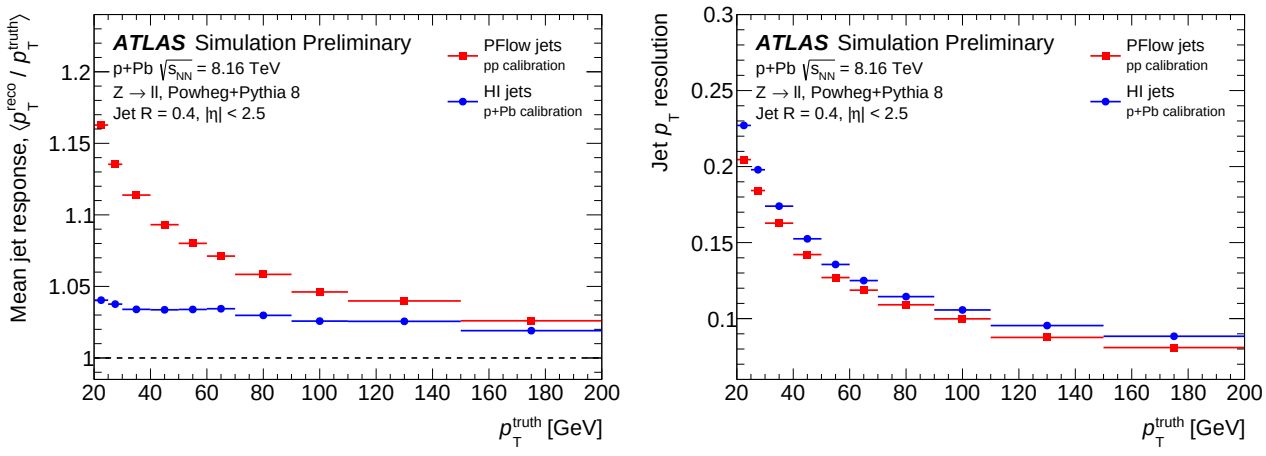

(a) (b)

Figure 4.3: The (a) mean jet response and (b) jet p_{T} resolution evaluated in 2016 p+Pb simulation as a function of generated jet $p_{\mathrm{T}}^{\mathrm{truth}}$ for the PF and HI jets [155].

composition of the $Z \to \ell\ell$ process. Increased values at low $p_{\mathrm{T}}^{\mathrm{truth}}$ for the PF jets originate from the underlying event contribution in p+Pb collisions, while this effect is not present for the HI jets, which include the dedicated underlying-event subtraction. The jet p_{T} resolution notably improves with rising $p_{\mathrm{T}}^{\mathrm{truth}}$ for both types of jets.

Another approach to study jet performance, referred to as the Z-jet balance method, is based on a momentum balance between the Z boson and the jet. The advantage of this technique is the fact that it can be applied in both data and MC simulation. It uses reconstructed jets recoiling against a Z boson, which further decays to a lepton pair. Selected events are required to contain exactly two oppositely charged electrons or muons and at least one HI or PF jet. To ensure the back-to-back emission of the Z boson and the jet, a pairing criterion of $|\Delta\phi(\mathrm{Z,jet})| > 2.8$ is applied, where $|\Delta\phi(\mathrm{Z,jet})|$ denotes the azimuthal angle between the Z boson and the jet. The jet p_{T} response is calculated as $p_{\mathrm{T}}^{\mathrm{reco}}/p_{\mathrm{T}}^{\mathrm{ref}}$, where the reference transverse momentum $p_{\mathrm{T}}^{\mathrm{ref}} = p_{\mathrm{T}}^{Z}|\cos\Delta\phi(Z,\mathrm{jet})|$ is the projection of the Z boson transverse momentum p_{T}^{Z} along the jet axis. Similarly to the truth method, the mean jet response $\langle p_{\mathrm{T}}^{\mathrm{reco}}/p_{\mathrm{T}}^{\mathrm{ref}}\rangle$ is obtained as the mean of a Gaussian fit to the jet p_{T} response distribution, while the jet p_{T} resolution is determined as the ratio of the standard deviation over the mean of the same fit. The overall jet p_{T} resolution is expected to be higher compared to the truth method due to intrinsic broadening originating from the physics of $Z \to \ell\ell$ decays.

The mean jet response and p_{T} resolution in the data and MC simulation for the HI jets are presented in Figure 4.4. Systematic uncertainties correspond to jet calibration and its application to HI jets, as described in Section 4.7.6. The mean jet response is below unity and rises with $p_{\mathrm{T}}^{\mathrm{ref}}$, while the jet p_{T} resolution improves with increasing $p_{\mathrm{T}}^{\mathrm{ref}}$. Good agreement is observed between data and MC simulation in the mean jet response, while a small MC non-closure is observed in the jet p_{T} resolution at jet $p_{\mathrm{T}}^{\mathrm{ref}} > 50$ GeV.

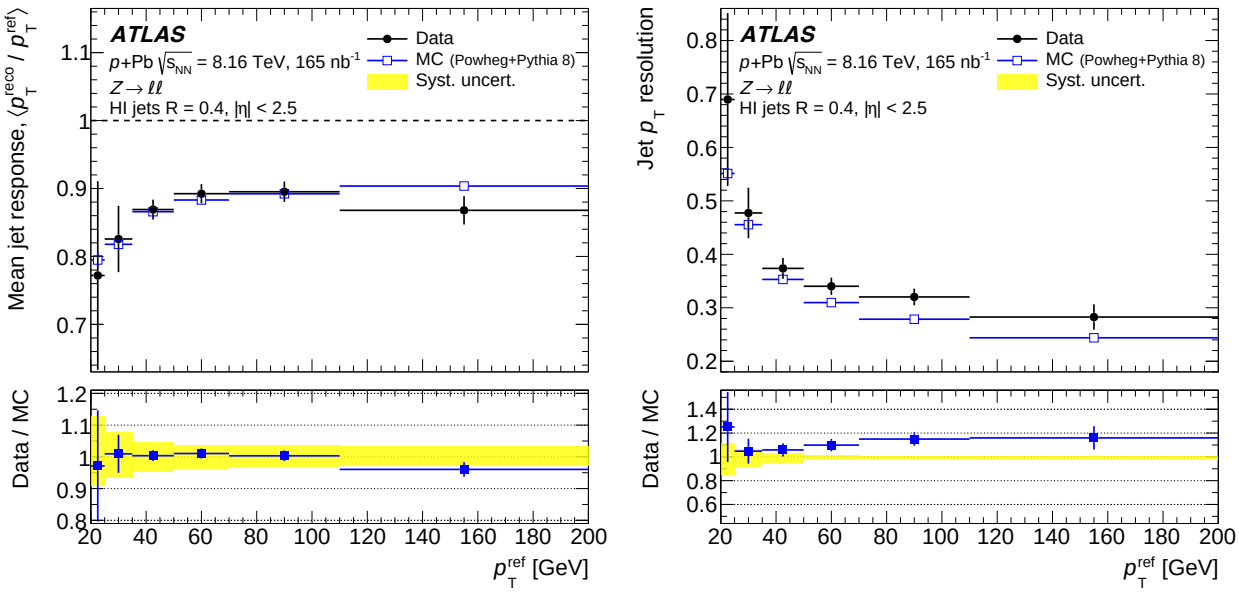

(a) (b)

Figure 4.4: The (a) mean jet response and (b) jet p_{T} resolution evaluated in data and simulation as a function of reference jet $p_{\mathrm{T}}^{\mathrm{ref}}$ for the HI jets. The bottom panels show the data-to-MC ratio with error bars and yellow boxes representing statistical and systematic uncertainties, respectively [39].

Figure 4.5 shows the mean jet response and p_{T} resolution in the data and MC simulation for the PF jets. Systematic uncertainties correspond to jet calibration, as described in Section 4.7.6. The mean jet response values at low $p_{\mathrm{T}}^{\mathrm{ref}}$ are increased by the underlying event, leading to a flat $p_{\mathrm{T}}^{\mathrm{ref}}$ dependence. The resolution is found to be better than for the HI jets and improves with rising $p_{\mathrm{T}}^{\mathrm{ref}}$. The data and MC simulation exhibit good consistency in the mean jet response, while the jet p_{T} resolution shows a slight MC non-closure at jet $p_{\mathrm{T}}^{\mathrm{ref}} > 35$ GeV.

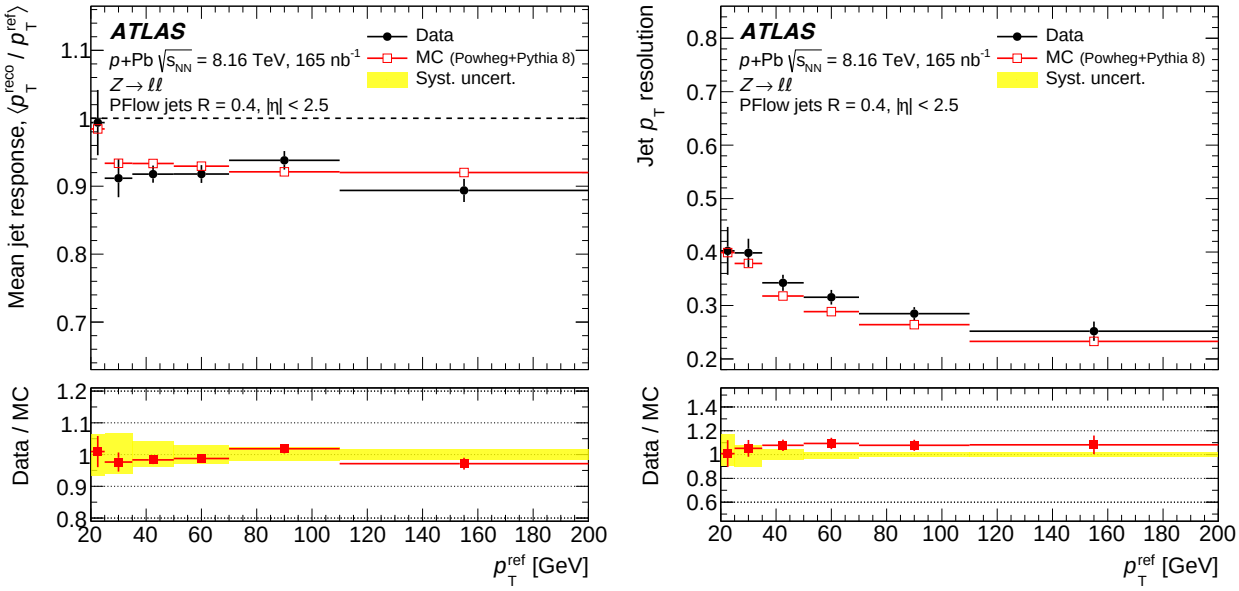

(a) (b)

Figure 4.5: The (a) mean jet response and (b) jet p_{T} resolution evaluated in data and simulation as a function of reference jet $p_{\mathrm{T}}^{\mathrm{ref}}$ for the PF jets. The bottom panels show the data-to-MC ratio with error bars and yellow boxes representing statistical and systematic uncertainties, respectively [39].

Figure 4.6 shows HI jet p_{T} distributions in the six signal regions. The fake-lepton background is evaluated from data, following the method specified in Section 4.6. Predictions are adjusted using the fit detailed in Section 4.8. The data show good consistency with the sum of predictions in all the signal regions.

4.5.3 *b*-tagged jets

PF jets likely to originate from b-hadron decays are tagged using the DL1r algorithm [156], a multivariate discriminant based on deep-learning techniques. The classifier is trained on simulated $t\bar{t}$ events, treating b-quark jets as the signal and c-, light-quark, and gluon jets as the background. Figure 4.7 shows distributions of the b-tag discriminant in the four signal regions, corresponding to two $t\bar{t}$ decay modes and two b-tagged jet categories. Higher b-tag discriminant values indicate a higher probability of a jet originating from a b-hadron. A working point with 85% efficiency, optimised for tagging b-quark jets from $t\bar{t}$ decays in pp collisions at $\sqrt{s} = 13$ TeV, is used in the analysis. The distinct discontinuity observed in the b-tag discriminant around unity corresponds to the threshold applied for b-tagged jets. This requirement results in rejection factors of approximately 3 and 40 against b-quark and light-quark/gluon jets, respectively.

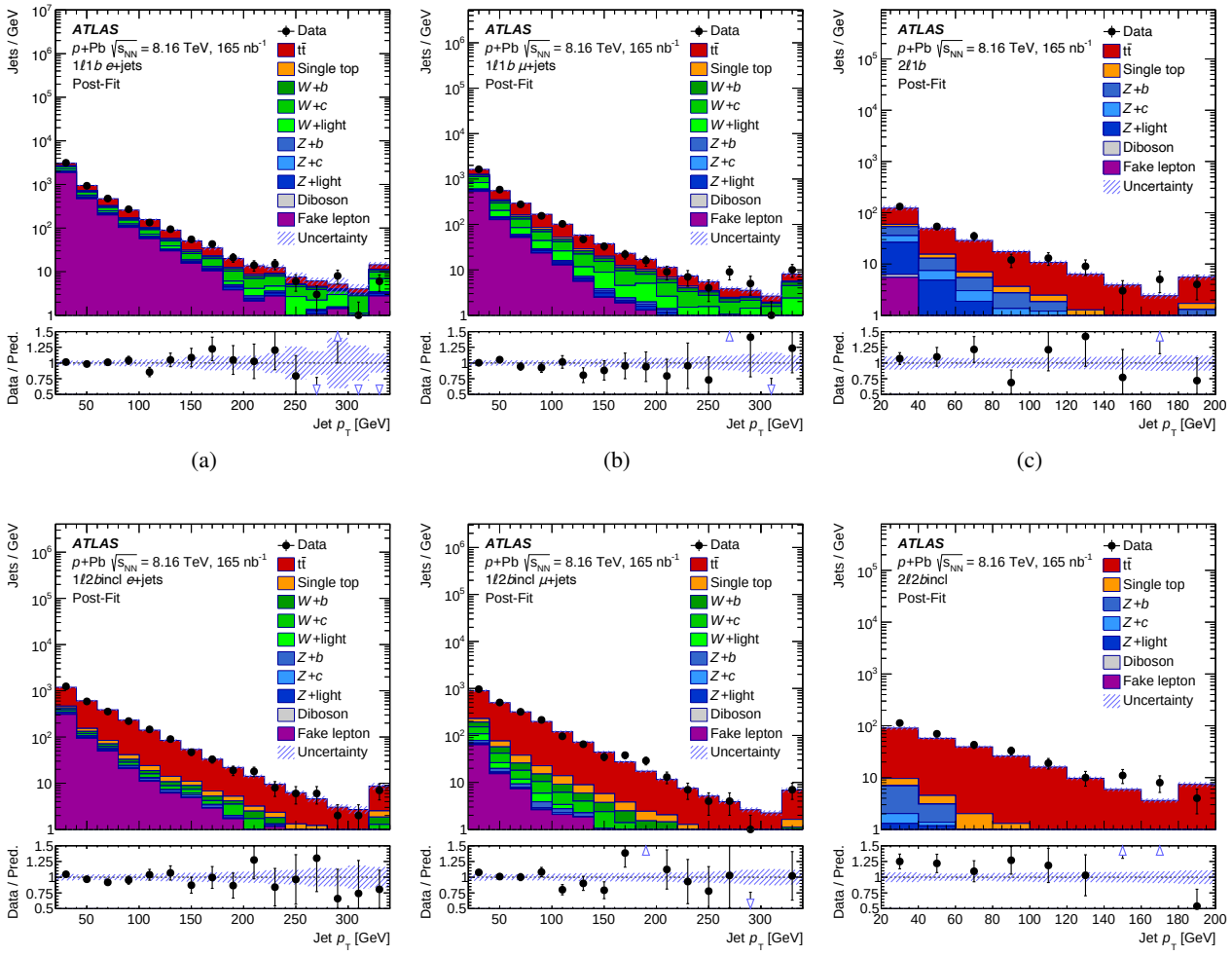

Figure 4.6: Post-fit jet p_{T} distributions in the six signal regions (e+jets: (a) $1\ell 1b$ and (d) $1\ell 2b\mathrm{incl}$, μ+jets: (b) $1\ell 1b$ and (e) $1\ell 2b\mathrm{incl}$, dilepton: (c) $2\ell 1b$ and (f) $2\ell 2b\mathrm{incl}$). Post-fit uncertainties are represented by the hatched area. The full markers in the bottom panels show a ratio of data and a sum of predictions. Open triangles indicate bins with entries that are outside the ratio range. The last bin includes overflow events [39].

4.5.4 Missing transverse energy

The missing transverse energy, $E_{\mathrm{T}}^{\mathrm{miss}}$, is used to estimate the momentum carried by neutrinos escaping the detector [157]. It is calculated using the following formula:

$$E_{\mathrm{T}}^{\mathrm{miss}} = \left|\boldsymbol{p}_{\mathrm{T}}^{\mathrm{miss}}\right| = \left|-\sum_{i} \boldsymbol{p}_{\mathrm{T},i}\right|, \tag{4.1}$$

where $\boldsymbol{p}_{\mathrm{T},i}$ denotes the transverse momentum vector of fully calibrated leptons, photons, PF jets, and the soft hadronic activity reconstructed from charged-particle tracks not associated with the hard objects. Due to technical limitations and high detector occupancy in heavy-ion collisions, HI jets are typically not used in the $E_{\mathrm{T}}^{\mathrm{miss}}$ computation. Therefore, no requirement on $E_{\mathrm{T}}^{\mathrm{miss}}$ is imposed in the main analysis. $E_{\mathrm{T}}^{\mathrm{miss}}$ is only used to define a dedicated control region for fake-lepton background estimation as described in Section 4.6.

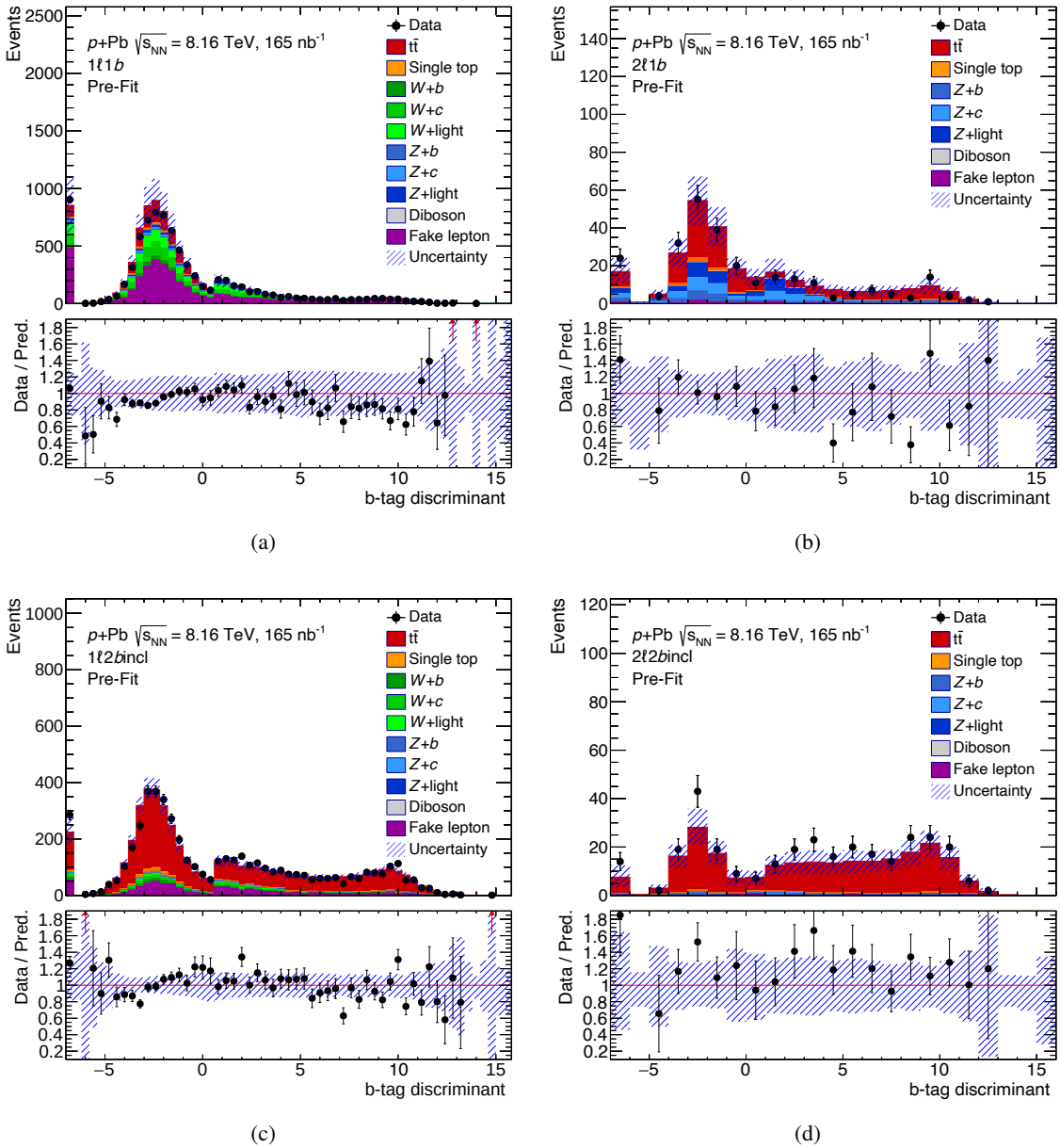

Figure 4.7: Pre-fit distributions of the b-tag discriminant in the four signal regions: (a) $1\ell 1b$, (b) $2\ell 1b$, (c) $1\ell 2b\text{incl}$, and (d) $2\ell 2b\text{incl}$. Pre-fit uncertainties are represented by the hatched area. The full markers in the bottom panels show a ratio of data and a sum of predictions. Arrows indicate bins with entries that are outside the ratio range. The first and last bins include underflow and overflow events, respectively.

Figure 4.8 displays per-event $E_{\mathrm{T}}^{\mathrm{miss}}$ distributions in the six signal regions. The fake-lepton background is estimated from data, as explained in Section 4.6. Predictions are obtained after the fit outlined in Section 4.8. Reasonable agreement is found between the data and the sum of predictions in all the signal regions.

4.5.5 Overlap removal

To prevent overlap between selected objects, several requirements are imposed, referred to as overlap removal. If an electron is matched to the same track as a muon, the electron is removed. To avoid the double counting

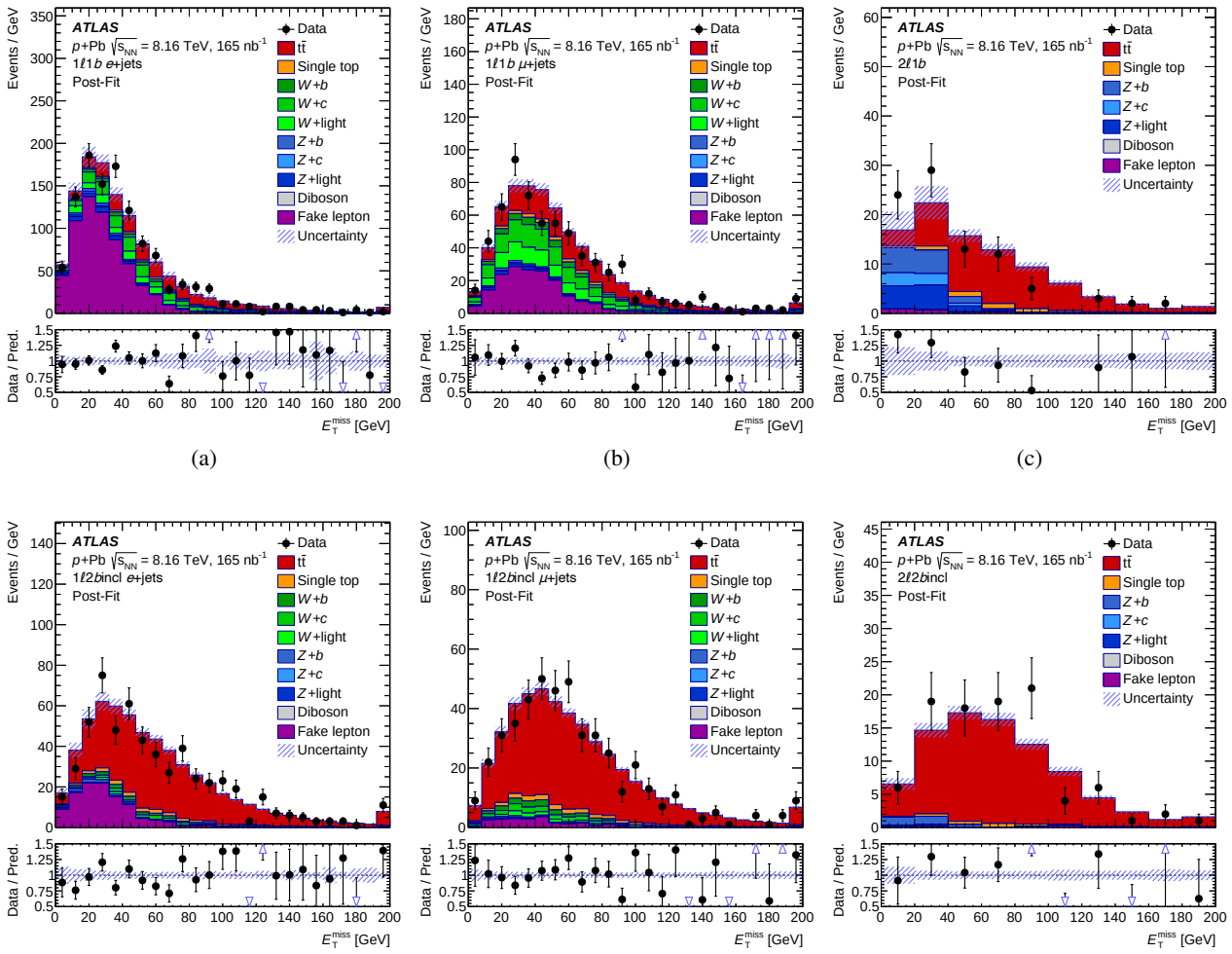

Figure 4.8: Post-fit $E_{\mathrm{T}}^{\mathrm{miss}}$ distributions in the six signal regions (e+jets: (a) $1\ell 1b$ and (d) $1\ell 2b$incl, μ+jets: (b) $1\ell 1b$ and (e) $1\ell 2b$incl, dilepton: (c) $2\ell 1b$ and (f) $2\ell 2b$incl). Post-fit uncertainties are represented by the hatched area. The full markers in the bottom panels show a ratio of data and a sum of predictions. Open triangles indicate bins with entries that are outside the ratio range. The last bin includes overflow events [39].

of electrons as jets, the closest jet to an electron is discarded if it is within a distance of $\Delta R \leq 0.2$ from the electron. To reduce the contribution of non-prompt leptons from heavy-flavour hadron decays inside jets, leptons within a distance of $\Delta R \leq 0.4$ from a jet are removed. However, if the lepton is a muon and the jet has fewer than three associated tracks, the jet is discarded instead. This procedure is applied to both HI and PF jets, prior to the jet matching.

4.6 Fake-lepton background estimation

4.6.1 Matrix method

The fake-lepton background includes non-prompt leptons, originating from semileptonic decays of heavy-flavour quarks and electrons from photon conversions, and light hadrons misidentified as leptons. This type

of background is estimated using a data-driven technique, referred to as the Matrix Method [158]. It relies on dividing the total number of events, N_{tot}, with leptons meeting Loose requirements into two categories of events containing real leptons (N_{R}) and fake leptons (N_{F}). Another categorisation splits events into two groups, with leptons passing the Tight selection (N_{T}) and satisfying Loose but not satisfying Tight criteria (N_{L}). Tight requirements align with the nominal lepton selection detailed in Section 4.5.1, with electrons and muons satisfying Medium identification and isolation criteria. The Loose selection imposes no isolation requirements on both lepton types, the LooseAndBLayer identification working point on electrons and the Medium identification criteria on muons. To provide a fake-lepton enriched region, events with exactly one lepton with $p_{\text{T}} > 18$ GeV, at least one jet with $p_{\text{T}} > 18$ GeV, and $E_{\text{T}}^{\text{miss}} < 20$ GeV are selected for the fake-lepton estimate. The total number of events is constrained as follows:

$$N_{\text{tot}} = N_{\text{T}} + N_{\text{L}} = N_{\text{R}} + N_{\text{F}}. \tag{4.2}$$

The relation between the two categories of events can be expressed by a matrix equation,

$$\begin{bmatrix} N_{\text{T}} \\ N_{\text{L}} \end{bmatrix} = \begin{bmatrix} \varepsilon_{\text{r}} & \varepsilon_{\text{f}} \\ 1-\varepsilon_{\text{r}} & 1-\varepsilon_{\text{f}} \end{bmatrix} \begin{bmatrix} N_{\text{R}} \\ N_{\text{F}} \end{bmatrix}, \tag{4.3}$$

where ε_{r} and ε_{f} are the fractions of events with real and fake leptons satisfying Tight criteria, referred to as real- and fake-lepton efficiency, respectively. In order to estimate the number of events with real and fake leptons, Equation 4.3 can be inverted as follows:

$$\begin{bmatrix} N_{\text{R}} \\ N_{\text{F}} \end{bmatrix} = \frac{1}{\varepsilon_{\text{r}} - \varepsilon_{\text{f}}} \begin{bmatrix} 1-\varepsilon_{\text{f}} & -\varepsilon_{\text{f}} \\ \varepsilon_{\text{r}}-1 & \varepsilon_{\text{r}} \end{bmatrix} \begin{bmatrix} N_{\text{T}} \\ N_{\text{L}} \end{bmatrix}. \tag{4.4}$$

The number of events with real (N_{R}^{T}) and fake (N_{F}^{T}) leptons meeting Tight requirements can be expressed as

$$N_{\text{R}}^{\text{T}} = \varepsilon_{\text{r}} N_{\text{R}} = \frac{\varepsilon_{\text{r}}}{\varepsilon_{\text{r}} - \varepsilon_{\text{f}}}(N_{\text{T}} - \varepsilon_{\text{f}}(N_{\text{T}} + N_{\text{L}})), \tag{4.5}$$

$$N_{\text{F}}^{\text{T}} = \varepsilon_{\text{f}} N_{\text{F}} = \frac{\varepsilon_{\text{f}}}{\varepsilon_{\text{r}} - \varepsilon_{\text{f}}}(\varepsilon_{\text{r}}(N_{\text{T}} + N_{\text{L}}) - N_{\text{T}}). \tag{4.6}$$

Based on Equation 4.6, the following weights are defined for events passing Tight (w_{F}^{T}) and Loose (w_{F}^{L}) selections

$$N_{\text{F}}^{\text{T}} = w_{\text{F}}^{\text{T}} N_{\text{T}} + w_{\text{F}}^{\text{L}} N_{\text{L}}, \tag{4.7}$$

$$w_{\text{F}}^{\text{T}} = \frac{\varepsilon_{\text{f}}(\varepsilon_{\text{r}} - 1)}{\varepsilon_{\text{r}} - \varepsilon_{\text{f}}}, \tag{4.8}$$

$$w_{\text{F}}^{\text{L}} = \frac{\varepsilon_{\text{f}}\varepsilon_{\text{r}}}{\varepsilon_{\text{r}} - \varepsilon_{\text{f}}}. \tag{4.9}$$

These weights are derived using real- and fake-lepton efficiencies, obtained from MC simulation in multiple lepton p_{T} and η regions. In the main measurement, w_{F}^{T} and w_{F}^{L} weights are applied to data to estimate the fake-lepton background normalisation and shape.

4.6.2 Real-lepton efficiency

The simulated-lepton efficiency, $\varepsilon_{\text{truth}}$, is calculated as a fraction of events with leptons matched to generated objects using truth information in MC simulation ($N_{\text{T}}^{\text{truth}}$), expressed by the following formula:

$$\varepsilon_{\text{truth}} = \frac{N_{\text{T}}^{\text{truth}}}{N_{\text{tot}}^{\text{truth}}}. \tag{4.10}$$

The real-lepton efficiency is obtained by correcting the simulated-lepton efficiency for eventual efficiency mis-modelling in MC simulation, using lepton scale factors as follows:

$$\varepsilon_{\mathrm{r}} = \varepsilon_{\mathrm{truth}} \times \frac{\mathrm{SF_T}}{\mathrm{SF_L}}, \tag{4.11}$$

where $\mathrm{SF_T}$ and $\mathrm{SF_L}$ are the total scale-factor corrections for electrons or muons satisfying Tight and Loose criteria, respectively. Figure 4.9 shows the real-lepton efficiency for electrons and muons as a function of lepton p_{T} for 0, 1, $\geq$2 b-tagged jets in the event and inclusive. The overall efficiency rises with lepton p_{T}, starting from around 0.8 and reaching a plateau of approximately 0.95 at lepton $p_{\mathrm{T}} \approx 50$ GeV. A slight decrease in efficiency is observed with an increasing number of b-tagged jets. Efficiency values are found to be comparable between electrons and muons. The real-lepton efficiency as two-dimensional lepton p_{T}–η maps, which are used in the main measurement, is provided in Appendix B.1.

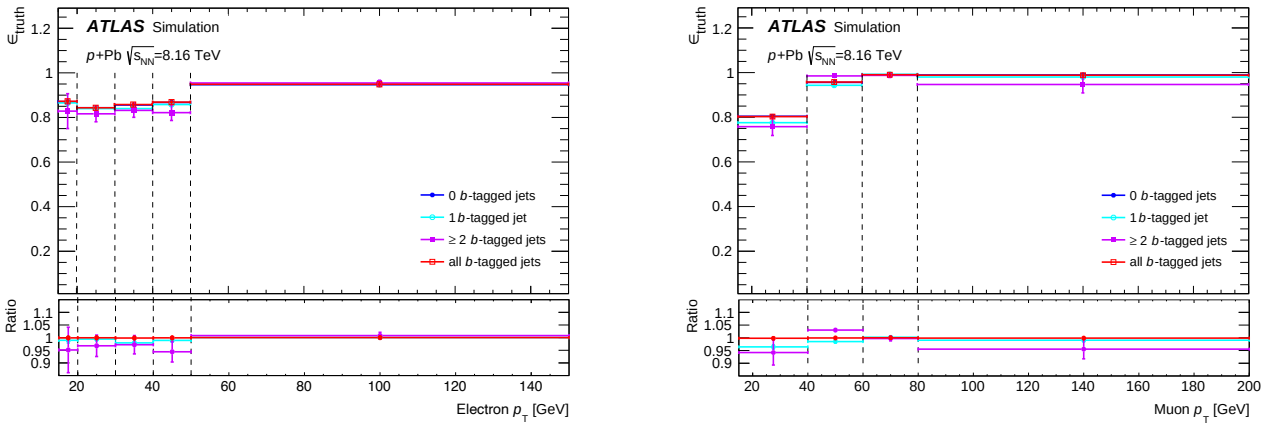

(a) (b)

Figure 4.9: The real-lepton efficiency for (a) electrons and (b) muons as a function of lepton p_{T} for a varying number of b-tagged jets in the event. The bottom panels show a ratio of events for different b-tagged jet multiplicities to the number of events with zero b-tagged jets [39].

4.6.3 Fake-lepton efficiency

The fake-lepton efficiency is derived as a fraction of data events containing non-prompt leptons passing the Tight selection. The number of prompt leptons (N^{prompt}), obtained by matching reconstructed leptons to generated objects, is subtracted. The fake-lepton efficiency is described by the following formula:

$$\varepsilon_{\mathrm{f}} = \frac{N_{\mathrm{T}} - N_{\mathrm{T}}^{\mathrm{prompt}}}{N_{\mathrm{tot}} - N_{\mathrm{tot}}^{\mathrm{prompt}}}. \tag{4.12}$$

Figure 4.10 presents the fake-lepton efficiency for electrons and muons as a function of lepton p_{T} for 0, 1, $\geq$2 b-tagged jets in the event and inclusive. The overall efficiency decreases with lepton p_{T}, starting from 0.22 (0.10) and dropping to 0.18 (0.03) for electrons (muons). No strong dependence of the efficiency on the number of b-tagged jets is observed. The fake-lepton efficiency is found to be significantly higher for electrons than for muons. The fake-lepton efficiency as a function of lepton p_{T} and $|\eta|$, used in the nominal analysis, is documented in Appendix B.2. Due to limited statistics, the efficiency is estimated using two bins in p_{T} and two bins in $|\eta|$.

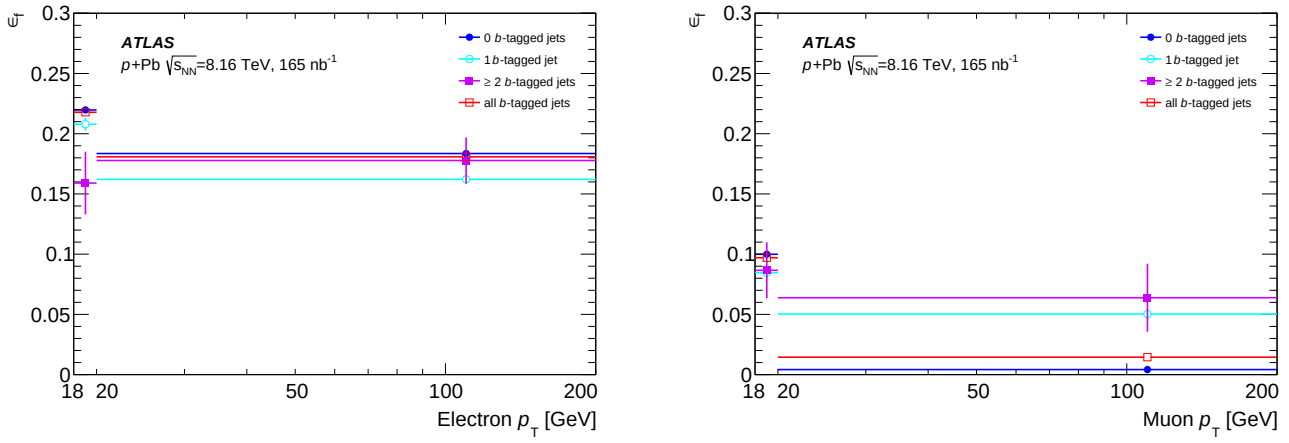

(a) (b)

Figure 4.10: The fake-lepton efficiency for (a) electrons and (b) muons as a function of lepton p_{T} for a varying number of b-tagged jets in the event [39].

4.7 Systematic uncertainties

Systematic uncertainties affecting the $t\bar{t}$ measurement arise from multiple sources. An uncertainty in the integrated luminosity is obtained from luminosity calibration. Signal $t\bar{t}$ modelling uncertainties include variations of the h_{damp} parameter, ME, PS, and PDF set in simulated samples, and uncertainties in the initial-state (ISR) and final-state (FSR) radiation. Background modelling uncertainties consist of normalisation variations for single-top, diboson, W+jets, and Z+jets contributions, with additional uncertainties in the tW diagram removal scheme. Lepton uncertainties originate from calibration and scale-factor corrections, separately for electrons and muons. Jet uncertainties come from jet energy scale and resolution, the dedicated jet matching, and the b-tagging procedure. Uncertainties in the fake-lepton contribution are assessed by varying the real- and fake-lepton efficiency, normalisation, and shape of the background. Table 4.2 summarises all systematic uncertainties, including the number of components in each of the groups.

4.7.1 Luminosity

The uncertainty in the integrated luminosity is estimated from the calibration of the luminosity scale using x–y beam-separation scans [114]. The LUCID-2 detector is used for the primary luminosity measurements [159]. The uncertainty in the combined 2016 p+Pb data sample amounts to 2.4%.

4.7.2 $t\bar{t}$ modelling

Uncertainties in signal $t\bar{t}$ modelling are assessed by varying the h_{damp} parameter, ME, and PS, using alternative MC samples described in Section 4.3, and symmetrised. Separate components are considered for the normalisation and shape of the $t\bar{t}$ contribution. Additional PDF uncertainties are estimated using the PDF4LHC15 Hessian method [160]. Uncertainties in the ISR are evaluated by modifying both the renormalisation (μ_{r}) and factorisation scales (μ_{f}) by factors of 0.5 and 2. Another variation applies a different α_s constant using the VAR3C A14 [135] set of tuned parameters, and modifies both μ_{r} and μ_{f} by a factor of 0.5 with $h_{\mathrm{damp}} = 3m_t$

Table 4.2: Summary of systematic uncertainties with the number of components in each group.

Systematic group	Systematic uncertainty	Number of components
Luminosity	Calibration	1
$t\bar{t}$ modelling	$t\bar{t}\,h_{\mathrm{damp}}$	2
	$t\bar{t}$ ME	2
	$t\bar{t}$ PS	2
	$t\bar{t}$ PDF	30
	ISR / FSR	3
Background modelling	Single top	4
	Diboson	1
	W+jets	6
	Z+jets	3
Electron	Calibration	2
	Scale factors	4
Muon	Calibration	4
	Scale factors	10
Jet	Jet energy scale	20
	Jet energy resolution	9
	Jet matching	2
	b-tagging	19
Fake lepton	Efficiency	7
	Normalisation	1
	Shape	4

and a factor of 2 with $h_{\mathrm{damp}} = 1.5m_t$. An FSR uncertainty is obtained by changing μ_{r} for emissions from the PS by factors of 0.5 and 2.

4.7.3 Background modelling

An uncertainty of 9.5% is applied to the normalisation of the tW and t-channel single-top background [161], which includes scale variations and PDF uncertainties, evaluated from the MSTW2008 [141] PDF 90% confidence-level uncertainties. To assess uncertainties from the interference between the $t\bar{t}$ and tW processes, alternative variations of diagram removal and diagram subtraction are used [162]. A conservative 50% normalisation uncertainty is applied to the diboson background. Uncertainties in the normalisation of the W+jets and Z+jets backgrounds, divided into the b-, c-, and light quarks contributions and additionally split for events with one and at least two b-tagged jets for the W+jets process, are derived using the Berends scaling method [163].

4.7.4 Electron

Uncertainties associated with electrons stem in part from the low-pileup energy calibration [127]. Additional uncertainties due to scale factors, related to electron reconstruction, identification, isolation, and trigger, are estimated by varying the corrections within their total uncertainties.

4.7.5 Muon

Uncertainties related to muons arise partially from the muon momentum scale and resolution [150]. Further uncertainties in scale factors, dedicated to muon reconstruction, isolation, track-to-vertex association, and trigger, are obtained by changing the corrections within their statistical and systematic uncertainties.

4.7.6 Jet

Uncertainties in jet calibration are determined from the comparison of the simulated jet response in MC samples from different generators and in situ studies of the calorimeter response [154]. Additional uncertainties arise from the application of the calibration to HI jets [164]. Uncertainties due to b-tagging are obtained by varying the scale-factor corrections within their uncertainties [156]. In order to assess uncertainties in jet matching, the distance requirement between HI and PF jets is changed to $\Delta R \leq 0.3 \pm 0.1$. Furthermore, a variation is considered, where HI jets lacking a PF jet counterpart are randomly considered as b-tagged based on the light-flavour jet mistag rate [165].

4.7.7 Fake-lepton background

Uncertainties in the fake-lepton background are estimated by varying real- and fake-lepton efficiencies within their uncertainties. The real-lepton efficiency is changed using statistical and systematic uncertainties separately, while the fake-lepton efficiency is modified using total uncertainties separately for electrons and muons in events with one and at least two b-tagged jets. Additionally, a variation is considered where charge-flip leptons, obtained as the number of leptons with different reconstructed and simulated charge signs, are subtracted in the numerator and denominator of Equation 4.12. A conservative uncertainty in the fake-lepton contribution normalisation of 50% in the e+jets and 100% in the μ+jets channels is applied.

To determine the fake-lepton background shape variations, all MC simulation events are subtracted from the data, and the difference is normalised to the total number of fake-lepton events. A ratio of subtracted and scaled data to the fake-lepton contribution is calculated as a function of the azimuthal angle, $\Delta\phi(\boldsymbol{p}_{\mathrm{T}}^{\mathrm{miss}}, \ell)$, between the lepton four-momentum and $\boldsymbol{p}_{\mathrm{T}}^{\mathrm{miss}}$, and fitted by a second-order polynomial. Values of the obtained ratio change from 0.5 to 3.5 in bins of $\Delta\phi(\boldsymbol{p}_{\mathrm{T}}^{\mathrm{miss}}, \ell)$. Shape variations of the fake-lepton background are defined separately for electrons and muons in events with one and at least two b-tagged jets using fit parameter uncertainties.

4.8 Fit Procedure

4.8.1 Profile-likelihood fit

The $t\bar{t}$ cross section is extracted using a binned profile-likelihood fit [166] method. It relies on a likelihood function expressed with the following formula:

$$L(\mu, \boldsymbol{\theta}) = \prod_{i}^{N} \frac{(\mu s_i(\boldsymbol{\theta}) + b_i(\boldsymbol{\theta}))^{n_i}}{n_i!} e^{-(\mu s_i(\boldsymbol{\theta}) + b_i(\boldsymbol{\theta}))} \prod_{\theta_k \in \boldsymbol{\theta}} \rho(\theta_k), \tag{4.13}$$

which depends on the signal strength, μ, defined as the ratio of the fitted signal to the theory expectation, and a set of nuisance parameters $\boldsymbol{\theta}$, which control systematic variations. n_i denotes the number of data events in bin i out of N. The number of expected signal and background events in bin i are represented by s_i and b_i, respectively. $\rho(\theta_k)$ stands for the probability density function for the θ_k parameter. Most parameters are constrained by a Gaussian-distributed probability density, while a log-normal distribution is used for positively defined parameters, such as luminosity. To test a hypothesised value of μ, the profile likelihood ratio is constructed as

$$\lambda(\mu) = \frac{L(\mu, \hat{\hat{\boldsymbol{\theta}}})}{L(\hat{\mu}, \hat{\boldsymbol{\theta}})}. \tag{4.14}$$

$L(\mu, \hat{\hat{\boldsymbol{\theta}}})$ is the conditional maximum-likelihood estimator, where $\hat{\hat{\boldsymbol{\theta}}}$ maximises L for a specified μ, while $L(\hat{\mu}, \hat{\boldsymbol{\theta}})$ is the unconditional maximum-likelihood estimator, where $\hat{\mu}$ and $\hat{\boldsymbol{\theta}}$ maximise L. The profile likelihood ratio lies within the range of $0 \leq \lambda \leq 1$, with λ values close to 1 indicating good agreement between the data and the hypothesised value of μ. Based on the profile likelihood ratio, the test statistic, t_μ, is defined as

$$t_\mu = -2 \ln \lambda(\mu). \tag{4.15}$$

Lower values of t_μ correspond to better agreement between the data and the hypothesis. To quantify the level of agreement, the p-value is calculated for a given μ value (p_μ) as

$$p_\mu = \int_{t_\mu^{\text{obs}}}^{\infty} f(t_\mu|\mu)\ dt_\mu, \tag{4.16}$$

where t_μ^{obs} denotes the value of t_μ observed from the data and $f(t_\mu|\mu)$ is the probability density function of t_μ under the assumption of the signal strength μ. In the presence of a new signal, signal strength is assumed to be non-negative, $\mu \geq 0$. In this case, a modified profile likelihood ratio, $\tilde{\lambda}(\mu)$, is defined as

$$\tilde{\lambda}(\mu) = \begin{cases} \frac{L(\mu, \hat{\hat{\boldsymbol{\theta}}}(\mu))}{L(\hat{\mu}, \hat{\boldsymbol{\theta}})} & \hat{\mu} \geq 0, \\ \frac{L(\mu, \hat{\hat{\boldsymbol{\theta}}}(\mu))}{L(0, \hat{\hat{\boldsymbol{\theta}}}(0))} & \hat{\mu} < 0. \end{cases} \tag{4.17}$$

Similarly, a modified test statistic, $\tilde{t}_\mu$, is constructed as

$$\tilde{t}_\mu = -2 \ln \tilde{\lambda}(\mu) = \begin{cases} -2 \ln \frac{L(\mu, \hat{\hat{\boldsymbol{\theta}}}(\mu))}{L(\hat{\mu}, \hat{\boldsymbol{\theta}})} & \hat{\mu} \geq 0, \\ -2 \ln \frac{L(\mu, \hat{\hat{\boldsymbol{\theta}}}(\mu))}{L(0, \hat{\hat{\boldsymbol{\theta}}}(0))} & \hat{\mu} < 0. \end{cases} \tag{4.18}$$

A special case of the statistic $\tilde{t}_\mu$, denoted as q_0, is used for the discovery of a positive signal. It tests a background-only hypothesis, $\mu = 0$, which leads to the following formula:

$$q_0 = \tilde{t}_0 = \begin{cases} -2 \ln \lambda(0) & \hat{\mu} \geq 0, \\ 0 & \hat{\mu} < 0. \end{cases} \tag{4.19}$$

The corresponding p-value, p_0, can be expressed as

$$p_0 = \int_{q_0^{\text{obs}}}^{\infty} f(q_0|0)\ dq_0, \tag{4.20}$$

where $f(q_0|0)$ represents the probability density function of the statistic q_0 under the assumption of the background-only hypothesis. The p-value is often translated to the signal significance,

$$Z = \Phi^{-1}(1 - p), \tag{4.21}$$

where Φ^{-1} is the inverse of the cumulative distribution of the standard Gaussian. It can be interpreted as a Gaussian-distributed variable found Z standard deviations above its mean. Significance exceeding five standard deviations is considered an appropriate level to reject the background-only hypothesis and constitute a discovery.

4.8.2 Fit strategy

In the $t\bar{t}$ measurement, the signal strength $\mu_{t\bar{t}}$ is determined as the ratio of the observed $t\bar{t}$ cross section in the combined ℓ+jets and dilepton channels to the SM expectation with no nPDF effects involved. A profile-likelihood fit to $H_{\mathrm{T}}^{\ell,j}$ distributions is performed simultaneously in the six signal regions described in Section 4.4, where $H_{\mathrm{T}}^{\ell,j}$ is defined as the scalar sum of lepton and jet p_{T}.

Figure 4.11 presents $H_{\mathrm{T}}^{\ell,j}$ distributions in each of the six signal regions before the fit (pre-fit). Reasonable agreement is observed between data and the sum of predictions within total uncertainties, indicated by the hatched area. The highest number of $t\bar{t}$ candidates is found in events with at least two b-tagged jets in the ℓ+jets channel, while the events with at least two b-tagged jets in the dilepton decay mode are characterised by the best signal purity.

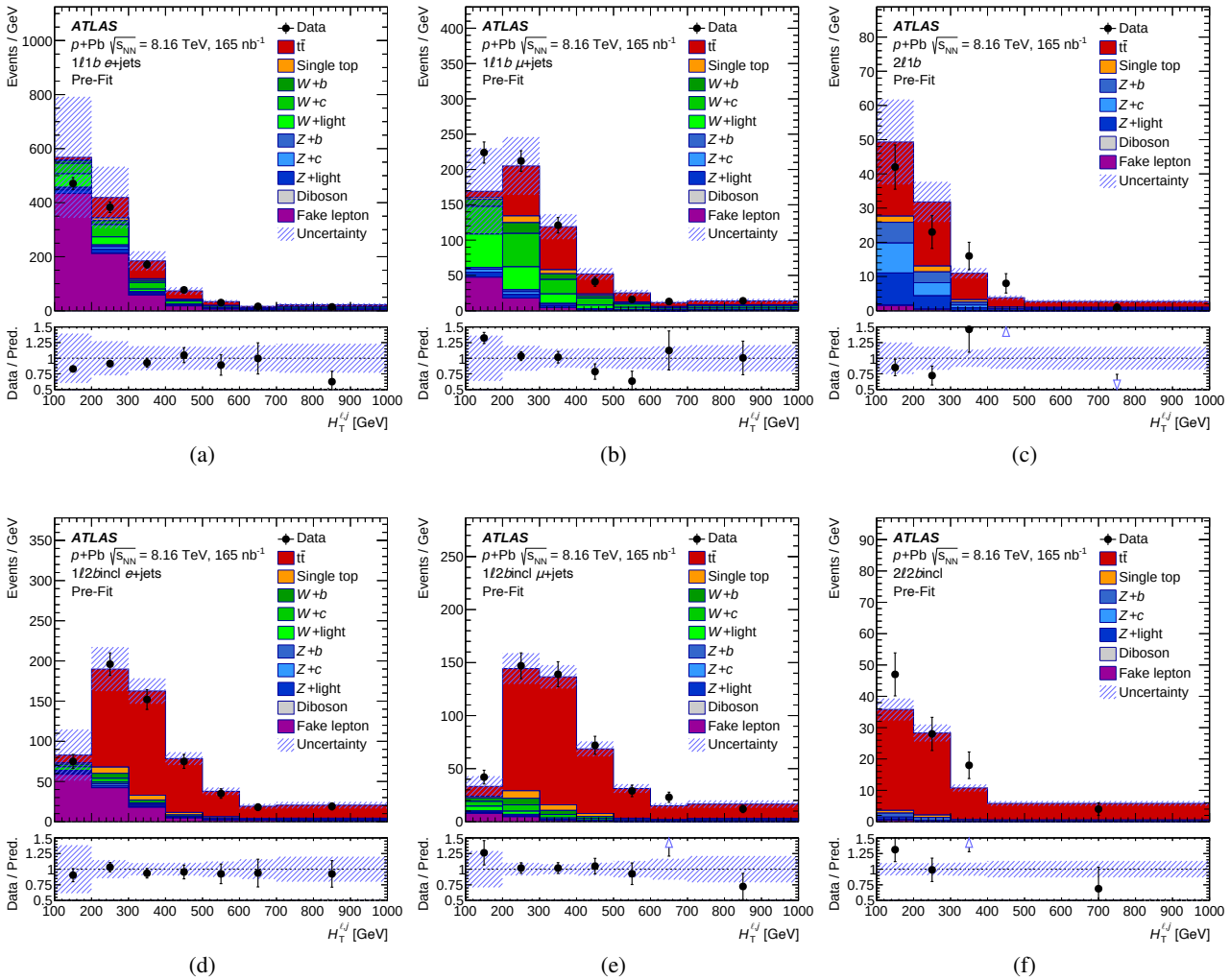

Figure 4.11: Comparison of data and total pre-fit prediction for the $H_{\mathrm{T}}^{\ell,j}$ distribution in each of the six signal regions (e+jets: (a) $1\ell1b$ and (d) $1\ell2b$incl, μ+jets: (b) $1\ell1b$ and (e) $1\ell2b$incl, dilepton: (c) $2\ell1b$ and (f) $2\ell2b$incl), with uncertainties represented by the hatched area. The full markers in the bottom panels show a ratio of data and a sum of predictions. Arrows indicate bins with entries that are outside the ratio range [39].

4.8.3 Fit results

In the fitting procedure, the nuisance parameters are allowed to shift from their expected values of zero to achieve the best agreement between the data and the sum of predictions. It leads to an improved description of data and a reduction of the total systematic uncertainty after the fit (post-fit) in the $H_{\mathrm{T}}^{\ell,j}$ distributions in the six signal regions, as shown in Figure 4.12. This effect can also be observed in a comparison between data and predicted event yields in each signal region before and after the fit in Figure 4.13.

Tables 4.3 and 4.4 show data and predicted pre- and post-fit event yields in the six signal regions of the fit. Owing to rounding effects and small correlations between the different sources of uncertainties, the total systematic uncertainty is different from the sum in quadrature of the individual sources.

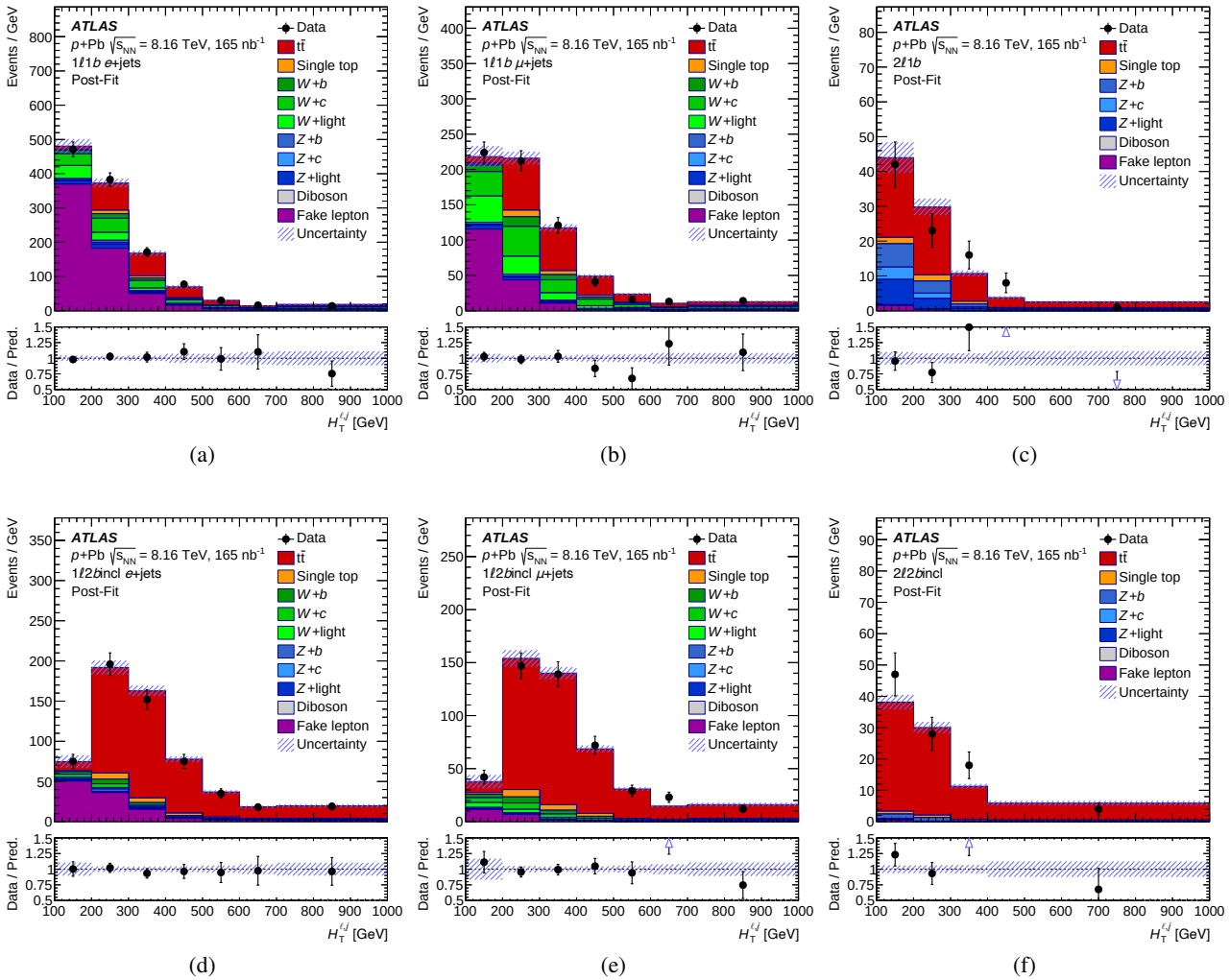

Figure 4.12: Comparison of data and total post-fit prediction for the $H_{\mathrm{T}}^{\ell,j}$ distribution in each of the six signal regions (e+jets: (a) $1\ell 1b$ and (d) $1\ell 2b$incl, μ+jets: (b) $1\ell 1b$ and (e) $1\ell 2b$incl, dilepton: (c) $2\ell 1b$ and (f) $2\ell 2b$incl), with uncertainties represented by the hatched area. The full markers in the bottom panels show a ratio of data and a sum of predictions. Arrows indicate bins with entries that are outside the ratio range [39].

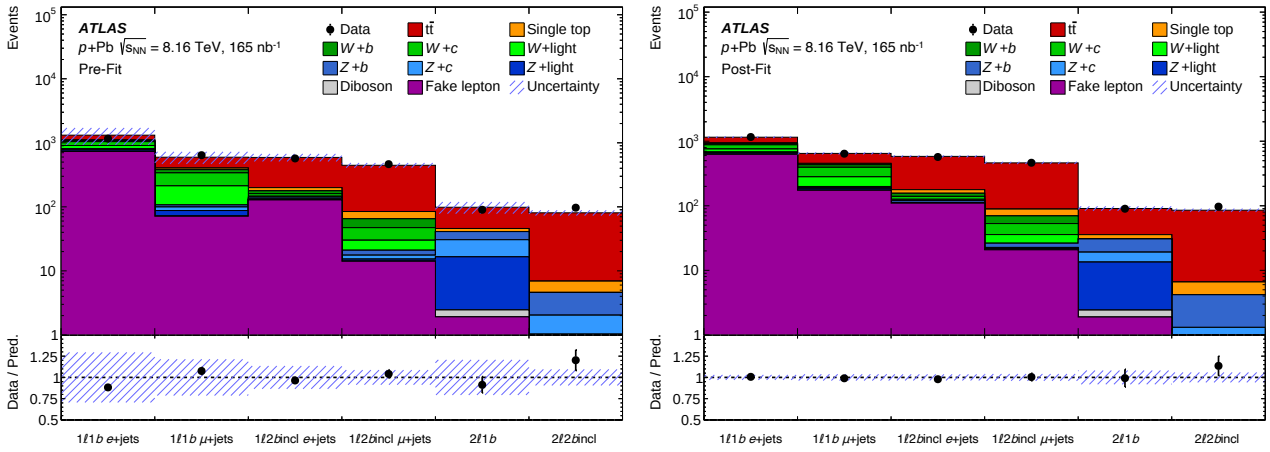

(a) (b)

Figure 4.13: Data and predicted (a) pre-fit and (b) post-fit event yields in each of the six signal regions. The total uncertainties in the sum of the signal and background are represented by the blue hatched band. The bottom panels show the ratio of the data and prediction [39].

The signal strength is extracted from the combined fit to $H_{\mathrm{T}}^{\ell,j}$ distributions in the six signal regions. The observed $\mu_{t\bar{t}}$ value with statistical and systematic uncertainties amounts to

$$\mu_{t\bar{t}} = 1.042\ ^{+0.037}_{-0.036}\ (\mathrm{stat.})\ ^{+0.087}_{-0.080}\ (\mathrm{syst.}) = 1.042\ ^{+0.094}_{-0.088}\ (\mathrm{tot.}). \tag{4.22}$$

Figure 4.14 displays the observed $\mu_{t\bar{t}}$ values obtained from the individual fits in each signal region and in the combined fit. $\mu_{t\bar{t}}$ values in all signal regions are consistent with each other and the SM prediction, $\mu_{t\bar{t}} = 1$, within the total uncertainties. The total uncertainty in $\mu_{t\bar{t}}$ is dominated by the systematic component in the ℓ+jets

Table 4.3: Data and predicted pre-fit event yields in the six signal regions. The total uncertainty is a quadrature sum of statistical and systematic uncertainties.

Region	**1ℓ1b e+jets**	**1ℓ1b μ+jets**	**1ℓ2$b$incl e+jets**	**1ℓ2$b$incl μ+jets**	**2ℓ1b**	**2ℓ2$b$incl**
$t\bar{t}$	211 ± 18	193 ± 16	392 ± 30	361 ± 27	52.7 ± 3.5	74 ± 7
t-channel	7.1 ± 1.0	6.7 ± 1.1	7.9 ± 1.0	7.2 ± 0.9	0 ± 0	0 ± 0
W+b	41 ± 21	41 ± 21	17 ± 9	18 ± 9	–	–
W+c	130 ± 70	130 ± 70	14 ± 8	17 ± 9	–	–
W+light	100 ± 60	110 ± 60	5 ± 4	9 ± 6	–	–
Z+b	15 ± 15	8 ± 8	8 ± 8	3.4 ± 3.5	10 ± 10	2.6 ± 2.6
Z+c	24 ± 24	12 ± 12	4 ± 4	2.3 ± 2.4	14 ± 14	1.0 ± 1.0
Z+light	36 ± 20	16 ± 9	1.7 ± 2.2	1.1 ± 0.8	14 ± 8	0.5 ± 0.4
Diboson	0.33 ± 0.17	0.30 ± 0.15	0.055 ± 0.030	0.040 ± 0.022	0.54 ± 0.28	0.048 ± 0.026
tW	17.1 ± 3.1	15.6 ± 2.9	13.7 ± 3.4	12.2 ± 3.1	4.9 ± 2.0	2.3 ± 1.2
Fake lepton	700 ± 400	70 ± 70	130 ± 70	14 ± 14	1.9 ± 1.4	0.5 ± 0.9
Total	1300 ± 400	600 ± 130	590 ± 80	450 ± 40	99 ± 20	81 ± 8
Data	1162	641	570	464	90	97

Table 4.4: Data and predicted post-fit event yields in the six signal regions. The total uncertainty is a quadrature sum of statistical and systematic uncertainties.

Region	**1ℓ1b e+jets**	**1ℓ1b μ+jets**	**1ℓ2$b$incl e+jets**	**1ℓ2$b$incl μ+jets**	**2ℓ1b**	**2ℓ2$b$incl**
$t\bar{t}$	214 ± 24	194 ± 21	405 ± 21	373 ± 19	55 ± 6	79 ± 5
t-channel	6.9 ± 1.0	6.4 ± 1.0	7.7 ± 0.9	7.1 ± 0.9	0 ± 0	0 ± 0
W+b	37 ± 19	37 ± 19	16 ± 8	17 ± 9	–	–
W+c	120 ± 40	110 ± 40	14 ± 7	17 ± 8	–	–
W+light	80 ± 40	80 ± 40	4.8 ± 3.1	9 ± 5	–	–
Z+b	16 ± 13	8 ± 7	8 ± 7	3.7 ± 3.0	12 ± 9	2.9 ± 2.4
Z+c	9 ± 14	5 ± 7	1.7 ± 2.6	0.9 ± 1.4	6 ± 9	0.4 ± 0.6
Z+light	28 ± 16	12 ± 7	1.2 ± 1.1	0.9 ± 0.5	11 ± 6	0.34 ± 0.25
Diboson	0.32 ± 0.16	0.29 ± 0.15	0.055 ± 0.029	0.039 ± 0.02	0.53 ± 0.27	0.049 ± 0.025
tW	17.1 ± 3.0	15.5 ± 2.7	13.6 ± 3.2	12.1 ± 2.9	5.1 ± 2	2.4 ± 1.2
Fake lepton	630 ± 50	170 ± 40	110 ± 19	21 ± 12	1.9 ± 1	0.51 ± 0.27
Total	1154 ± 34	648 ± 24	582 ± 21	462 ± 18	91 ± 7	85 ± 5
Data	1162	641	570	464	90	97

channel and the statistical component in the dilepton final state. The background-only hypothesis is rejected with a significance exceeding five standard deviations, resulting in the observation of $t\bar{t}$ production in p+Pb collisions in the ATLAS experiment. The observed significance is above five standard deviations separately in ℓ+jets and dilepton final states, leading to the first observation of the $t\bar{t}$ process in the dilepton channel in p+Pb collisions.

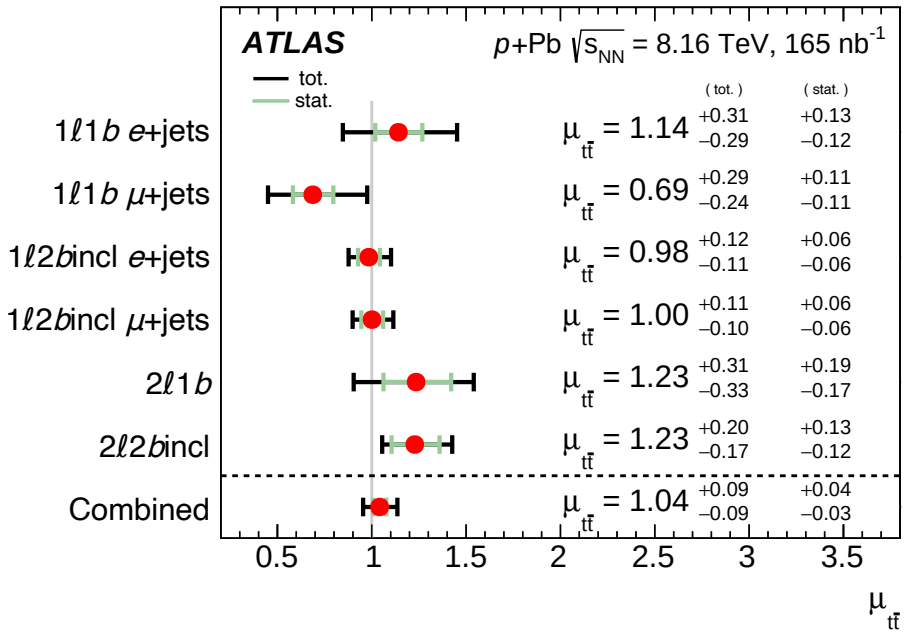

Figure 4.14: Observed best-fit values of $\mu_{t\bar{t}}$ with statistical and systematic uncertainties in each signal region and in the combined fit [39].

Systematic uncertainties in the fit are treated as correlated over the signal regions, unless stated otherwise in Section 4.7. A breakdown of relative systematic uncertainties on the $\mu_{t\bar{t}}$ value is summarised in Table 4.5. The uncertainties are obtained by repeating the fit with a group of nuisance parameters fixed to their fitted values and subtracting in quadrature the resulting total uncertainty from the uncertainty of the complete fit. This approach neglects correlations between the different groups, leading to a different total uncertainty than the quadratic sum of the grouped impacts. The leading contribution to the total systematic uncertainty arises from the jet energy scale, followed by signal $t\bar{t}$ modelling. The total relative systematic uncertainty in the measurement amounts to 8%.

Table 4.5: Summary of the impact of the systematic uncertainties on $\mu_{t\bar{t}}$ grouped into different categories and combined [39].

Source	$\Delta\sigma_{t\bar{t}}/\sigma_{t\bar{t}}$	
	Up unc. [%]	**Down unc. [%]**
Jet energy scale	+4.6	-4.1
$t\bar{t}$ generator	+4.5	-4.0
Fake-lepton background	+3.1	-2.8
Background	+3.1	-2.6
Luminosity	+2.8	-2.5
Muon uncertainties	+2.3	-2.0
W+jets	+2.2	-2.0
b-tagging	+2.1	-1.9
Electron uncertainties	+1.8	-1.5
MC statistical uncertainties	+1.1	-1.0
Jet energy resolution	+0.4	-0.4
$t\bar{t}$ PDF	+0.1	-0.1
Systematic uncertainty	**+8.3**	**-7.6**

The impact of the 20 most significant systematic uncertainties on the fitted signal strength ($\hat{\mu}$) is presented in Figure 4.15. The filled boxes show variations of $\hat{\mu}$ from the central value ($\Delta\hat{\mu}$) when fixing the corresponding individual nuisance parameter (θ) to its post-fit value ($\hat{\theta}$) modified upwards or downwards by its post-fit uncertainty ($\Delta\hat{\theta}$), while the empty boxes represent the corresponding pre-fit impact. The black points show shifts in fitted values of the nuisance parameters ($\hat{\theta} - \theta_0$) relative to their pre-fit uncertainties ($\Delta\theta$). The black error bars represent post-fit uncertainties of the nuisance parameters relative to their nominal uncertainties, indicated by the dashed line. The leading systematic components include fake-lepton background variations and signal $t\bar{t}$ modelling. The uncertainties related to the fake-lepton background are significantly constrained during the fitting procedure.

The correlations between all nuisance parameters are also studied. Figure 4.16 displays correlations for parameters with at least one correlation value above 30%. The largest correlation of 64% is observed for the

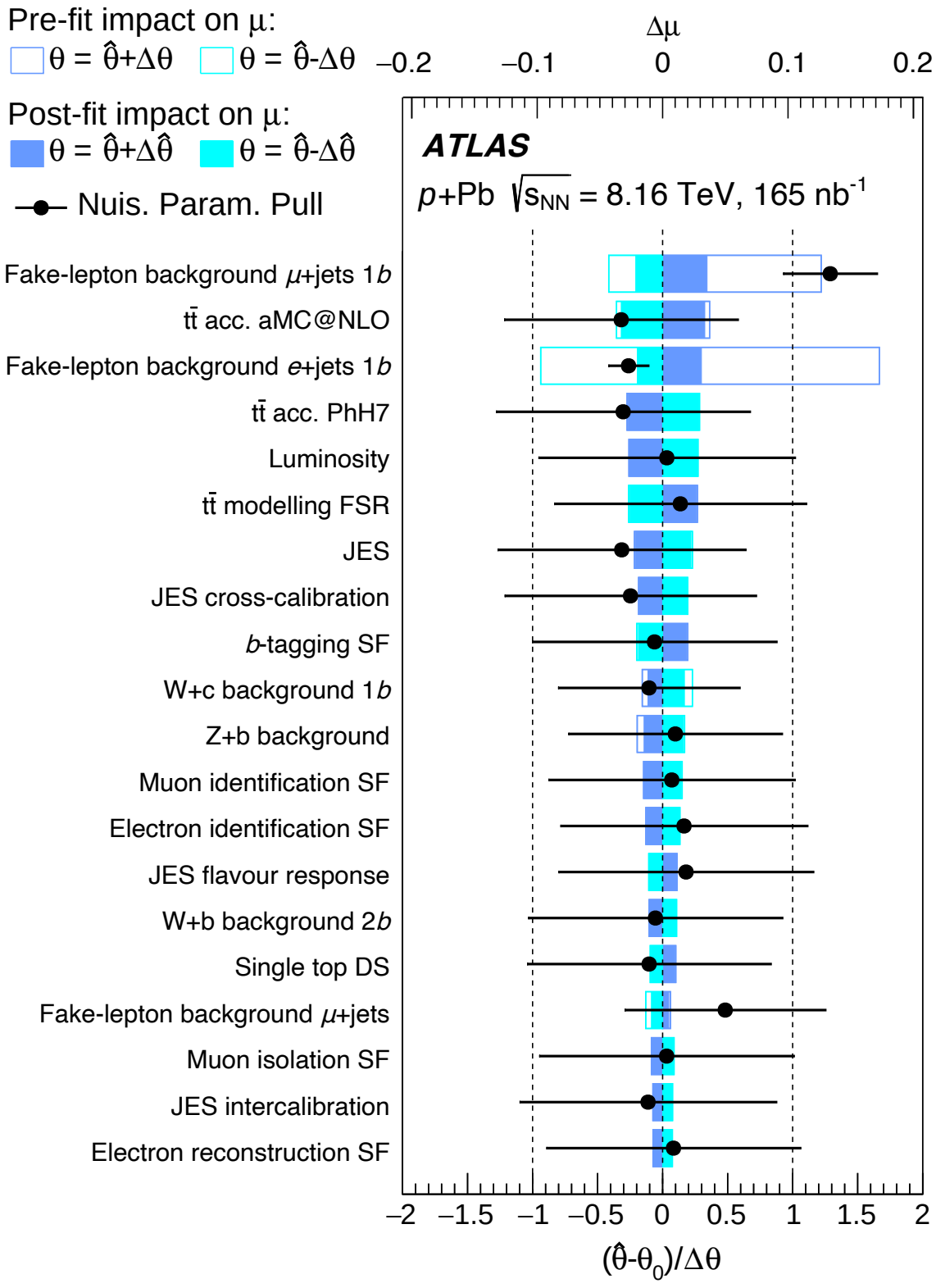

Figure 4.15: The impact of systematic uncertainties on the fitted signal strength [39].

fake-lepton background normalisation in e+jets and μ+jets final states. The largest anticorrelation of -55% is found between the W+jets and fake-lepton background normalisation components.

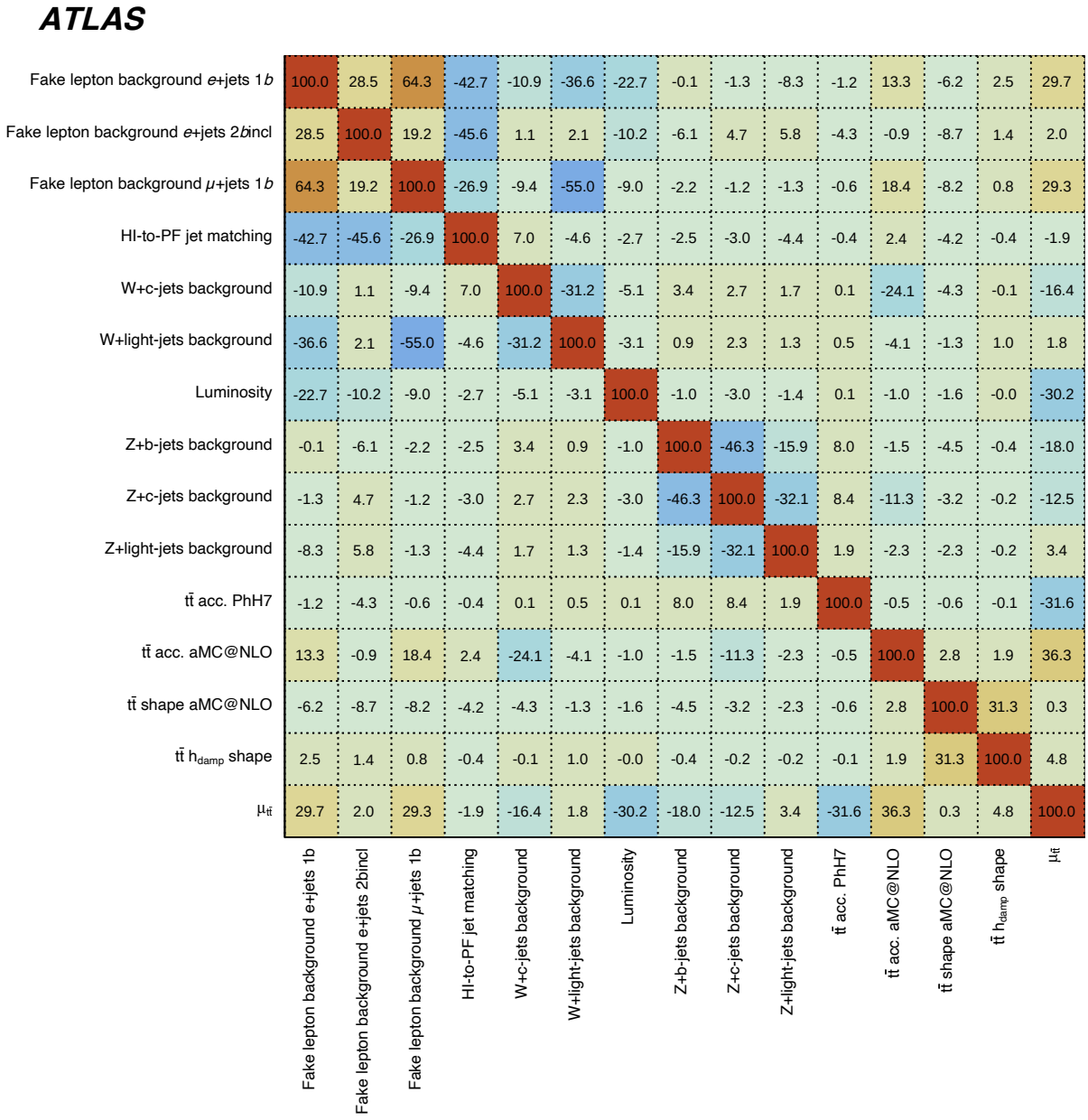

Figure 4.16: Correlation matrix of the fit parameters with at least one correlation value greater than 30% [39].

4.9 Control distributions

4.9.1 Hadronically decaying W boson

Reconstructed hadronically decaying W bosons are studied in the ℓ+jets channel, split into two lepton flavours and two b-tagged jet categories. The mass of the hadronic W-boson is constructed from two highest-p_{T} jets, which are not b-tagged. Figure 4.17 shows mass distributions of the hadronically decaying W-boson candidates in the four signal regions. A distinct peak at around 80 GeV is observed, consistent with the W-boson mass. Good agreement is observed between the data and the sum of predictions.

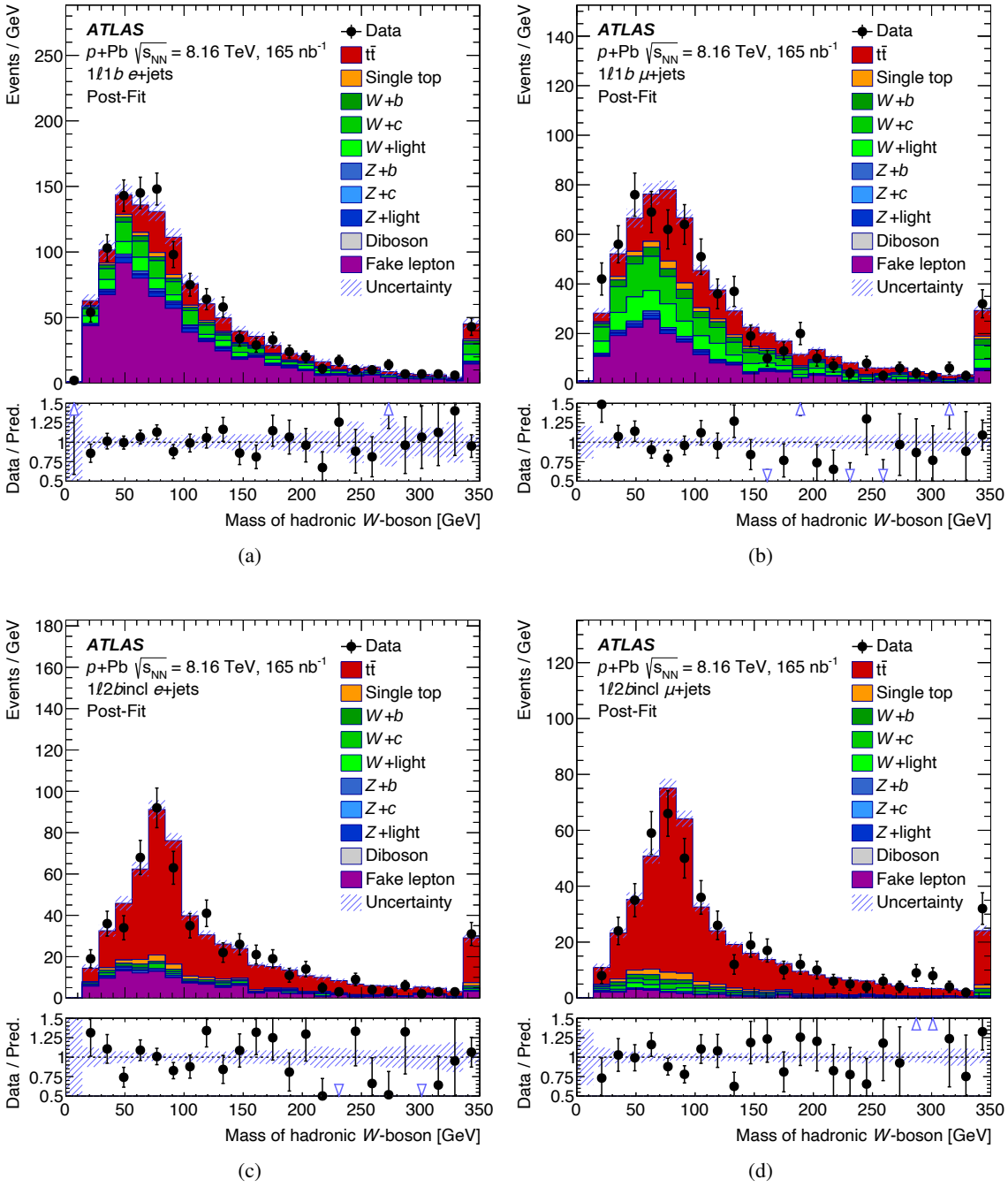

Figure 4.17: Post-fit mass distributions of the reconstructed hadronically decaying W-boson candidates in the four signal regions (e+jets: (a) $1\ell 1b$ and (c) $1\ell 2b$incl, μ+jets: (b) $1\ell 1b$ and (d) $1\ell 2b$incl). Post-fit uncertainties are represented by the hatched area. The full markers in the bottom panels show a ratio of data and a sum of predictions. Open triangles indicate bins with entries that are outside the ratio range. The last bin includes overflow events [39].

4.9.2 Hadronically decaying top quark

Reconstructed hadronically decaying top quarks are also examined in the ℓ+jets decay mode, categorised by lepton flavour and b-tagged jet multiplicity. The mass of the hadronic top quark is constructed from two highest-

p_{T} jets, which are not b-tagged, and the b-tagged jet, which is angularly farther from the lepton. Figure 4.18 presents mass distributions of the hadronically decaying top-quark candidates in the four signal regions. In events with at least two b-tagged jets, an evident peak at around 170 GeV is found, which corresponds to the top-quark mass. The data distributions are consistent with the sum of predictions within total uncertainties.

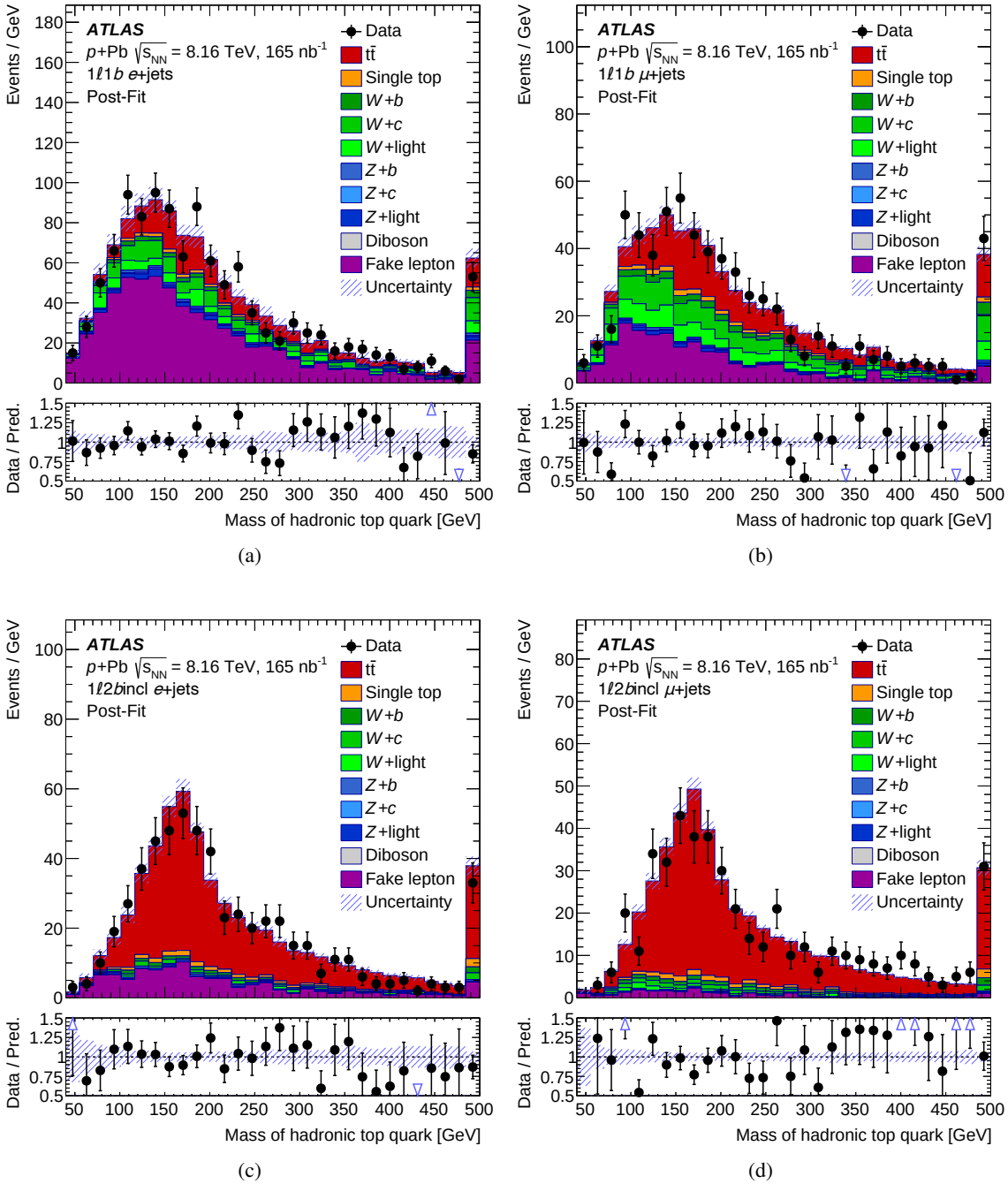

Figure 4.18: Post-fit mass distributions of the reconstructed hadronically decaying top-quark candidates in the four signal regions (e+jets: (a) $1\ell 1b$ and (c) $1\ell 2b$incl, μ+jets: (b) $1\ell 1b$ and (d) $1\ell 2b$incl). Post-fit uncertainties are represented by the hatched area. The full markers in the bottom panels show a ratio of data and a sum of predictions. Open triangles indicate bins with entries that are outside the ratio range. The last bin includes overflow events [39].

4.10 Results

4.10.1 Inclusive integrated cross section

The measured $\mu_{t\bar{t}}$ value is converted into the $t\bar{t}$ production cross section in p+Pb collisions, $\sigma_{t\bar{t}}^{p+\mathrm{Pb}}$, using the following formula:

$$\sigma_{t\bar{t}}^{p+\mathrm{Pb}} = \mu_{t\bar{t}} \cdot A_{\mathrm{Pb}} \cdot \sigma_{t\bar{t}}^{\mathrm{th}}, \tag{4.23}$$

where $A_{\mathrm{Pb}} = 208$ denotes the lead mass number and $\sigma_{t\bar{t}}^{\mathrm{th}} = 268$ pb is the inclusive theoretical $t\bar{t}$ cross section in nucleon–nucleon collisions calculated at NNLO precision in QCD. The measured $t\bar{t}$ cross section in p+Pb collisions at $\sqrt{s_{\mathrm{NN}}} = 8.16$ TeV with statistical and systematic uncertainties amounts to

$$\sigma_{t\bar{t}}^{p+\mathrm{Pb}} = 58.1 \pm 2.0\ (\mathrm{stat.})\ ^{+4.8}_{-4.4}\ (\mathrm{syst.})\ \mathrm{nb} = 58.1\ ^{+5.2}_{-4.9}\ (\mathrm{tot.})\ \mathrm{nb}. \tag{4.24}$$

The total relative uncertainty amounts to 9% and is dominated by the systematic component, resulting in the most precise $t\bar{t}$ cross-section measurement in heavy-ion collisions to date.

The observed $t\bar{t}$ cross section is compared with predictions based on four different nPDF sets: EPPS21 [40], nNNPDF3.0 [41], nCTEQ15HQ [167], and TUJU21 [43]. Theoretical values are calculated at NLO precision using the `MCFM` code [168] and scaled to the p+Pb system by A_{Pb}. Predictions are adjusted to NNLO precision in QCD using the K-factor$= 1.139$, derived using the TOP++ V2 program. Table 4.6 summarises theoretical $t\bar{t}$ cross sections in p+Pb collisions with total uncertainties for the four nPDF sets.

Table 4.6: Theoretical predictions of the $t\bar{t}$ cross section in p+Pb collisions based on four nPDF sets.

nPDF set	$\boldsymbol{\sigma_{t\bar{t}}^{p+\mathrm{Pb}}}$ **[nb]**
TUJU21	$58.3\ ^{+2.2}_{-2.5}$
nNNPDF3.0	$67.1\ ^{+2.0}_{-2.0}$
nCTEQ15HQ	$58.4\ ^{+5.0}_{-5.0}$
EPPS21	$60.4\ ^{+5.6}_{-3.8}$

The measured $t\bar{t}$ cross section is contrasted with the latest theoretical predictions and other experimental results in Figure 4.19. The measurement is in agreement with predictions based on the four nPDF sets. The nNNPDF3.0 nPDF set shows the largest discrepancy, as it does not incorporate the recent Run 2 LHC data on heavy-flavour production in p+Pb collisions [169]. The result is consistent with the $t\bar{t}$ cross section measured by CMS, using the ℓ+jets channel of $t\bar{t}$ decay [74]. The measurement is also in agreement within one standard deviation with the combined $t\bar{t}$ cross section in pp collisions at $\sqrt{s} = 8$ TeV by ATLAS and CMS [72]. The result in pp collisions is scaled to the p+Pb system by A_{Pb} and extrapolated from $\sqrt{s} = 8$ TeV to $\sqrt{s} = 8.16$ TeV using the extrapolation factor of $1.0528 \pm 0.0005\ (\mathrm{PDF})\ ^{+0.0001}_{-0.0013}\ (\mathrm{scale})$.

4.10.2 Nuclear modification factor

The nuclear modification factor, $R_{p\mathrm{A}}$, for $t\bar{t}$ production in p+Pb collisions is defined as the ratio of the $t\bar{t}$ cross section in p+Pb collisions to the geometric expectation from the pp system, expressed by the formula

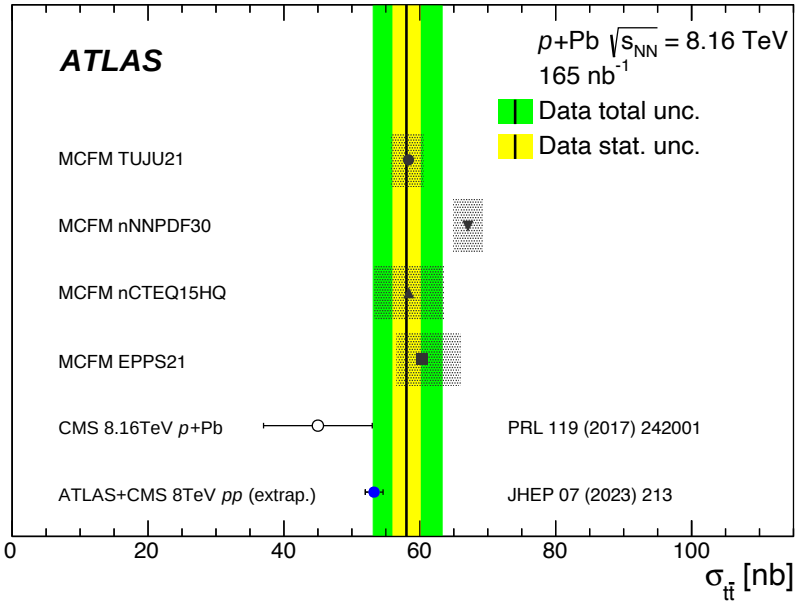

Figure 4.19: Comparison between measured and predicted values of $\sigma_{t\bar{t}}$. The result, represented by the solid black line, is compared with the measurement in p+Pb collisions at $\sqrt{s_{\mathrm{NN}}} = 8.16$ TeV by CMS, and the combined measurement in pp collisions at $\sqrt{s} = 8$ TeV by ATLAS and CMS. The latter is extrapolated to the centre-of-mass energy of this measurement and scaled by A_{Pb}. Predictions based on four nPDF sets are calculated at NNLO precision in QCD and scaled to the p+Pb system [39].

$$R_{p\mathrm{A}} = \frac{\sigma_{t\bar{t}}^{p+\mathrm{Pb}}}{A_{\mathrm{Pb}} \cdot \sigma_{t\bar{t}}^{pp}}. \tag{4.25}$$

$\sigma_{t\bar{t}}^{pp}$ stands for the combined $t\bar{t}$ cross section in pp collisions at $\sqrt{s} = 8$ TeV by ATLAS and CMS [72], extrapolated to the centre-of-mass energy of this measurement. All uncertainties in the cross-section measurements in the p+Pb and pp systems are treated as uncorrelated. The resulting $R_{p\mathrm{A}}$ value is measured to be

$$R_{p\mathrm{A}} = 1.090 \pm 0.039\ (\mathrm{stat.})\ ^{+0.094}_{-0.087}\ (\mathrm{syst.}) = 1.090 \pm 0.100\ (\mathrm{tot.}) \tag{4.26}$$

The $R_{p\mathrm{A}}$ value is observed to be one standard deviation above unity, which could hint at an enhancement of $t\bar{t}$ production in p+Pb collisions compared to the geometric expectation from the pp system.

An alternative approach to the $R_{p\mathrm{A}}$ calculation is studied, using the $t\bar{t}$ cross section in pp collisions at $\sqrt{s} = 8$ TeV in Run 1 by ATLAS [170], extrapolated to the centre-of-mass energy of this measurement, as the reference cross section $\sigma_{t\bar{t}}^{pp}$ in Equation 4.25. Due to significant differences in the software versions between Run 1 and Run 2, only two systematic components, $t\bar{t}$ modelling and the flavour composition in jet calibration, are found to be fully correlated between the measurements in the pp and p+Pb systems. In the presence of fully correlated systematic uncertainties, the total relative systematic uncertainty on $R_{p\mathrm{A}}$ is reduced as follows:

$$(\delta_{\mathrm{tot}}^{R_{p\mathrm{A}}})^2 = (\delta_{\mathrm{tot}}^{p+\mathrm{Pb}})^2 + (\delta_{\mathrm{tot}}^{pp})^2 - 2\,\delta_{\mathrm{corr}}^{p+\mathrm{Pb}}\,\delta_{\mathrm{corr}}^{pp}, \tag{4.27}$$

where $\delta_{\mathrm{tot}}^{p+\mathrm{Pb}}$ ($\delta_{\mathrm{tot}}^{pp}$) and $\delta_{\mathrm{corr}}^{p+\mathrm{Pb}}$ ($\delta_{\mathrm{corr}}^{pp}$) represent the total and fully correlated relative systematic uncertainties in p+Pb (pp) collisions, respectively. The resulting nuclear modification factor in this scenario amounts to

$R_{p\mathrm{A}} = 1.092 \pm 0.039\ (\mathrm{stat.})\ ^{+0.089}_{-0.082}\ (\mathrm{syst.}) = 1.092\ ^{+0.097}_{-0.091}\ (\mathrm{tot.})$. The precision of this result is comparable to that obtained using the combined $t\bar{t}$ cross section by ATLAS and CMS [72], which has a lower uncertainty than the ATLAS-only measurement [170]. Given the negligible improvement at the sub-percent level and the potential differences in systematic uncertainties between this analysis and the measurement in pp collisions in Run 1, the $R_{p\mathrm{A}}$ value in Equation 4.26 is presented as the final result.

The observed $R_{p\mathrm{A}}$ value is contrasted with predictions based on the four nPDF sets. Theoretical values are derived from $t\bar{t}$ cross sections in p+Pb and pp collisions, computed at NNLO precision in QCD using the `MCFM` code with nPDF and corresponding baseline PDF sets, respectively. The uncertainty related to the baseline PDF for pp interactions is assumed to be fully correlated and cancels out in the ratio. Table 4.7 lists theoretical $R_{p\mathrm{A}}$ values with total uncertainties based on the four nPDF sets.

Table 4.7: Theoretical predictions of the nuclear modification factor based on four nPDF sets.

nPDF set	$\boldsymbol{R_{p\mathrm{A}}}$
TUJU21	$1.147\ ^{+0.054}_{-0.063}$
nNNPDF3.0	$1.251\ ^{+0.049}_{-0.049}$
nCTEQ15HQ	$1.107\ ^{+0.087}_{-0.087}$
EPPS21	$1.117\ ^{+0.109}_{-0.077}$

In Figure 4.20, the observed $R_{p\mathrm{A}}$ value is compared with theoretical predictions based on the four nPDF sets. The measured $R_{p\mathrm{A}}$ is consistent with the theoretical predictions for four nPDF sets. The largest difference of more than one standard deviation above the observed $R_{p\mathrm{A}}$ value is found for the nNNPDF3.0 nPDF set.

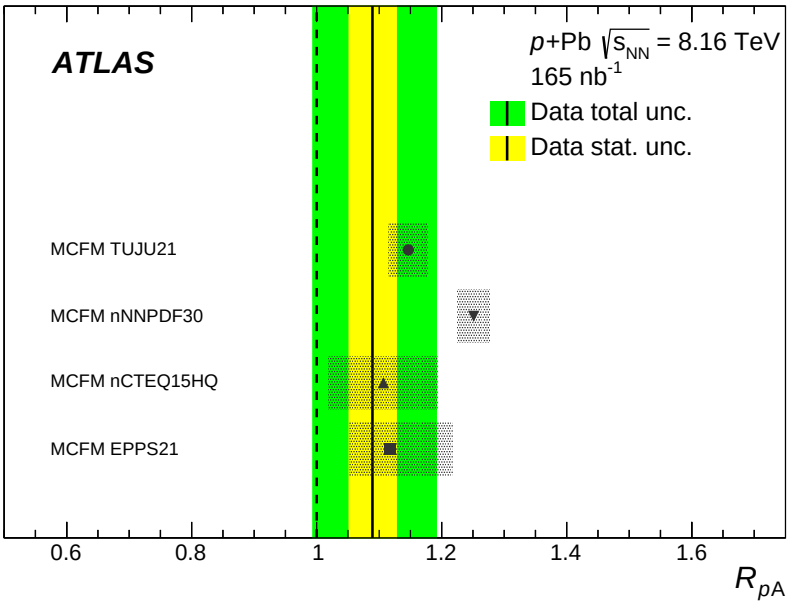

Figure 4.20: Comparison between measured and predicted values of $R_{p\mathrm{A}}$. The measurement, represented by the solid black line, is compared with theoretical predictions based on four nPDF sets, calculated at NNLO precision in QCD and scaled to the p+Pb system [39].

Chapter 5

Top-quark pair production in Pb+Pb collisions

5.1 Motivation

The top quark remains the only quark that has not yet been directly observed in Pb+Pb collisions with a significance of five standard deviations. As the heaviest elementary particle, top quarks are expected to offer new experimental insights into the QGP. Specifically, hadronically decaying W bosons from top-quark decays could be used to explore the time structure of the QGP. An observation of $t\bar{t}$ production in Pb+Pb collisions is a crucial first step toward enabling further studies of the QGP. Due to jet quenching in heavy-ion collisions, the dilepton decay mode, which has only two jets in the final state, is the most feasible channel for top-quark observation. Using the full Pb+Pb dataset recorded during Run 2 at $\sqrt{s_{\mathrm{NN}}} = 5.02$ TeV, $t\bar{t}$ production is measured with significance exceeding five standard deviations, leading to the first observation of this process in Pb+Pb collisions [171]. The inclusive $t\bar{t}$ cross section is extracted in the $e\mu$ channel and compared with theoretical predictions based on various nPDF sets. The measurement is published in Ref. [171], with a leading contribution by the Author of this thesis. The results were recognised as an Editors' Suggestion in Physical Review Letters [172] and featured as a Research Highlight in Nature [173].

5.2 Data

The discussed measurement is based on the full Pb+Pb dataset collected with the ATLAS detector during Run 2. The data taking took place in 2015 and 2018, providing a total integrated luminosity of 0.5 nb^{-1} and 1.4 nb^{-1}, respectively. The lead beams were configured with an energy of 2.51 TeV per nucleon, leading to a nucleon–nucleon centre-of-mass energy of $\sqrt{s_{\mathrm{NN}}} = 5.02$ TeV. The data were recorded under low-pileup conditions with an average pileup of $\langle\mu\rangle = 1.76 \cdot 10^{-3}$ and $\langle\mu\rangle = 2.58 \cdot 10^{-3}$ in 2015 and 2018, respectively.

Figure 5.1 shows an event display of a 2018 Pb+Pb collision with a $t\bar{t}$ candidate produced in the $e\mu$ channel. The event contains four jets (yellow cones), one electron (green line), and one muon (red line). Tracks of charged particles in the inner detector are visualised as orange lines. Green and yellow rectangles correspond to energy

deposits in cells of the EM and hadronic calorimeter, respectively. Muon chambers in the barrel region are represented as transparent blue boxes with detailed measurements shown within as green lines.

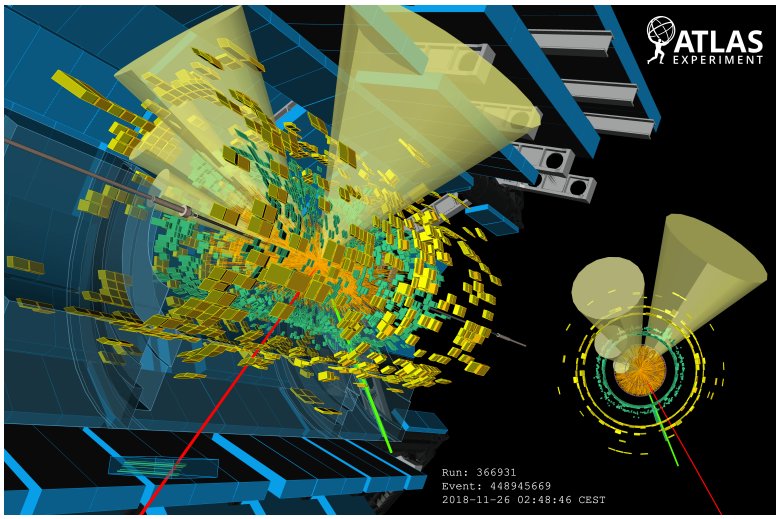

Figure 5.1: Event display of a Pb+Pb collision at $\sqrt{s_{\mathrm{NN}}} = 5.02$ TeV collected in 2018, containing a $t\bar{t}$ candidate.

5.3 Simulation

MC simulation is employed to evaluate signal and background yields and deliver predictions for comparison with the data. MC simulation samples are produced with the full ATLAS detector simulation [121], utilising the GEANT4 framework [122]. Four datasets are generated for each process, covering all isospin combinations: proton–proton, proton–neutron, neutron–proton, and neutron–neutron. Simulated nucleon–nucleon interactions are embedded into HIJING [136] minimum-bias Pb+Pb events for underlying-event modelling. To match the centrality distribution in data, MC events are reweighted to the shape of the FCal ΣE_{T} distribution in data, normalised to unity after the selection described in Section 5.4, as shown in Figure 5.2. All MC samples are normalised to their predicted cross sections at $\sqrt{s_{\mathrm{NN}}} = 5.02$ TeV, obtained at NNLO precision in QCD for the signal $t\bar{t}$ process and NLO precision in QCD for the background contributions. The EVTGEN [139] program is used in datasets generated with POWHEG BOX V2 [123] to simulate decays of b- and c-flavoured hadrons. In particular, particle interactions with the QGP are not modelled in MC simulation. All MC simulation samples employed in the analysis, including their parameters are listed in Table 5.1.

5.3.1 $t\bar{t}$ simulation

Nominal signal $t\bar{t}$ samples are produced at NLO precision in QCD with POWHEG BOX V2 MC generator for the ME, interfaced with PYTHIA8 [124] as the PS model, using NNPDF3.0NNLO [141] PDF set and the A14 [135] set of tuned parameters. The resummation damping parameter, h_{damp}, amounts to $1.5m_t$, where $m_t = 172.5$ GeV is the top-quark mass. The $t\bar{t}$ MC samples are normalised to the NNLO + NNLL theoretical cross section, derived using the TOP++ V2 [142] program.

Systematic uncertainties in signal modelling are assessed using three alternative signal $t\bar{t}$ datasets. Uncertainties related to PS radiation are evaluated by changing the h_{damp} parameter to $3m_t$. The uncertainty in the ME and

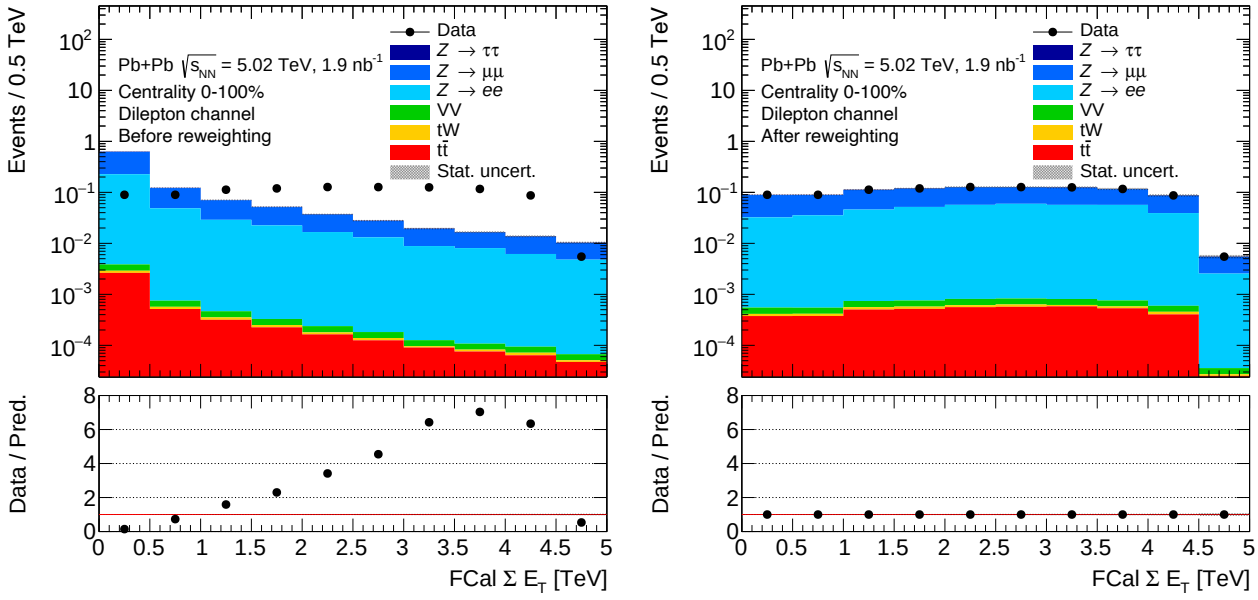

(a) (b)

Figure 5.2: Distributions of FCal ΣE_{T} in data and a sum of predictions (a) before and (b) after applying the centrality reweighting.

PS matching is obtained using an alternative POWHEG BOX v2 + PYTHIA8 dataset with the internal pTHARD parameter of POWHEG BOX, which controls the phase-space region vetoed in the showering, set to 1 [174]. Another sample, generated using POWHEG BOX v2 and HERWIG v7.2 [143] with the H7.2-DEFAULT [144] set of tuned parameters, is used to estimate the uncertainty in PS modelling.

5.3.2 Single-top simulation

Single-top background samples cover the tW process, which has the largest contribution, while other processes are negligible given the limited statistics of the Pb+Pb data. tW MC datasets are generated with POWHEG BOX v2 + PYTHIA8, using the NNPDF3.0NNLO PDF set and the A14 set of tuned parameters. The diagram removal scheme [145] is used for the interference between the $t\bar{t}$ and tW final states.

Table 5.1: List of simulated samples for the $t\bar{t}$ analysis in Pb+Pb collisions.

Process	ME generator	PS model	ME PDF	Tune	Events
$t\bar{t}$ nominal	POWHEG v2	PYTHIA8	NNPDF3.0NNLO	A14	400k
$t\bar{t}$ $h_{\mathrm{damp}} = 3m_t$	POWHEG v2	PYTHIA8	NNPDF3.0NNLO	A14	400k
$t\bar{t}$ alternative ME	POWHEG v2	PYTHIA8	NNPDF3.0NNLO	A14 pTHARD=1	400k
$t\bar{t}$ alternative PS	POWHEG v2	HERWIG7	NNPDF3.0NNLO	H7.2-DEFAULT	400k
Single top tW	POWHEG v2	PYTHIA8	NNPDF3.0NNLO	A14	80k
Diboson VV	SHERPA v2.2.14		NNPDF3.0NNLO	–	200k
Z+jets	POWHEG v1	PYTHIA8	CTEQ6L1	AZNLO	600k

5.3.3 Diboson simulation

Diboson (VV) simulation consists of WW and ZZ production in association with jets, filtered for decays with two leptons and two neutrinos. Datasets are produced using SHERPA v2.2.14 [146] MC generator with the NNPDF3.0NNLO PDF set. MEs are computed at NLO precision in QCD for up to one parton and at LO precision for up to three partons [147].

5.3.4 Z-boson simulation

Vector-boson MC samples encompass Z-boson production, which has the dominant contribution in the dilepton channel of $t\bar{t}$ decays. The simulation covers Z-boson production in association with jets and leptonic Z-boson decays, $Z \to ee$, $Z \to \mu\mu$, and $Z \to \tau\tau$ with leptonically decaying τ-leptons. MC samples are generated using POWHEG BOX v1 [175] MC generator interfaced with PYTHIA8, using NNPDF3.0NNLO PDF set and the A14 set of tuned parameters.

5.4 Event selection

In the event selection, single-electron and single-muon triggers are used with minimum p_{T} requirements of 15 and 8 GeV, respectively [133, 148]. Events must have exactly one primary vertex, reconstructed from at least two good-quality charged-particle tracks with $p_{\mathrm{T}} > 0.5$ GeV [149]. To avoid contributions from photon-induced processes, only events in the 0–80% centrality interval are used [119]. Final states containing exactly two oppositely charged leptons, electrons or muons, are chosen and divided into categories with electron–electron (ee), muon–muon ($\mu\mu$), and electron–muon ($e\mu$) pairs, containing 5,718, 6,636, and 94 data events, respectively.

Events in the $e\mu$ channel are used in the main $t\bar{t}$ measurement. To minimise the fake-lepton background contribution, the invariant mass of the $e\mu$ pair, $m_{e\mu}$, is required to be above 30 GeV. Events must contain at least two jets with $p_{\mathrm{T}} > 35$ GeV. To minimise the impact of jet mismodelling in MC simulation, only a requirement on the number of jets is imposed and jet kinematics are not used in the discriminating variable for the $t\bar{t}$ cross-section measurement.

Same-flavour channels, ee and $\mu\mu$, are used for validation and performance studies. The invariant mass of the dilepton pair, m_{ee} or $m_{\mu\mu}$, must be within the Z-boson mass window of 66–116 GeV. No requirements on jets are imposed in the selection.

5.5 Object selection

5.5.1 Leptons

Electron candidates are built by pairing an EM cluster in the calorimeter with a track from the inner detector. Candidates have to originate from the primary vertex, meeting requirements on the impact parameters of $|d_0|/\sigma(d_0) < 5$ and $|\Delta z_0 \sin\theta| < 0.5$ mm. Electrons must have $p_{\mathrm{T}} > 18$ GeV and $|\eta| < 2.47$, and be identified using the LooseAandBLayer operating point [127]. Electron efficiency in MC simulation is corrected

using standard 13 TeV pp scale factors related to electron reconstruction and dedicated Pb+Pb scale factors for identification, isolation, and trigger.

Muon candidates are reconstructed using a reconstructed track in the MS matched to a track in the inner detector. Candidates have to be associated with the primary vertex, satisfying requirements on the impact parameters of $|d_0|/\sigma(d_0) < 3$ and $|\Delta z_0 \sin\theta| < 0.5$ mm. Muons must have $p_{\mathrm{T}} > 15$ GeV and $|\eta| < 2.5$, and pass Loose identification requirements [150]. Muon efficiency in MC simulation is corrected using standard 13 TeV pp scale factors related to muon reconstruction and track-to-vertex association and dedicated Pb+Pb scale factors for identification, isolation, and trigger.

Both lepton types are required to be isolated using fixed cuts on calorimeter and track isolation variables, described in Section 3.2.5. A ratio of the calorimeter isolation, $E^{\mathrm{isol}}_{\mathrm{T,cone}}$, and lepton p_{T} must be below 0.14, while a ratio of the track isolation, $p^{\mathrm{isol}}_{\mathrm{T,cone}}$, and lepton p_{T} has to be below 0.06. To account for the high-occupancy environment of Pb+Pb collisions, the p_{T} threshold for tracks used in the isolation variable calculation is increased to 2 GeV, replacing the standard cut of 1 GeV. Figure 5.3 shows distributions of $E^{\mathrm{isol}}_{\mathrm{T,cone}}$ and $p^{\mathrm{isol}}_{\mathrm{T,cone}}$ for leptons in the $e\mu$ channel for data and MC simulation. The difference between the data and the sum of predictions arises from the fake-lepton background contribution (Section 5.6), which is not included in these figures. Distributions of isolation variables separately for electrons and muons in all three dilepton channels are provided in Appendix C.1.

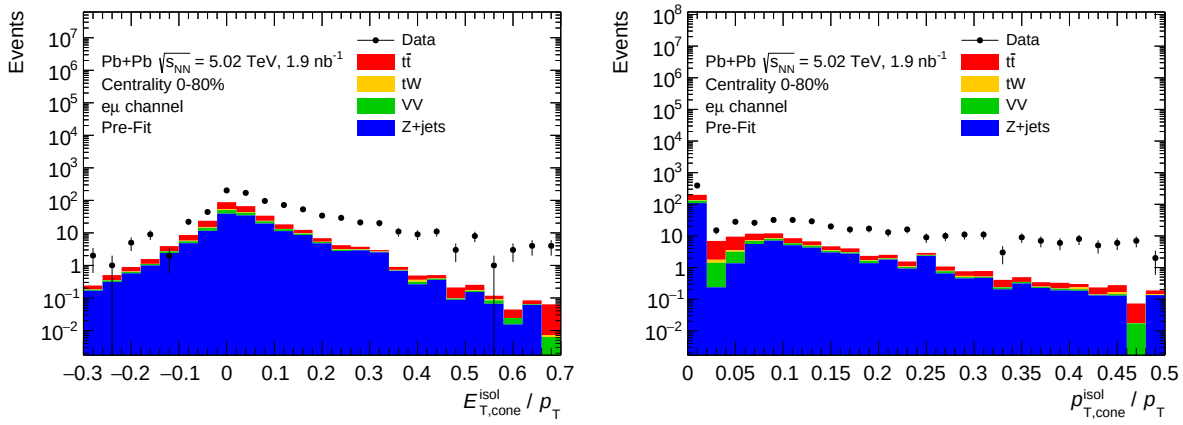

(a) (b)

Figure 5.3: Distributions of (a) calorimeter and (b) track isolation variables for leptons in the $e\mu$ channel.

Figure 5.4 presents pre-fit distributions of p_{T} of lepton pairs in the three dilepton channels, with the total uncertainties including statistical and systematic components. Good agreement is observed between the data and the sum of predictions, with significant fluctuations in the data due to limited statistics.

5.5.2 Jets

Jets are built following the HI-jet definition [153], using the anti-k_t method [151] implemented via the FastJet [152] package, with a radius parameter set to $R = 0.4$. Massless calorimeter towers, each with a size of $\Delta\eta \times \Delta\phi = 0.1 \times \pi/32$, serve as inputs to the jet algorithm. The background energy associated with the

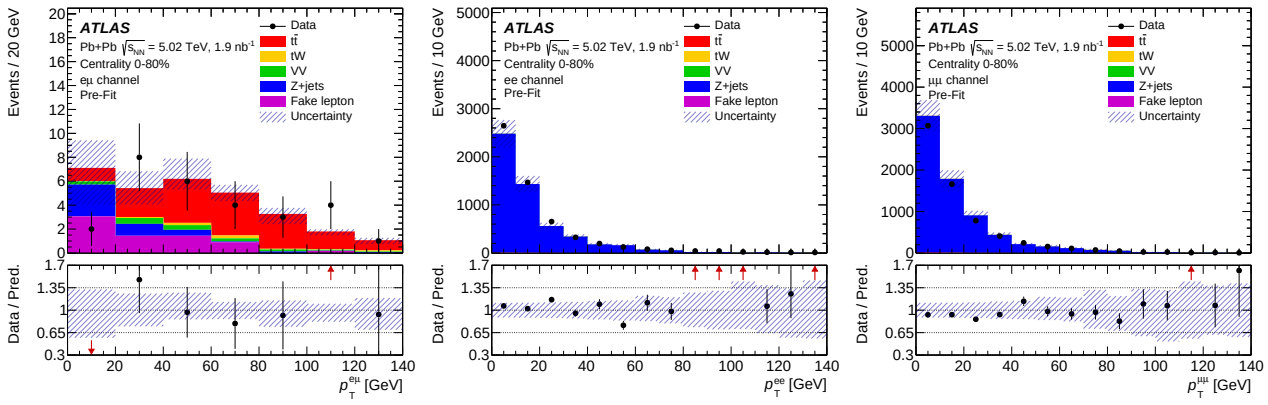

(a) (b) (c)

Figure 5.4: Pre-fit distributions of p_{T} of lepton pairs in the (a) $e\mu$, (b) ee, and (c) $\mu\mu$ channels. Pre-fit uncertainties are represented by the hatched area. The full markers in the bottom panels show a ratio of data and a sum of predictions. Red arrows indicate bins with entries that are outside the ratio range [171].

underlying event is removed from each tower. A dedicated low-pileup jet calibration is used, tailored for Pb+Pb collisions at $\sqrt{s_{\mathrm{NN}}} = 5.02$ TeV, based on simulations of the calorimeter response and in-situ measurements of the absolute energy scale. A cross-calibration is applied to transfer in-situ studies conducted in the pp system to Pb+Pb collisions. Jets have to satisfy the $p_{\mathrm{T}} > 35$ GeV and $|\eta| < 2.5$ requirements. No b-tagging is available for HI jets and is therefore not used in the analysis.

Effects related to jet quenching are not modelled in MC samples, leading to discrepancies between data and simulation. To correct jet spectra in MC simulation, the probability density function for the jet energy loss [176] is used, which is expressed as

$$f(x) = \frac{\gamma_1^{\gamma_0}}{\Gamma(\gamma_0)} \cdot x^{\gamma_0 - 1} \cdot e^{-\gamma_1 \cdot x}, \tag{5.1}$$

where $\gamma_0 = 1.38$ and $\gamma_1 = 0.26$ parameters are derived using Pb+Pb collisions at $\sqrt{s_{\mathrm{NN}}} = 5.02$ TeV. Jet p_{T}, matched to generated jets in MC simulation within $\Delta R < 0.3$, is corrected as follows:

$$p_{\mathrm{T}}^{\mathrm{jet}} \to p_{\mathrm{T}}^{\mathrm{jet}} - \mu \cdot \frac{X}{\langle f(x) \rangle}, \quad X \sim f(x). \tag{5.2}$$

X denotes a random variable drawn from the probability density function given in Equation 5.1, while μ is an adjustable parameter of the jet-quenching correction. The parameter value is optimised using $Z \to \ell\ell$ ($\ell = e, \mu$) events, separately in 0–30% (central) and 30–100% (peripheral) centrality intervals. Events with exactly two leptons and at least one jet are selected for this purpose. To ensure the contribution of jets from the hard scattering, p_{T} of the reconstructed Z boson is required to be $p_{\mathrm{T}}^{Z} > 45$ GeV, and the azimuthal angle between the Z boson and the leading jet must satisfy $\Delta\phi > 2.8$. Distributions of the difference in Z boson and leading jet p_{T} ($p_{\mathrm{T}}^{Z} - p_{\mathrm{T}}^{\mathrm{leadjet}}$), normalised to unity, are used to derive the μ parameter. The value of $\mu = 6$ (3) GeV is found to provide the best χ^2 fit between the $p_{\mathrm{T}}^{Z} - p_{\mathrm{T}}^{\mathrm{leadjet}}$ distributions in data and simulation for central (peripheral) collisions. The correction is more significant in central collisions, where larger jet-quenching effects are expected. Figure 5.5 shows the distributions of $p_{\mathrm{T}}^{Z} - p_{\mathrm{T}}^{\mathrm{leadjet}}$ in central and peripheral collisions before and after

applying the jet-quenching correction. Improved agreement is observed between the data and simulation after applying the correction.

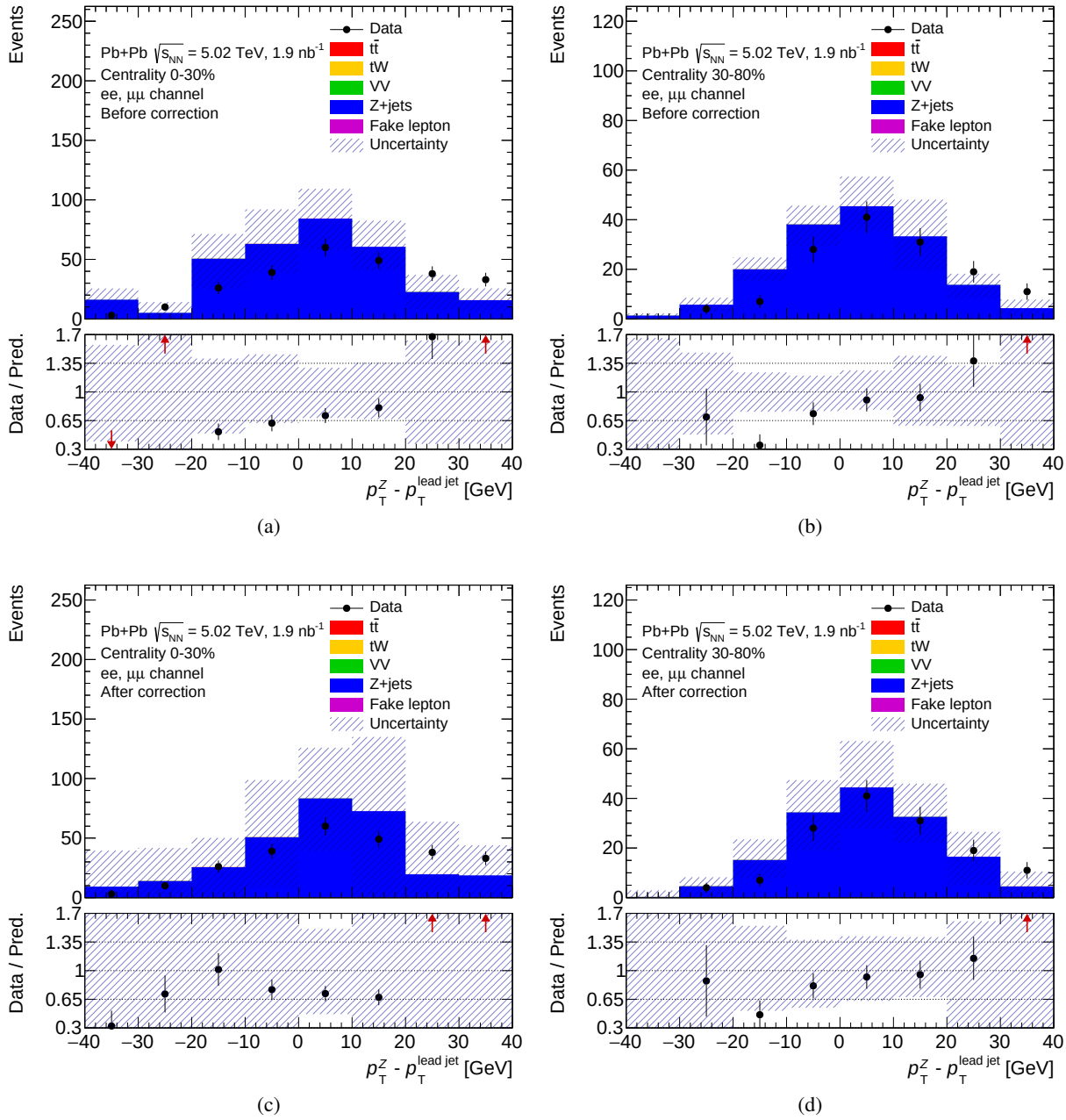

Figure 5.5: Distributions of $p_{\mathrm{T}}^{Z} - p_{\mathrm{T}}^{\mathrm{leadjet}}$ in central (a, c) and peripheral (b, d) collisions before (a, b) and after (c, d) applying the jet-quenching correction.

Jet spectra are also affected by soft jets from the underlying event and random energy fluctuations reconstructed as jets, referred to as fake jets. The potential mismodelling of fake jets in MC simulation is treated by using the following jet energy scale correction:

$$p_{\mathrm{T}}^{\mathrm{jet}} \rightarrow p_{\mathrm{T}}^{\mathrm{jet}} - X, \quad X \sim G(\mu, \sigma), \tag{5.3}$$

which is applied to p_{T} of jets that are not matched to generated jets in MC simulation within $\Delta R < 0.3$. X represents a random variable drawn from the Gaussian distribution with mean μ and standard deviation σ. The μ and σ parameters are optimised using jet-multiplicity distributions of $Z \to \ell\ell$ ($\ell = e, \mu$) events with exactly two leptons, normalised to unity, in 0–30% (central) and 30–100% (peripheral) collision centrality classes. The values of $\mu = 5$ (4) GeV and $\sigma = 4$ (0) GeV are derived using the best χ^2 fit between the jet multiplicity distributions in data and simulation for central (peripheral) collisions. The correction has a greater impact in central collisions, where the underlying event and higher detector occupancy result in a greater fake-jet contribution. Figure 5.6 presents jet-multiplicity distributions in central and peripheral collisions before

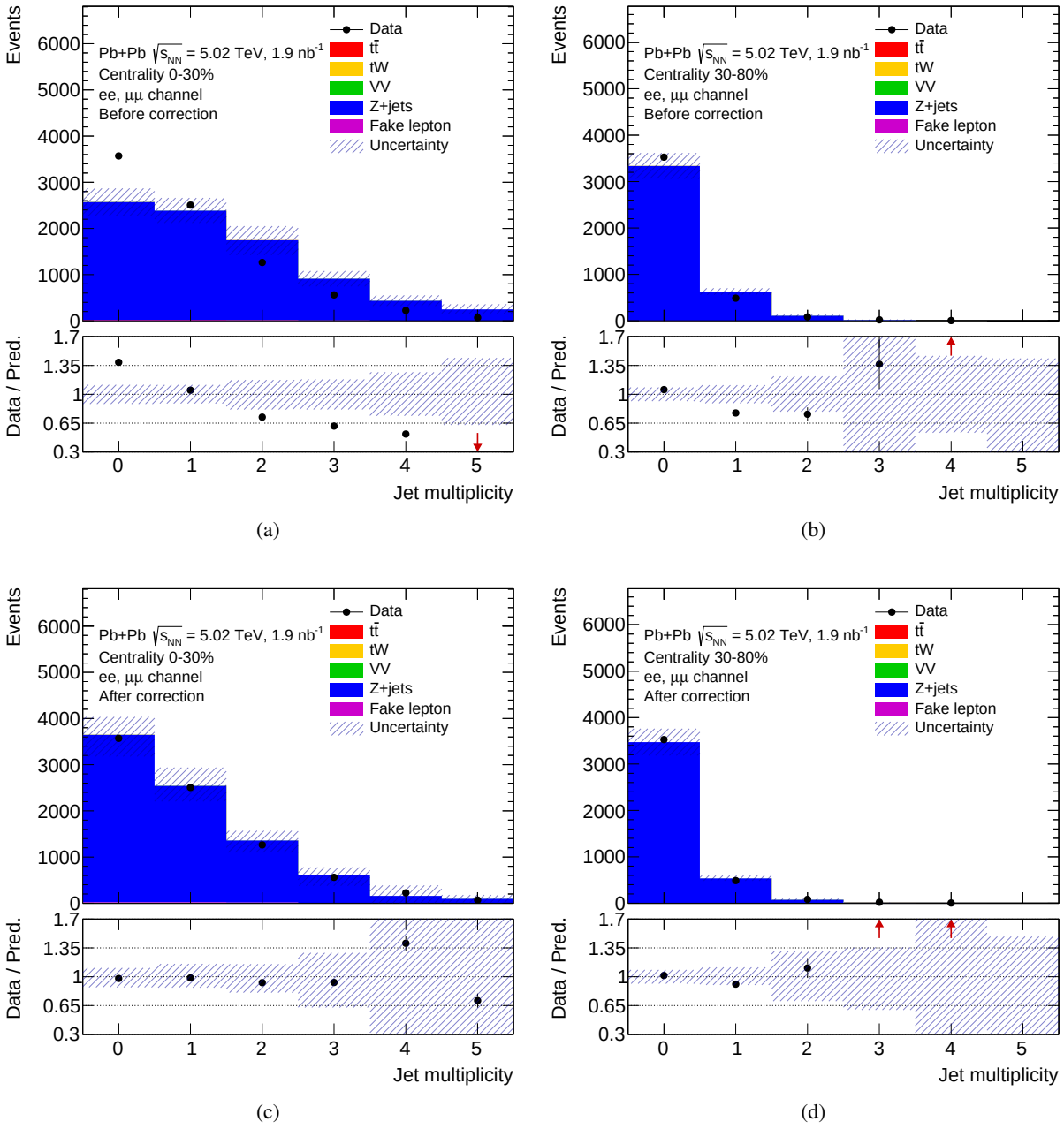

Figure 5.6: Distributions of the number of jets in central (a, c) and peripheral (b, d) collisions before (a, b) and after (c, d) applying the fake-quenching correction.

and after applying the fake-jet correction. Enhanced agreement is found between the data and simulation after applying the correction.

Pre-fit distributions of the number of jets in the three dilepton channels, after applying all jet-related corrections, are displayed in Figure 5.7, with the total uncertainties composed of statistical and systematic components. The data are found to be consistent with the sum of predictions within the total uncertainties. A cut of at least two jets is imposed in the $e\mu$ channel to enhance the signal-to-background ratio.

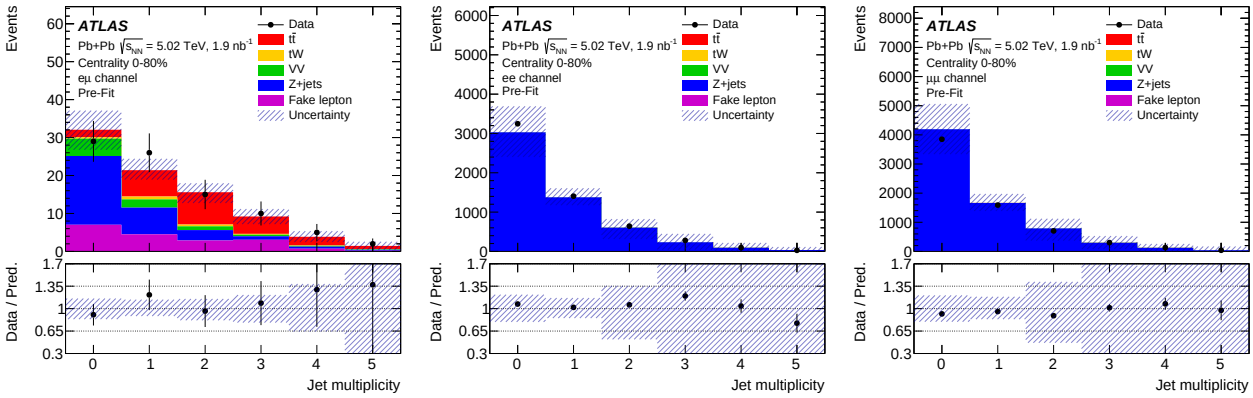

(a) (b) (c)

Figure 5.7: Pre-fit distributions of the number of jets in the (a) $e\mu$, (b) ee, and (c) $\mu\mu$ channels. Pre-fit uncertainties are represented by the hatched area. The full markers in the bottom panels show a ratio of data to a sum of predictions [171].

5.5.3 Overlap removal

To avoid double-counting between selected objects, the overlap removal is applied. An electron is discarded if it is matched to the same track as a muon. To prevent the reconstruction of jets from electrons, the closest jet to an electron is removed if it is within a $\Delta R \leq 0.2$ distance from the electron. To limit non-prompt leptons from heavy-flavour hadron decays, leptons within a $\Delta R \leq 0.4$ distance from a jet are rejected, unless the lepton is a muon and the jet has fewer than three associated tracks, in which case the jet is removed.

5.6 Fake-lepton background estimation

The fake-lepton contribution consists of non-prompt leptons, arising from semileptonic decays of heavy-flavour hadrons and electrons produced through photon conversions, as well as misidentified light hadrons. Due to limited data statistics, the fake-lepton background is evaluated using the ABCD data-driven technique. The method relies on the factorisation of background events in the plane of two uncorrelated variables. In this analysis, charge signs of lepton pairs and lepton isolation criteria are used to define four regions, summarised in Table 5.2. Owing to limited data, the fake-lepton background is evaluated inclusively for electrons and muons.

The requirement for isolated leptons is met when both leptons satisfy the isolation criteria described in Section 5.5.1, whereas the non-isolated leptons condition is fulfilled if at least one lepton fails these criteria. With

Table 5.2: Definition of the regions in fake-lepton estimation.

Region	Opposite-sign charge	Same-sign charge
Isolated leptons	A	B
Non-isolated leptons	C	D

these requirements, region A corresponds to the signal region in the $t\bar{t}$ measurement, while regions B–D are enriched with fake-lepton contributions. Assuming no correlations between charge and the isolation conditions, the number of fake-lepton events in the signal region A can be estimated as

$$N_{\mathrm{A}} = \frac{N_{\mathrm{B}} \cdot N_{\mathrm{C}}}{N_{\mathrm{D}}}, \tag{5.4}$$

where N_{i} represents the number of data events in the control region i after subtracting the contribution from the MC simulation. To increase data statistics, no cuts are imposed on $m_{e\mu}$ and the number of jets in the $e\mu$ channel, while a loose requirement of $41 < m_{ee}(m_{\mu\mu}) < 141$ GeV is used in the same-flavour channels. In order to avoid counts from the $Z \to \ell\ell$ process in the same-flavour channels, the contribution in the $81 < m_{ee}(m_{\mu\mu}) < 101$ GeV range is evaluated using an exponential function fit to sidebands of the m_{ee} ($m_{\mu\mu}$) distribution. Figure 5.8 shows the number of events in the $e\mu$ channel in the A–D regions, corresponding to N_{i} numbers in Equation 5.4. The number of events in the region A is calculated based on the number of events in the regions B–D. Similar distributions for the ee and $\mu\mu$ channels are documented in Appendix C.2.

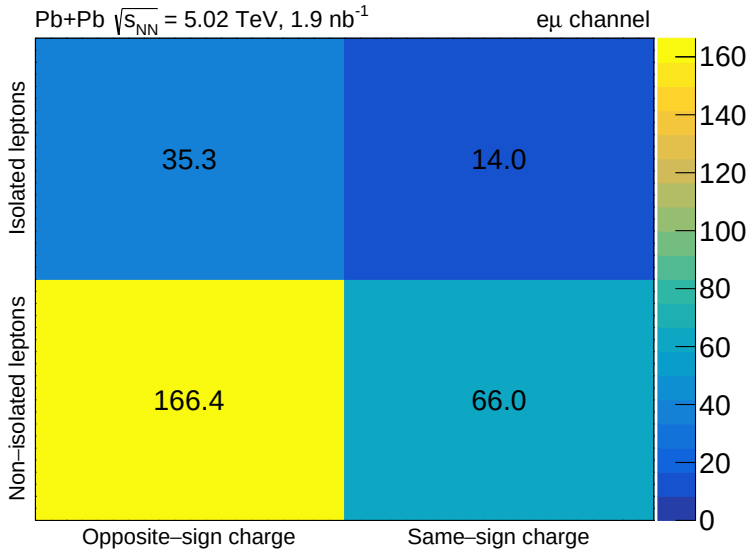

Figure 5.8: Number of events in the regions in fake-lepton estimation in the $e\mu$ channel.

The shape of a given kinematic distribution is estimated using the distribution of events in the control region C. Limited data statistics result in potential fluctuations of the fake-lepton background contributions. Therefore, the shape of the invariant-mass distribution, which is used in the fitting procedure described in Section 5.8, is smoothened using an exponential function fit. Figure 5.9 displays pre-fit distributions of the invariant mass of

lepton pairs in the three dilepton channels, with the total uncertainties including statistical and systematic components. The estimated numbers of fake-lepton events constitute 22%, 0.4%, and 0.6% of the total prediction in the $e\mu$, ee, and $\mu\mu$ channels, respectively.

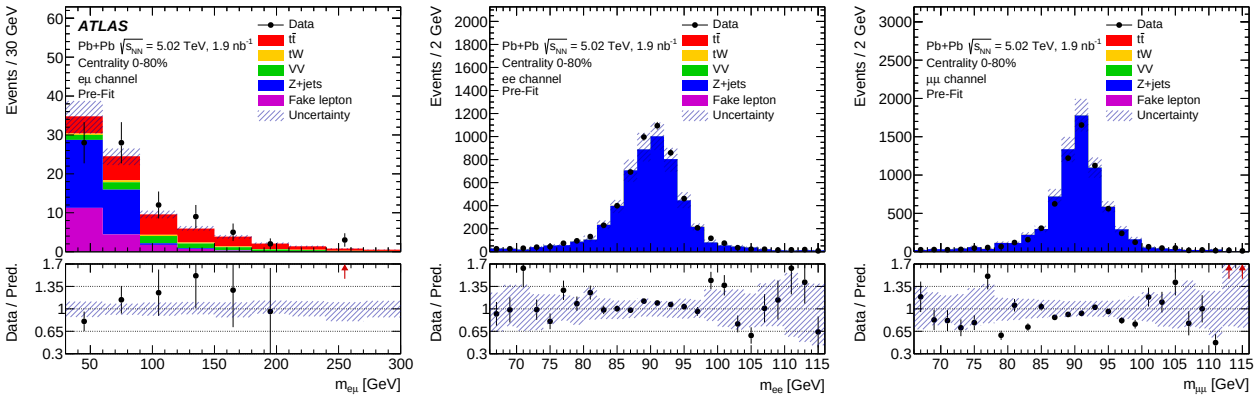

(a) (b) (c)

Figure 5.9: Pre-fit distributions of the invariant mass in the (a) $e\mu$, (b) ee, and (c) $\mu\mu$ channels. Pre-fit uncertainties are represented by the hatched area. The full markers in the bottom panels show a ratio of data to a sum of predictions. Red arrows indicate bins with entries that are outside the ratio range [171].

5.7 Systematic uncertainties

Due to the limited data sample, the $t\bar{t}$ measurement is primarily dominated by statistical uncertainties, whereas the systematic component has a smaller impact on the total uncertainties. Systematic uncertainties influencing the result originate from the following sources. An uncertainty in the integrated luminosity is determined through luminosity calibration. Uncertainties due to signal $t\bar{t}$ modelling encompass variations of the h_{damp} parameter, as well as ME and PS models. Background modelling uncertainties include normalisation variations of tW, VV, and Z+jets yields. Uncertainties in electron and muon performance arise from lepton calibration and scale-factor corrections. Jet-related uncertainties originate from jet energy scale and resolution, and the dedicated jet-quenching and fake-jet corrections. Uncertainties in the fake-lepton background are divided into normalisation and shape components. All systematic uncertainties, including the number of components in each of the groups, are listed in Table 5.3.

5.7.1 Luminosity

The uncertainty related to luminosity is based on the calibration of the luminosity scale through x–y beam-separation scans [114]. The primary luminosity measurements are carried out using the LUCID-2 detector [159]. The obtained relative uncertainty in the combined 2015 and 2018 Pb+Pb dataset is 1.5%.

5.7.2 $t\bar{t}$ modelling

Uncertainties due to signal $t\bar{t}$ modelling are evaluated by using MC simulation variations detailed in Section 5.3 and symmetrised. Uncertainties in PS radiation are assessed by increasing the h_{damp} parameter to $3m_t$. The

Table 5.3: Summary of systematic uncertainties with the number of components in each group.

Systematic group	Systematic uncertainty	Number of components
Luminosity	Calibration	1
$t\bar{t}$ modelling	$t\bar{t}\,h_{\mathrm{damp}}$	1
	$t\bar{t}$ ME	1
	$t\bar{t}$ PS	1
Background modelling	tW	1
	VV	1
	Z+jets	1
Electron	Calibration	2
	Scale factors	4
Muon	Calibration	4
	Scale factors	7
Jet	Jet energy scale	20
	Jet energy resolution	9
	Jet-quenching correction	3
	Fake-jet correction	3
Fake lepton	Normalisation	2
	Shape	1

alternative POWHEG BOX V2+PYTHIA8 sample is used to estimate the uncertainty in the ME and PS matching, while the POWHEG BOX V2+HERWIG V7.2 sample is employed to obtain the uncertainty in PS modelling. Uncertainties related to the PDF choice, ISR, and FSR are subdominant and therefore not considered.

5.7.3 Background modelling

Uncertainties in background modelling are accounted for by varying the normalisation of each process. An uncertainty of 9.5% is used for the normalisation of the tW background [161]. The VV background normalisation is varied by 26%, corresponding to the uncertainty in SHERPA V2.2.14 MC generator predictions, extrapolated to the centre-of-mass energy of the Pb+Pb system [177]. The normalisation uncertainty of 10% is applied to the Z+jets background, which reflects the uncertainty of the Z-boson measurement in Pb+Pb collisions [60].

5.7.4 Electron

Uncertainties related to electrons arise partially from the low-pileup energy calibration [127]. Uncertainties in electron reconstruction scale factors are obtained by changing the correction within the total uncertainty. Additional uncertainties are considered for Pb+Pb scale factors, corresponding to electron identification, isolation, and trigger, by modifying the corrections within the total uncertainties.

5.7.5 Muon

Uncertainties due to muon performance stem in part from momentum scale and resolution [150]. Uncertainties in muon reconstruction and track-to-vertex-association scale factors are evaluated by changing the corrections within their statistical and systematic uncertainties. Further uncertainties are assigned for Pb+Pb scale factors, related to muon identification, isolation, and trigger, by varying the corrections within the total uncertainties.

5.7.6 Jet

Uncertainties associated with jet calibration are estimated using the comparison of the simulated jet response in MC simulation from different generators and in-situ studies of the calorimeter response [154]. Further uncertainties are considered due to the application of the calibration to jets reconstructed in the Pb+Pb environment [164]. Additionally, uncertainties of 100% are applied to corrections related to jet quenching and fake jets, separately for the signal and background components, such that the downward systematic variation corresponds to the unmodified jet p_{T} spectrum.

5.7.7 Fake-lepton background

Uncertainties in the fake-lepton background include variations in both normalisation and shape components by modifying the fake-lepton background estimation described in Section 5.6. Statistical uncertainties in normalisation are calculated by propagating statistical uncertainties from control regions B, C, and D to signal region A. Systematic uncertainties in normalisation are evaluated by changing the isolation requirements by $\pm 50\%$ in control regions C and D with non-isolated leptons. The variation in background distribution shape is obtained by using events with same-sign charged leptons, corresponding to the combined regions C and D. The shape-related uncertainty is derived from the one-sided variation and symmetrised.

5.8 Fit procedure

5.8.1 Boosted decision tree

To study the discrimination between signal and background, a boosted decision tree (BDT) is used. A classifier with 10,000 trees is trained using the TMVA framework [178]. For this purpose, an independent MC simulation of pp collisions at $\sqrt{s} = 5.02$ TeV is employed, with $t\bar{t}$ as the signal. The Z+jet process, as the primary background contribution, is used as the background in the training. Events with exactly one electron and one muon are selected for the classification. The BDT is trained exclusively on lepton quantities to minimise effects of the imprecise knowledge of jet kinematics in Pb+Pb collisions. In total, 11 input variables based on lepton properties are used in the classifier, listed in Table 5.4.

For each variable, separation, $\langle S^2 \rangle$, is evaluated using the following expression:

$$\langle S^2 \rangle = \frac{1}{2} \int \frac{\left(P_{\mathrm{S}}(x) - P_{\mathrm{B}}(x)\right)^2}{P_{\mathrm{S}}(x) + P_{\mathrm{B}}(x)} dx, \tag{5.5}$$

where $P_{\mathrm{S}}(x)$ and $P_{\mathrm{B}}(x)$ stand for probability density functions of variable x for signal and background, respectively. $\langle S^2 \rangle$ is zero for identical shapes for signal and background, and one for shapes with no overlap. The best separation power is observed for the $p_{\mathrm{T}}^{e\mu}$ variable. Input variable importance in the BDT is calculated by counting how often the variable is used to split decision tree nodes, and weighting each split occurrence by the separation gain squared and the number of events in the node [179]. The $\Delta R\ (e, \mu)$ variable is found to be ranked the highest in the classifier.

Figure 5.10 presents distributions of $p_{\mathrm{T}}^{e\mu}$ and $m_{e\mu}$ variables, which show the highest separation power, in data and MC simulation. Distributions of the remaining variables are provided in Appendix C.3. A relation between

Table 5.4: Definition of input variables used in the BDT, including separation power and importance in the classifier.

Variable	Separation	Importance	Definition
$p_{\mathrm{T}}^{e\mu}$	0.597	0.079	p_{T} of the dilepton system
$m_{e\mu}$	0.442	0.079	Invariant mass of the dilepton system
$\Delta\phi\ (e,\mu)$	0.354	0.112	Difference in ϕ between the electron and the muon
p_{T}^{μ}	0.338	0.064	muon p_{T}
p_{T}^{e}	0.332	0.057	electron p_{T}
$\eta^{e\mu}$	0.289	0.082	η of the dilepton system
$\Delta R\ (e,\mu)$	0.278	0.140	ΔR between the electron and the muon
$\lvert\Delta p_{\mathrm{T}}\ (e,\mu)\rvert$	0.276	0.058	Absolute difference in p_{T} between the electron and the muon
$\lvert\Delta\eta\ (e,\mu)\rvert$	0.069	0.103	Absolute difference in η between the electron and the muon
η^{e}	0.038	0.112	electron η
η^{μ}	0.037	0.115	muon η

signal efficiency and background rejection, referred to as the receiver operating characteristic (ROC), is displayed in Figure 5.11a. The area under the ROC curve, which evaluates the classifier performance, amounts to 0.96. Figure 5.11b shows the distribution of the BDT output for data and MC simulation events in the $e\mu$ channel in Pb+Pb collisions, selected using criteria described in Section 5.4. The output ranges from -1 to 1, corresponding to pure background and signal, respectively. Setting a threshold for the signal at zero, 96% of $t\bar{t}$ events are kept, while 42% (72%) of the overall (Z+jet) background is rejected.

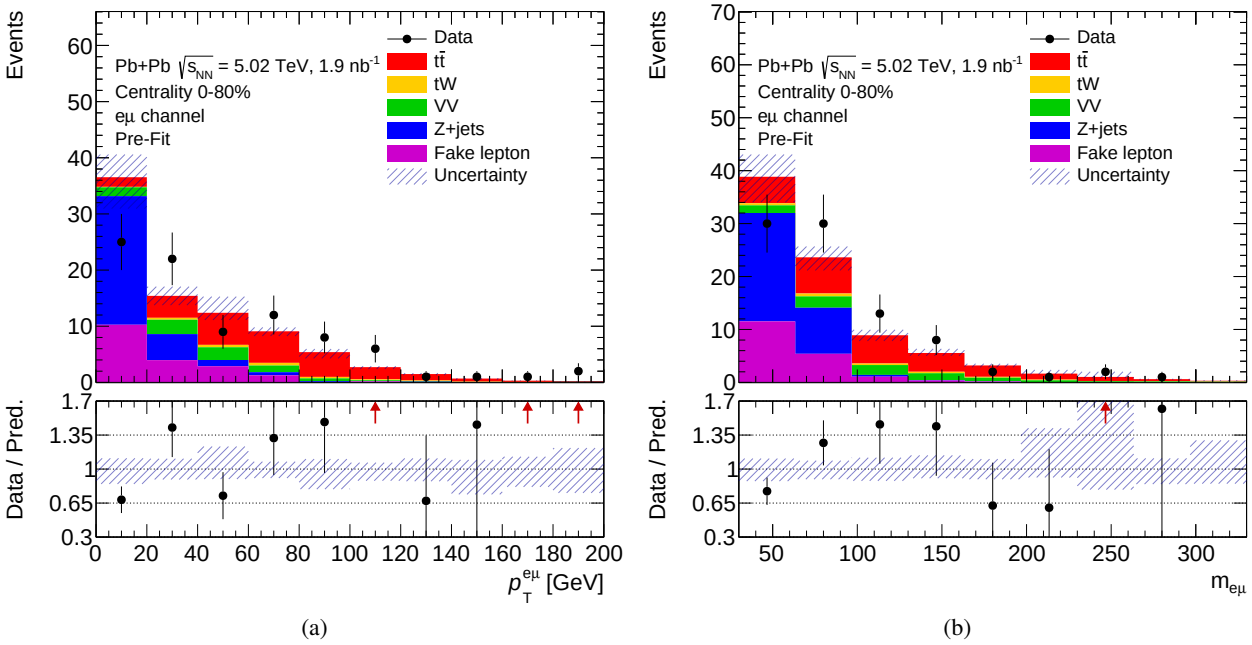

(a) (b)

Figure 5.10: Distributions of two input variables used in the BDT classifier with the highest separation power: (a) $p_{\mathrm{T}}^{e\mu}$ and (b) $m_{e\mu}$.

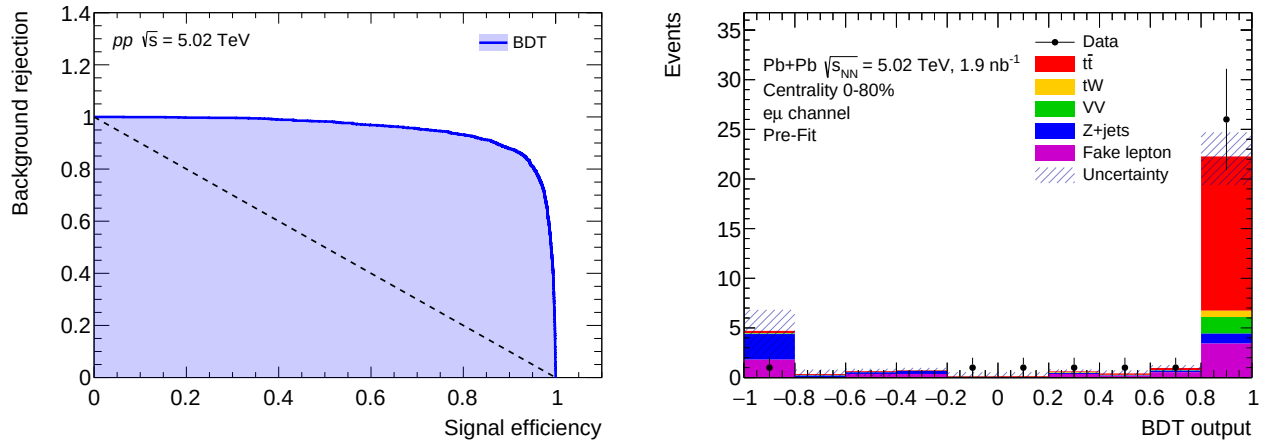

(a) (b)

Figure 5.11: (a) Receiver operating characteristic of the BDT classifier. (b) Distribution of the BDT output for data and MC simulation.

Based on these studies, the fit strategy has been developed, explained in detail in Section 5.8.2. The variable with the highest separation power, $p_{\mathrm{T}}^{e\mu}$, is used to distribute events into two signal regions of the fit. The variable with the second highest separation power, $m_{e\mu}$, is used to define distributions for the binned profile-likelihood fit, introduced in Section 4.8.1.

5.8.2 Fit strategy

Events in the $e\mu$ channel, selected using criteria described in Section 5.4, are divided into two signal regions (SR_1 and SR_2). Events with dilepton transverse momentum $p_{\mathrm{T}}^{e\mu} > 40$ GeV constitute the SR_1, whereas the remaining events form the SR_2. The requirement is optimised to achieve the best signal-to-background ratio in SR_1, while maintaining sufficient data statistics. Despite the significant contamination by the background, the additional signal region, SR_2, provides more information to the fit, enhancing the resulting signal significance. The signal strength $\mu_{t\bar{t}}$ is defined as the ratio of the measured $t\bar{t}$ cross section in the $e\mu$ channel to the SM expectation with no nPDF effects involved.

A profile-likelihood fit, detailed in Section 4.8.1, is performed simultaneously in the two signal regions using $m_{e\mu}$ distributions, presented in Figure 5.12. Due to limited Z+jet statistics at high $m_{e\mu}$ values, the Z+jet and VV processes are merged into a single background component to ensure non-zero entries in each bin. Reasonable agreement is found between data and the sum of predictions within total uncertainties, represented by the hatched area.

5.8.3 Fit results

After the fitting procedure, an improved data-to-prediction ratio and lower systematic uncertainties are achieved, as shown in Figure 5.13. The fit favours smaller background contributions than predicted, resulting in a higher signal yield after the fit. In the post-fit distribution, unlike in the pre-fit ones, both statistical and systematic uncertainties in $\mu_{t\bar{t}}$ are included in the uncertainty band. This leads to higher uncertainties in SR_1

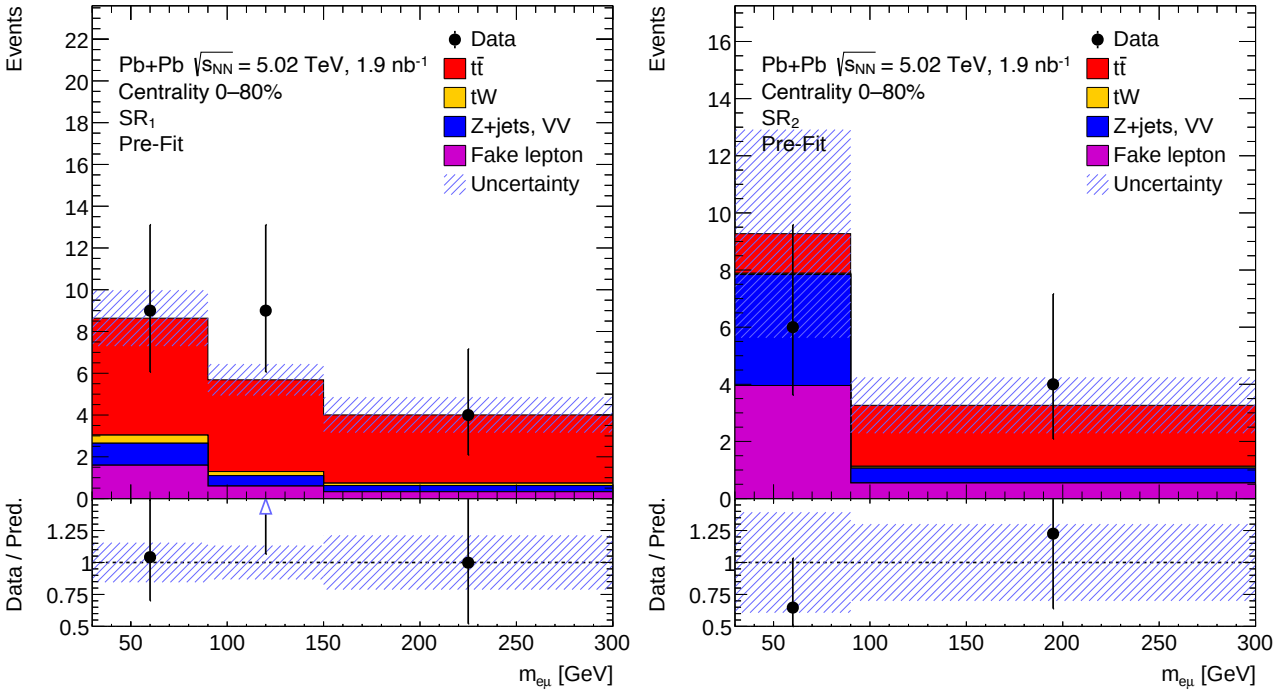

(a) (b)

Figure 5.12: Data pre-fit plots representing the $m_{e\mu}$ variable in the two signal regions (a) SR_1 and (d) SR_2, with uncertainties represented by the hatched area. The full markers in the bottom panels show a ratio of data and a sum of predictions. Arrows indicate bins with entries that are outside the ratio range.

and only slightly lower uncertainties in SR_2 before and after the fit. Figure 5.14 displays a comparison between data and predicted event yields in the two signal regions. Better agreement between data and prediction in both signal regions and a decrease of the total uncertainty in SR_2 are found after the fit.

Tables 5.5 and 5.6 show data and predicted pre- and post-fit event yields in the two signal regions of the fit. Owing to rounding effects and small correlations between the different sources of uncertainties, the total systematic uncertainty is different from the sum in quadrature of the individual sources.

Table 5.5: Data and predicted pre-fit event yields in the two signal regions. The total uncertainty is a quadrature sum of statistical and systematic uncertainties.

Region	**SR1**	**SR2**
$t\bar{t}$	13.3 ± 2.4	3.5 ± 0.6
tW	0.70 ± 0.19	0.11 ± 0.10
Z, VV	1.8 ± 0.8	4.4 ± 3.5
Fake lepton	2.5 ± 0.8	4.5 ± 1.5
Total	18.3 ± 2.7	12.5 ± 4.0
Data	22	10

Table 5.6: Data and predicted post-fit event yields in the two signal regions. The total uncertainty is a quadrature sum of statistical and systematic uncertainties.

Region	**SR1**	**SR2**
$t\bar{t}$	17.3 ± 4.5	4.6 ± 1.4
tW	0.71 ± 0.19	0.10 ± 0.09
Z, VV	1.5 ± 0.5	2.3 ± 1.8
Fake lepton	2.3 ± 0.7	4.1 ± 1.3
Total	21.8 ± 4.4	11.1 ± 2.1
Data	22	10

The signal strength is determined from the combined fit to $m_{e\mu}$ distributions in the two signal regions. The $\mu_{t\bar{t}}$ value with statistical and systematic uncertainties is measured to be

$$\mu_{t\bar{t}} = 1.33\ ^{+0.36}_{-0.32}\ (\text{stat.})\ ^{+0.28}_{-0.18}\ (\text{syst.}) = 1.33\ ^{+0.46}_{-0.37}\ (\text{tot.}). \tag{5.6}$$

The observed $\mu_{t\bar{t}}$ values extracted from the individual fits in each signal region and in the combined fit are presented in Figure 5.15. $\mu_{t\bar{t}}$ values in SR_1 and SR_2 are in agreement with each other and the SM prediction, $\mu_{t\bar{t}} = 1$, within the total uncertainties. The total uncertainty in $\mu_{t\bar{t}}$ is dominated by the statistical component due to limited data statistics. The background-only hypothesis in individual SR_1 and SR_2 is rejected with

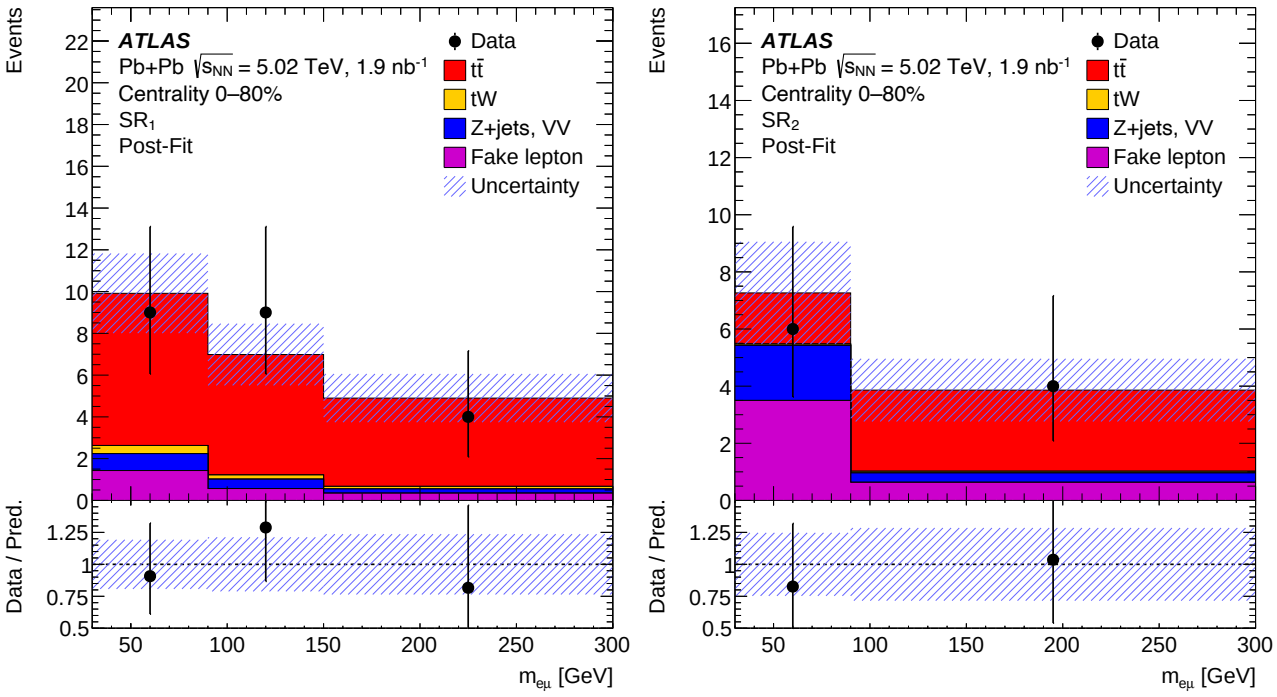

(a) (b)

Figure 5.13: Data post-fit plots representing the $m_{e\mu}$ variable in the two signal regions (a) SR_1 and (d) SR_2, with uncertainties represented by the hatched area. The full markers in the bottom panels show a ratio of data and a sum of predictions. Arrows indicate bins with entries that are outside the ratio range [171].

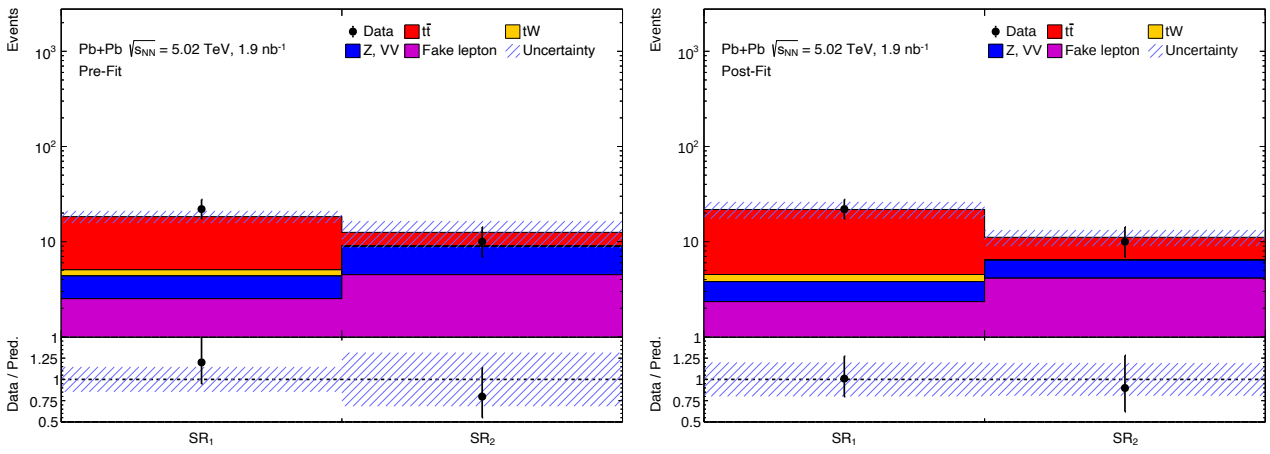

(a) (b)

Figure 5.14: Data and predicted (a) pre-fit and (b) post-fit event yields in the two signal regions. The total uncertainties in the sum of the signal and background are represented by the blue hatched band. Bottom panel shows the ratio of the data and prediction.

an observed (expected) signal significance of 4.9 (4.0) and 1.4 (1.2), respectively. The observed (expected) significance in the combined fit amounts to 5.0 (4.1) standard deviations, leading to the first observation of $t\bar{t}$ production in Pb+Pb collisions.

Systematic uncertainties in the fit are considered correlated across the two signal regions. Table 5.7 provides a summary of the relative uncertainties in the $\mu_{t\bar{t}}$ value, divided into systematic categories. The group uncertainties are calculated by performing the fit with a set of nuisance parameters fixed to their fitted values and

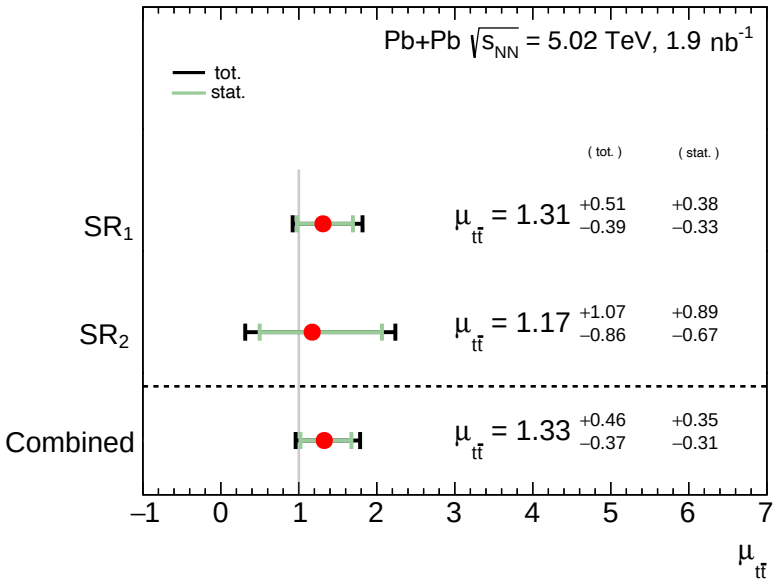

Figure 5.15: Observed best-fit values of the signal strength $\mu_{t\bar{t}}$ with statistical and systematic uncertainties in each signal region and in the combined fit.

Table 5.7: Summary of the impact of the systematic uncertainties on $\mu_{t\bar{t}}$ grouped into different categories and combined [171].

Source	$\Delta\sigma_{t\bar{t}}/\sigma_{t\bar{t}}$	
	Up unc. [%]	**Down unc. [%]**
Signal modelling	+16	-9.6
Jet	+14	-8.8
Fake-lepton background	+7.3	-6.6
Electron	+3.5	-2.1
Muon	+3.3	-2.0
Luminosity	+2.3	-1.5
MC sample size	+2.1	-1.6
Background modelling	+1.5	-1.6
Systematic uncertainty	**+21**	**-14**

subtracting in quadrature the obtained total uncertainty from the uncertainty of the full fit. Due to the neglect of correlations between the different categories, the total uncertainty differs from the quadratic sum of the impacts of each group. The dominant contribution to the total systematic uncertainty is signal modelling, followed by jet performance. The total relative systematic uncertainty is measured to be 18%.

Figure 5.16 shows the impact of the 10 leading systematic components on the observed signal strength ($\hat{\mu}$). Variations of $\hat{\mu}$ from the central value ($\Delta\hat{\mu}$) when fixing the corresponding individual nuisance parameter (θ) to its post-fit value ($\hat{\theta}$) modified upwards or downwards by its post-fit uncertainty ($\Delta\hat{\theta}$) are represented by the filled boxes, whereas the corresponding pre-fit impact is illustrated by the empty boxes. Changes in fitted values

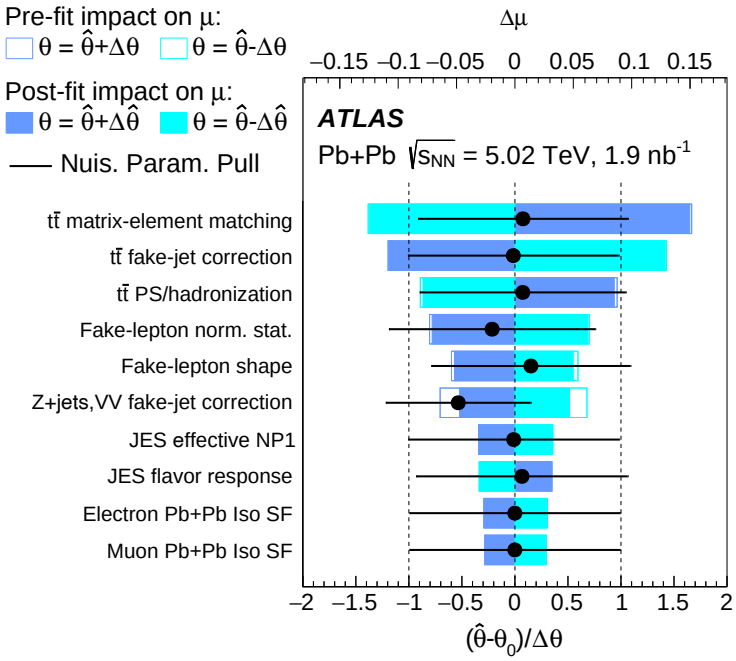

Figure 5.16: The impact of systematic uncertainties on the fitted signal strength [171].

of the nuisance parameters ($\hat{\theta} - \theta_0$) relative to their pre-fit uncertainties ($\Delta\theta$) are denoted by the black points. Black error bars indicate post-fit uncertainties of the nuisance parameters relative to their nominal uncertainties, marked by the dashed line. The most significant systematic uncertainties are related to signal modelling and the dedicated fake-jet correction applied to the $t\bar{t}$ contribution. The largest pull is observed for the fake-jet correction in the combined Z+jets and VV contributions, leading to the smaller background yield after the fit.

The correlations between nuisance parameters with at least one correlation value above 10% are displayed in Figure 5.17. $t\bar{t}$ ME matching and $\mu_{t\bar{t}}$ show the largest correlation of 34%. The largest anticorrelation of -29% is observed between the fake-jet correction in the $t\bar{t}$ sample and $\mu_{t\bar{t}}$.

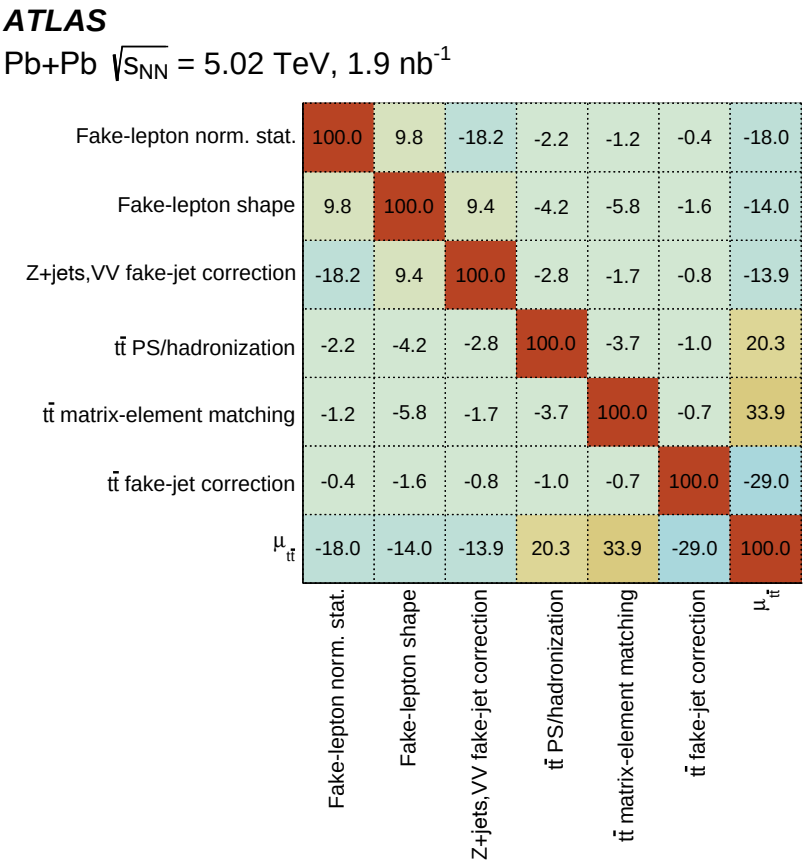

Figure 5.17: Correlation matrix of the fit parameters with at least one correlation value greater than 10% [171].

5.9 Results

5.9.1 Inclusive integrated cross section

The observed $\mu_{t\bar{t}}$ value is translated into the inclusive $t\bar{t}$ production cross section in Pb+Pb collisions in the 0-100% centrality interval, $\sigma_{t\bar{t}}^{\mathrm{Pb+Pb}}$, with the expression

$$\sigma_{t\bar{t}}^{\mathrm{Pb+Pb}} = \mu_{t\bar{t}} \cdot \sigma_{t\bar{t}}^{\mathrm{th}}, \tag{5.7}$$

where $\sigma_{t\bar{t}}^{\mathrm{th}} = 2.71\ \mu\mathrm{b}$ denotes the inclusive theoretical $t\bar{t}$ cross section in Pb+Pb collisions in the 0–100% centrality class, calculated at NNLO precision in QCD.

The obtained $t\bar{t}$ cross section in Pb+Pb collisions at $\sqrt{s_{\mathrm{NN}}} = 5.02$ TeV is

$$\sigma_{t\bar{t}}^{\mathrm{Pb+Pb}} = 3.6\ ^{+1.0}_{-0.9}\ (\mathrm{stat.})\ ^{+0.8}_{-0.5}\ (\mathrm{syst.})\ \mu\mathrm{b} = 3.6\ ^{+1.2}_{-1.0}\ (\mathrm{tot.})\ \mu\mathrm{b}. \tag{5.8}$$

The total relative uncertainty of the measurement is 31% and is dominated by the statistical component of 26%, leading to the most precise measurement of the $t\bar{t}$ process in Pb+Pb collisions to date.

The measured $t\bar{t}$ cross section is contrasted with theoretical results for four nPDF sets: EPPS21 [40], nNNPDF3.0 [41], nCTEQ15HQ [167], and TUJU21 [43]. Predictions are computed at NLO precision with the MCFM code [168] and scaled to the Pb+Pb system by A_{Pb}^2. Theoretical values are adjusted to NNLO precision in QCD using the K-factor$= 1.149$, derived using the TOP++ V2 program. Predicted $t\bar{t}$ cross-section values in Pb+Pb collisions with total uncertainties based on the four nPDF sets are listed in Table 5.8.

Table 5.8: Theoretical predictions of the $t\bar{t}$ cross section in Pb+Pb collisions based on four nPDF sets.

nPDF set	$\sigma_{t\bar{t}}^{\mathrm{Pb+Pb}}$ [μb]
TUJU21	$2.70\ ^{+0.14}_{-0.15}$
nNNPDF3.0	$3.32\ ^{+0.18}_{-0.18}$
nCTEQ15HQ	$2.74\ ^{+0.33}_{-0.33}$
EPPS21	$2.90\ ^{+0.34}_{-0.22}$

Figure 5.18 presents the observed $t\bar{t}$ cross section, compared with the state-of-the-art theoretical predictions and other experimental measurements. The result aligns with theoretical results for all four nPDF sets. The

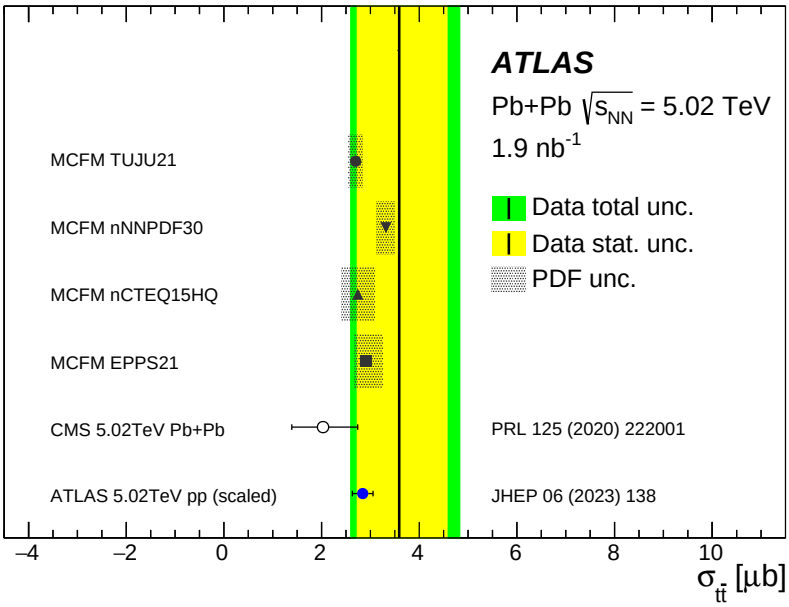

Figure 5.18: Comparison between measured and predicted values of $\sigma_{t\bar{t}}$. The result, represented by the solid black line, is compared with the measurement in Pb+Pb collisions at $\sqrt{s_{\mathrm{NN}}} = 5.02$ TeV by CMS, and the measurement in pp collisions at $\sqrt{s} = 5.02$ TeV by ATLAS, scaled by A_{Pb}^2. Predictions based on four nPDF sets are calculated at NNLO precision in QCD and scaled to the Pb+Pb system [171].

measurement is in agreement within total uncertainties with the $t\bar{t}$ cross section reported by CMS [79]. The result is also consistent with the $t\bar{t}$ cross section in pp collisions at $\sqrt{s} = 5.02$ TeV by ATLAS [161], scaled to the Pb+Pb system by A^2_{Pb}. Given the limited precision of the measurement, no indication of nuclear modification is observed for the $t\bar{t}$ process.

Chapter 6

Conclusions and outlook

The work presented in this thesis focuses on measurements of heavy-ion collisions using hard probes, top quarks and Z bosons, in the ATLAS experiment at the LHC. Hard probes in heavy-ion collisions play a crucial role in constraining nuclear modification to PDFs. Top-quark pair production, which is dominated by gluon-fusion processes, is especially sensitive to the gluon nPDF. Hard probes are also expected to interact with the QGP, produced in nucleus–nucleus collisions at ultra-relativistic energies, allowing the study of its properties. As the heaviest elementary particle, the top quark offers a unique probe of the strongly interacting matter.

Both p+Pb and Pb+Pb collisions, collected by ATLAS during Run 2, are analysed as part of this thesis. p+Pb data were recorded in 2016 at a nucleon–nucleon centre-of-mass energy of $\sqrt{s_{\mathrm{NN}}} = 8.16$ TeV, and correspond to the total integrated luminosity of 165 nb^{-1}. Pb+Pb data taking took place in 2015 and 2018 at a nucleon–nucleon centre-of-mass energy of $\sqrt{s_{\mathrm{NN}}} = 5.02$ TeV, providing the total integrated luminosity of 1.9 nb^{-1}. Both collision types were collected under low-pileup conditions.

Electrons constitute an essential part of the $t\bar{t}$ decay modes, particularly the ℓ+jets and dilepton channels with electrons in the final state. Electron performance is studied using the $Z \to e^+e^-$ resonance decay in both p+Pb and Pb+Pb collisions. Efficiencies in data and MC simulation, related to electron reconstruction, identification, isolation, and trigger, are derived in p+Pb collisions. The corresponding scale-factor corrections play an important role in the $t\bar{t}$ measurement in p+Pb collisions. Furthermore, four electron likelihood identification selections, HITight, HIMedium, HILoose, and HIVeryLoose, are optimised for Pb+Pb collisions. The obtained working points are the baseline identification criteria in Pb+Pb collisions in Run 3. The results of this work were approved by the ATLAS Collaboration and integrated by the Author of this thesis with the software versions of the experiment. They can be utilised in other analyses involving electrons in the final state based on p+Pb data from 2016 and Pb+Pb data recorded as part of the Run 3 campaign.

The production of $t\bar{t}$ pairs is studied in the ℓ+jets and dilepton channels in p+Pb collisions at $\sqrt{s_{\mathrm{NN}}} = 8.16$ TeV. The inclusive $t\bar{t}$ cross section is measured to be $\sigma_{t\bar{t}}^{p+\mathrm{Pb}} = 58.1 \pm 2.0\ (\mathrm{stat.})\ ^{+4.8}_{-4.4}\ (\mathrm{syst.})\ \mathrm{nb}$. The total relative uncertainty amounts to 9%, resulting in the most precise $t\bar{t}$ cross-section measurement in heavy-ion collisions to date. The signal significance exceeds five standard deviations separately in the ℓ+jets and dilepton channels, leading to the first observation of the $t\bar{t}$ process in the dilepton decay mode in p+Pb collisions.

The nuclear modification factor for the $t\bar{t}$ process is extracted for the first time, yielding a value of $R_{p\mathrm{A}} = 1.090 \pm 0.039\ (\mathrm{stat.})\ ^{+0.094}_{-0.087}\ (\mathrm{syst.})$. The values of $\sigma_{t\bar{t}}^{p+\mathrm{Pb}}$ and $R_{p\mathrm{A}}$ are found to be consistent with theoretical predictions for four state-of-the-art nPDF sets. The results of this measurement were published in the Journal of High Energy Physics [39].

The $t\bar{t}$ process is also analysed in the dilepton decay mode in Pb+Pb collisions at $\sqrt{s_{\mathrm{NN}}} = 5.02$ TeV. The inclusive $t\bar{t}$ cross section is extracted, yielding a value of $\sigma_{t\bar{t}}^{\mathrm{Pb+Pb}} = 3.6\ ^{+1.0}_{-0.9}\ (\mathrm{stat.})\ ^{+0.8}_{-0.5}\ (\mathrm{syst.})\ \mu\mathrm{b} = 3.6\ ^{+1.2}_{-1.0}\ (\mathrm{tot.})\ \mu\mathrm{b}$. The total relative uncertainty is 31%, leading to the most precise $t\bar{t}$ cross-section measurement in Pb+Pb collisions achieved so far. The observed signal significance amounts to 5.0 standard deviations, resulting in the first observation of $t\bar{t}$ production in Pb+Pb collisions. The measured $\sigma_{t\bar{t}}^{\mathrm{Pb+Pb}}$ value is in agreement with the CMS result and theoretical predictions based on the four latest nPDF sets. The results of this measurement were published in Physical Review Letters [171] and recognised as Editors' Suggestion.

The presented measurements establish analysis methods for top-quark production in heavy-ion collisions using ℓ+jets and dilepton decays. Moreover, they mark the start of the heavy-ion physics program with top quarks at the LHC. In particular, they pave a new way for further studies of nPDFs and QGP at the LHC. The precise measurement of the $t\bar{t}$ process in p+Pb collisions provides valuable insights for constraining nPDFs in the high Bjorken-x region. The observation of top quarks in Pb+Pb collisions consolidates the evidence of the presence of all quark flavours in the pre-equilibrium stage of the QGP. This study opens a possibility of studying the time structure of the QGP via hadronically decaying W bosons from top-quark decays.

New data from Pb+Pb collisions, collected during the ongoing Run 3 data-taking campaign, will allow further studies of the $t\bar{t}$ process. So far, 1.7 nb^{-1} and 1.6 nb^{-1} of Pb+Pb data have been recorded with the ATLAS detector in 2023 and 2024, respectively, nearly doubling the integrated luminosity available in Run 2. The first analysis of the ℓ+jets channel of $t\bar{t}$ decays could provide input to the time structure of the QGP. However, a novel development of the b-tagging algorithm in Pb+Pb collisions would be essential for effectively suppressing the background processes in that decay mode. The p+Pb data statistics collected in Run 2 are sufficient for the first differential $t\bar{t}$ cross-section measurement. The $t\bar{t}$ cross section as a function of $t\bar{t}$ p_{T} or η could have a significant impact on the gluon nPDF.

Bibliography

[1] E. Fermi, *On the Quantization of the Monoatomic Ideal Gas*, *Rendiconti Lincei*, no. 3, pp. 145–149, 1926. arXiv: cond-mat/9912229 (cit. on p. 1).

[2] P. A. M. Dirac, *On the Theory of quantum mechanics*, *Proc. Roy. Soc. Lond. A*, vol. 112, pp. 661–677, 1926. DOI: 10.1098/rspa.1926.0133 (cit. on p. 1).

[3] S. N. Bose, *Plancks Gesetz und Lichtquantenhypothese*, *Zeitschrift für Physik*, vol. 26, no. 1, pp. 178–181, 1926. DOI: 10.1007/BF01327326 (cit. on p. 1).

[4] A. Einstein, *Quantentheorie des einatomigen idealen Gases. Zweite Abhandlung*, *Sitz.ber. Preuss. Akad. Wiss. Phys.*, vol. 23, pp. 245–257, Aug. 2006. DOI: 10.1002/3527608958.ch28 (cit. on p. 1).

[5] A. Pais and S. B. Treiman, *How Many Charm Quantum Numbers Are There?*, *Phys. Rev. Lett.*, vol. 35, p. 1556, 1975. DOI: 10.1103/PhysRevLett.35.1556 (cit. on p. 1).

[6] P. A. M. Dirac, *The quantum theory of the electron*, *Proc. Roy. Soc. Lond. A*, vol. 117, pp. 610–624, 1928. DOI: 10.1098/rspa.1928.0023 (cit. on p. 1).

[7] C.-N. Yang and R. L. Mills, *Conservation of Isotopic Spin and Isotopic Gauge Invariance*, *Phys. Rev.*, vol. 96, pp. 191–195, 1954. DOI: 10.1103/PhysRev.96.191 (cit. on p. 1).

[8] S. Tomonaga, *On a relativistically invariant formulation of the quantum theory of wave fields*, *Prog. Theor. Phys.*, vol. 1, pp. 27–42, 1946. DOI: 10.1143/PTP.1.27 (cit. on p. 1).

[9] J. S. Schwinger, *On Quantum electrodynamics and the magnetic moment of the electron*, *Phys. Rev.*, vol. 73, pp. 416–417, 1948. DOI: 10.1103/PhysRev.73.416 (cit. on p. 1).

[10] R. P. Feynman, *Space - time approach to quantum electrodynamics*, *Phys. Rev.*, vol. 76, pp. 769–789, 1949. DOI: 10.1103/PhysRev.76.769 (cit. on p. 1).

[11] S. L. Glashow, *Partial Symmetries of Weak Interactions*, *Nucl. Phys.*, vol. 22, pp. 579–588, 1961. DOI: 10.1016/0029-5582(61)90469-2 (cit. on p. 1).

[12] F. Englert and R. Brout, *Broken Symmetry and the Mass of Gauge Vector Mesons*, *Phys. Rev. Lett.*, vol. 13, pp. 321–323, 1964. DOI: 10.1103/PhysRevLett.13.321 (cit. on p. 1).

[13] P. W. Higgs, *Broken Symmetries and the Masses of Gauge Bosons*, *Phys. Rev. Lett.*, vol. 13, pp. 508–509, 1964. DOI: 10.1103/PhysRevLett.13.508 (cit. on p. 1).

[14] G. S. Guralnik, C. R. Hagen, and T. W. B. Kibble, *Global Conservation Laws and Massless Particles*, *Phys. Rev. Lett.*, vol. 13, pp. 585–587, 1964. DOI: 10.1103/PhysRevLett.13.585 (cit. on p. 1).

[15] S. Weinberg, *A Model of Leptons*, *Phys. Rev. Lett.*, vol. 19, pp. 1264–1266, 1967. DOI: 10.1103/PhysRevLett.19.1264 (cit. on p. 1).

[16] A. Salam, *Weak and Electromagnetic Interactions*, *Conf. Proc. C*, vol. 680519, pp. 367–377, 1968. DOI: 10.1142/9789812795915_0034 (cit. on p. 1).

[17] H. Fritzsch, M. Gell-Mann, and H. Leutwyler, *Advantages of the Color Octet Gluon Picture*, *Phys. Lett. B*, vol. 47, pp. 365–368, 1973. DOI: 10.1016/0370-2693(73)90625-4 (cit. on p. 1).

[18] D. J. Gross and F. Wilczek, *Ultraviolet Behavior of Nonabelian Gauge Theories*, *Phys. Rev. Lett.*, vol. 30, pp. 1343–1346, 1973. DOI: 10.1103/PhysRevLett.30.1343 (cit. on p. 1).

[19] H. D. Politzer, *Reliable Perturbative Results for Strong Interactions?*, *Phys. Rev. Lett.*, vol. 30, pp. 1346–1349, 1973. DOI: 10.1103/PhysRevLett.30.1346 (cit. on p. 1).

[20] Cush, *Standard model of elementary particles*, URL: https://en.m.wikipedia.org/wiki/File:Standard_Model_of_Elementary_Particles.svg (cit. on p. 2).

[21] A. Salam and J. C. Ward, *Electromagnetic and weak interactions*, *Phys. Lett.*, vol. 13, pp. 168–171, 1964. DOI: 10.1016/0031-9163(64)90711-5 (cit. on p. 2).

[22] H. Georgi and S. L. Glashow, *Unity of All Elementary Particle Forces*, *Phys. Rev. Lett.*, vol. 32, pp. 438–441, 1974. DOI: 10.1103/PhysRevLett.32.438 (cit. on p. 2).

[23] S. Carlip, *Quantum gravity: A Progress report*, *Rept. Prog. Phys.*, vol. 64, p. 885, 2001. DOI: 10.1088/0034-4885/64/8/301. arXiv: gr-qc/0108040 (cit. on p. 2).

[24] R. P. Feynman, *Very high-energy collisions of hadrons*, *Phys. Rev. Lett.*, vol. 23, pp. 1415–1417, 1969. DOI: 10.1103/PhysRevLett.23.1415 (cit. on p. 3).

[25] D. d'Enterria *et al.*, *The strong coupling constant: state of the art and the decade ahead*, *J. Phys. G*, vol. 51, no. 9, p. 090 501, 2024. DOI: 10.1088/1361-6471/ad1a78. arXiv: 2203.08271 [hep-ph] (cit. on p. 3).

[26] Y. L. Dokshitzer, *Calculation of the Structure Functions for Deep Inelastic Scattering and e^+e^- Annihilation by Perturbation Theory in Quantum Chromodynamics. Sov. Phys. JETP*, vol. 46, pp. 641–653, 1977 (cit. on p. 3).

[27] V. N. Gribov and L. N. Lipatov, *Deep inelastic e p scattering in perturbation theory*, *Sov. J. Nucl. Phys.*, vol. 15, pp. 438–450, 1972 (cit. on p. 3).

[28] G. Altarelli and G. Parisi, *Asymptotic Freedom in Parton Language*, *Nucl. Phys. B*, vol. 126, pp. 298–318, 1977. DOI: 10.1016/0550-3213(77)90384-4 (cit. on p. 3).

[29] T.-J. Hou *et al.*, *New CTEQ global analysis of quantum chromodynamics with high-precision data from the LHC*, *Phys. Rev. D*, vol. 103, no. 1, p. 014 013, 2021. DOI: 10.1103/PhysRevD.103.014013. arXiv: 1912.10053 [hep-ph] (cit. on pp. 3, 4).

[30] R. D. Ball *et al.*, *Parton distributions from high-precision collider data*, *Eur. Phys. J. C*, vol. 77, no. 10, p. 663, 2017. DOI: 10.1140/epjc/s10052-017-5199-5. arXiv: 1706.00428 [hep-ph] (cit. on p. 3).

[31] S. Bailey, T. Cridge, L. A. Harland-Lang, A. D. Martin, and R. S. Thorne, *Parton distributions from LHC, HERA, Tevatron and fixed target data: MSHT20 PDFs*, *Eur. Phys. J. C*, vol. 81, no. 4, p. 341, 2021. DOI: 10.1140/epjc/s10052-021-09057-0. arXiv: 2012.04684 [hep-ph] (cit. on p. 3).

[32] K. J. Eskola, P. Paakkinen, H. Paukkunen, and C. A. Salgado, *EPPS21: a global QCD analysis of nuclear PDFs*, *Eur. Phys. J. C*, vol. 82, no. 5, p. 413, 2022. DOI: 10.1140/epjc/s10052-022-10359-0. arXiv: 2112.12462 [hep-ph] (cit. on p. 5).

[33] B. J. Gilbert, *Measurement of dijet production in UPC with the ATLAS detector*, XXXth International Conference on Ultra-relativistic Nucleus-Nucleus Collisions, Sep. 2023, URL: https://indico.cern.ch/event/1139644/contributions/5542628/ (cit. on p. 5).

[34] European Muon Collaboration, *The ratio of the nucleon structure functions $F2_n$ for iron and deuterium*, *Phys. Lett. B*, vol. 123, pp. 275–278, 1983. DOI: 10.1016/0370-2693(83)90437-9 (cit. on p. 5).

[35] LHCb Collaboration, *Study of prompt D^0 meson production in pPb collisions at $\sqrt{s_{\mathrm{NN}}} = 5$ TeV*, *JHEP*, vol. 10, p. 090, 2017. DOI: 10.1007/JHEP10(2017)090. arXiv: 1707.02750 [hep-ex] (cit. on p. 5).

[36] CMS Collaboration, *Constraining gluon distributions in nuclei using dijets in proton-proton and proton-lead collisions at $\sqrt{s_{\mathrm{NN}}} = 5.02$ TeV*, *Phys. Rev. Lett.*, vol. 121, no. 6, p. 062 002, 2018. DOI: 10.1103/PhysRevLett.121.062002. arXiv: 1805.04736 [hep-ex] (cit. on p. 5).

[37] ATLAS Collaboration, *Measurement of the Centrality Dependence of the Dijet Yield in p+Pb Collisions at sNN=8.16 TeV with the ATLAS Detector*, *Phys. Rev. Lett.*, vol. 132, no. 10, p. 102 301, 2024. DOI: 10.1103/PhysRevLett.132.102301. arXiv: 2309.00033 [nucl-ex] (cit. on p. 5).

[38] ATLAS Collaboration, *Measurement of photonuclear jet production in ultra-peripheral Pb+Pb collisions at $\sqrt{s_{NN}} = 5.02$ TeV with the ATLAS detector*, Sep. 2024. arXiv: 2409.11060 [nucl-ex] (cit. on p. 5).

[39] ATLAS Collaboration, *Observation of $t\bar{t}$ production in the lepton+jets and dilepton channels in p+Pb collisions at $\sqrt{s_{\mathrm{NN}}} = 8.16$ TeV with the ATLAS detector*, *JHEP*, vol. 11, p. 101, 2024. DOI: 10.1007/JHEP11(2024)101. arXiv: 2405.05078 [nucl-ex] (cit. on pp. 5, 30, 53, 57, 59–61, 63, 65, 66, 70–78, 80, 81, 105).

[40] K. J. Eskola, P. Paakkinen, H. Paukkunen, and C. A. Salgado, *EPPS21: a global QCD analysis of nuclear PDFs*, *Eur. Phys. J. C*, vol. 82, no. 5, p. 413, 2022. DOI: 10.1140/epjc/s10052-022-10359-0. arXiv: 2112.12462 [hep-ph] (cit. on pp. 6, 79, 102).

[41] R. Abdul Khalek, R. Gauld, T. Giani, E. R. Nocera, T. R. Rabemananjara, and J. Rojo, *nNNPDF3.0: evidence for a modified partonic structure in heavy nuclei*, *Eur. Phys. J. C*, vol. 82, no. 6, p. 507, 2022. DOI: 10.1140/epjc/s10052-022-10417-7. arXiv: 2201.12363 [hep-ph] (cit. on pp. 6, 79, 102).

[42] P. Duwentäster *et al.*, *Impact of inclusive hadron production data on nuclear gluon PDFs*, *Phys. Rev. D*, vol. 104, p. 094 005, 2021. DOI: 10.1103/PhysRevD.104.094005. arXiv: 2105.09873 [hep-ph] (cit. on p. 6).

[43] I. Helenius, M. Walt, and W. Vogelsang, *TUJU21: nuclear PDFs with electroweak-boson data at NNLO*, in *29th International Workshop on Deep-Inelastic Scattering and Related Subjects*, Jul. 2022. arXiv: 2207.04654 [hep-ph] (cit. on pp. 6, 79, 102).

[44] M. Arneodo, *Nuclear effects in structure functions*, *Phys. Rept.*, vol. 240, pp. 301–393, 1994. DOI: 10.1016/0370-1573(94)90048-5 (cit. on p. 6).

[45] A. Bodek and J. L. Ritchie, *Fermi Motion Effects in Deep Inelastic Lepton Scattering from Nuclear Targets*, *Phys. Rev. D*, vol. 23, p. 1070, 1981. DOI: 10.1103/PhysRevD.23.1070 (cit. on p. 6).

[46] P. Paakkinen, *Constraining PDFs and nPDFs with recent data*, XXIXth International Conference on Ultra-relativistic Nucleus-Nucleus Collisions, Apr. 2022, URL: https://indico.cern.ch/event/895086/contributions/4615173/ (cit. on p. 6).

[47] D. d'Enterria, K. Krajczár, and H. Paukkunen, *Top-quark production in proton–nucleus and nucleus–nucleus collisions at LHC energies and beyond*, *Phys. Lett. B*, vol. 746, pp. 64–72, 2015. DOI: 10.1016/j.physletb.2015.04.044. arXiv: 1501.05879 [hep-ph] (cit. on pp. 6, 7).

[48] R. L. Workman *et al.*, *Review of Particle Physics*, *PTEP*, vol. 2022, p. 083C01, 2022. DOI: 10.1093/ptep/ptac097 (cit. on pp. 7, 10–12).

[49] M. A. Shifman, A. I. Vainshtein, and V. I. Zakharov, *QCD and Resonance Physics. Theoretical Foundations*, *Nucl. Phys. B*, vol. 147, pp. 385–447, 1979. DOI: 10.1016/0550-3213(79)90022-1 (cit. on p. 7).

[50] PHENIX Collaboration, *Formation of dense partonic matter in relativistic nucleus-nucleus collisions at RHIC: Experimental evaluation by the PHENIX collaboration*, *Nucl. Phys. A*, vol. 757, pp. 184–283, 2005. DOI: 10.1016/j.nuclphysa.2005.03.086. arXiv: nucl-ex/0410003 (cit. on p. 8).

[51] A. Bzdak, S. Esumi, V. Koch, J. Liao, M. Stephanov, and N. Xu, *Mapping the Phases of Quantum Chromodynamics with Beam Energy Scan*, *Phys. Rept.*, vol. 853, pp. 1–87, 2020. DOI: 10.1016/j.physrep.2020.01.005. arXiv: 1906.00936 [nucl-th] (cit. on p. 8).

[52] P. Braun-Munzinger and J. Wambach, *The Phase Diagram of Strongly-Interacting Matter*, *Rev. Mod. Phys.*, vol. 81, pp. 1031–1050, 2009. DOI: 10.1103/RevModPhys.81.1031. arXiv: 0801.4256 [hep-ph] (cit. on p. 8).

[53] M. G. Alford, A. Schmitt, K. Rajagopal, and T. Schäfer, *Color superconductivity in dense quark matter*, *Rev. Mod. Phys.*, vol. 80, pp. 1455–1515, 2008. DOI: 10.1103/RevModPhys.80.1455. arXiv: 0709.4635 [hep-ph] (cit. on p. 8).

[54] W. Busza, K. Rajagopal, and W. van der Schee, *Heavy Ion Collisions: The Big Picture, and the Big Questions*, *Ann. Rev. Nucl. Part. Sci.*, vol. 68, pp. 339–376, 2018. DOI: 10.1146/annurev-nucl-101917-020852. arXiv: 1802.04801 [hep-ph] (cit. on p. 9).

[55] P. Achenbach *et al.*, *The present and future of QCD*, *Nucl. Phys. A*, vol. 1047, p. 122 874, 2024. DOI: 10.1016/j.nuclphysa.2024.122874. arXiv: 2303.02579 [hep-ph] (cit. on p. 9).

[56] L. Cunqueiro and A. M. Sickles, *Studying the QGP with Jets at the LHC and RHIC*, *Prog. Part. Nucl. Phys.*, vol. 124, p. 103 940, 2022. DOI: 10.1016/j.ppnp.2022.103940. arXiv: 2110.14490 [nucl-ex] (cit. on p. 9).

[57] ATLAS Collaboration, *Measurement of the nuclear modification factor for inclusive jets in Pb+Pb collisions at $\sqrt{s_{\mathrm{NN}}} = 5.02$ TeV with the ATLAS detector*, *Phys. Lett. B*, vol. 790, pp. 108–128, 2019. DOI: 10.1016/j.physletb.2018.10.076. arXiv: 1805.05635 [nucl-ex] (cit. on pp. 9, 10).

[58] ATLAS Collaboration, *Measurement of the production and lepton charge asymmetry of W bosons in Pb+Pb collisions at $\sqrt{s_{\mathrm{NN}}} = 2.76\ TeV$ with the ATLAS detector*, *Eur. Phys. J. C*, vol. 75, no. 1, p. 23, 2015. DOI: 10.1140/epjc/s10052-014-3231-6. arXiv: 1408.4674 [hep-ex] (cit. on p. 9).

[59] CMS Collaboration, *Study of W Boson Production in PbPb and pp Collisions at $\sqrt{s_{NN}} = 2.76$ TeV*, *Phys. Lett. B*, vol. 715, pp. 66–87, 2012. DOI: 10.1016/j.physletb.2012.07.025. arXiv: 1205.6334 [nucl-ex] (cit. on p. 9).

[60] ATLAS Collaboration, *Measurement of the centrality dependence of J/ψ yields and observation of Z production in lead–lead collisions with the ATLAS detector at the LHC*, *Phys. Lett. B*, vol. 697, pp. 294–312, 2011. DOI: 10.1016/j.physletb.2011.02.006. arXiv: 1012.5419 [hep-ex] (cit. on pp. 9, 93).

[61] CMS Collaboration, *Study of Z boson production in PbPb collisions at $\sqrt{s_{NN}}$ = 2.76 TeV*, *Phys. Rev. Lett.*, vol. 106, p. 212 301, 2011. DOI: 10.1103/PhysRevLett.106.212301. arXiv: 1102.5435 [nucl-ex] (cit. on p. 9).

[62] ATLAS Collaboration, *Measurement of the nuclear modification factor of b-jets in 5.02 TeV Pb+Pb collisions with the ATLAS detector*, *Eur. Phys. J. C*, vol. 83, no. 5, p. 438, 2023. DOI: 10.1140/epjc/s10052-023-11427-9. arXiv: 2204.13530 [nucl-ex] (cit. on p. 9).

[63] CMS Collaboration, *Evidence of b-Jet Quenching in PbPb Collisions at $\sqrt{s_{NN}} = 2.76$ TeV*, *Phys. Rev. Lett.*, vol. 113, no. 13, p. 132 301, 2014. DOI: 10.1103/PhysRevLett.113.132301. arXiv: 1312.4198 [nucl-ex] (cit. on p. 9).

[64] ATLAS Collaboration, *Observation of the $\gamma\gamma \to \tau\tau$ Process in Pb+Pb Collisions and Constraints on the τ-Lepton Anomalous Magnetic Moment with the ATLAS Detector*, *Phys. Rev. Lett.*, vol. 131, no. 15, p. 151 802, 2023. DOI: 10.1103/PhysRevLett.131.151802. arXiv: 2204.13478 [hep-ex] (cit. on p. 9).

[65] CMS Collaboration, *Observation of τ Lepton Pair Production in Ultraperipheral Pb-Pb Collisions at $\sqrt{s_{NN}} = 5.02$ TeV*, *Phys. Rev. Lett.*, vol. 131, p. 151 803, 2023. DOI: 10.1103/PhysRevLett.131.151803. arXiv: 2206.05192 [nucl-ex] (cit. on p. 9).

[66] L. Apolinário, J. G. Milhano, G. P. Salam, and C. A. Salgado, *Probing the time structure of the quark-gluon plasma with top quarks*, *Phys. Rev. Lett.*, vol. 120, no. 23, p. 232 301, 2018. DOI: 10.1103/PhysRevLett.120.232301. arXiv: 1711.03105 [hep-ph] (cit. on p. 10).

[67] A. Giammanco and R. Schwienhorst, *Single top-quark production at the Tevatron and the LHC*, *Rev. Mod. Phys.*, vol. 90, no. 3, p. 035 001, 2018. DOI: 10.1103/RevModPhys.90.035001. arXiv: 1710.10699 [hep-ex] (cit. on p. 10).

[68] W. Bernreuther, M. Fucker, and Z.-G. Si, *Weak interaction corrections to hadronic top quark pair production: Contributions from quark-gluon and b anti-b induced reactions*, *Phys. Rev. D*, vol. 78, p. 017 503, 2008. DOI: 10.1103/PhysRevD.78.017503. arXiv: 0804.1237 [hep-ph] (cit. on p. 10).

[69] J. L. Diaz-Cruz, R. Gaitan-Lozano, G. Lopez-Castro, and C. E. Pagliarone, *CKM-suppressed top quark decays $t \to s\,(d) + W$ in the standard model and beyond*, *Phys. Rev. D*, vol. 77, p. 094 010, 2008. DOI: 10.1103/PhysRevD.77.094010. arXiv: 0712.3782 [hep-ph] (cit. on p. 11).

[70] ATLAS Collaboration, *Measurement of the $t\bar{t}$ cross section and its ratio to the Z production cross section using pp collisions at s=13.6 TeV with the ATLAS detector*, *Phys. Lett. B*, vol. 848, p. 138 376, 2024. DOI: 10.1016/j.physletb.2023.138376. arXiv: 2308.09529 [hep-ex] (cit. on pp. 12, 13).

[71] R. D. Ball *et al.*, *The PDF4LHC21 combination of global PDF fits for the LHC Run III*, *J. Phys. G*, vol. 49, no. 8, p. 080 501, 2022. DOI: 10.1088/1361-6471/ac7216. arXiv: 2203.05506 [hep-ph] (cit. on p. 12).

[72] ATLAS, CMS Collaborations, *Combination of inclusive top-quark pair production cross-section measurements using ATLAS and CMS data at $\sqrt{s}$ = 7 and 8 TeV*, *JHEP*, vol. 07, p. 213, 2023. DOI: 10.1007/JHEP07(2023)213. arXiv: 2205.13830 [hep-ex] (cit. on pp. 13, 79–81).

[73] CMS Collaboration, *Measurement of the inclusive $t\bar{t}$ cross section in final states with at least one lepton and additional jets with 302 pb^{-1} of pp collisions at $\sqrt{s}$ = 5.0 TeV*, *JHEP*, vol. 04, p. 099, 2025. DOI: 10.1007/JHEP04(2025)099. arXiv: 2410.21631 [hep-ex] (cit. on p. 14).

[74] CMS Collaboration, *Observation of top quark production in proton-nucleus collisions*, *Phys. Rev. Lett.*, vol. 119, no. 24, p. 242 001, 2017. DOI: 10.1103/PhysRevLett.119.242001. arXiv: 1709.07411 [nucl-ex] (cit. on pp. 14, 15, 79).

[75] S. Dulat *et al.*, *New parton distribution functions from a global analysis of quantum chromodynamics*, *Phys. Rev. D*, vol. 93, no. 3, p. 033 006, 2016. DOI: 10.1103/PhysRevD.93.033006. arXiv: 1506.07443 [hep-ph] (cit. on p. 14).

[76] K. J. Eskola, P. Paakkinen, H. Paukkunen, and C. A. Salgado, *EPPS16: Nuclear parton distributions with LHC data*, *Eur. Phys. J. C*, vol. 77, no. 3, p. 163, 2017. DOI: 10.1140/epjc/s10052-017-4725-9. arXiv: 1612.05741 [hep-ph] (cit. on p. 14).

[77] CMS Collaboration, *Measurements of the $t\bar{t}$ production cross section in lepton+jets final states in pp collisions at 8 TeV and ratio of 8 to 7 TeV cross sections*, *Eur. Phys. J. C*, vol. 77, no. 1, p. 15, 2017. DOI: 10.1140/epjc/s10052-016-4504-z. arXiv: 1602.09024 [hep-ex] (cit. on p. 14).

[78] CMS Collaboration, *Measurement of the $t\bar{t}$ production cross section in the $e\mu$ channel in proton-proton collisions at $\sqrt{s} = 7$ and 8 TeV*, *JHEP*, vol. 08, p. 029, 2016. DOI: 10.1007/JHEP08(2016)029. arXiv: 1603.02303 [hep-ex] (cit. on p. 14).

[79] CMS Collaboration, *Evidence for Top Quark Production in Nucleus-Nucleus Collisions*, *Phys. Rev. Lett.*, vol. 125, no. 22, p. 222 001, 2020. DOI: 10.1103/PhysRevLett.125.222001. arXiv: 2006.11110 [hep-ex] (cit. on pp. 14, 15, 103).

[80] CMS Collaboration, *Measurement of the inclusive $t\bar{t}$ cross section in pp collisions at $\sqrt{s} = 5.02$ TeV using final states with at least one charged lepton*, *JHEP*, vol. 03, p. 115, 2018. DOI: 10.1007/JHEP03(2018)115. arXiv: 1711.03143 [hep-ex] (cit. on p. 14).

[81] L. Evans and P. Bryant, *LHC Machine*, *JINST*, vol. 3, no. 08, S08001, Aug. 2008. DOI: 10.1088/1748-0221/3/08/S08001 (cit. on p. 16).

[82] V. Shiltsev, *The story of the Tevatron accelerators: Accelerator science and technology breakthroughs, achievements and lessons*, *Modern Physics Letters A*, vol. 27, no. 01, p. 1 230 001, 2012. DOI: 10.1142/S0217732312300017 (cit. on p. 16).

[83] Forthommel, *Map of the CERN accelerator complex*, URL: https://commons.wikimedia.org/wiki/File:Cern-accelerator-complex.svg (cit. on p. 17).

[84] ATLAS Collaboration, *The ATLAS Experiment at the CERN Large Hadron Collider*, *JINST*, vol. 3, no. 08, S08003, Aug. 2008. DOI: 10.1088/1748-0221/3/08/S08003 (cit. on pp. 17, 18).

[85] CMS Collaboration, *The CMS experiment at the CERN LHC*, *JINST*, vol. 3, no. 08, S08004, Aug. 2008. DOI: 10.1088/1748-0221/3/08/S08004 (cit. on p. 17).

[86] ALICE Collaboration, *The ALICE experiment at the CERN LHC*, *JINST*, vol. 3, no. 08, S08002, Aug. 2008. DOI: 10.1088/1748-0221/3/08/S08002 (cit. on p. 17).

[87] LHCb Collaboration, *The LHCb Detector at the LHC*, *JINST*, vol. 3, no. 08, S08005, Aug. 2008. DOI: 10.1088/1748-0221/3/08/S08005 (cit. on p. 17).

[88] TOTEM Collaboration, *The TOTEM Experiment at the CERN Large Hadron Collider*, *JINST*, vol. 3, no. 08, S08007, Aug. 2008. DOI: 10.1088/1748-0221/3/08/S08007 (cit. on p. 18).

[89] LHCf Collaboration, *The LHCf detector at the CERN Large Hadron Collider*, *JINST*, vol. 3, no. 08, S08006, Aug. 2008. DOI: 10.1088/1748-0221/3/08/S08006 (cit. on p. 18).

[90] MoEDAL Collaboration, *Technical Design Report of the MoEDAL Experiment*, CERN-LHCC-2009-006, Jun. 2009 (cit. on p. 18).

[91] FASER Collaboration, *The FASER detector*, *JINST*, vol. 19, no. 05, P05066, May 2024. DOI: 10.1088/1748-0221/19/05/P05066 (cit. on p. 18).

[92] SND@LHC Collaboration, *SND@LHC: the scattering and neutrino detector at the LHC*, *JINST*, vol. 19, no. 05, P05067, May 2024. DOI: 10.1088/1748-0221/19/05/P05067 (cit. on p. 18).

[93] CERN Document Server, *Computer generated image of the whole ATLAS detector*, URL: https://cds.cern.ch/record/1095924 (cit. on p. 18).

[94] T. Lenzi, *Development and Study of Different Muon Track Reconstruction Algorithms for the Level-1 Trigger for the CMS Muon Upgrade with GEM Detectors*, M.S. thesis, U. Brussels, 2013. arXiv: 1306.0858 [physics.ins-det] (cit. on p. 19).

[95] ATLAS Collaboration, *Study of the material of the ATLAS inner detector for Run 2 of the LHC*, *JINST*, vol. 12, no. 12, P12009, Dec. 2017. DOI: 10.1088/1748-0221/12/12/P12009 (cit. on p. 20).

[96] ATLAS Collaboration, *Software and computing for Run 3 of the ATLAS experiment at the LHC*, *Eur. Phys. J. C*, vol. 85, no. 3, p. 234, 2025. DOI: 10.1140/epjc/s10052-024-13701-w. arXiv: 2404.06335 [hep-ex] (cit. on p. 20).

[97] CERN Document Server, *Computer generated image of the ATLAS Inner Detector*, URL: https://cds.cern.ch/record/1095926 (cit. on p. 21).

[98] ATLAS Collaboration, *ATLAS pixel detector electronics and sensors*, *JINST*, vol. 3, no. 07, P07007, Jul. 2008. DOI: 10.1088/1748-0221/3/07/P07007 (cit. on p. 21).

[99] ATLAS Collaboration, *The ATLAS Insertable B-Layer: from construction to operation*, *JINST*, vol. 11, no. 12, p. C12036, 2016. DOI: 10.1088/1748-0221/11/12/C12036. arXiv: 1610.01994 [physics.ins-det] (cit. on p. 21).

[100] ATLAS Collaboration, *Operation and performance of the ATLAS semiconductor tracker*, *JINST*, vol. 9, no. 08, P08009, Aug. 2014. DOI: 10.1088/1748-0221/9/08/P08009 (cit. on p. 21).

[101] ATLAS Collaboration, *The ATLAS Transition Radiation Tracker (TRT) proportional drift tube: design and performance*, *JINST*, vol. 3, no. 02, P02013, Feb. 2008. DOI: 10.1088/1748-0221/3/02/P02013 (cit. on p. 22).

[102] ATLAS Collaboration, *ATLAS calorimeter performance Technical Design Report*, CERN-LHCC-96-40, Dec. 1996 (cit. on p. 22).

[103] CERN Document Server, *Computer Generated image of the ATLAS calorimeter*, URL: https://cds.cern.ch/record/1095927 (cit. on p. 23).

[104] ATLAS Collaboration, *ATLAS liquid argon calorimeter: Technical design report*, Dec. 1996, CERN-LHCC-96-041 (cit. on p. 22).

[105] ATLAS Collaboration, *ATLAS tile calorimeter: Technical design report*, CERN-LHCC-96-042, Dec. 1996 (cit. on p. 22).

[106] ATLAS Collaboration, *The ATLAS Forward Calorimeter*, *JINST*, vol. 3, no. 02, P02010, Feb. 2008. DOI: 10.1088/1748-0221/3/02/P02010 (cit. on p. 23).

[107] ATLAS Collaboration, *ATLAS muon spectrometer: Technical design report*, CERN-LHCC-97-22, Jun. 1997 (cit. on pp. 23, 24).

[108] CERN Document Server, *Computer generated image of the ATLAS Muons subsystem*, URL: https://cds.cern.ch/record/1095929 (cit. on p. 24).

[109] ATLAS Collaboration, *Resolution of the ATLAS muon spectrometer monitored drift tubes in LHC Run 2*, *JINST*, vol. 14, no. 09, P09011, Sep. 2019. DOI: 10.1088/1748-0221/14/09/P09011 (cit. on p. 23).

[110] G. Aielli, M. Bindi, and A. Polini, *Performance, operation and detector studies with the ATLAS Resistive Plate Chambers*, *JINST*, vol. 8, no. 02, P02020, Feb. 2013. DOI: 10.1088/1748-0221/8/02/P02020 (cit. on p. 24).

[111] W. Herr and B. Muratori, *Concept of luminosity*, *Proceedings of CERN Accelerator School*, 2006. DOI: 10.5170/CERN-2006-002.361 (cit. on p. 24).

[112] ATLAS Collaboration, *Public ATLAS Luminosity Results for Run-2 of the LHC*, URL: https://twiki.cern.ch/twiki/bin/view/AtlasPublic/LuminosityPublicResultsRun2 (cit. on pp. 25, 26).

[113] J. Arjona Martínez, O. Cerri, M. Pierini, M. Spiropulu, and J.-R. Vlimant, *Pileup mitigation at the Large Hadron Collider with graph neural networks*, *Eur. Phys. J. Plus*, vol. 134, no. 7, p. 333, 2019. DOI: 10.1140/epjp/i2019-12710-3. arXiv: 1810.07988 [hep-ph] (cit. on p. 26).

[114] ATLAS Collaboration, *Luminosity determination in pp collisions at $\sqrt{s} = 13$ TeV using the ATLAS detector at the LHC*, *Eur. Phys. J. C*, vol. 83, no. 10, p. 982, 2023. DOI: 10.1140/epjc/s10052-023-11747-w. arXiv: 2212.09379 [hep-ex] (cit. on pp. 26, 66, 92).

[115] LHCb Collaboration, *Centrality determination in heavy-ion collisions with the LHCb detector*, *JINST*, vol. 17, no. 05, P05009, 2022. DOI: 10.1088/1748-0221/17/05/P05009. arXiv: 2111.01607 [nucl-ex] (cit. on p. 27).

[116] M. L. Miller, K. Reygers, S. J. Sanders, and P. Steinberg, *Glauber modeling in high energy nuclear collisions*, *Ann. Rev. Nucl. Part. Sci.*, vol. 57, pp. 205–243, 2007. DOI: 10.1146/annurev.nucl.57.090506.123020. arXiv: nucl-ex/0701025 (cit. on pp. 27, 28).

[117] G. G. Adamian, N. V. Antonenko, H. Lenske, S. V. Tolokonnikov, and E. E. Saperstein, *Isotopic trends of nuclear surface properties of spherical nuclei*, *Phys. Rev. C*, vol. 94, no. 5, p. 054 309, 2016. DOI: 10.1103/PhysRevC.94.054309 (cit. on p. 27).

[118] B. Alver, M. Baker, C. Loizides, and P. Steinberg, *The PHOBOS Glauber Monte Carlo*, May 2008. arXiv: 0805.4411 [nucl-ex] (cit. on p. 27).

[119] ATLAS Collaboration, *Measurement of photon–jet transverse momentum correlations in 5.02 TeV Pb+Pb and pp collisions with ATLAS*, *Phys. Lett. B*, vol. 789, pp. 167–190, 2019. DOI: 10.1016/j.physletb.2018.12.023. arXiv: 1809.07280 [nucl-ex] (cit. on pp. 29, 85).

[120] ATLAS Collaboration, *Electron efficiency measurements with the ATLAS detector using 2012 LHC proton–proton collision data*, *Eur. Phys. J. C*, vol. 77, no. 3, p. 195, 2017. DOI: 10.1140/epjc/s10052-017-4756-2. arXiv: 1612.01456 [hep-ex] (cit. on p. 30).

[121] ATLAS Collaboration, *The ATLAS Simulation Infrastructure*, *Eur. Phys. J. C*, vol. 70, pp. 823–874, 2010. DOI: 10.1140/epjc/s10052-010-1429-9. arXiv: 1005.4568 [physics.ins-det] (cit. on pp. 31, 54, 83).

[122] S. Agostinelli *et al.*, *GEANT4–a simulation toolkit*, *Nucl. Instrum. Meth. A*, vol. 506, pp. 250–303, 2003. DOI: 10.1016/S0168-9002(03)01368-8 (cit. on pp. 31, 54, 83).

[123] S. Alioli, P. Nason, C. Oleari, and E. Re, *A general framework for implementing NLO calculations in shower Monte Carlo programs: the POWHEG BOX*, *JHEP*, vol. 06, p. 043, 2010. DOI: 10.1007/JHEP06(2010)043. arXiv: 1002.2581 [hep-ph] (cit. on pp. 31, 54, 83).

[124] T. Sjöstrand *et al.*, *An introduction to PYTHIA 8.2*, *Comput. Phys. Commun.*, vol. 191, pp. 159–177, 2015. DOI: 10.1016/j.cpc.2015.01.024. arXiv: 1410.3012 [hep-ph] (cit. on pp. 31, 54, 83).

[125] J. Pumplin, D. R. Stump, J. Huston, H. L. Lai, P. M. Nadolsky, and W. K. Tung, *New generation of parton distributions with uncertainties from global QCD analysis*, *JHEP*, vol. 07, p. 012, 2002. DOI: 10.1088/1126-6708/2002/07/012. arXiv: hep-ph/0201195 (cit. on p. 31).

[126] ATLAS Collaboration, *Measurement of the Z/γ^* boson transverse momentum distribution in pp collisions at $\sqrt{s}$ = 7 TeV with the ATLAS detector*, *JHEP*, vol. 09, p. 145, 2014. DOI: 10.1007/JHEP09(2014)145. arXiv: 1406.3660 [hep-ex] (cit. on p. 31).

[127] ATLAS Collaboration, *Electron and photon performance measurements with the ATLAS detector using the 2015–2017 LHC proton-proton collision data*, *Journal of Instrumentation*, vol. 14, no. 12, P12006–P12006, Dec. 2019. DOI: 10.1088/1748-0221/14/12/p12006 (cit. on pp. 31, 36, 56, 67, 85, 93).

[128] P. A. Potępa, *Measurement of high-p_T electron performance in proton-lead collisions in the ATLAS experiment*, *PoS*, vol. LHCP2022, p. 314, 2023. DOI: 10.22323/1.422.0314 (cit. on pp. 32, 34, 37, 40, 42).

[129] W. Lampl *et al.*, *Calorimeter Clustering Algorithms: Description and Performance*, ATL-LARG-PUB-2008-002, Geneva, 2008 (cit. on p. 33).

[130] ATLAS Collaboration, *Electron reconstruction and identification in the ATLAS experiment using the 2015 and 2016 LHC proton-proton collision data at $\sqrt{s}$ = 13 TeV*, *Eur. Phys. J. C*, vol. 79, no. 8, p. 639, 2019. DOI: 10.1140/epjc/s10052-019-7140-6. arXiv: 1902.04655 [physics.ins-det] (cit. on pp. 35, 37, 39).

[131] M. Cacciari and G. P. Salam, *Pileup subtraction using jet areas*, *Phys. Lett. B*, vol. 659, pp. 119–126, 2008. DOI: 10.1016/j.physletb.2007.09.077. arXiv: 0707.1378 [hep-ph] (cit. on p. 38).

[132] ATLAS Collaboration, *Performance of the ATLAS Trigger System in 2015*, *Eur. Phys. J. C*, vol. 77, no. 5, p. 317, 2017. DOI: 10.1140/epjc/s10052-017-4852-3. arXiv: 1611.09661 [hep-ex] (cit. on p. 41).

[133] ATLAS Collaboration, *Performance of electron and photon triggers in ATLAS during LHC Run 2*, *Eur. Phys. J. C*, vol. 80, no. 1, p. 47, 2020. DOI: 10.1140/epjc/s10052-019-7500-2. arXiv: 1909.00761 [hep-ex] (cit. on pp. 41, 56, 85).

[134] R. D. Ball *et al.*, *Parton distributions with LHC data*, *Nucl. Phys. B*, vol. 867, p. 244, 2013. DOI: 10.1016/j.nuclphysb.2012.10.003. arXiv: 1207.1303 [hep-ph] (cit. on p. 43).

[135] ATLAS Collaboration, *ATLAS Pythia 8 tunes to 7 TeV data*, ATL-PHYS-PUB-2014-021, Geneva, 2014 (cit. on pp. 43, 54, 66, 83).

[136] G. Bíró *et al.*, *Hijing++, a heavy ion jet interaction generator for the high-luminosity era of the lhc and beyond*, 2018. arXiv: 1811.02131 [physics.comp-ph] (cit. on pp. 43, 83).

[137] D. Scott, *Multivariate Density Estimation: Theory, Practice, and Visualization*. Wiley, 1992, ISBN: 9780471547709. DOI: 10.1002/9780470316849 (cit. on p. 47).

[138] J. Kremer, *Measurement of W boson production in pp collisions at 5.02 TeV and optimisation of electron identification in Pb+Pb collisions with the ATLAS detector*, CERN-THESIS-2019-172, 2019 (cit. on p. 51).

[139] D. J. Lange, *The EvtGen particle decay simulation package*, *Nucl. Instrum. Meth. A*, vol. 462, p. 152, 2001. DOI: 10.1016/S0168-9002(01)00089-4 (cit. on pp. 54, 83).

[140] J. Alwall *et al.*, *The automated computation of tree-level and next-to-leading order differential cross sections, and their matching to parton shower simulations*, *JHEP*, vol. 07, p. 079, 2014. DOI: 10.1007/JHEP07(2014)079. arXiv: 1405.0301 [hep-ph] (cit. on p. 54).

[141] NNPDF Collaboration, *Parton distributions for the LHC Run II*, *JHEP*, vol. 04, p. 040, 2015. DOI: 10.1007/JHEP04(2015)040. arXiv: 1410.8849 [hep-ph] (cit. on pp. 54, 67, 83).

[142] M. Czakon and A. Mitov, *Top++: A Program for the Calculation of the Top-Pair Cross-Section at Hadron Colliders*, *Comput. Phys. Commun.*, vol. 185, p. 2930, 2014. DOI: 10.1016/j.cpc.2014.06.021. arXiv: 1112.5675 [hep-ph] (cit. on pp. 54, 83).

[143] J. Bellm *et al.*, *Herwig 7.0/Herwig++ 3.0 release note*, *Eur. Phys. J. C*, vol. 76, no. 4, p. 196, 2016. DOI: 10.1140/epjc/s10052-016-4018-8. arXiv: 1512.01178 [hep-ph] (cit. on pp. 55, 84).

[144] J. Bellm *et al.*, *Herwig 7.2 release note*, *Eur. Phys. J. C*, vol. 80, no. 5, p. 452, 2020. DOI: 10.1140/epjc/s10052-020-8011-x. arXiv: 1912.06509 [hep-ph] (cit. on pp. 55, 84).

[145] S. Frixione, E. Laenen, P. Motylinski, C. White, and B. R. Webber, *Single-top hadroproduction in association with a W boson*, *JHEP*, vol. 07, p. 029, 2008. DOI: 10.1088/1126-6708/2008/07/029. arXiv: 0805.3067 [hep-ph] (cit. on pp. 55, 84).

[146] E. Bothmann *et al.*, *Event Generation with Sherpa 2.2*, *SciPost Phys.*, vol. 7, no. 3, p. 034, 2019. DOI: 10.21468/SciPostPhys.7.3.034. arXiv: 1905.09127 [hep-ph] (cit. on pp. 55, 85).

[147] S. Höche, F. Krauss, M. Schönherr, and F. Siegert, *W+ n-Jet predictions at the Large Hadron Collider at next-to-leading order matched with a parton shower*, *Phys. Rev. Lett.*, vol. 110, no. 5, p. 052 001, 2013. DOI: 10.1103/PhysRevLett.110.052001. arXiv: 1201.5882 [hep-ph] (cit. on pp. 55, 85).

[148] ATLAS Collaboration, *Performance of the ATLAS muon triggers in Run 2*, *JINST*, vol. 15, no. 09, P09015, 2020. DOI: 10.1088/1748-0221/15/09/p09015. arXiv: 2004.13447 [physics.ins-det] (cit. on pp. 56, 85).

[149] ATLAS Collaboration, *Vertex Reconstruction Performance of the ATLAS Detector at $\sqrt{s} = 13$ TeV*, ATL-PHYS-PUB-2015-026, 2015 (cit. on pp. 56, 85).

[150] ATLAS Collaboration, *Muon reconstruction and identification efficiency in ATLAS using the full Run 2 pp collision data set at $\sqrt{s} = 13$ TeV*, *Eur. Phys. J. C*, vol. 81, no. 7, p. 578, 2021. DOI: 10.1140/epjc/s10052-021-09233-2. arXiv: 2012.00578 [hep-ex] (cit. on pp. 56, 67, 86, 93).

[151] M. Cacciari, G. P. Salam, and G. Soyez, *The anti-k_t jet clustering algorithm*, *JHEP*, vol. 04, p. 063, 2008. DOI: 10.1088/1126-6708/2008/04/063. arXiv: 0802.1189 [hep-ph] (cit. on pp. 57, 86).

[152] M. Cacciari, G. P. Salam, and G. Soyez, *FastJet User Manual*, *Eur. Phys. J. C*, vol. 72, p. 1896, 2012. DOI: 10.1140/epjc/s10052-012-1896-2. arXiv: 1111.6097 [hep-ph] (cit. on pp. 57, 86).

[153] ATLAS Collaboration, *Measurement of the nuclear modification factor for inclusive jets in Pb+Pb collisions at $\sqrt{s_{\mathrm{NN}}} = 5.02$ TeV with the ATLAS detector*, *Phys. Lett. B*, vol. 790, pp. 108–128, 2019. DOI: 10.1016/j.physletb.2018.10.076. arXiv: 1805.05635 [nucl-ex] (cit. on pp. 58, 86).

[154] ATLAS Collaboration, *Jet energy scale and resolution measured in proton–proton collisions at $\sqrt{s} = 13$ TeV with the ATLAS detector*, *Eur. Phys. J. C*, vol. 81, no. 8, p. 689, 2021. DOI: 10.1140/epjc/s10052-021-09402-3. arXiv: 2007.02645 [hep-ex] (cit. on pp. 58, 68, 94).

[155] P. A. Potępa, *Comparison of two approaches to jet reconstruction in proton-lead collisions in ATLAS*, *PoS*, vol. LHCP2023, p. 259, 2024. DOI: 10.22323/1.450.0259 (cit. on p. 58).

[156] ATLAS Collaboration, *ATLAS b-jet identification performance and efficiency measurement with $t\bar{t}$ events in pp collisions at $\sqrt{s} = 13$ TeV*, *Eur. Phys. J. C*, vol. 79, no. 11, p. 970, 2019. DOI: 10.1140/epjc/s10052-019-7450-8. arXiv: 1907.05120 [hep-ex] (cit. on pp. 60, 68).

[157] ATLAS Collaboration, *Performance of missing transverse momentum reconstruction with the ATLAS detector using proton–proton collisions at $\sqrt{s} = 13$ TeV*, *Eur. Phys. J. C*, vol. 78, p. 903, 2018. DOI: 10.1140/epjc/s10052-018-6288-9. arXiv: 1802.08168 [hep-ex] (cit. on p. 61).

[158] ATLAS Collaboration, *Tools for estimating fake/non-prompt lepton backgrounds with the ATLAS detector at the LHC*, *JINST*, vol. 18, no. 11, T11004, 2023. DOI: 10.1088/1748-0221/18/11/T11004. arXiv: 2211.16178 [hep-ex] (cit. on p. 64).

[159] G. Avoni *et al.*, *The new LUCID-2 detector for luminosity measurement and monitoring in ATLAS*, vol. 13, no. 07, P07017–P07017, Jul. 2018. DOI: 10.1088/1748-0221/13/07/p07017 (cit. on pp. 66, 92).

[160] J. Butterworth *et al.*, *PDF4LHC recommendations for LHC Run II*, *J. Phys. G*, vol. 43, p. 023 001, 2016. DOI: 10.1088/0954-3899/43/2/023001. arXiv: 1510.03865 [hep-ph] (cit. on p. 66).

[161] ATLAS Collaboration, *Measurement of the $t\bar{t}$ production cross-section in pp collisions at $\sqrt{s}$ = 5.02 TeV with the ATLAS detector*, *JHEP*, vol. 06, p. 138, 2023. DOI: 10.1007/JHEP06(2023)138. arXiv: 2207.01354 [hep-ex] (cit. on pp. 67, 93, 103).

[162] E. Re, *Single-top Wt-channel production matched with parton showers using the POWHEG method*, *Eur. Phys. J. C*, vol. 71, p. 1547, 2011. DOI: 10.1140/epjc/s10052-011-1547-z. arXiv: 1009.2450 [hep-ph] (cit. on p. 67).

[163] C. F. Berger *et al.*, *Precise Predictions for W + 4-Jet Production at the Large Hadron Collider*, *Phys. Rev. Lett.*, vol. 106, p. 092 001, 2011. DOI: 10.1103/PhysRevLett.106.092001. arXiv: 1009.2338 [hep-ph] (cit. on p. 67).

[164] ATLAS Collaboration, *Jet energy scale and its uncertainty for jets reconstructed using the ATLAS heavy ion jet algorithm*, ATLAS-CONF-2015-016, Geneva, 2015 (cit. on pp. 68, 94).

[165] ATLAS Collaboration, *Calibration of the light-flavour jet mistagging efficiency of the b-tagging algorithms with Z+jets events using 139 fb^{-1} of ATLAS proton–proton collision data at $\sqrt{s} = 13$ TeV*, *Eur. Phys. J. C*, vol. 83, p. 728, 2023. DOI: 10.1140/epjc/s10052-023-11736-z. arXiv: 2301.06319 [hep-ex] (cit. on p. 68).

[166] K. Cranmer, G. Lewis, L. Moneta, A. Shibata, and W. Verkerke, *HistFactory: A tool for creating statistical models for use with RooFit and RooStats*, CERN-OPEN-2012-016, New York, 2012. DOI: 10.17181/CERN-OPEN-2012-016 (cit. on p. 68).

[167] P. Duwentäster *et al.*, *Impact of heavy quark and quarkonium data on nuclear gluon PDFs*, *Phys. Rev. D*, vol. 105, no. 11, p. 114 043, 2022. DOI: 10.1103/PhysRevD.105.114043. arXiv: 2204.09982 [hep-ph] (cit. on pp. 79, 102).

[168] J. M. Campbell, D. Wackeroth, and J. Zhou, *Study of weak corrections to Drell-Yan, top-quark pair, and dijet production at high energies with MCFM*, *Phys. Rev. D*, vol. 94, no. 9, p. 093 009, 2016. DOI: 10.1103/PhysRevD.94.093009. arXiv: 1608.03356 [hep-ph] (cit. on pp. 79, 102).

[169] M. Klasen and H. Paukkunen, *Nuclear PDFs After the First Decade of LHC Data*, Nov. 2023. arXiv: 2311.00450 [hep-ph] (cit. on p. 79).

[170] ATLAS Collaboration, *Measurement of the $t\bar{t}$ production cross-section using $e\mu$ events with b-tagged jets in pp collisions at $\sqrt{s}$ = 7 and 8* TeV *with the ATLAS detector*, *Eur. Phys. J. C*, vol. 74, no. 10, p. 3109, 2014. DOI: 10.1140/epjc/s10052-016-4501-2. arXiv: 1406.5375 [hep-ex] (cit. on pp. 80, 81).

[171] ATLAS Collaboration, *Observation of top-quark pair production in lead-lead collisions at* $\sqrt{s_{\mathrm{NN}}} = 5.02$ *TeV with the ATLAS detector*, *Phys. Rev. Lett.*, vol. 134, p. 142 301, Apr. 2025. DOI: 10.1103/PhysRevLett.134.142301. arXiv: 2411.10186 [hep-ex] (cit. on pp. 82, 87, 90, 92, 98, 100–102, 105).

[172] N. M. Abdelrahman, *Primordial Soup Was Full of Flavors*, *PRL Editors' Suggestion*, Apr. 2025, URL: https://physics.aps.org/articles/v18/75 (cit. on p. 82).

[173] Research Highlight, *Top quarks spotted at mega-detector could reveal clues to early Universe*, *Nature*, vol. 640, p. 573, Apr. 2025. DOI: 10.1038/d41586-025-01075-2 (cit. on p. 82).

[174] S. Höche, S. Mrenna, S. Payne, C. T. Preuss, and P. Skands, *A Study of QCD Radiation in VBF Higgs Production with Vincia and Pythia*, *SciPost Phys.*, vol. 12, no. 1, p. 010, 2022. DOI: 10.21468/SciPostPhys.12.1.010. arXiv: 2106.10987 [hep-ph] (cit. on p. 84).

[175] C. Oleari, *The POWHEG-BOX*, *Nucl. Phys. B Proc. Suppl.*, vol. 205-206, pp. 36–41, 2010. DOI: 10.1016/j.nuclphysbps.2010.08.016. arXiv: 1007.3893 [hep-ph] (cit. on p. 85).

[176] Y. He, L.-G. Pang, and X.-N. Wang, *Bayesian extraction of jet energy loss distributions in heavy-ion collisions*, *Phys. Rev. Lett.*, vol. 122, no. 25, p. 252 302, 2019. DOI: 10.1103/PhysRevLett.122.252302. arXiv: 1808.05310 [hep-ph] (cit. on p. 87).

[177] ATLAS Collaboration, *Measurements of the W production cross sections in association with jets with the ATLAS detector*, *Eur. Phys. J. C*, vol. 75, 82, p. 82, Feb. 2015. DOI: 10.1140/epjc/s10052-015-3262-7. arXiv: 1409.8639 [hep-ex] (cit. on p. 93).

[178] A. Hocker *et al.*, *TMVA - Toolkit for Multivariate Data Analysis*, Mar. 2007. arXiv: physics/0703039 (cit. on p. 94).

[179] L. Breiman, J. Friedman, C. Stone, and R. Olshen, *Classification and Regression Trees*. Taylor & Francis, 1984, ISBN: 9780412048418. DOI: 10.1201/9781315139470 (cit. on p. 94).

Appendix A

Electron performance

A.1 Electron performance in *p*+Pb collisions

A.1.1 Electron identification

Figures A.3–A.1 present scale factors for electron identification as a function of electron E_{T} and η for the Loose, LooseAndBLayer, and Tight working points.

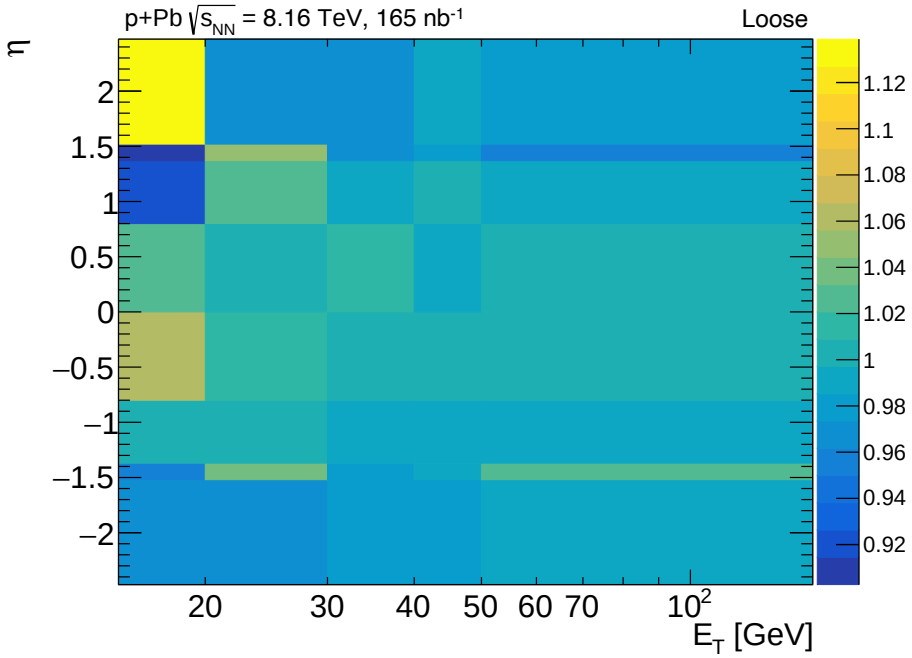

Figure A.1: Scale factors for electron identification as a function of electron E_{T} and η for the Loose working point. Total uncertainties are composed of statistical and systematic components added in quadrature.

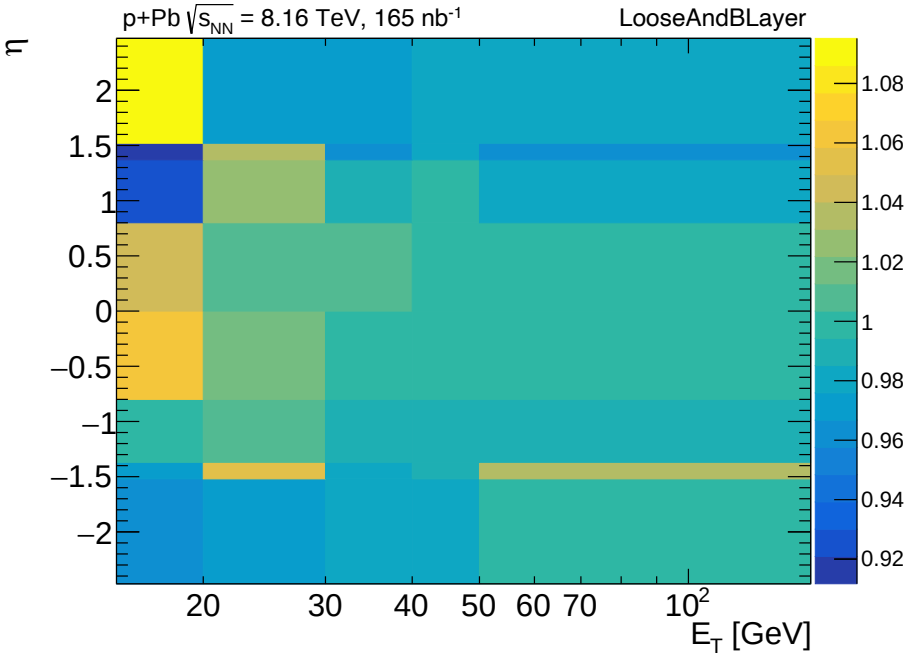

Figure A.2: Scale factors for electron identification as a function of electron E_{T} and η for the LooseAndBLayer working point. Total uncertainties are composed of statistical and systematic components added in quadrature.

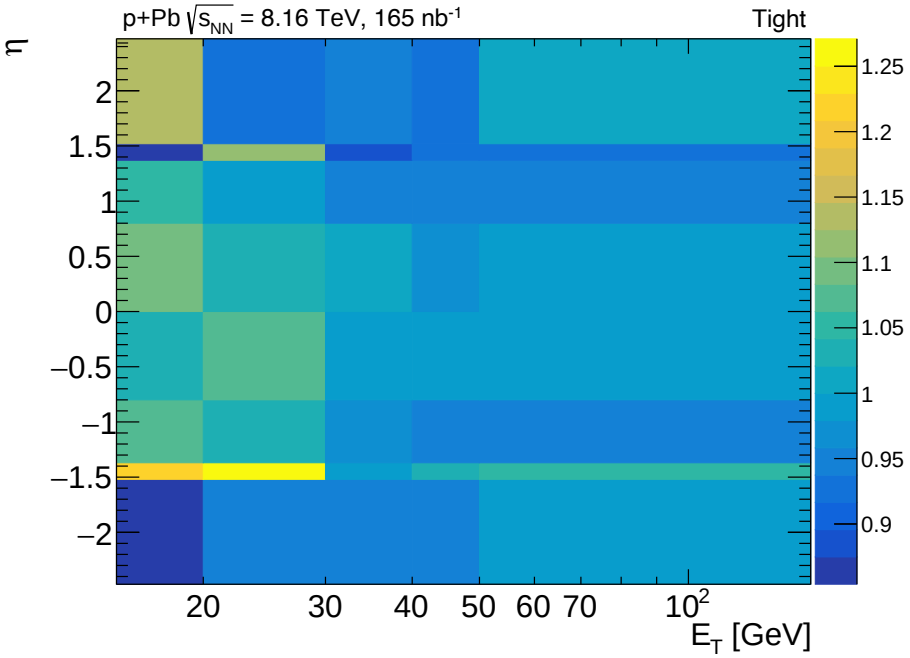

Figure A.3: Scale factors for electron identification as a function of electron E_{T} and η for the Tight working point. Total uncertainties are composed of statistical and systematic components added in quadrature.

A.1.2 Electron isolation

Figures A.6–A.4 present scale factors for electron isolation as a function of electron E_{T} and η for the FCLoose, FCHighPtCaloOnly, and FCTight working points.

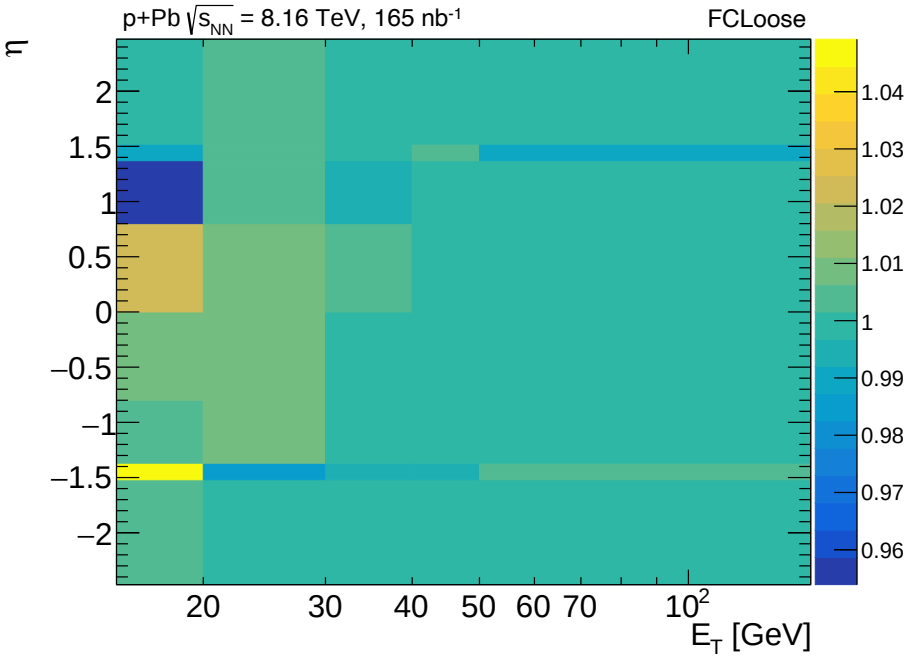

Figure A.4: Scale factors for electron identification as a function of electron E_{T} and η for the FCLoose working point. Total uncertainties are composed of statistical and systematic components added in quadrature.

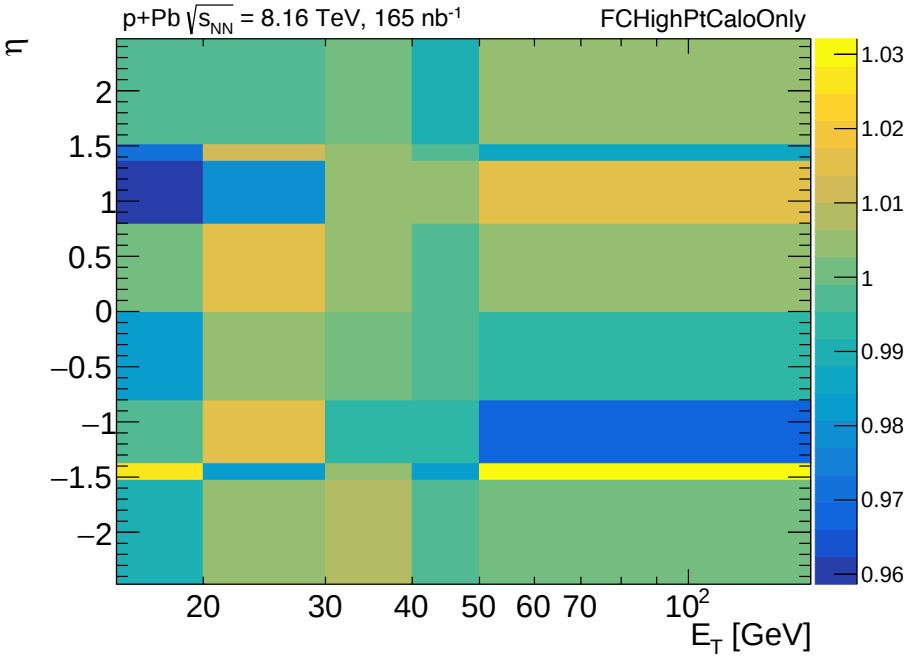

Figure A.5: Scale factors for electron identification as a function of electron E_{T} and η for the FCHighPtCaloOnly working point. Total uncertainties are composed of statistical and systematic components added in quadrature.

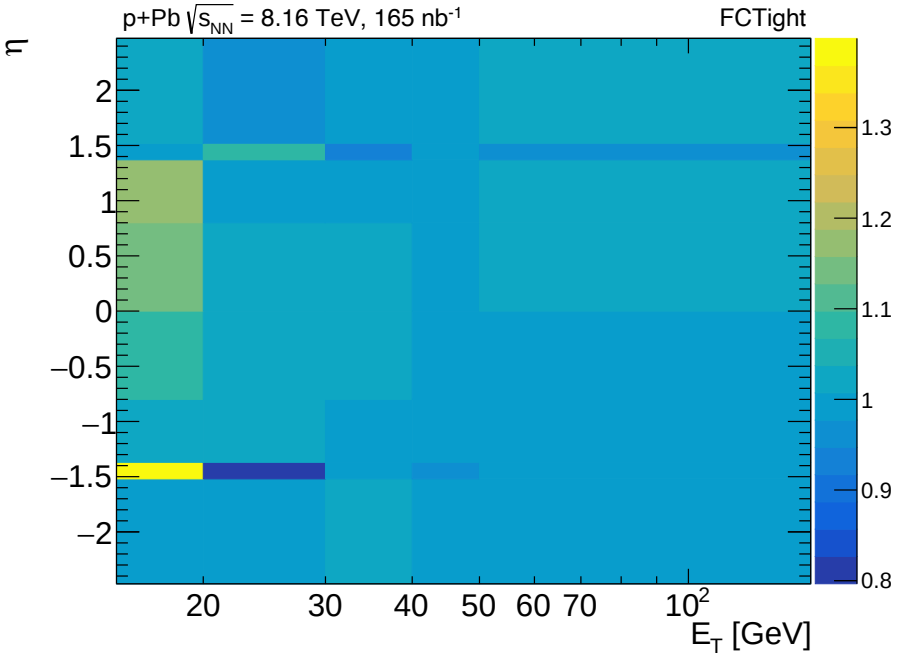

Figure A.6: Scale factors for electron identification as a function of electron E_{T} and η for the FCTight working point. Total uncertainties are composed of statistical and systematic components added in quadrature.

A.2 Electron performance in Pb+Pb collisions

A.2.1 Vertex position

Figures A.7–A.13 show distributions of electron discriminating variables for two MC samples with $z_0 = 0$ mm and $z_0 = 64$ mm.

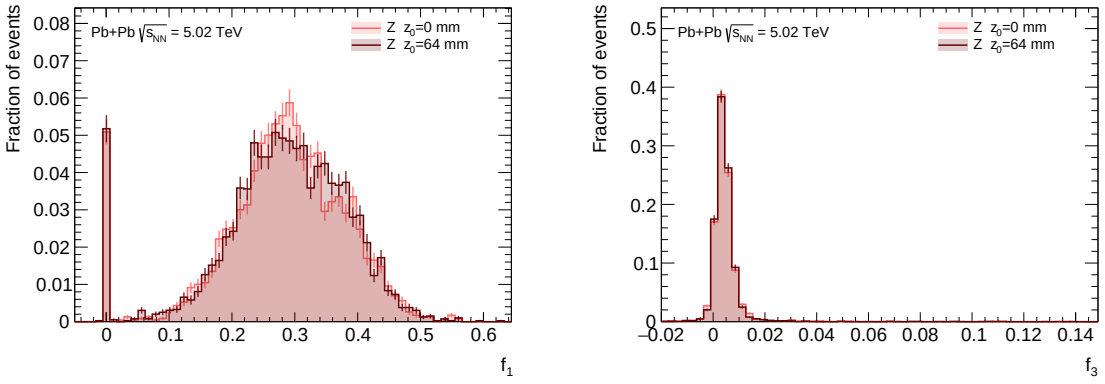

(a) (b)

Figure A.7: Distributions of the (a) f_1 and (b) f_3 electron discriminating variables for two fixed z_0 vertex positions. Error bars denote statistical uncertainties.

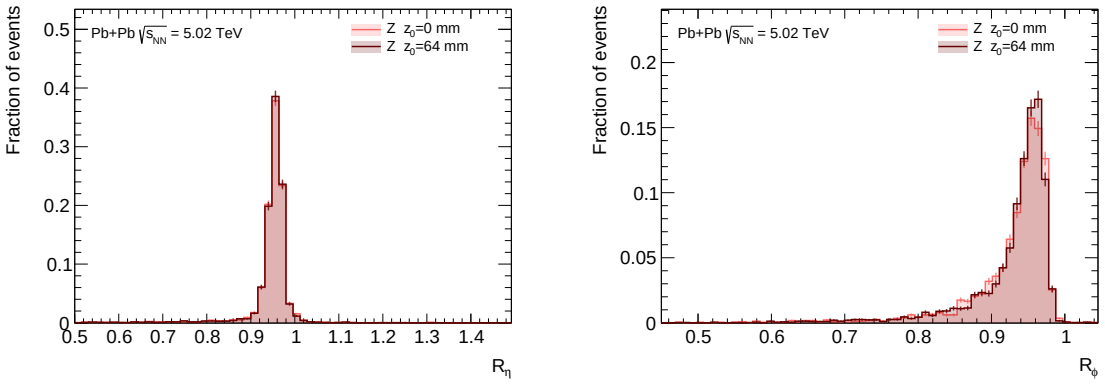

(a) (b)

Figure A.8: Distributions of the (a) R_η and (b) R_ϕ electron discriminating variables for two fixed z_0 vertex positions. Error bars denote statistical uncertainties.

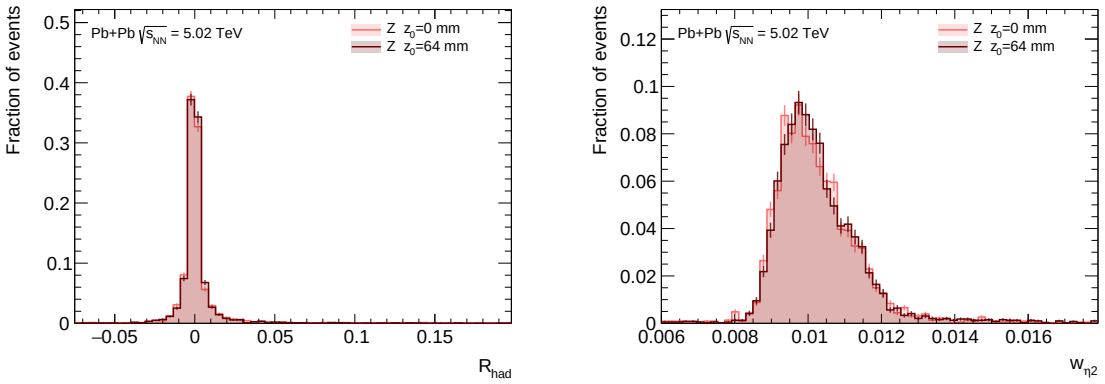

(a) (b)

Figure A.9: Distributions of the (a) R_{had} and (b) $w_{\eta 2}$ electron discriminating variables for two fixed z_0 vertex positions. Error bars denote statistical uncertainties.

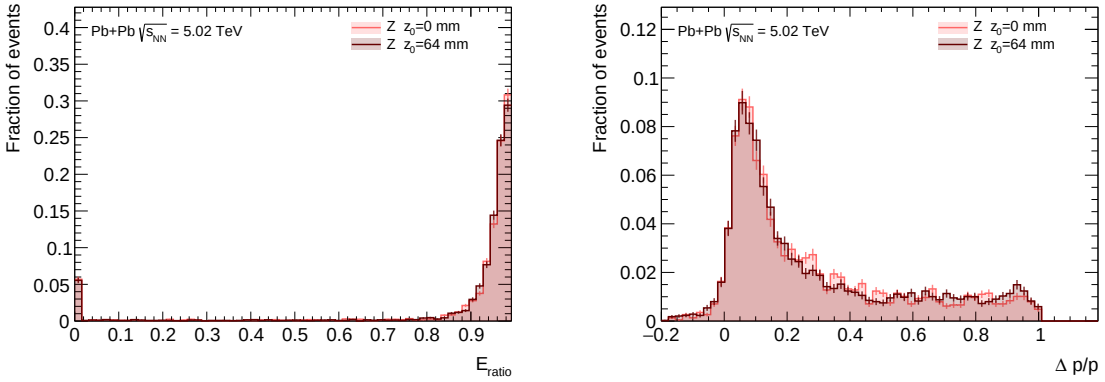

(a) (b)

Figure A.10: Distributions of the (a) E_{ratio} and (b) $\Delta p/p$ electron discriminating variables for two fixed z_0 vertex positions. Error bars denote statistical uncertainties.

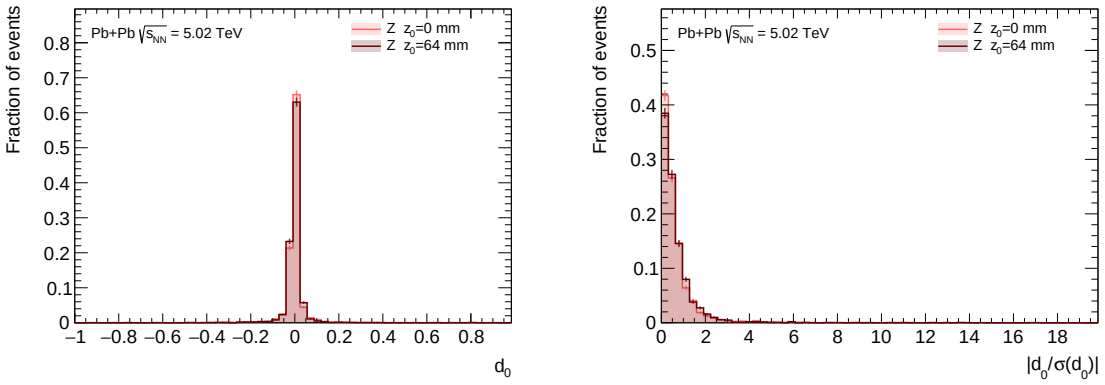

(a) (b)

Figure A.11: Distributions of the (a) d_0 and (b) $|d_0/\sigma(d0)|$ electron discriminating variables for two fixed z_0 vertex positions. Error bars denote statistical uncertainties.

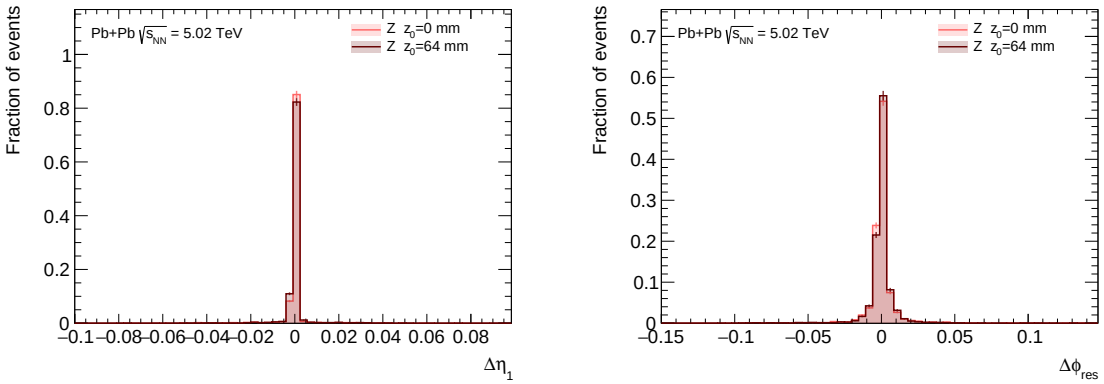

(a) (b)

Figure A.12: Distributions of the (a) $\Delta\eta_1$ and (b) $\Delta\phi_{\text{res}}$ electron discriminating variables for two fixed z_0 vertex positions. Error bars denote statistical uncertainties.

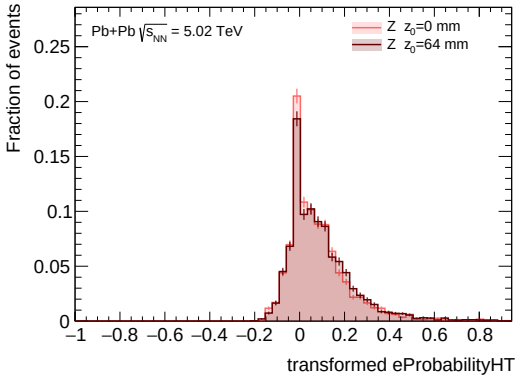

Figure A.13: Distribution of the eProbabilityHT electron discriminating variable for two fixed z_0 vertex positions. Error bars denote statistical uncertainties.

A.2.2 Collision centrality

Figures A.14–A.26 present distributions of electron discriminating variables for central and peripheral Pb+Pb collisions and as a function of centrality.

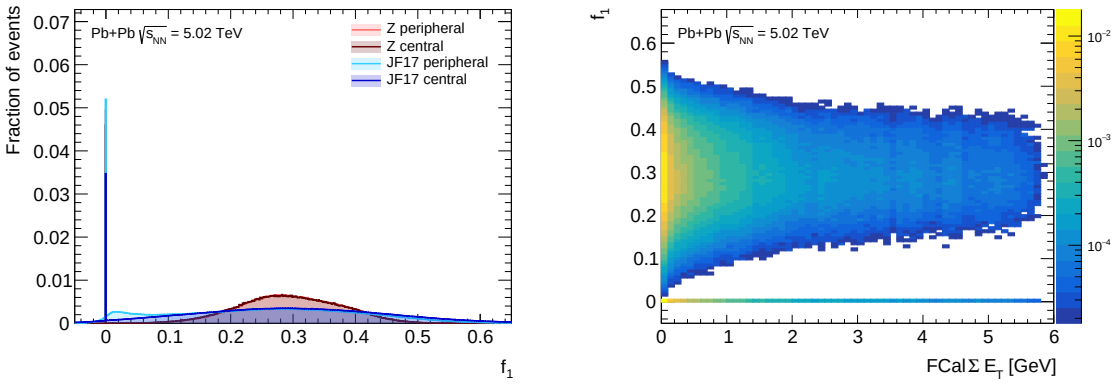

(a) (b)

Figure A.14: Distribution of the f_1 electron discriminating variable (a) for signal and background electrons in central and peripheral Pb+Pb collisions, and (b) for signal electrons as a function of centrality.

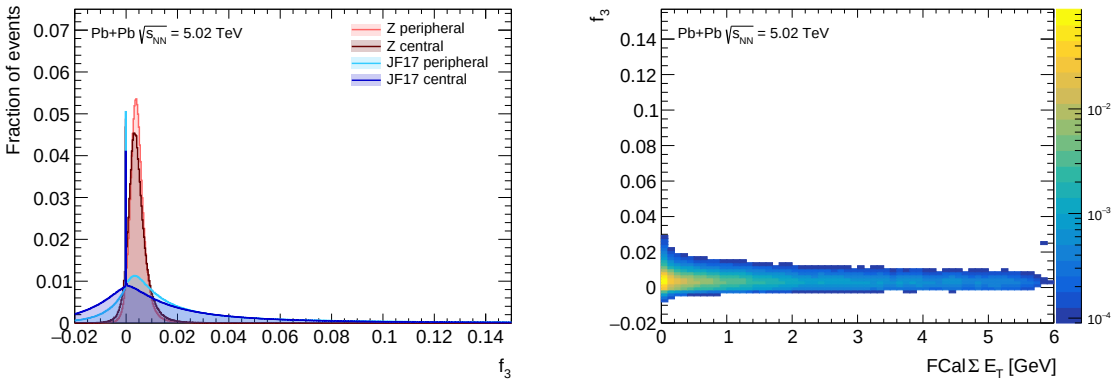

(a) (b)

Figure A.15: Distribution of the f_3 electron discriminating variable (a) for signal and background electrons in central and peripheral Pb+Pb collisions, and (b) for signal electrons as a function of centrality.

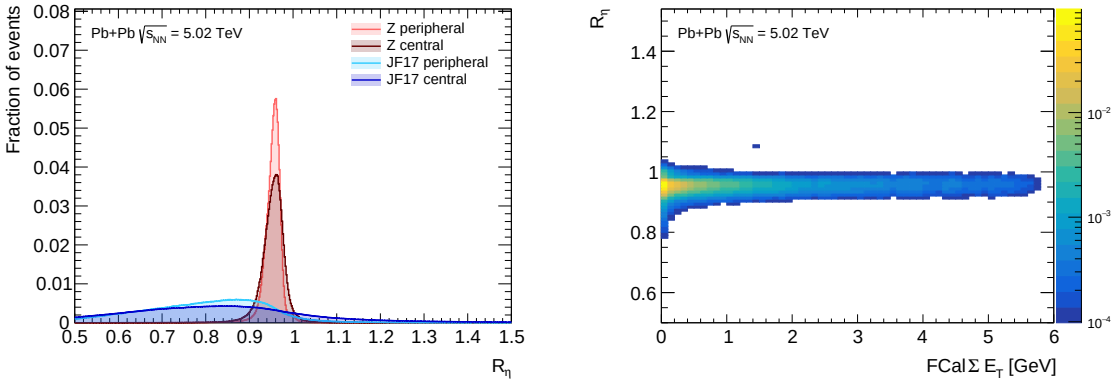

(a) (b)

Figure A.16: Distribution of the R_η electron discriminating variable (a) for signal and background electrons in central and peripheral Pb+Pb collisions, and (b) for signal electrons as a function of centrality.

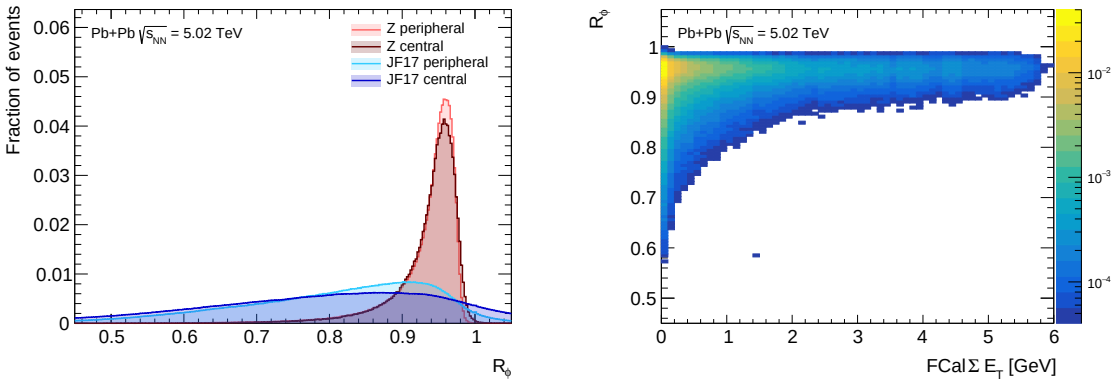

(a) (b)

Figure A.17: Distribution of the R_ϕ electron discriminating variable (a) for signal and background electrons in central and peripheral Pb+Pb collisions, and (b) for signal electrons as a function of centrality.

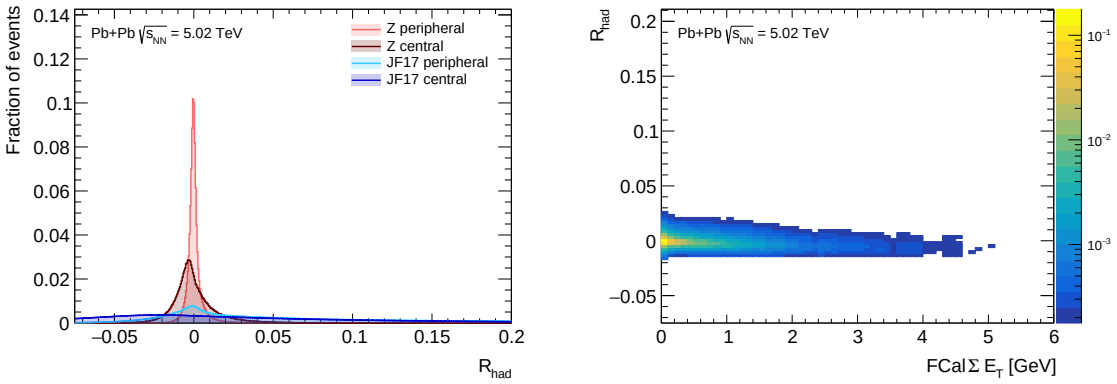

(a) (b)

Figure A.18: Distribution of the R_{had} electron discriminating variable (a) for signal and background electrons in central and peripheral Pb+Pb collisions, and (b) for signal electrons as a function of centrality.

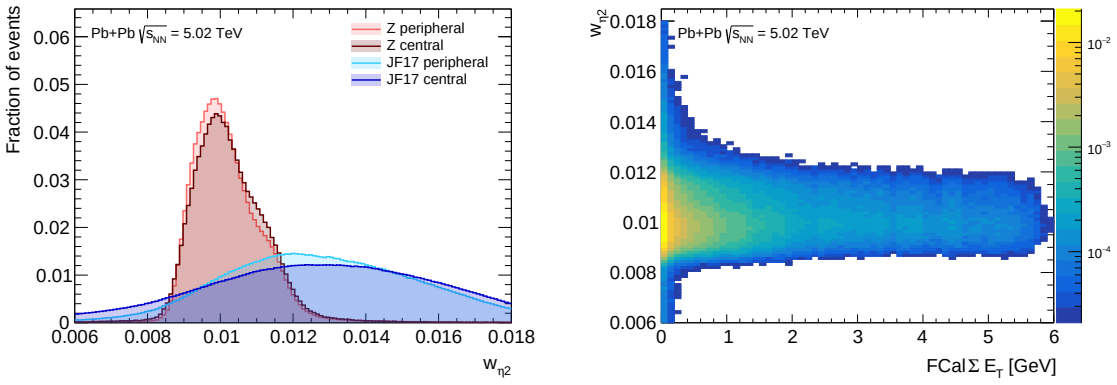

(a) (b)

Figure A.19: Distribution of the $w_{\eta 2}$ electron discriminating variable (a) for signal and background electrons in central and peripheral Pb+Pb collisions, and (b) for signal electrons as a function of centrality.

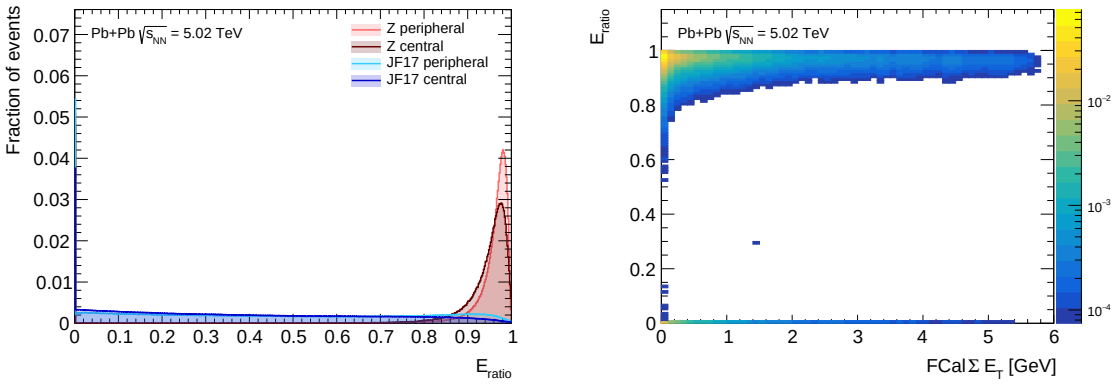

(a) (b)

Figure A.20: Distribution of the E_{ratio} electron discriminating variable (a) for signal and background electrons in central and peripheral Pb+Pb collisions, and (b) for signal electrons as a function of centrality.

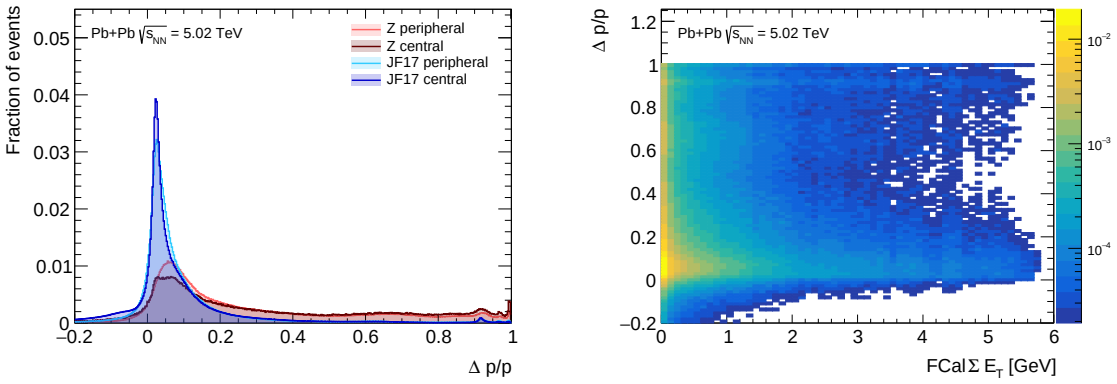

(a) (b)

Figure A.21: Distribution of the $\Delta p/p$ electron discriminating variable (a) for signal and background electrons in central and peripheral Pb+Pb collisions, and (b) for signal electrons as a function of centrality.

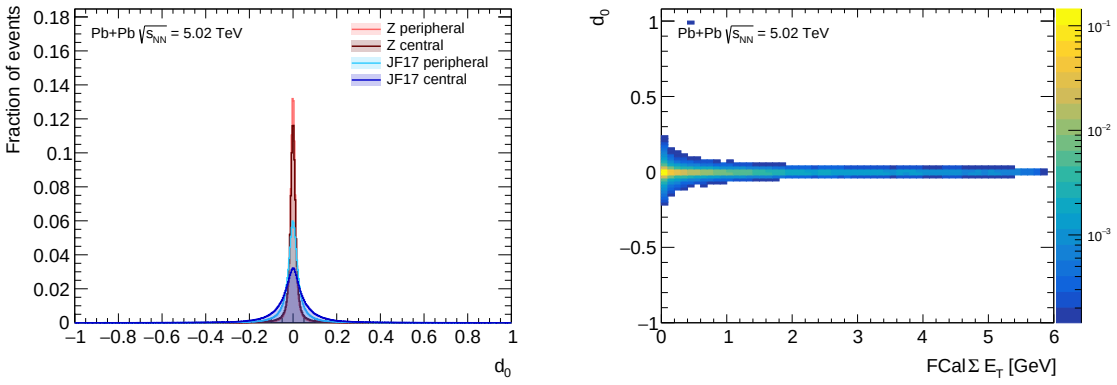

(a) (b)

Figure A.22: Distribution of the d_0 electron discriminating variable (a) for signal and background electrons in central and peripheral Pb+Pb collisions, and (b) for signal electrons as a function of centrality.

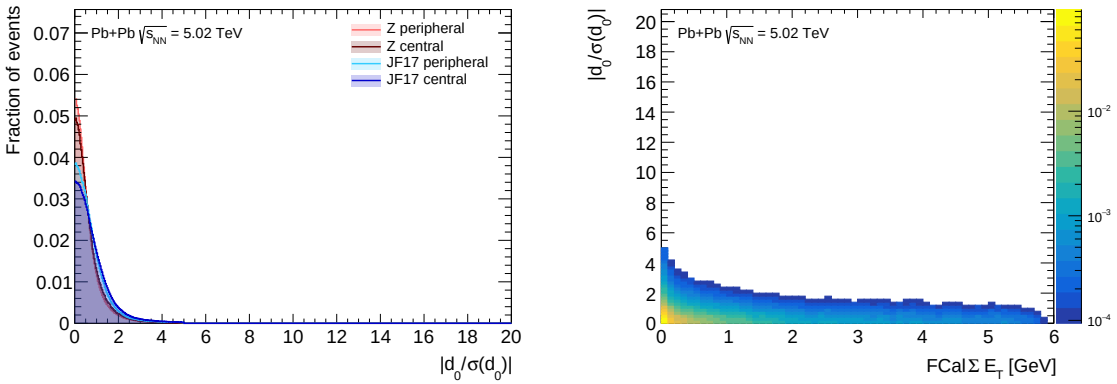

(a) (b)

Figure A.23: Distribution of the $|d_0/\sigma(d0)|$ electron discriminating variable (a) for signal and background electrons in central and peripheral Pb+Pb collisions, and (b) for signal electrons as a function of centrality.

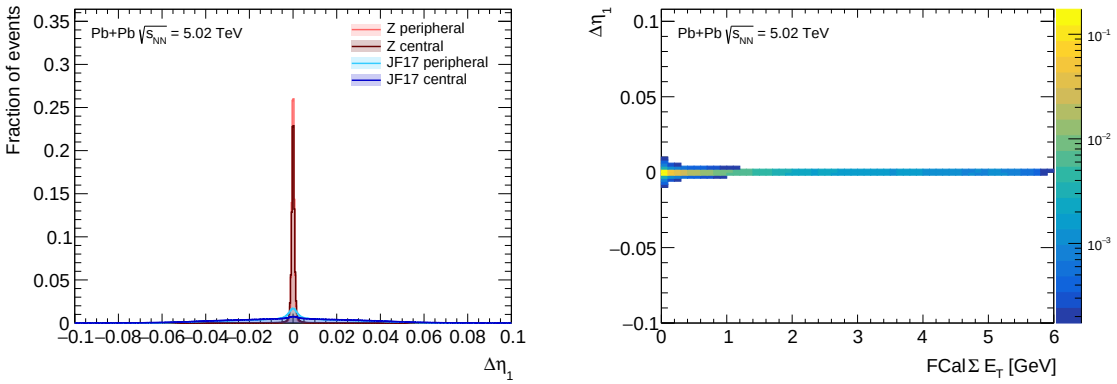

(a) (b)

Figure A.24: Distribution of the $\Delta\eta_1$ electron discriminating variable (a) for signal and background electrons in central and peripheral Pb+Pb collisions, and (b) for signal electrons as a function of centrality.

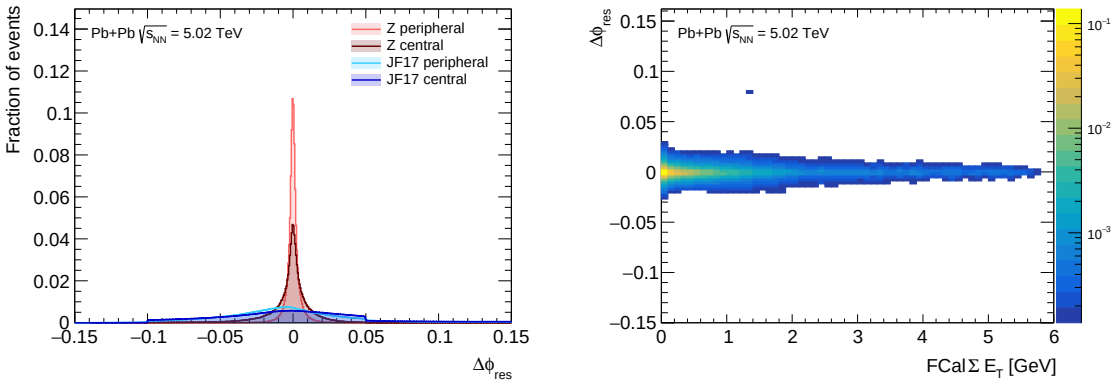

(a) (b)

Figure A.25: Distribution of the $\Delta\phi_{\mathrm{res}}$ electron discriminating variable (a) for signal and background electrons in central and peripheral Pb+Pb collisions, and (b) for signal electrons as a function of centrality.

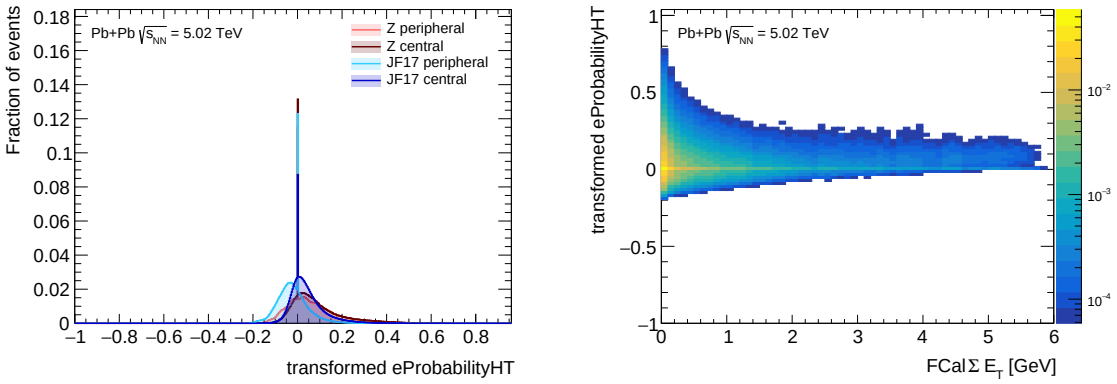

(a) (b)

Figure A.26: Distribution of the eProbabilityHT electron discriminating variable (a) for signal and background electrons in central and peripheral Pb+Pb collisions, and (b) for signal electrons as a function of centrality.

A.2.3 Probability distribution functions

Figures A.27–A.32 display probability distribution functions of electron discriminating variables for signal and background electrons in the kinematic range of $20 < E_{\mathrm{T}} < 30$ GeV and $0 < |\eta| < 0.6$.

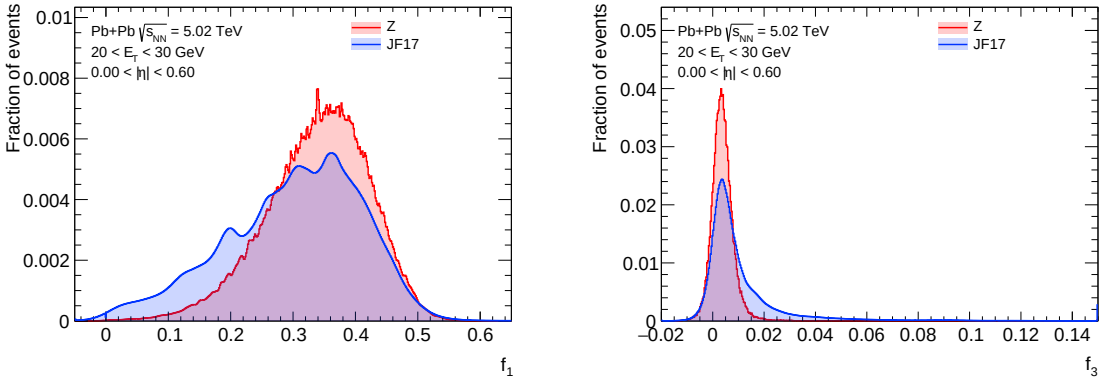

(a) (b)

Figure A.27: Probability distribution functions of the (a) f_1 and (b) f_3 electron discriminating variables for signal and background electrons.

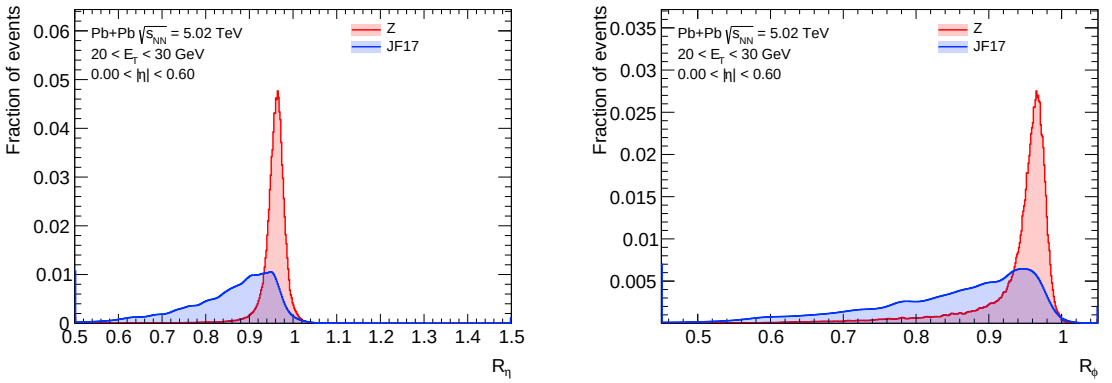

(a) (b)

Figure A.28: Probability distribution functions of the (a) R_η and (b) R_ϕ electron discriminating variables for signal and background electrons.

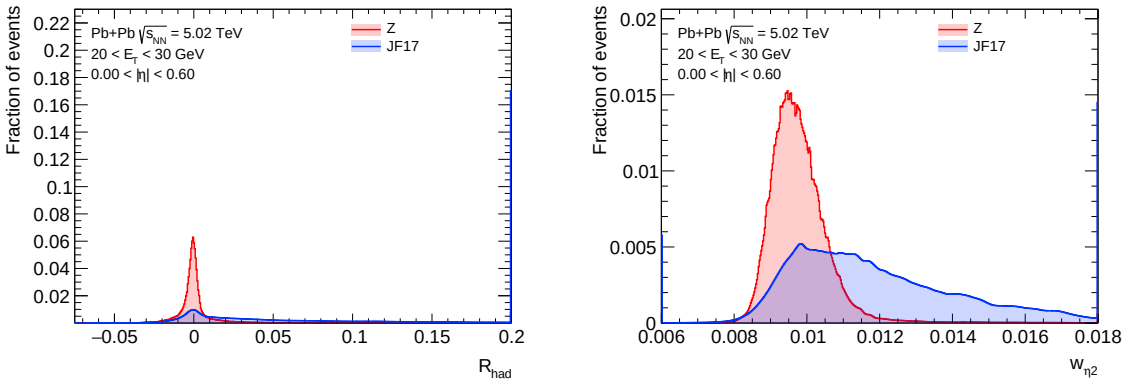

(a) (b)

Figure A.29: Probability distribution functions of the (a) R_{had} and (b) $w_{\eta 2}$ electron discriminating variables for signal and background electrons.

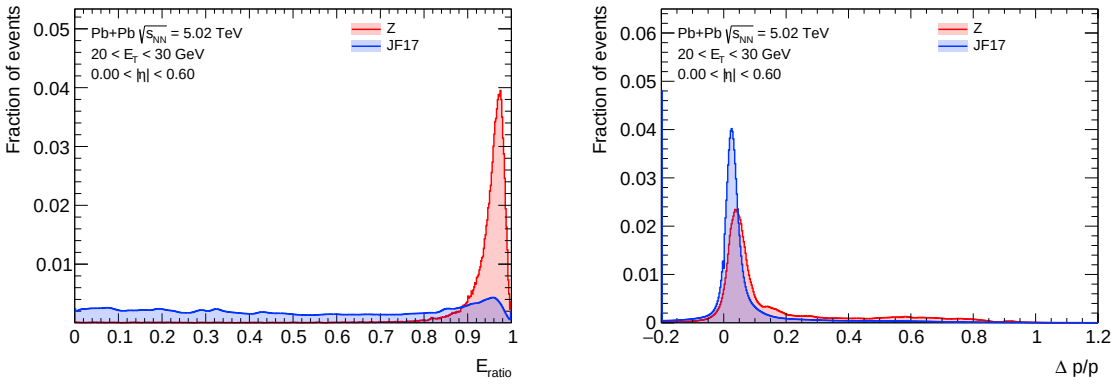

(a) (b)

Figure A.30: Probability distribution functions of the (a) E_{ratio} and (b) $\Delta p/p$ electron discriminating variables for signal and background electrons.

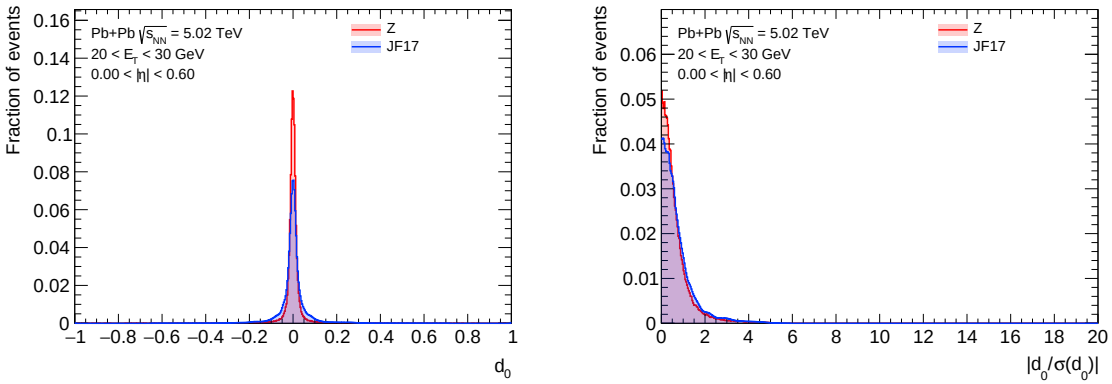

(a) (b)

Figure A.31: Probability distribution functions of the (a) d_0 and (b) $|d_0/\sigma(d0)|$ electron discriminating variables for signal and background electrons.

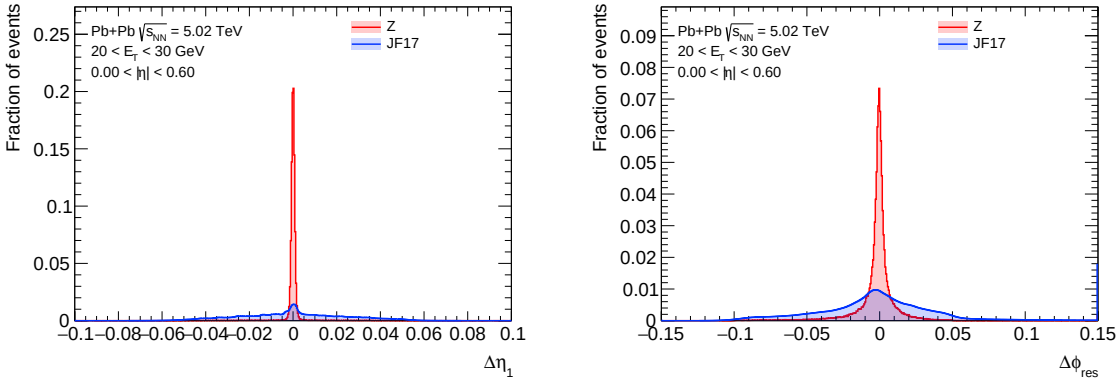

(a) (b)

Figure A.32: Probability distribution functions of the (a) $\Delta\eta_1$ and (b) $\Delta\phi_{\mathrm{res}}$ electron discriminating variables for signal and background electrons.

A.2.4 Optimisation of working points

Figures A.33–A.35 show the signal and background efficiencies for the HITight, HILoose, and HIVeryLoose working points.

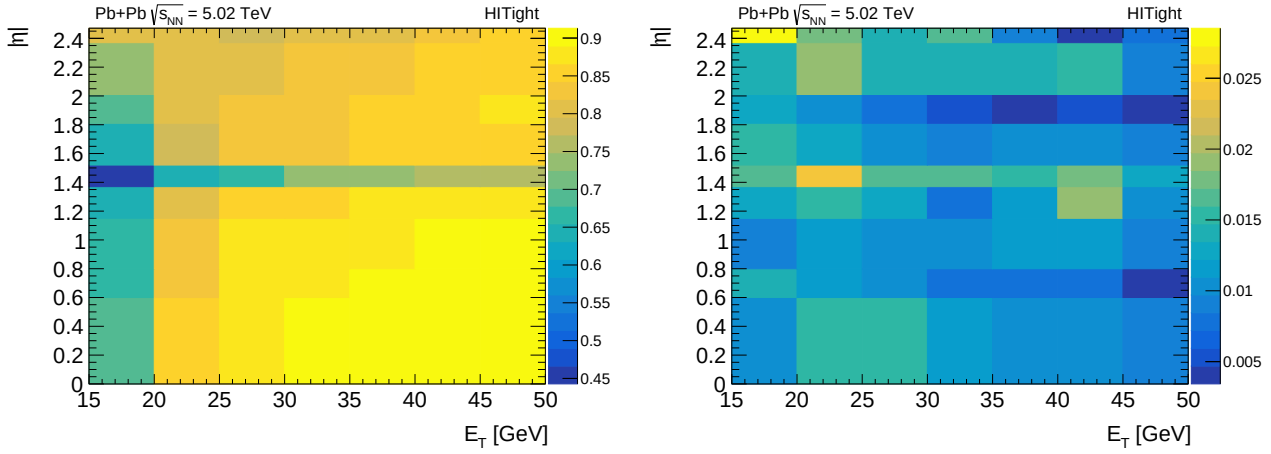

(a) (b)

Figure A.33: The (a) signal and (b) background efficiencies as a function of electron E_{T} and $|\eta|$ for the HITight working point.

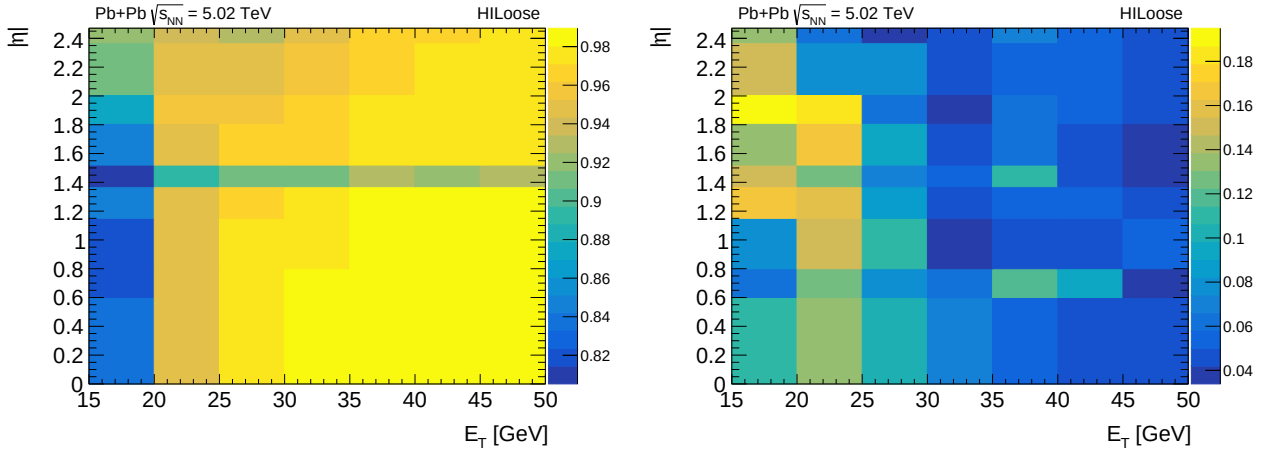

(a) (b)

Figure A.34: The (a) signal and (b) background efficiencies as a function of electron E_{T} and $|\eta|$ for the HILoose working point.

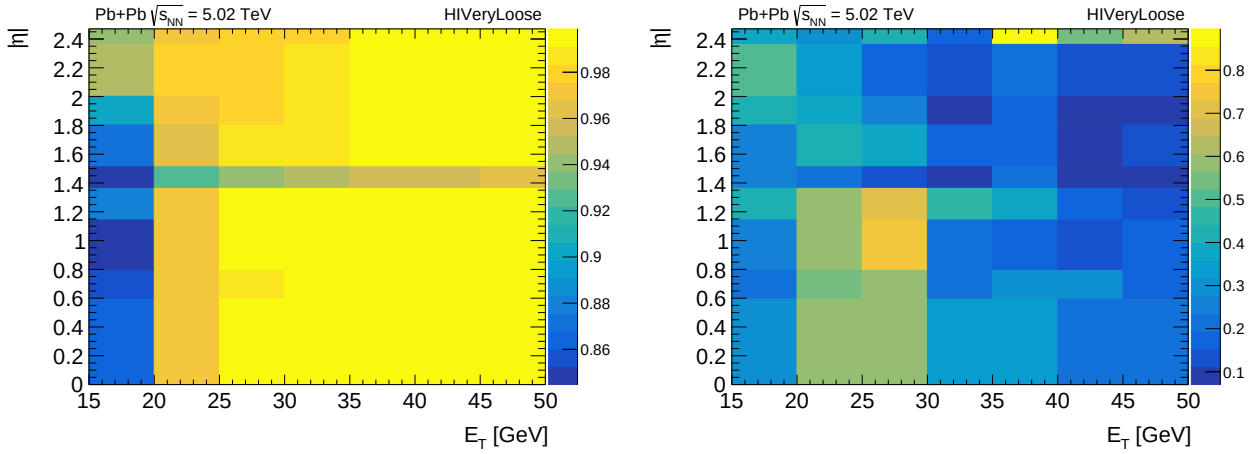

(a) (b)

Figure A.35: The (a) signal and (b) background efficiencies as a function of electron E_{T} and $|\eta|$ for the HIVeryLoose working point.

A.2.5 Invariant mass of electron pairs

Figures A.36 and A.37 present invariant mass distributions of opposite-sign electron pairs with reconstructed probes and probes passing the HIMedium identification selection, constituting the numerator and denominator of the identification efficiency, respectively, in different electron E_{T} and $|\eta|$ bins.

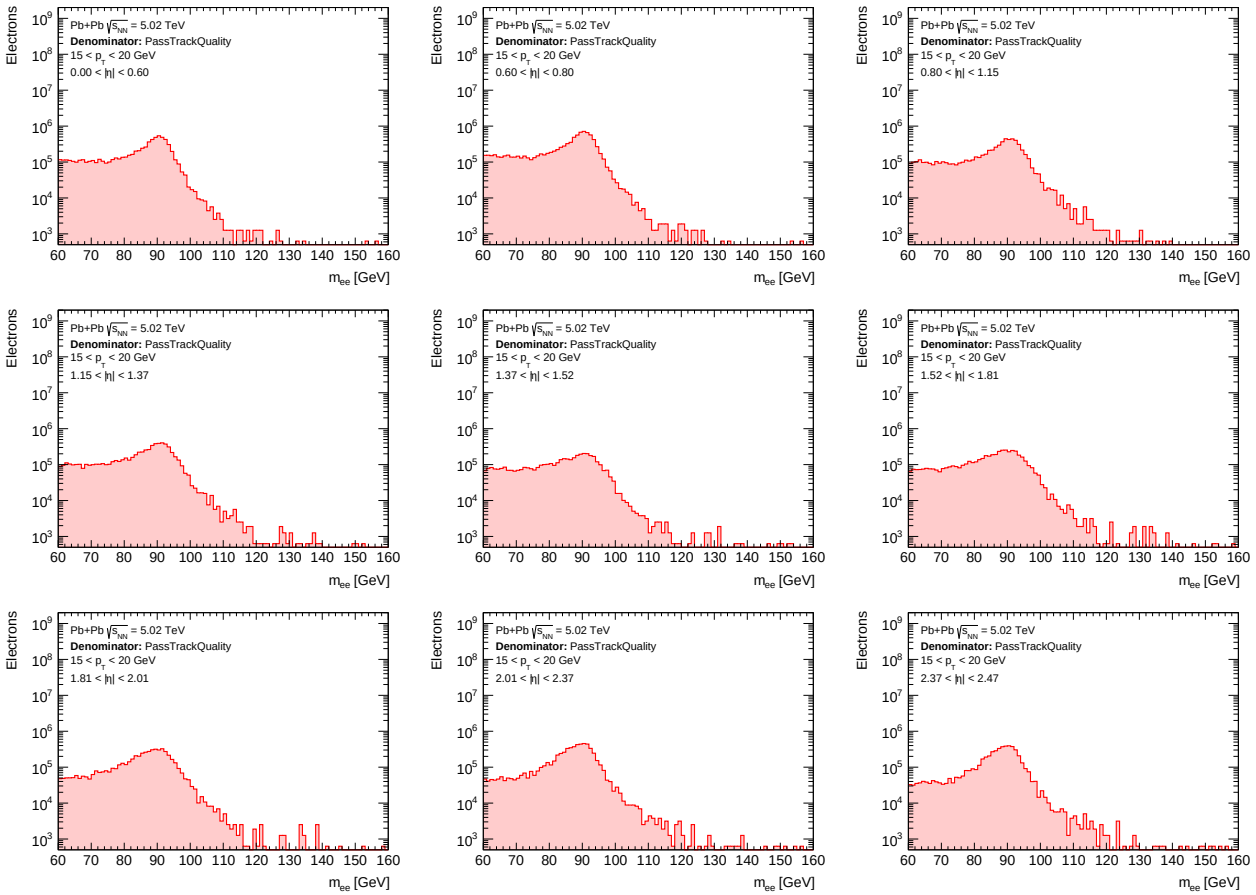

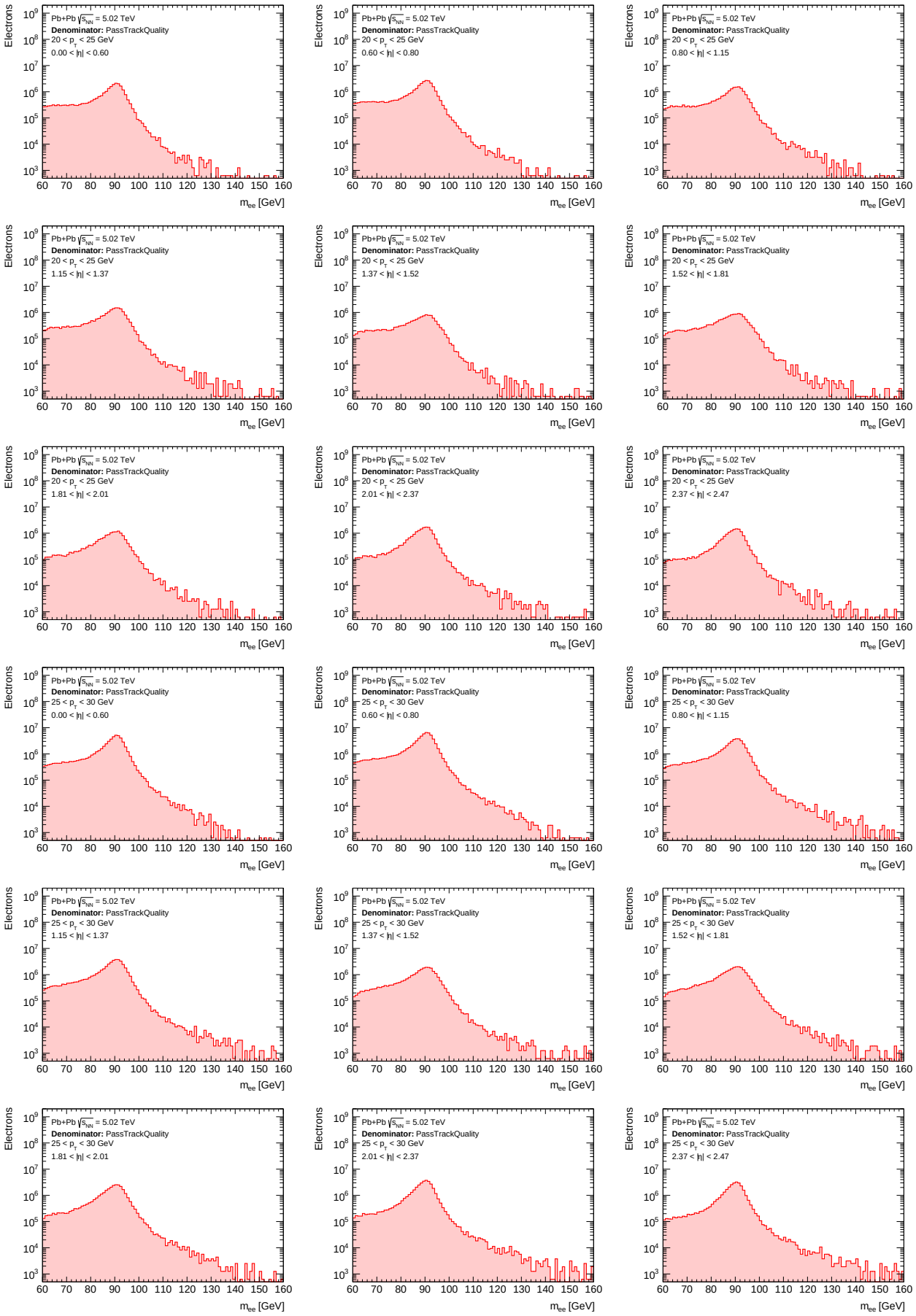
Electrons
Pb+Pb $\sqrt{s_{NN}}$ = 5.02 TeV
Denominator: PassTrackQuality
20 < p_T < 25 GeV
0.00 < |η| < 0.60
m_{ee} [GeV]
Pb+Pb $\sqrt{s_{NN}}$ = 5.02 TeV
Denominator: PassTrackQuality
20 < p_T < 25 GeV
0.60 < |η| < 0.80
m_{ee} [GeV]
Pb+Pb $\sqrt{s_{NN}}$ = 5.02 TeV
Denominator: PassTrackQuality
20 < p_T < 25 GeV
0.80 < |η| < 1.15
m_{ee} [GeV]
Pb+Pb $\sqrt{s_{NN}}$ = 5.02 TeV
Denominator: PassTrackQuality
20 < p_T < 25 GeV
1.15 < |η| < 1.37
m_{ee} [GeV]
Pb+Pb $\sqrt{s_{NN}}$ = 5.02 TeV
Denominator: PassTrackQuality
20 < p_T < 25 GeV
1.37 < |η| < 1.52
m_{ee} [GeV]
Pb+Pb $\sqrt{s_{NN}}$ = 5.02 TeV
Denominator: PassTrackQuality
20 < p_T < 25 GeV
1.52 < |η| < 1.81
m_{ee} [GeV]
Pb+Pb $\sqrt{s_{NN}}$ = 5.02 TeV
Denominator: PassTrackQuality
20 < p_T < 25 GeV
1.81 < |η| < 2.01
m_{ee} [GeV]
Pb+Pb $\sqrt{s_{NN}}$ = 5.02 TeV
Denominator: PassTrackQuality
20 < p_T < 25 GeV
2.01 < |η| < 2.37
m_{ee} [GeV]
Pb+Pb $\sqrt{s_{NN}}$ = 5.02 TeV
Denominator: PassTrackQuality
20 < p_T < 25 GeV
2.37 < |η| < 2.47
m_{ee} [GeV]
Pb+Pb $\sqrt{s_{NN}}$ = 5.02 TeV
Denominator: PassTrackQuality
25 < p_T < 30 GeV
0.00 < |η| < 0.60
m_{ee} [GeV]
Pb+Pb $\sqrt{s_{NN}}$ = 5.02 TeV
Denominator: PassTrackQuality
25 < p_T < 30 GeV
0.60 < |η| < 0.80
m_{ee} [GeV]
Pb+Pb $\sqrt{s_{NN}}$ = 5.02 TeV
Denominator: PassTrackQuality
25 < p_T < 30 GeV
0.80 < |η| < 1.15
m_{ee} [GeV]
Pb+Pb $\sqrt{s_{NN}}$ = 5.02 TeV
Denominator: PassTrackQuality
25 < p_T < 30 GeV
1.15 < |η| < 1.37
m_{ee} [GeV]
Pb+Pb $\sqrt{s_{NN}}$ = 5.02 TeV
Denominator: PassTrackQuality
25 < p_T < 30 GeV
1.37 < |η| < 1.52
m_{ee} [GeV]
Pb+Pb $\sqrt{s_{NN}}$ = 5.02 TeV
Denominator: PassTrackQuality
25 < p_T < 30 GeV
1.52 < |η| < 1.81
m_{ee} [GeV]
Pb+Pb $\sqrt{s_{NN}}$ = 5.02 TeV
Denominator: PassTrackQuality
25 < p_T < 30 GeV
1.81 < |η| < 2.01
m_{ee} [GeV]
Pb+Pb $\sqrt{s_{NN}}$ = 5.02 TeV
Denominator: PassTrackQuality
25 < p_T < 30 GeV
2.01 < |η| < 2.37
m_{ee} [GeV]
Pb+Pb $\sqrt{s_{NN}}$ = 5.02 TeV
Denominator: PassTrackQuality
25 < p_T < 30 GeV
2.37 < |η| < 2.47
m_{ee} [GeV]

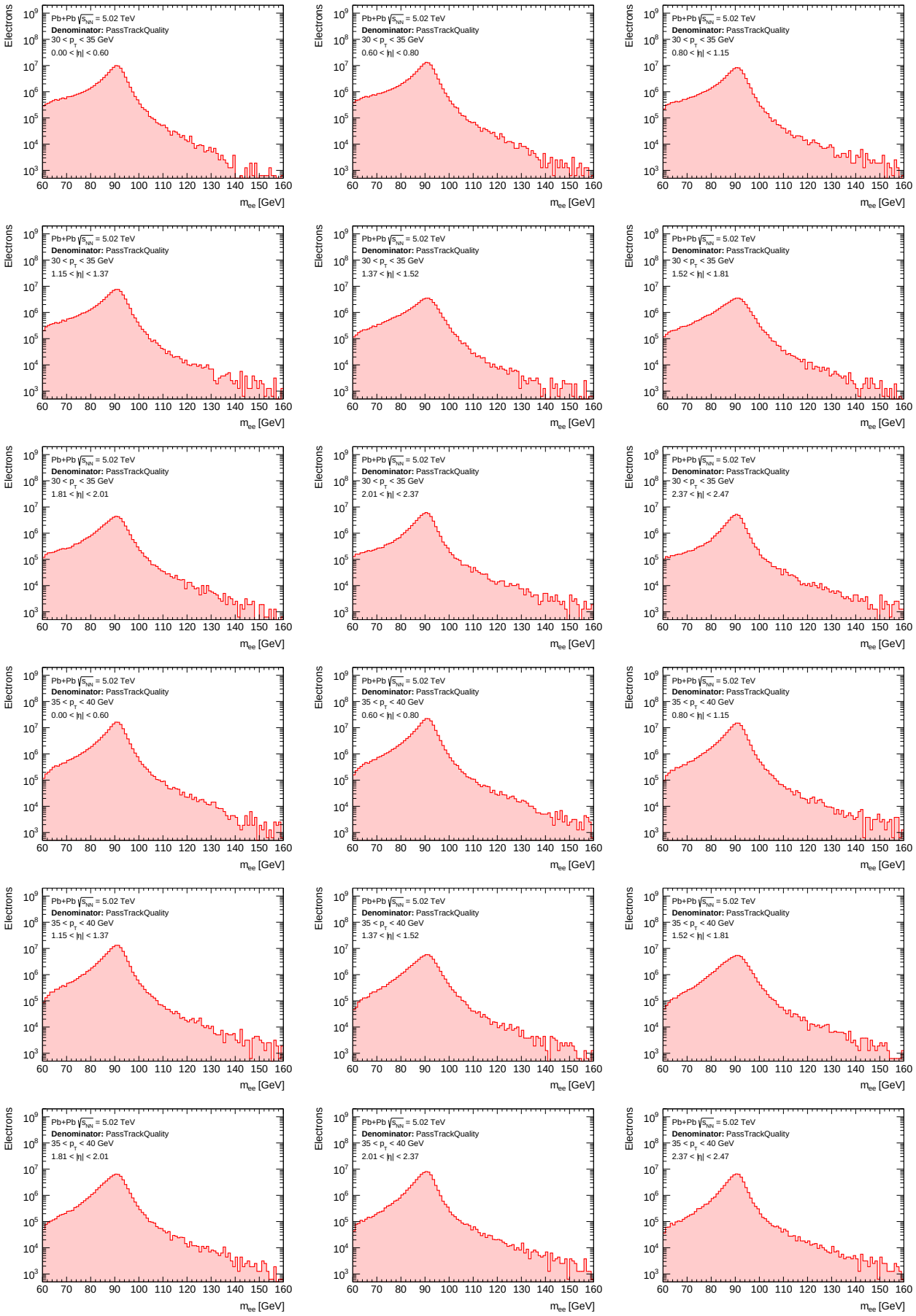
Pb+Pb $\sqrt{s_{NN}}$ = 5.02 TeV
Denominator: PassTrackQuality
30 < p_T < 35 GeV
0.00 < |η| < 0.60
30 < p_T < 35 GeV
0.60 < |η| < 0.80
30 < p_T < 35 GeV
0.80 < |η| < 1.15
30 < p_T < 35 GeV
1.15 < |η| < 1.37
30 < p_T < 35 GeV
1.37 < |η| < 1.52
30 < p_T < 35 GeV
1.52 < |η| < 1.81
30 < p_T < 35 GeV
1.81 < |η| < 2.01
30 < p_T < 35 GeV
2.01 < |η| < 2.37
30 < p_T < 35 GeV
2.37 < |η| < 2.47
35 < p_T < 40 GeV
0.00 < |η| < 0.60
35 < p_T < 40 GeV
0.60 < |η| < 0.80
35 < p_T < 40 GeV
0.80 < |η| < 1.15
35 < p_T < 40 GeV
1.15 < |η| < 1.37
35 < p_T < 40 GeV
1.37 < |η| < 1.52
35 < p_T < 40 GeV
1.52 < |η| < 1.81
35 < p_T < 40 GeV
1.81 < |η| < 2.01
35 < p_T < 40 GeV
2.01 < |η| < 2.37
35 < p_T < 40 GeV
2.37 < |η| < 2.47
Electrons
m_{ee} [GeV]

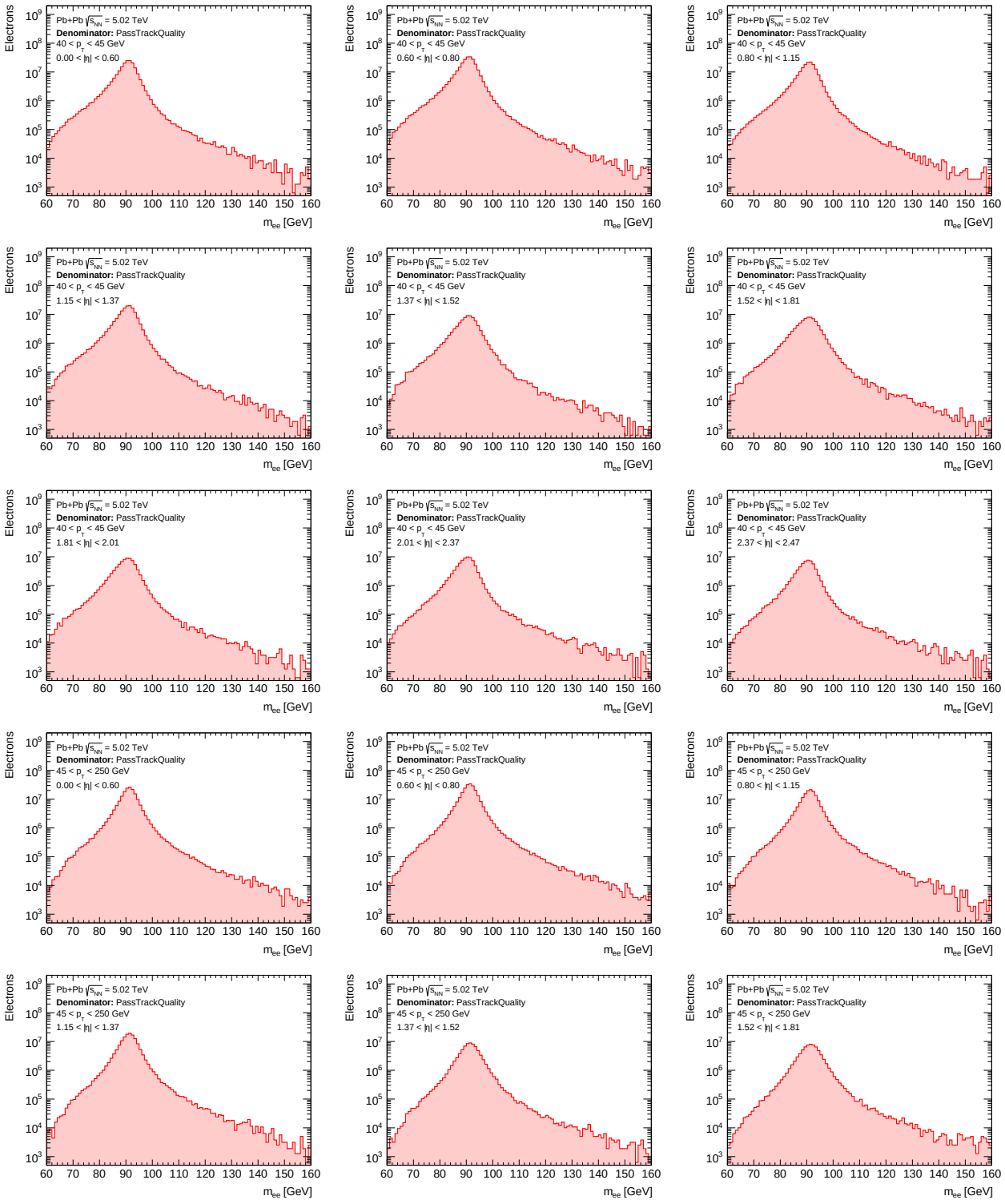
Pb+Pb $\sqrt{s_{NN}}$ = 5.02 TeV
Denominator: PassTrackQuality
40 < p_T < 45 GeV
0.00 < |η| < 0.60
0.60 < |η| < 0.80
0.80 < |η| < 1.15
1.15 < |η| < 1.37
1.37 < |η| < 1.52
1.52 < |η| < 1.81
1.81 < |η| < 2.01
2.01 < |η| < 2.37
2.37 < |η| < 2.47
45 < p_T < 250 GeV
Electrons
m_{ee} [GeV]

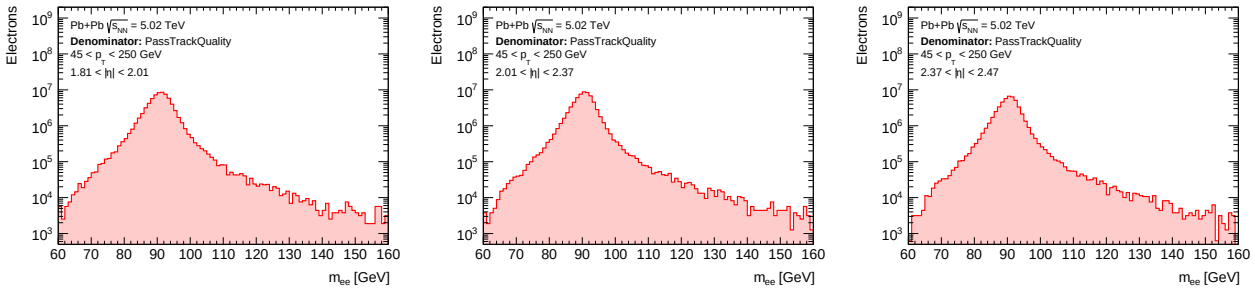

Figure A.36: Invariant-mass distributions of opposite-sign electron pairs with reconstructed probes, constituting the denominator of the identification efficiency, in different electron E_{T} and $|\eta|$ bins.

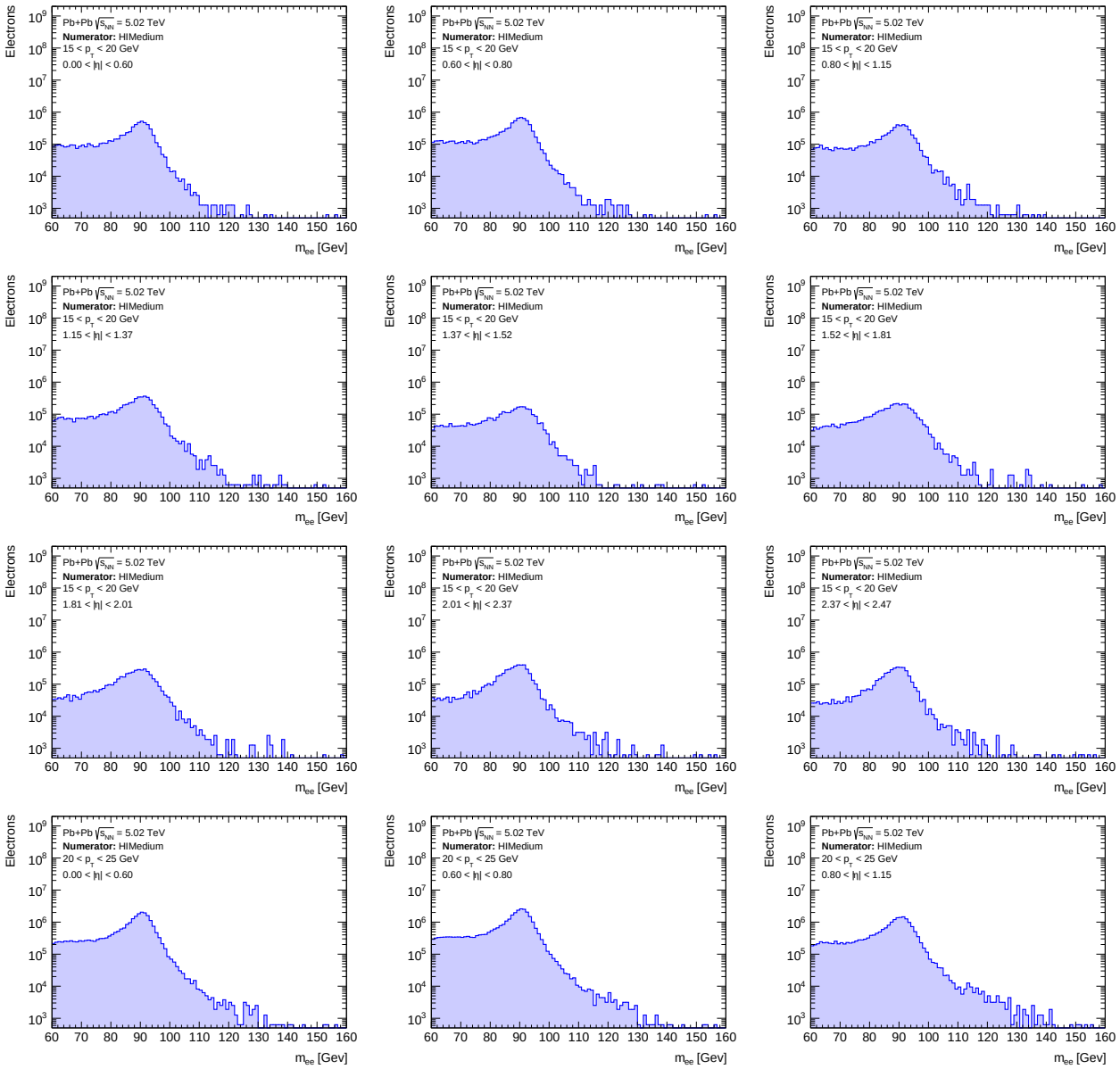

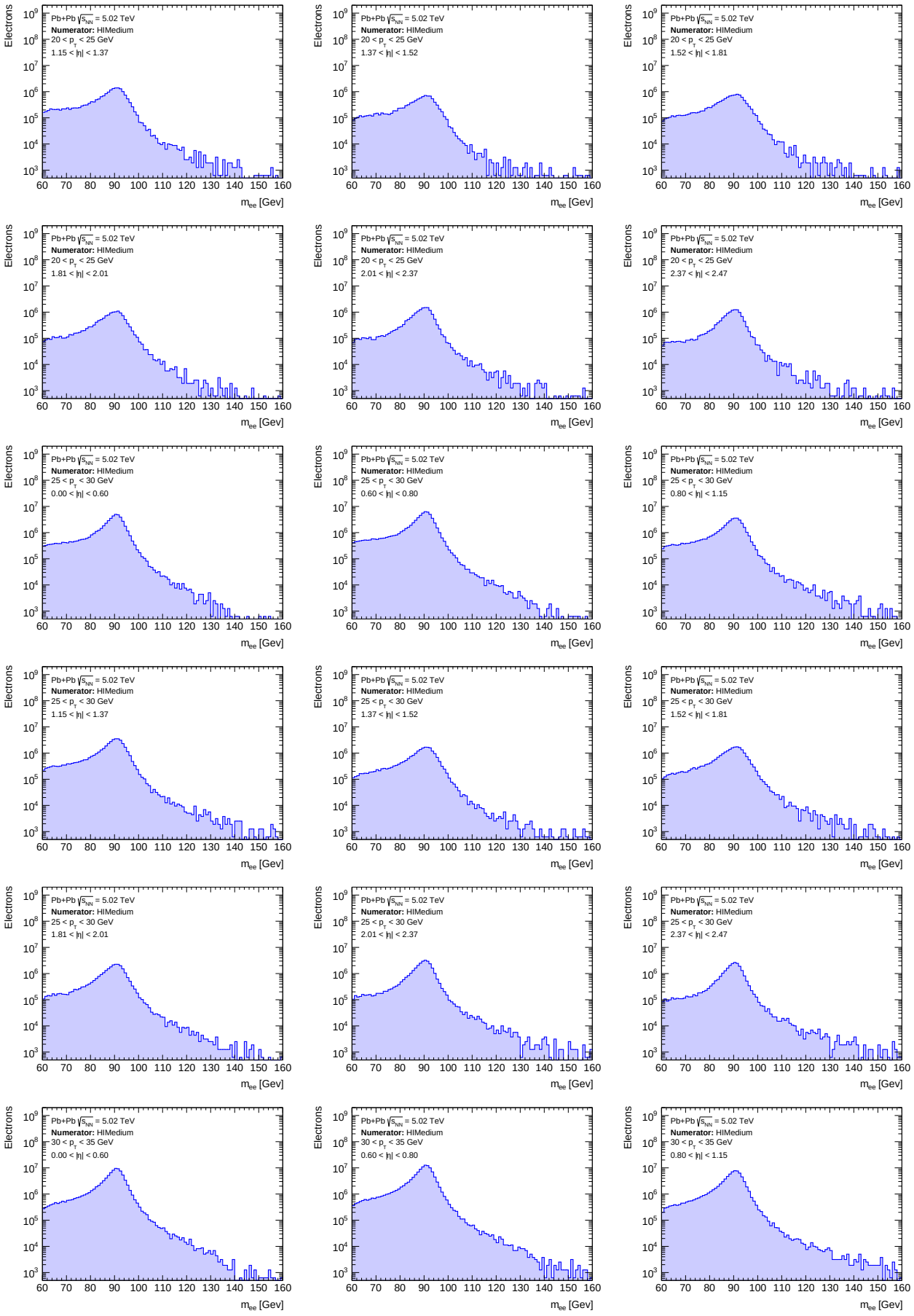
Pb+Pb $\sqrt{s_{NN}}$ = 5.02 TeV
Numerator: HIMedium
20 < p_T < 25 GeV
1.15 < |η| < 1.37
20 < p_T < 25 GeV
1.37 < |η| < 1.52
20 < p_T < 25 GeV
1.52 < |η| < 1.81
20 < p_T < 25 GeV
1.81 < |η| < 2.01
20 < p_T < 25 GeV
2.01 < |η| < 2.37
20 < p_T < 25 GeV
2.37 < |η| < 2.47
25 < p_T < 30 GeV
0.00 < |η| < 0.60
25 < p_T < 30 GeV
0.60 < |η| < 0.80
25 < p_T < 30 GeV
0.80 < |η| < 1.15
25 < p_T < 30 GeV
1.15 < |η| < 1.37
25 < p_T < 30 GeV
1.37 < |η| < 1.52
25 < p_T < 30 GeV
1.52 < |η| < 1.81
25 < p_T < 30 GeV
1.81 < |η| < 2.01
25 < p_T < 30 GeV
2.01 < |η| < 2.37
25 < p_T < 30 GeV
2.37 < |η| < 2.47
30 < p_T < 35 GeV
0.00 < |η| < 0.60
30 < p_T < 35 GeV
0.60 < |η| < 0.80
30 < p_T < 35 GeV
0.80 < |η| < 1.15
Electrons
m_{ee} [Gev]

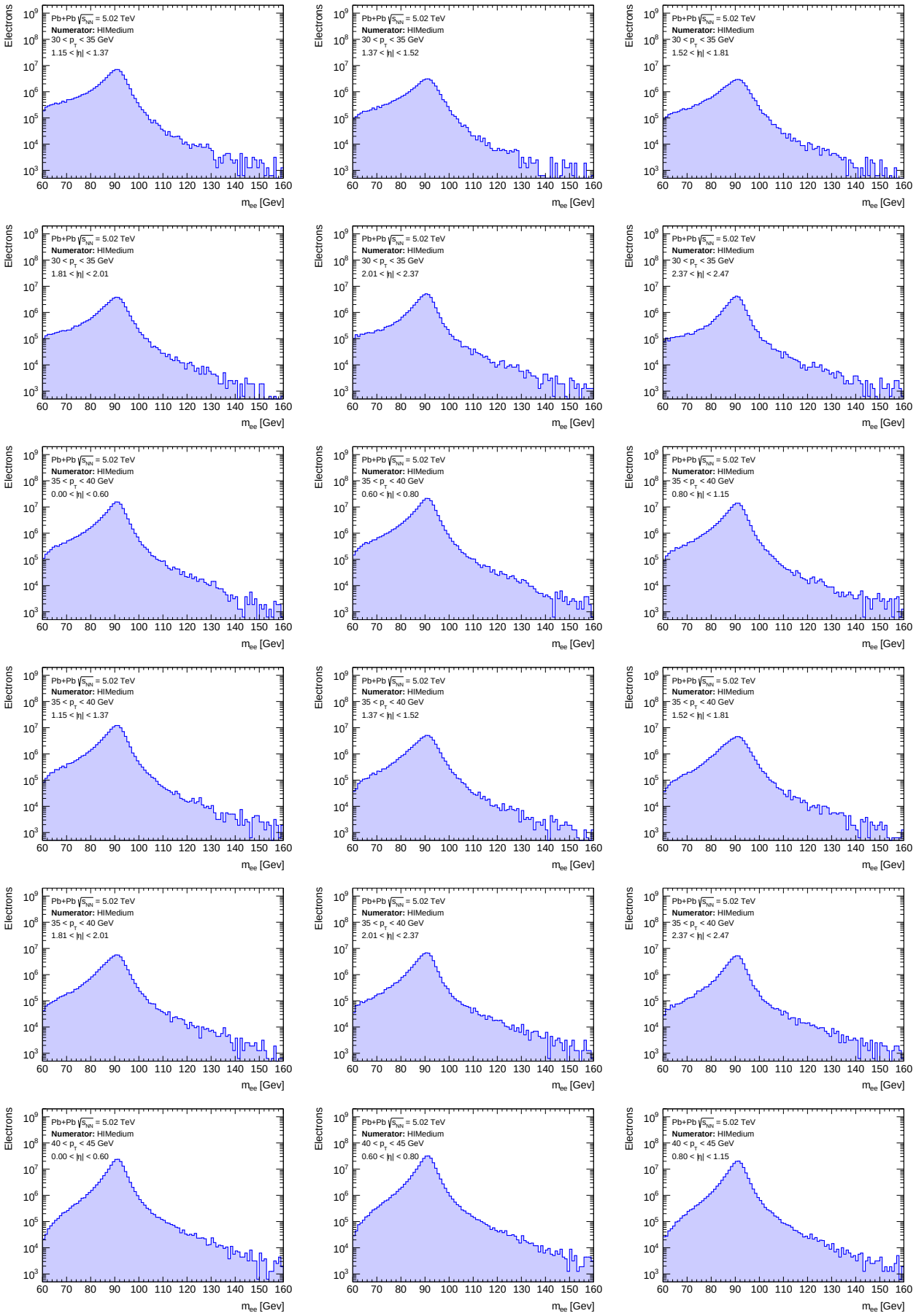
Pb+Pb $\sqrt{s_{NN}}$ = 5.02 TeV
Numerator: HIMedium
30 < p_T < 35 GeV
1.15 < |η| < 1.37
Pb+Pb $\sqrt{s_{NN}}$ = 5.02 TeV
Numerator: HIMedium
30 < p_T < 35 GeV
1.37 < |η| < 1.52
Pb+Pb $\sqrt{s_{NN}}$ = 5.02 TeV
Numerator: HIMedium
30 < p_T < 35 GeV
1.52 < |η| < 1.81
Pb+Pb $\sqrt{s_{NN}}$ = 5.02 TeV
Numerator: HIMedium
30 < p_T < 35 GeV
1.81 < |η| < 2.01
Pb+Pb $\sqrt{s_{NN}}$ = 5.02 TeV
Numerator: HIMedium
30 < p_T < 35 GeV
2.01 < |η| < 2.37
Pb+Pb $\sqrt{s_{NN}}$ = 5.02 TeV
Numerator: HIMedium
30 < p_T < 35 GeV
2.37 < |η| < 2.47
Pb+Pb $\sqrt{s_{NN}}$ = 5.02 TeV
Numerator: HIMedium
35 < p_T < 40 GeV
0.00 < |η| < 0.60
Pb+Pb $\sqrt{s_{NN}}$ = 5.02 TeV
Numerator: HIMedium
35 < p_T < 40 GeV
0.60 < |η| < 0.80
Pb+Pb $\sqrt{s_{NN}}$ = 5.02 TeV
Numerator: HIMedium
35 < p_T < 40 GeV
0.80 < |η| < 1.15
Pb+Pb $\sqrt{s_{NN}}$ = 5.02 TeV
Numerator: HIMedium
35 < p_T < 40 GeV
1.15 < |η| < 1.37
Pb+Pb $\sqrt{s_{NN}}$ = 5.02 TeV
Numerator: HIMedium
35 < p_T < 40 GeV
1.37 < |η| < 1.52
Pb+Pb $\sqrt{s_{NN}}$ = 5.02 TeV
Numerator: HIMedium
35 < p_T < 40 GeV
1.52 < |η| < 1.81
Pb+Pb $\sqrt{s_{NN}}$ = 5.02 TeV
Numerator: HIMedium
35 < p_T < 40 GeV
1.81 < |η| < 2.01
Pb+Pb $\sqrt{s_{NN}}$ = 5.02 TeV
Numerator: HIMedium
35 < p_T < 40 GeV
2.01 < |η| < 2.37
Pb+Pb $\sqrt{s_{NN}}$ = 5.02 TeV
Numerator: HIMedium
35 < p_T < 40 GeV
2.37 < |η| < 2.47
Pb+Pb $\sqrt{s_{NN}}$ = 5.02 TeV
Numerator: HIMedium
40 < p_T < 45 GeV
0.00 < |η| < 0.60
Pb+Pb $\sqrt{s_{NN}}$ = 5.02 TeV
Numerator: HIMedium
40 < p_T < 45 GeV
0.60 < |η| < 0.80
Pb+Pb $\sqrt{s_{NN}}$ = 5.02 TeV
Numerator: HIMedium
40 < p_T < 45 GeV
0.80 < |η| < 1.15
Electrons
m_{ee} [Gev]

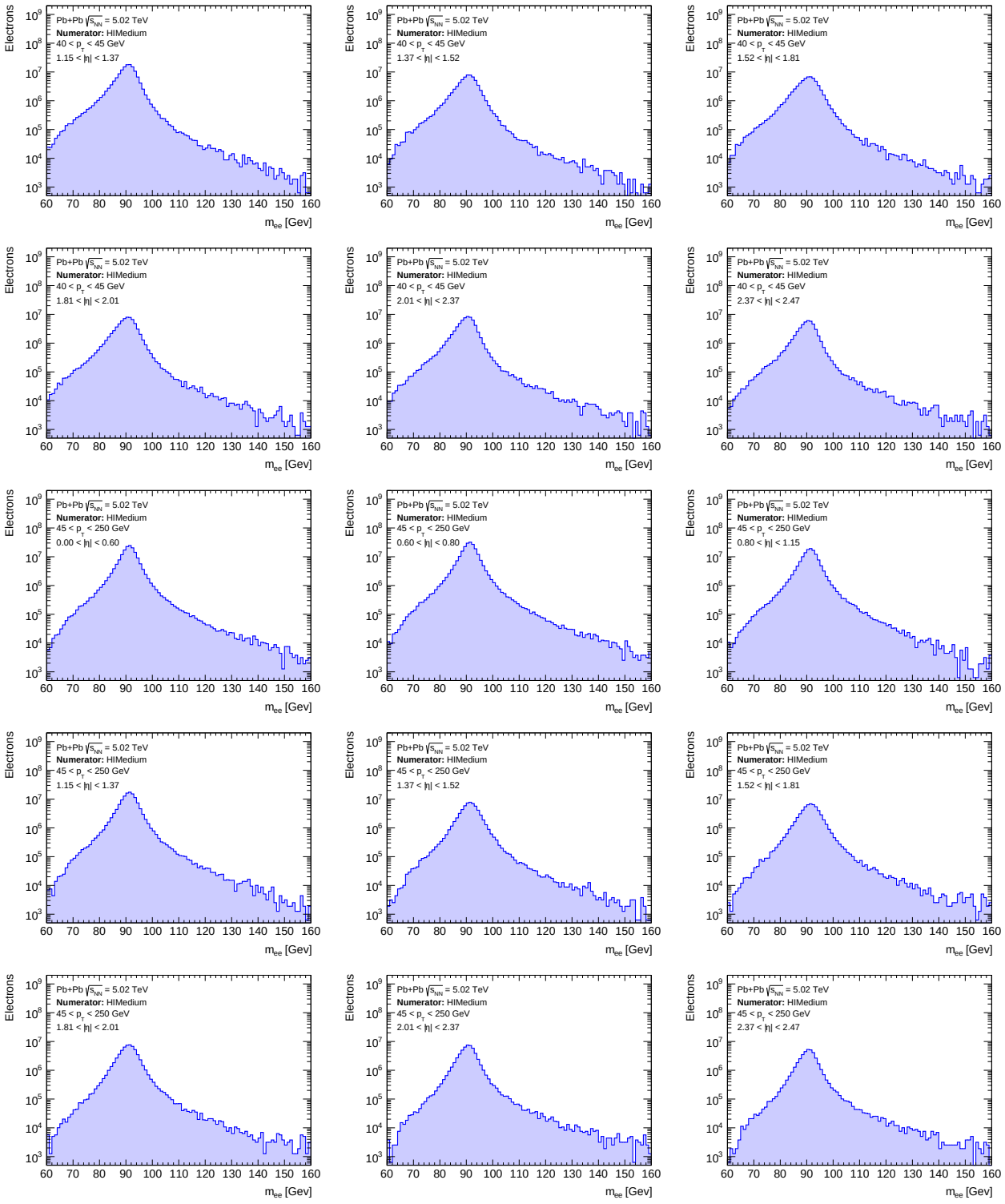

Figure A.37: Invariant mass distributions of opposite-sign electron pairs with probes passing the HIMedium identification requirements, constituting the numerator of the identification efficiency, in different electron E_{T} and $|\eta|$ bins.

A.2.6 Validation of working points

Figures A.38–A.40 present the measured identification efficiency and the relative difference between optimised and measured efficiencies for the HITight, HILoose, and HIVeryLoose working points. Total uncertainties of the measured efficiency are composed of statistical and systematic components added in quadrature. The relative difference is defined as the difference between measured and optimised efficiencies divided by the optimised efficiency.

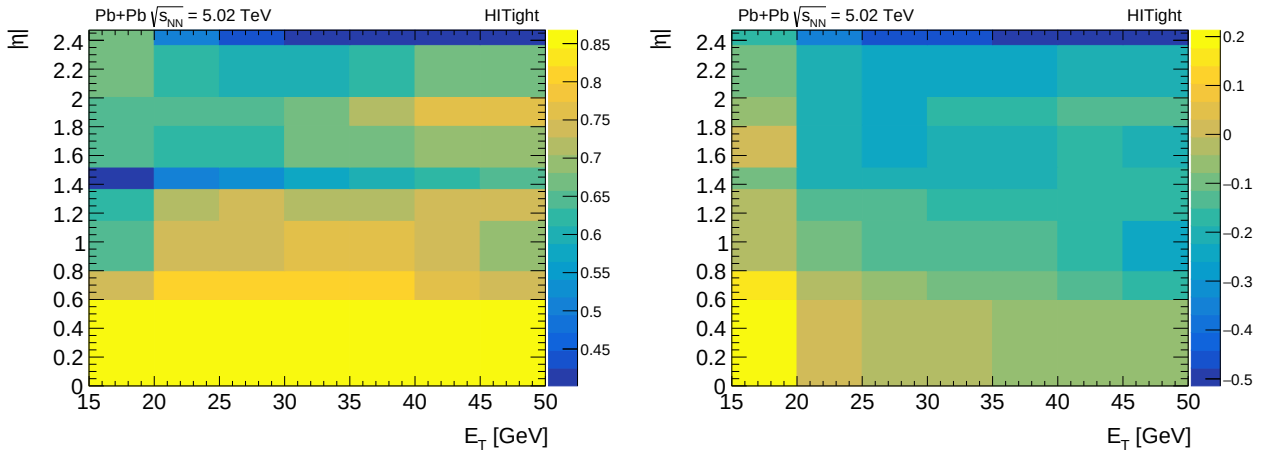

(a) (b)

Figure A.38: (a) The measured identification efficiency and (b) the relative difference between optimised and measured efficiencies as a function of electron E_{T} and $|\eta|$ for the HITight working point.

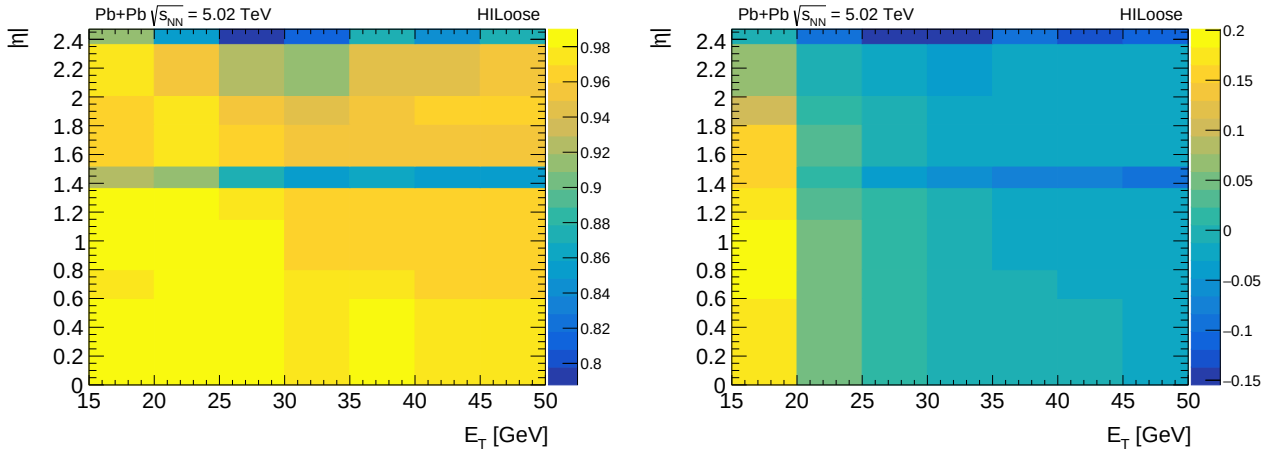

(a) (b)

Figure A.39: (a) The measured identification efficiency and (b) the relative difference between optimised and measured efficiencies as a function of electron E_{T} and $|\eta|$ for the HILoose working point.

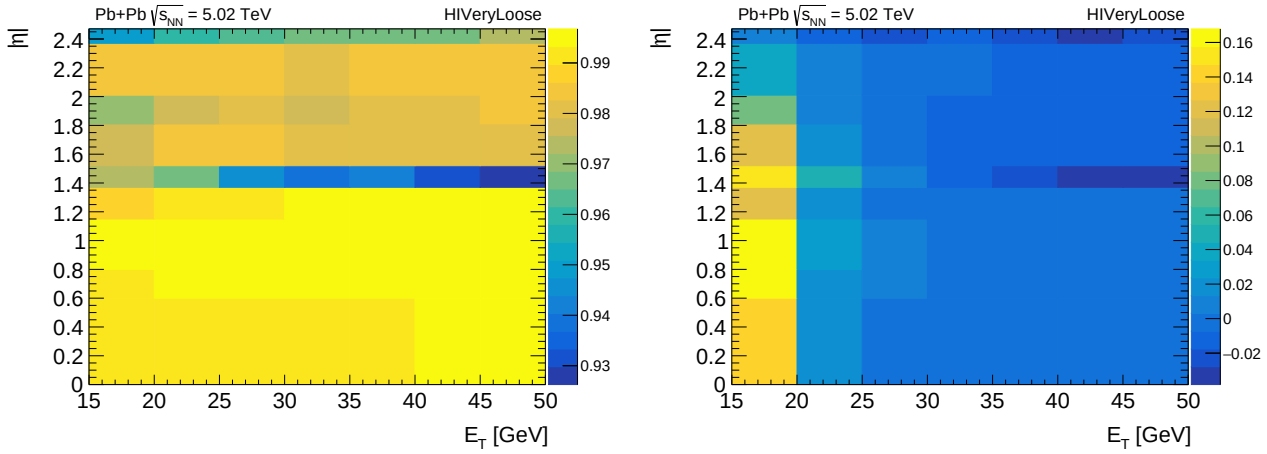

(a) (b)

Figure A.40: (a) The measured identification efficiency and (b) the relative difference between optimised and measured efficiencies as a function of electron E_{T} and $|\eta|$ for the HIVeryLoose working point.

Appendix B

Top-quark pair production in *p*+Pb collisions

B.1 Real-lepton efficiency

Figures B.1 and B.2 present the real-lepton efficiency as a function of lepton p_{T} and η for electrons and muons, respectively.

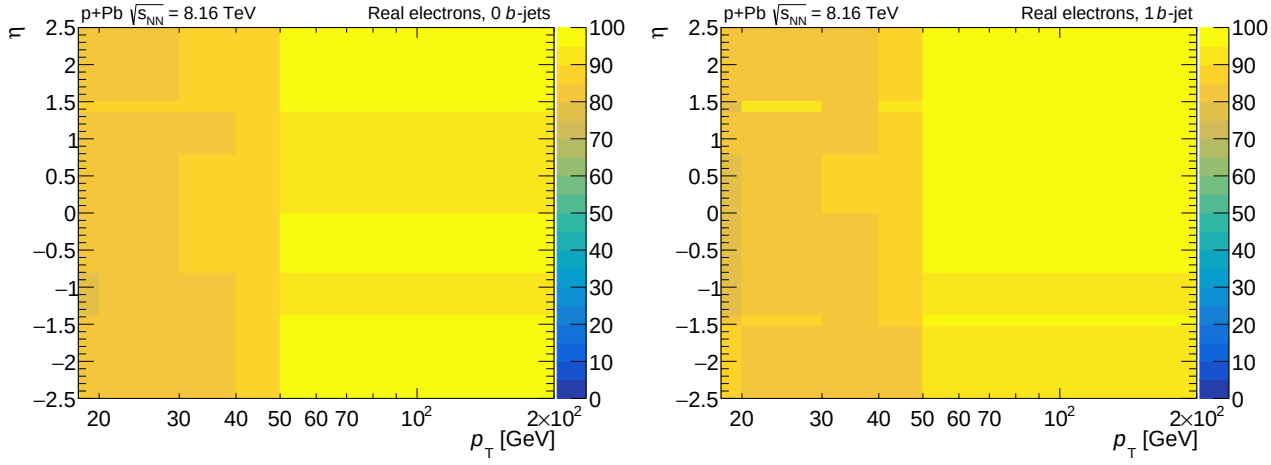

(a) (b)

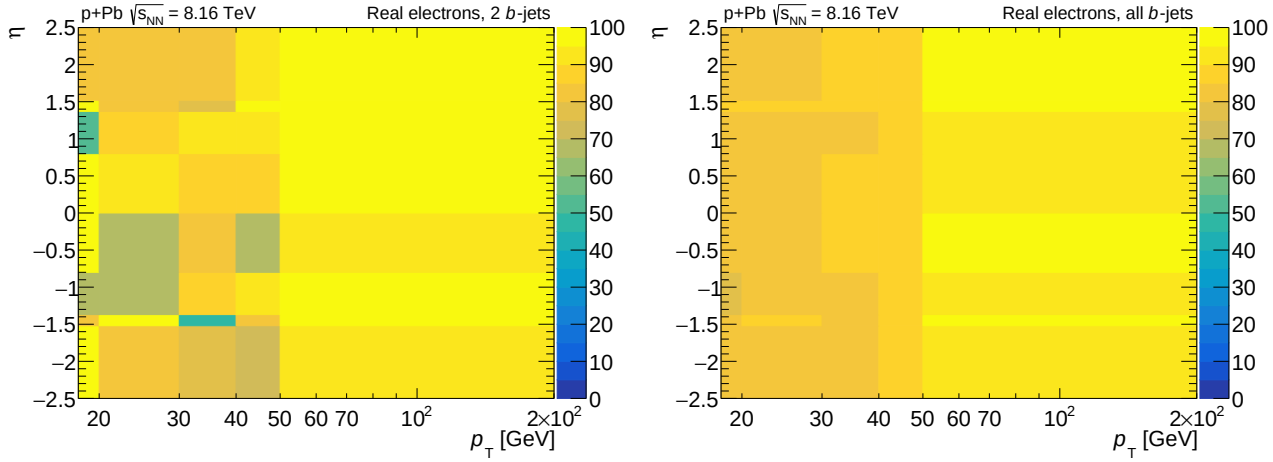

(c) (d)

Figure B.1: The real-lepton efficiency for electrons as a function of electron p_{T} and η for (a) 0, (b) 1, (c) $\geq$2, and (d) inclusive number of b-tagged jets in the event.

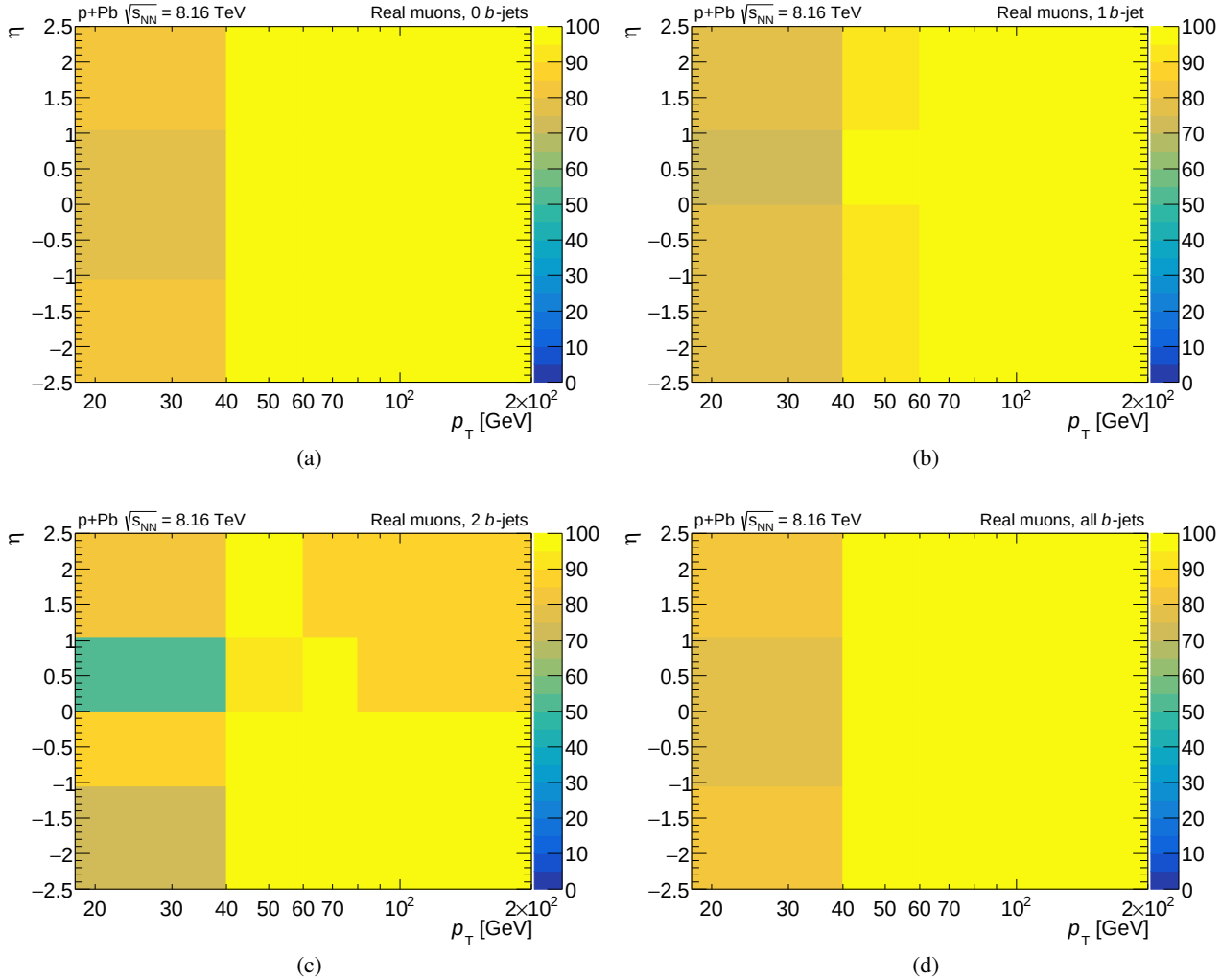

(a) (b)

(c) (d)

Figure B.2: The real-lepton efficiency for muons as a function of muon p_{T} and η for (a) 0, (b) 1, (c) $\geq$2, and (d) inclusive number of b-tagged jets in the event.

B.2 Fake-lepton efficiency

Figures B.3 and B.4 show the fake-lepton efficiency as a function of lepton p_{T} and η for electrons and muons, respectively.

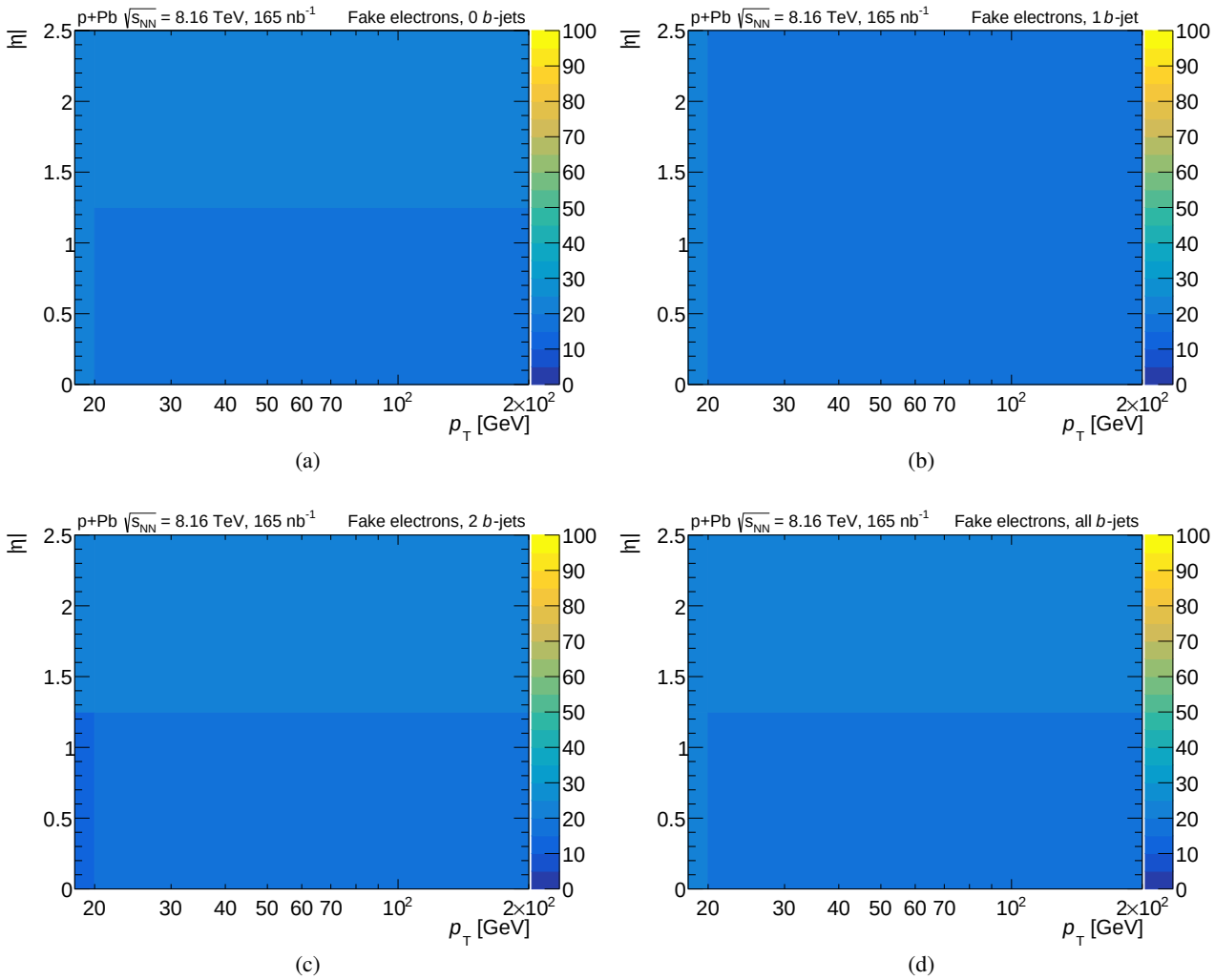

Figure B.3: The fake-lepton efficiency for electrons as a function of electron p_{T} and $|\eta|$ for (a) 0, (b) 1, (c) $\geq$2, and (d) inclusive number of b-tagged jets in the event.

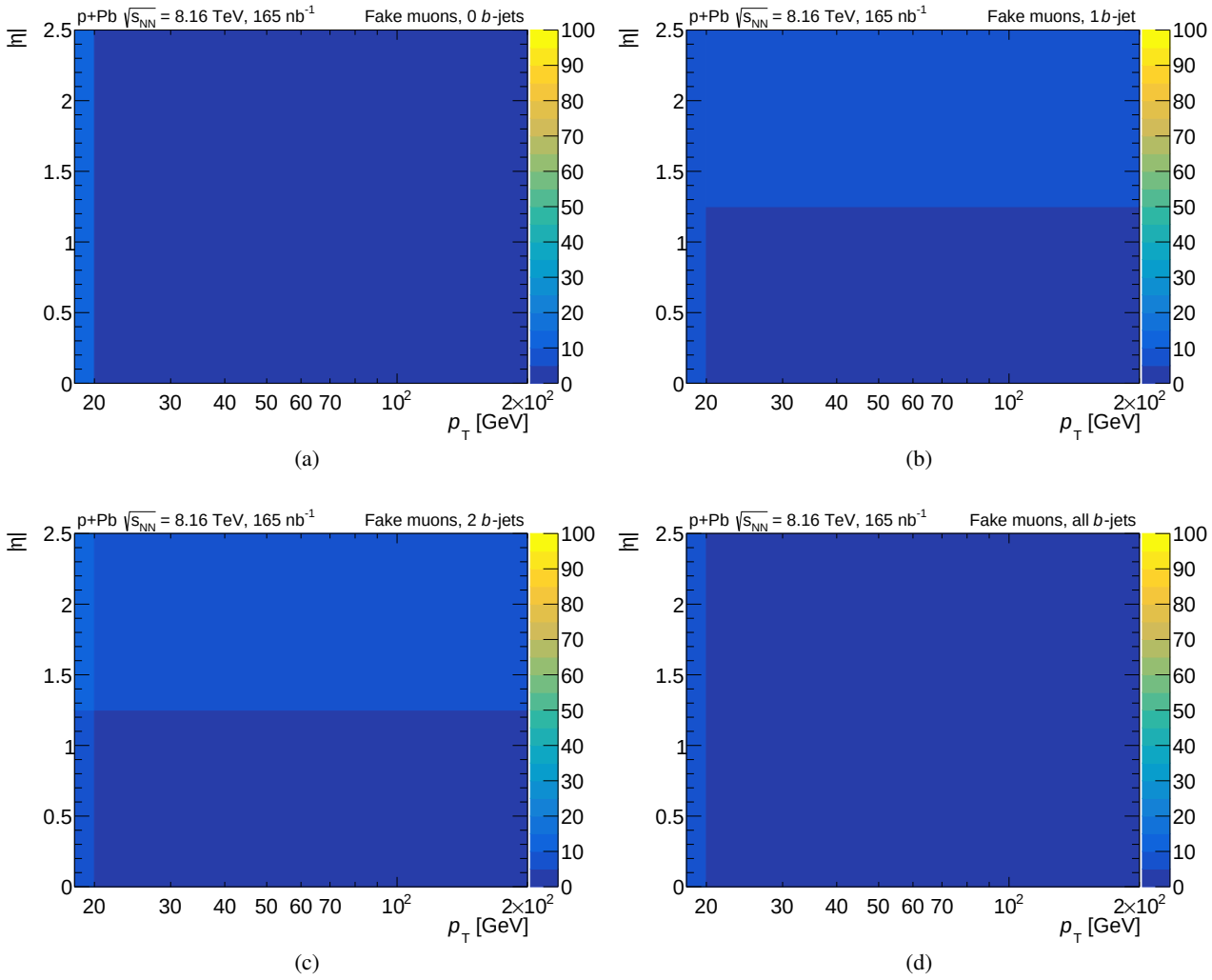

Figure B.4: The fake-lepton efficiency for muons as a function of muon p_{T} and $|\eta|$ for (a) 0, (b) 1, (c) $\geq$2, and (d) inclusive number of b-tagged jets in the event.

Appendix C

Top-quark pair production in Pb+Pb collisions

C.1 Lepton isolation

Figures C.1–C.4 show distributions of calorimeter and track isolation variables for electrons and muons in the $e\mu$, ee, and $\mu\mu$ channels.

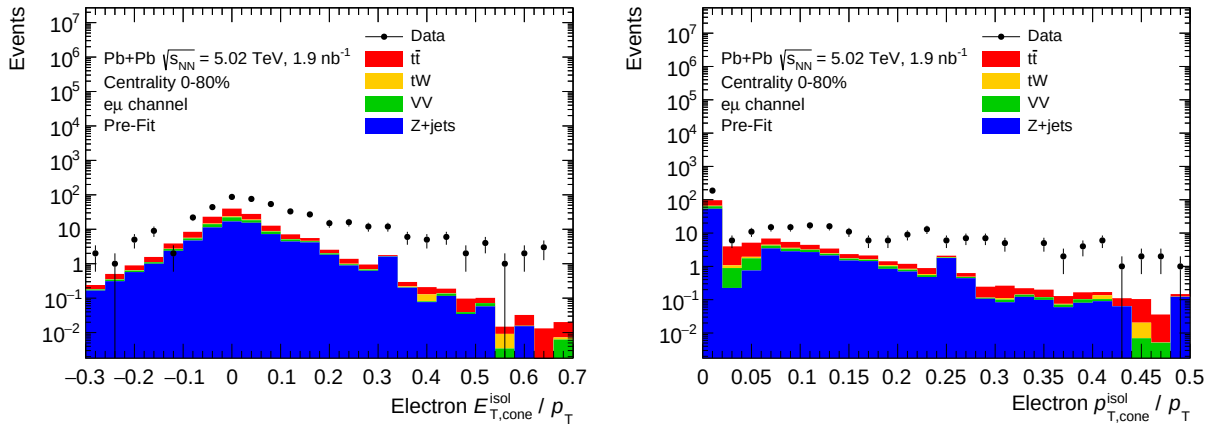

(a) (b)

Figure C.1: Distributions of (a) calorimeter and (b) track isolation variables for electrons in the $e\mu$ channel.

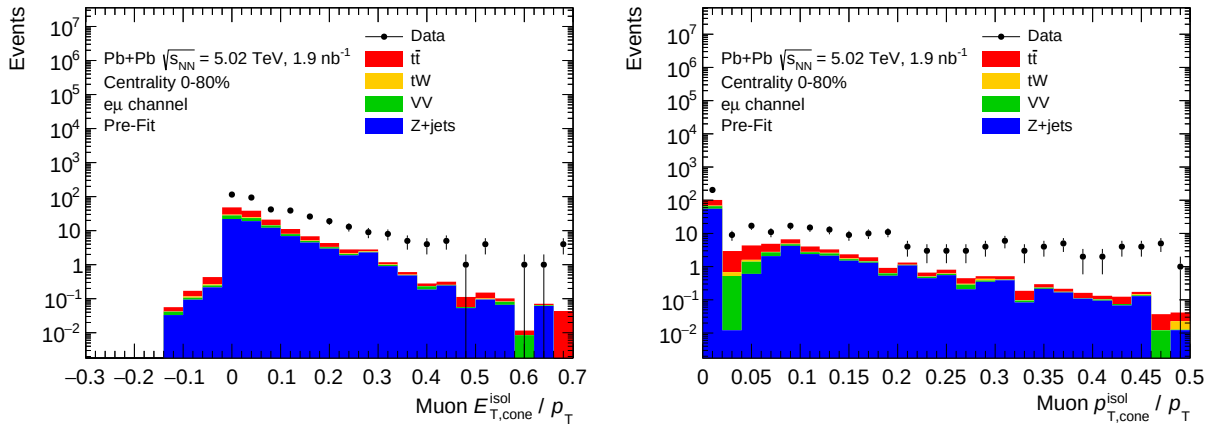

(a) (b)

Figure C.2: Distributions of (a) calorimeter and (b) track isolation variables for muons in the $e\mu$ channel.

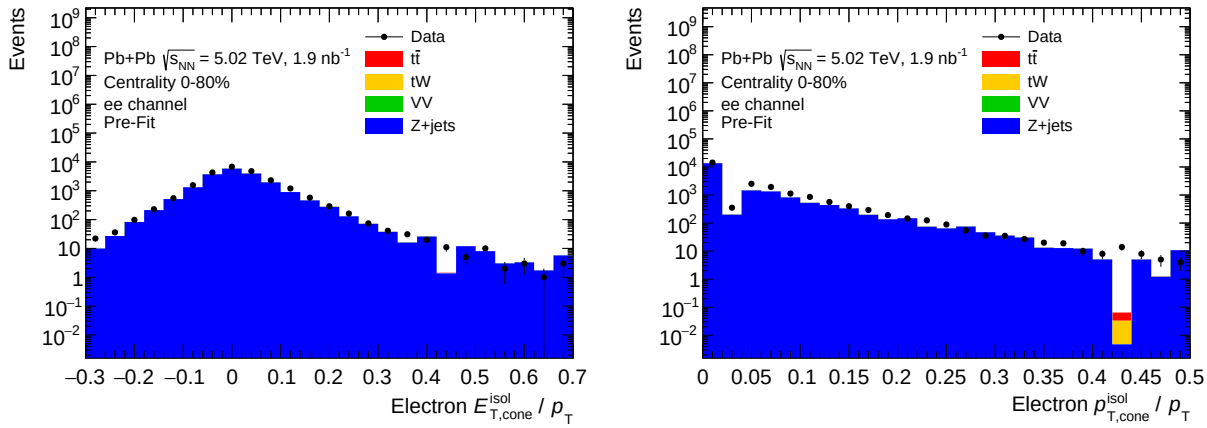

(a) (b)

Figure C.3: Distributions of (a) calorimeter and (b) track isolation variables for electrons in the ee channel.

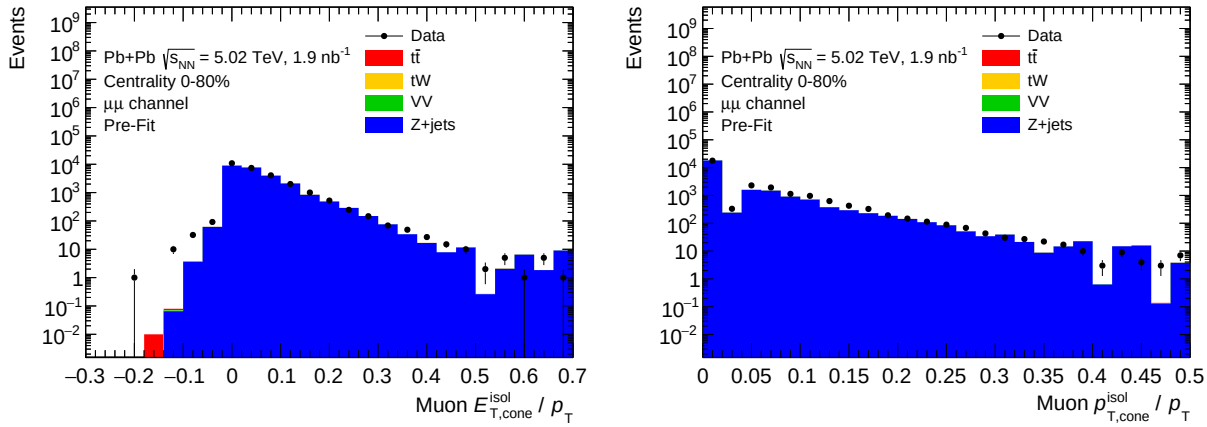

(a) (b)

Figure C.4: Distributions of (a) calorimeter and (b) track isolation variables for muons in the $\mu\mu$ channel.

C.2 Fake-lepton estimation

Figure C.5 presents the number of events in the ee and $\mu\mu$ channels in the A–D regions in fake-lepton estimation.

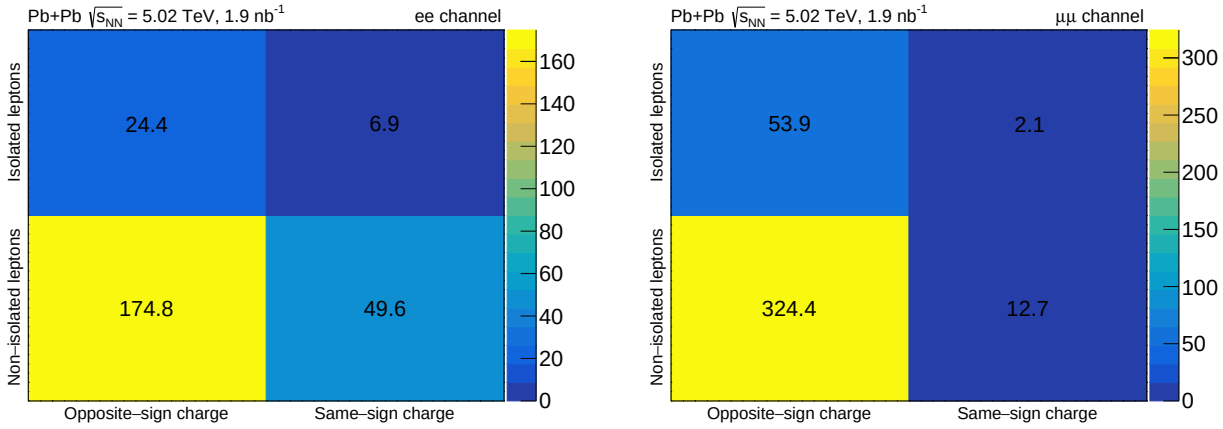

(a) (b)

Figure C.5: Number of events in the regions in fake-lepton estimation in the (a) ee and (b) $\mu\mu$ channels.

C.3 Boosted decision tree

Figure C.1 shows distributions of all 11 input variables used in the training of the BDT classifier.

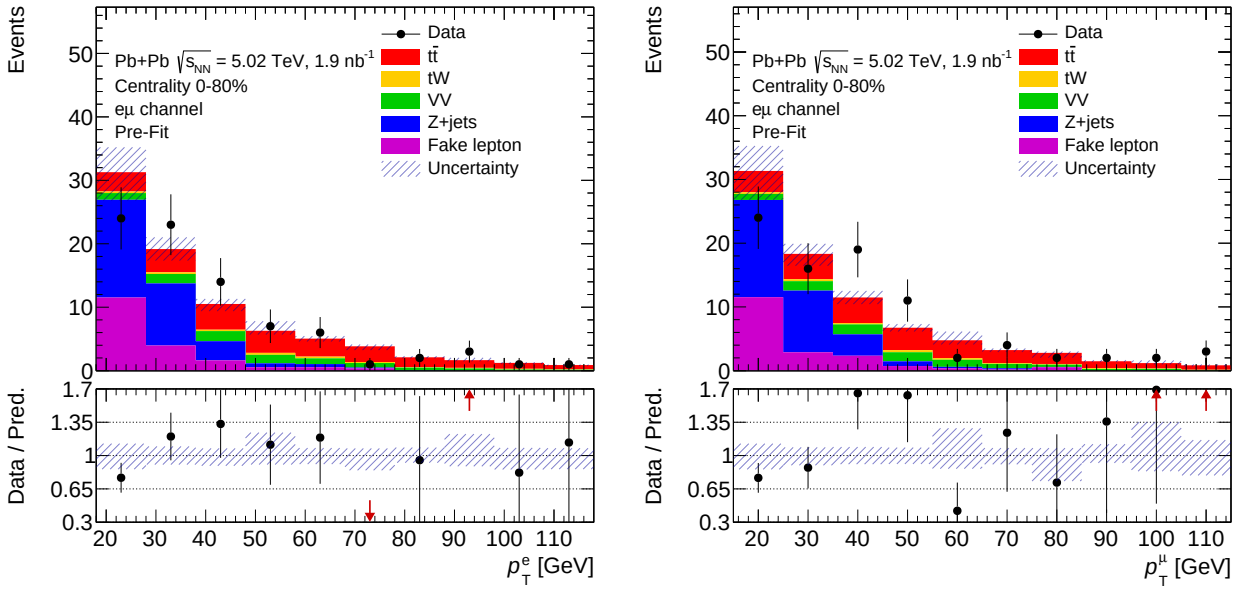

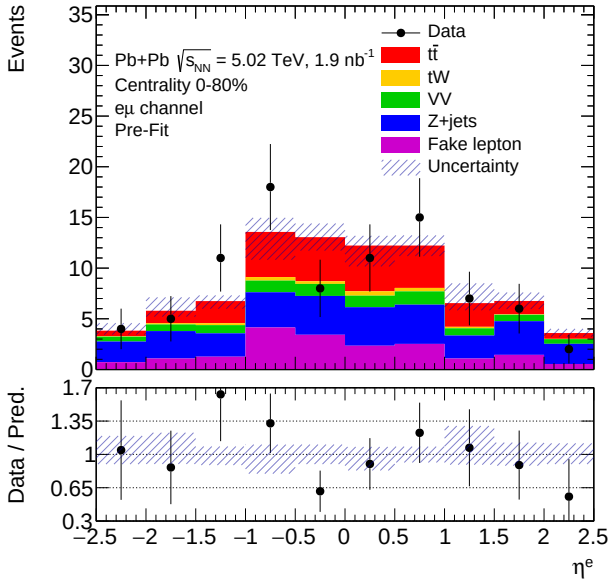
Events
Data / Pred.
Data
tt̄
tW
VV
Z+jets
Fake lepton
Uncertainty
Pb+Pb √s_NN = 5.02 TeV, 1.9 nb^-1
Centrality 0-80%
eμ channel
Pre-Fit
η^e

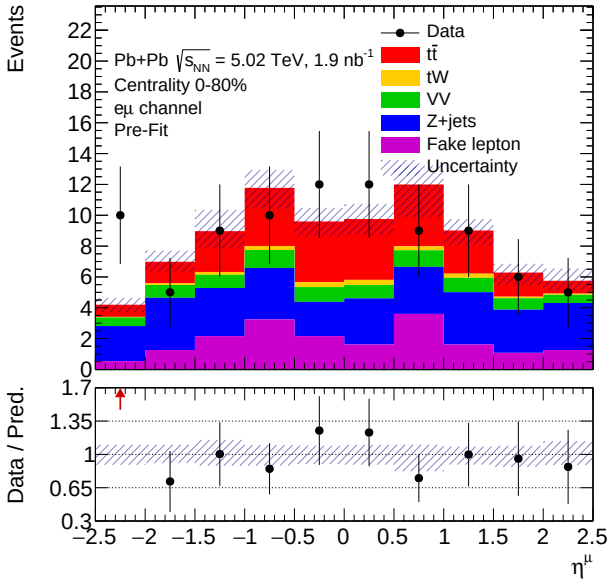
Events
Data / Pred.
Data
tt̄
tW
VV
Z+jets
Fake lepton
Uncertainty
Pb+Pb √s_NN = 5.02 TeV, 1.9 nb^-1
Centrality 0-80%
eμ channel
Pre-Fit
η^μ

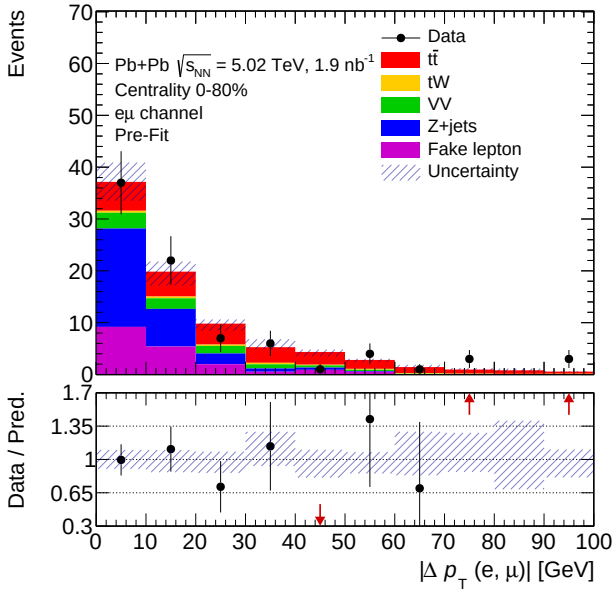
Events
Data / Pred.
Data
tt̄
tW
VV
Z+jets
Fake lepton
Uncertainty
Pb+Pb √s_NN = 5.02 TeV, 1.9 nb^-1
Centrality 0-80%
eμ channel
Pre-Fit
|Δ p_T (e, μ)| [GeV]

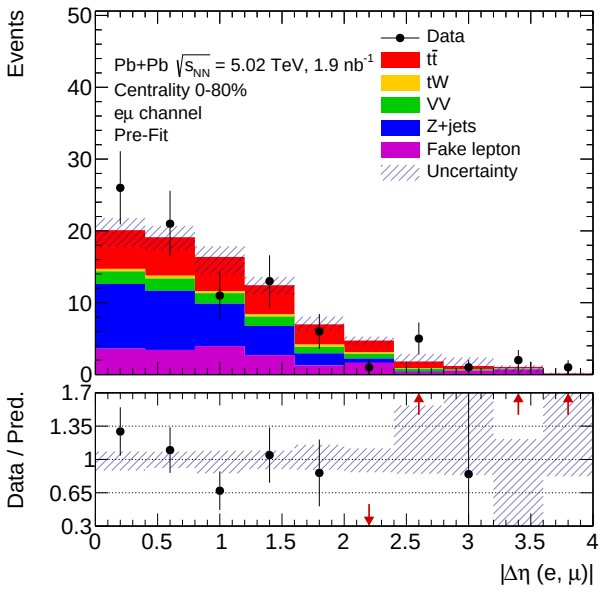
Events
Data / Pred.
Data
tt̄
tW
VV
Z+jets
Fake lepton
Uncertainty
Pb+Pb √s_NN = 5.02 TeV, 1.9 nb^-1
Centrality 0-80%
eμ channel
Pre-Fit
|Δη (e, μ)|

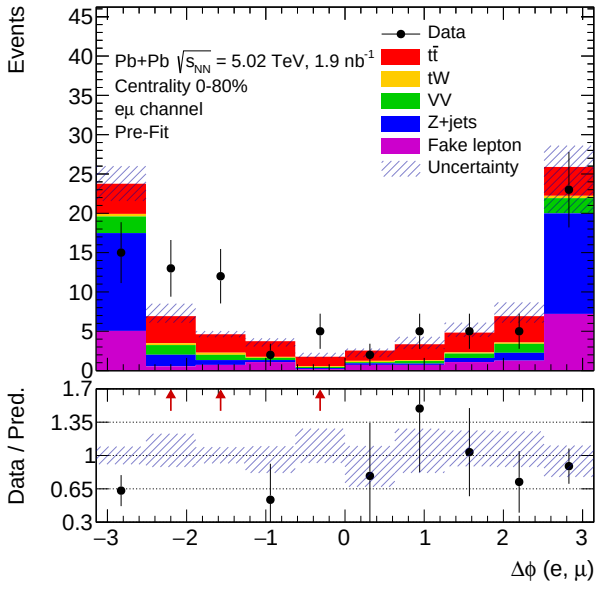
Events
Data / Pred.
Data
tt̄
tW
VV
Z+jets
Fake lepton
Uncertainty
Pb+Pb √s_NN = 5.02 TeV, 1.9 nb^-1
Centrality 0-80%
eμ channel
Pre-Fit
Δφ (e, μ)

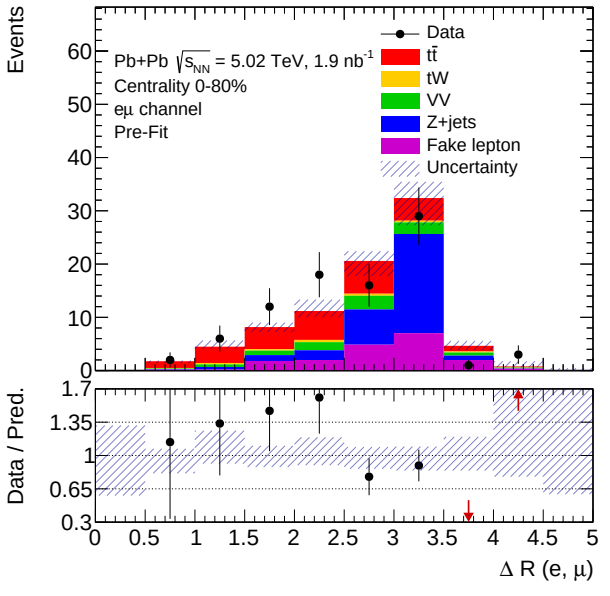
Events
Data / Pred.
Data
tt̄
tW
VV
Z+jets
Fake lepton
Uncertainty
Pb+Pb √s_NN = 5.02 TeV, 1.9 nb^-1
Centrality 0-80%
eμ channel
Pre-Fit
Δ R (e, μ)

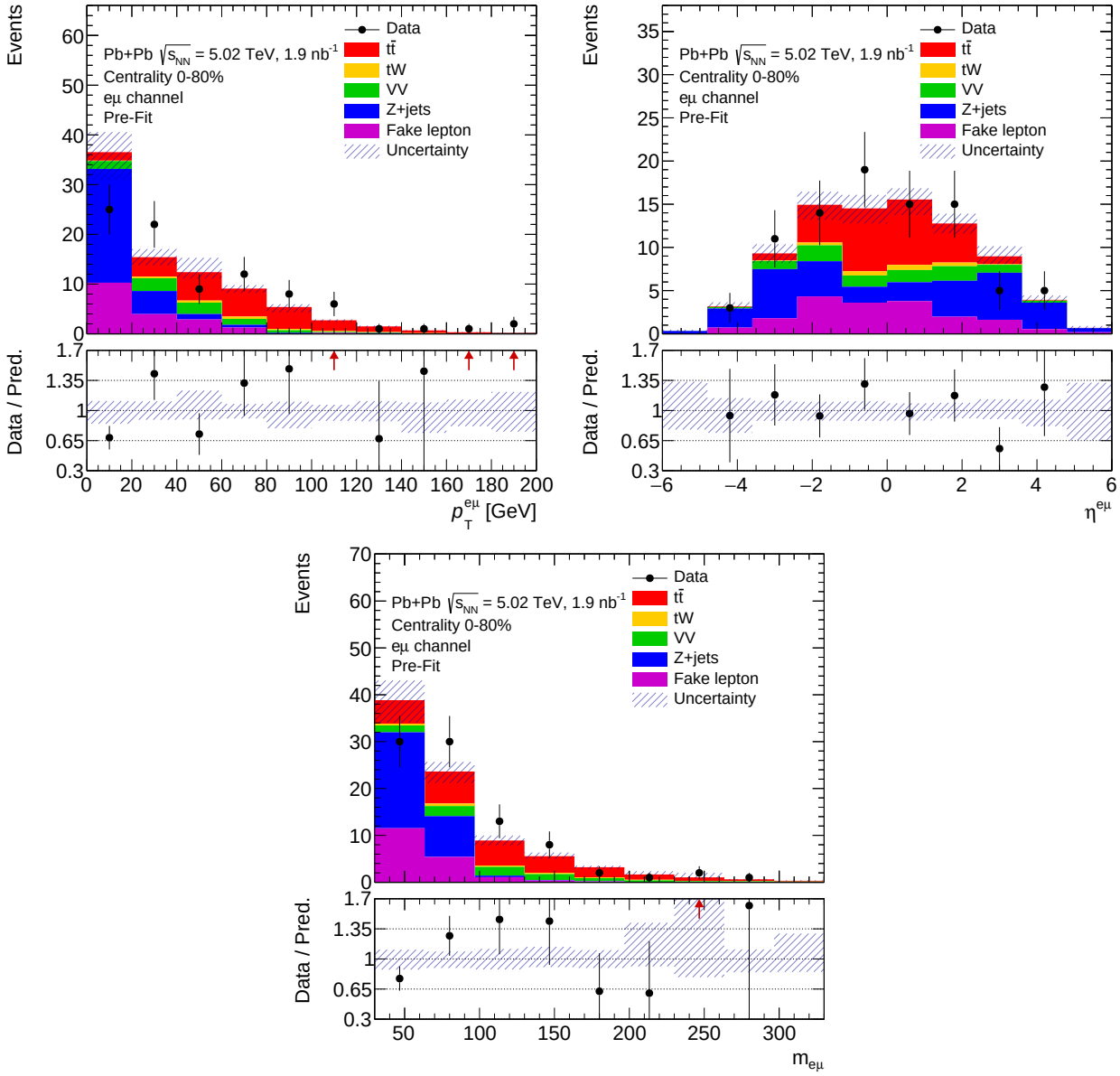

Figure C.1: Distributions of input variables used in the BDT classifier.